**Title**
Interactions of Plutonium and Neptunium with Iron Oxide Minerals Goethite and Hematite



**Author**
Wang, Deborah

**Publication Date**
2017

Peer reviewed|Thesis/dissertation

# Interactions of Plutonium and Neptunium with Iron Oxide Minerals Goethite and Hematite

by

Deborah L. Wang

A dissertation submitted in partial satisfaction of the

requirements for the degree of

Doctor of Philosophy

in

Chemistry

in the

Graduate Division

of the

University of California, Berkeley

Committee in charge:

Professor Darleane C. Hoffman, Chair
Professor Joseph Cerny
Professor John Arnold
Professor Karl van Bibber

Spring 2017

Interactions of Plutonium and Neptunium with Iron Oxide Minerals Goethite and Hematite

# ABSTRACT

Interactions of Plutonium and Neptunium with Iron Oxide Minerals Goethite and Hematite

by

Deborah L. Wang

Doctor of Philosphy in Chemistry

University of California, Berkeley

Professor Darleane C. Hoffman, Chair

The presence of actinides in the environment is a major concern due to their radiotoxicity and long-lived radioisotopes. Two notable examples of such are plutonium-239 (Pu-239) with half-life of ~24,000 years and neptunium-237 (Np-237) with half-life of ~2,000,000 years. Actinide migration is strongly affected by their interactions at the solid/water interface, such as sorption onto soils and sediments, and leads to the importance of understanding actinide sorption processes with environmental matrices, which contributes to accurate prediction of actinide mobility rates and development of transport models. Additionally, migration of actinides must be considered for safety assessment of long-term geological nuclear waste storage and help demonstrate good stewardship at radioactively contaminated sites. Therefore, an understanding of the interactions of actinides in the environment, with a particular focus on the sorption processes that may immobilize actinides, is of utmost importance to increasing knowledge of contaminant transport in environmental systems.

Investigations of the interactions of plutonium and neptunium with the iron oxide minerals goethite and hematite are presented in this work. A primary focus was to examine Pu(VI) sorption to goethite and 1% Al-substituted goethite at a fundamental level. The chemistry of plutonium is extremely complex, especially regarding solubility and oxidation state, with four different oxidation states accessible under various environmental conditions. The more oxidized forms [Pu(V) and Pu(VI)] are generally more soluble in aqueous solutions than the reduced forms [Pu(III) and Pu(IV)], and thus more mobile in oxic conditions. This underscores the importance of investigating plutonium sorption behavior of the more oxidized and soluble Pu(VI). Goethite is one of the most prevalent iron oxides in the environment. Because aluminum is often found as a minor component associated with minerals, a 1% Al-substituted goethite serves as an example of goethite as it might occur in nature.

Batch sorption experiments of plutonium on goethite and 1% Al-substituted goethite were conducted as a function of pH and contact time. Plutonium exhibits a complex sorption behavior with both minerals, and the data suggest sorption equilibration is reached after 7 days. As plutonium sorbed to a mineral surface will be less mobile, the presence of goethite in the environment can contribute to plutonium retardation. The complex sorption behavior indicates

the sorption process might involve a redox transformation. X-ray absorption spectroscopy (XAS) experiments were performed to directly determine, *in-situ*, the oxidation state of plutonium sorbed to goethite. X-ray absorption near-edge structure (XANES) measurements show the coexistence of multiple plutonium oxidation states, indicating reduction of Pu(VI) to the more insoluble Pu(IV). The extent of plutonium reduction was correlated with solution pH increasing across the point of zero charge (PZC) of goethite. This suggests the reduction of Pu(VI) to Pu(IV) is via a surface-mediated mechanism.

Another primary focus of this work was to examine the effect of temperature and ionic strength on Np(V) sorption to hematite. Numerous studies have been undertaken concerning the sorption behavior of neptunium with a multitude of mineral surfaces. However, most experiments have been conducted at ambient conditions, not under nuclear waste repository conditions. There is relatively little information regarding neptunium sorption at the varying temperatures encountered in nature or at the elevated temperatures (~80 °C) or ionic strengths expected in sealed geological repositories for nuclear waste. Understanding actinide sorption over a range of temperatures and ionic strengths is critical for predicting the chemical behavior of actinides for remediation efforts and for the storage of nuclear waste. Np-237 was chosen as the radionuclide of interest because of its long half-life and high levels in spent nuclear fuel (SNF). Np(V) also serves as a stable chemical analog for Pu(V), which is difficult to study experimentally due to plutonium's extreme redox sensitivity. Hematite was chosen as the solid phase because of its prevalence in nature, and also is representative of corrosion by-products expected to occur in future nuclear waste repositories when SNF will be stored in steel canisters.

Batch sorption experiments were conducted as a function of pH for temperatures of 25 °C, 35 °C, 50 °C, and 75 °C for ionic strengths of 0.01 M $NaClO_4$, 0.1 M $NaClO_4$, and 1 M $NaClO_4$. Np(V) sorption to hematite is temperature dependent, as greater sorption was observed with increasing temperature. Displacement of the hydrating waters may be the driving force behind the increased sorption, and the cause is postulated based on removal of water molecules from the primary hydration sphere to bulk water being entropically-driven. The positive entropy change that occurs during the sorption reaction is due to the increased disorder in the system as water molecules move from a fully coordinated state in the neptunium hydration sphere to the more disordered state of bulk water. Ionic strength does not have a significant effect on sorption, indicating that the sorption mechanism is based on the formation of inner-sphere Np(V)-hematite complexes. In support, XAS experiments also indicate inner-sphere complexation. Extended X-ray absorption fine structure (EXAFS) spectra and fits show no variation of the Np(V)-hematite complex as temperature and ionic strength are increased.

This work is by no means a complete study of actinide behavior in the environment, but represents a step toward a thorough understanding of the interactions of plutonium and neptunium with the iron oxide minerals goethite and hematite.

For Mommy, Daddy, and Goh

## ACKNOWLEDGEMENTS

*First and foremost, I give thanks to **GOD**. It is in His goodness that I have been abundantly blessed in my life, it is His guiding hand that has brought me to where I am today, and it is only through His strength that I was able to accomplish this work.*

It's a bit surreal to think that my time here at Berkeley is finally coming to a close. The past eight years have amounted to an unexpectedly long journey with many highs and lows, but I've been so very blessed to have a cadre of mentors, colleagues, family and friends to walk beside me along the way. I couldn't name them all, but thank you to the many individuals who have immeasurably helped me, both in grad school and in my life.

**Mommy**, **Daddy**, and **Goh** – I can never say "Thank you" enough. Thank you for your ceaseless support, encouragement, and prayers. Thank you for calming me down and reassuring me that everything would be okay whenever I was stressed, anxious, or panicked. Thank you for your patience and understanding all these years. Thank you for always being there for me. And thank you for your unconditional love.

To the **Nitsche Group**: Oh goodness, where do I even start? Thank you for your continual support and encouragement and belief in me; I truly could not have done this without all of you. Without a doubt, my grad school experience has been infinitely better because of ya'll. Tashi and Kestrel, thank you for training me in HERL and teaching me the ins and outs of plutonium chemistry. More importantly, thank you for all the happy times we had together, from enjoying long lunches to having to do pushups and crunches to sharing the Pu box to group meeting bingo. **Kestrel**, there're so many memories of our friendship and just to name a few off the top of my head: us fetching the couch, that beamtime where I lost my voice, full/fool and pull/pool, HoC, and Hawaii. **Tashi**, you are an absolute superstar of a scientist, mom, and friend. Not only were you the most patient teacher in HERL, you were so generous with your time to always help me, and always with the best attitude. Your support in all aspects means so much to me. Countless thank yous to the next set of Nitsche Group girls, Jen, Erin, Eva, and Carolina, for all the help in lab and fun times outside of lab. **Jen**, thank you for your invaluable science ideas, sharing your yummy baking creations, going to reactor school together (Del Taco, never again), and being fun and silly. **Erin**, thank you for being the kind and caring person that you are, and for the many parties and dinners that you and Alex have had me over for. **Eva**, thank you for the countless times you've trekked down to HERL on my behalf, for being my Core Blast buddy (eight, another set!), and being a countinuous cheerleader. **Carolina**, thank you for your meticulous lab notebooking skills, your hilariousness, getting coffee with me during the holidays every year, and sharing a love for throwback music from the early 90s. **Oliver**, **Nick**, **Philip**, and **Jeff**: From Pre-Thanksgivings and barbeques to watching GoT episodes to "attending" poster session, most of all, I'll always remember Friday lunches on Euclid with you guys. **Julie**, **Anthony**, and Dan: I couldn't ask for better post docs to work with. **Dan** especially, you've been so much help to me, from NEUP reports to continuously helping with XAS stuff to working out various lab issues. (And so many inside jokes!) Also, a shout-out to **Adam** and Dan for being fantastic officemates. Nitsche Group, I'm so thankful for all my wonderful groupmates and am especially thankful that ya'll are such dear friends. I am pleasured to be able to touch the landscape and feelings of Berkeley with you.

I'd like to express my sincerest gratitude to **Corwin**. You were the best XAS guru I could ask for, with never-ending insight and incredible patience concerning my data analyses.

Thank you also for being a great example that it's possible to be a good scientist and enjoy personal life as well. How many people can say they've had beamtimes with their step-adviser playing WoW at the beamline or going to watch old classics at a retro Hollywood theatre between runs or driving out of the way for a good bowl of ramen?

A great deal of this work was done in HERL, and **Wayne**, I appreciate your help so much. You have always been willing to help, from answering all my HERL questions and issues to reviving the LSC multiple times to unwarily inviting me in your office whenever I knocked on your door, and thank you for that.

There's a multitude of scientific staff that because of their help and support, this work could even happen. From RPG at LBL, there's John, Naomi, Paul, and Israel. From passouts to rad shipments, and contamination issues, thank you for helping me get my science done. (And clean it up when things didn't go so well… That $6 million U-233 spill was fun, huh?) Thank you to the RCTs of SLAC, Carol, Darryl, and Ray for rad support at the beamline, being reasonable about shipments, samples, and training, and bringing me coffee in the wee early morning hours. Thank you also to the SSRL beamline scientists Ryan, Matt, and Jeff for assistance and troubleshooting at 11-2 and 4-1, especially with software crashes and burning through liquid helium.

I'd also like to thank the members of my dissertation committee, Professors Darleane Hoffman, Joe Cerny, John Arnold, and Karl van Bibber for your critical eyes and expeditious review of this work. Darleane, I'm honored to be one of your academic granddaughters.

Before coming to UC Berkeley, the professors of the Chem Dept at Cal Poly helped lay an excellent chemistry foundation for me. Drs. Immoos, Schoonover, and Gragson, thank you for being my advisers and examples of excellent teachers. I have to credit Drs. Hagen and Bush for instilling in me a passion for teaching kids about science. Dean and Dr. Bailey, thank you for the rides home late at night and often having me over for dinner. Thank you all for being mentors in various aspects and helping me get to grad school, but most importantly, thank you all for caring for me.

And finally, **Heino**. Thank you for accepting me into your group and encouraging me to persevere. Thank you for your understanding during the times I was struggling and recognizing my helping others. Thank you for believing in me even when I did not. I'll cherish the memories of going to France together in your last days. I'd also like to extend my heartfelt thanks Martha, who has become a dear friend to me. Heino, I raise a glass to you – it has been an absolute honor to be a part of the Nitsche Group.

# TABLE OF CONTENTS

## LIST OF FIGURES

## LIST OF TABLES

## LIST OF ABBREVIATIONS AND ACRONYMS

| | |
|---|---|
| AEC | anion exchange capacity |
| ccp | cubic close-packed |
| CEC | cation exchange capacity |
| CIP | common intersection point |
| DOE | Department of Energy |
| EDL | electrical double layer |
| EXAFS | extended X-ray absorption fine structure |
| hcp | hexagonally close-packed |
| HIFR | High Flux Isotope Reactor |
| HPGe | high purity germanium |
| IEP | isoelectric point |
| LINAC | linear accelerator |
| LSC | liquid scintillation counting |
| MCA | multichannel analyzer |
| NASA | National Aeronautics and Space Administration |
| NEA | Nuclear Energy Agency |
| NTS | Nevada Test Site |
| NOAA | National Oceanic and Atmospheric Administration |
| OECD | Organisation for Economic Co-operation and Development |
| ORNL | Oak Ridge National Laboratory |
| PMT | photomultiplier tube |
| PZC | point of zero charge |

| | |
|---|---|
| PZNC | point of zero net charge |
| PZNPC | point of zero net proton charge |
| PZSE | point of zero salt effect |
| RSXAP | real-space X-ray analysis package |
| SCM | surface complexation model |
| SHE | standard hydrogen electrode |
| SNF | spent nuclear fuel |
| SRS | Savannah River Site |
| TEM | transmission electron microscopy |
| USGS | United States Geological Survey |
| XANES | X-ray absorption near-edge structure |
| XAS | X-ray absorption spectroscopy |
| XRD | X-ray diffraction |

# 1. INTRODUCTION

A thorough understanding of how actinides interact in the environment is of the utmost importance for a multitude of matters, ranging from the use of nuclear energy to risk assessment purposes in the event of contamination and nuclear weapons disarmament to remediation efforts of radioactively contaminated sites to demonstrating good stewardship at nuclear waste storage sites. Knowledge of actinide behavior contributes to the accurate development of flow and transport models, which in turn greatly aids the prediction of the fate and migration of actinides in various environmental systems.

Actinides are present in the environment from naturally occurring mineral deposits and anthropogenic activities. Decades of radionuclide research, uranium mining and milling, accidents at nuclear reactors, production and testing of nuclear weapons, and inadequate disposal practices associated with these activities has resulted in a whole host of actinide contamination. Of these contaminants, plutonium and neptunium are of particular concern, due to the long-lived radioisotopes Pu-239 and Np-237 and their high radiotoxicity. The biological toxicity stems from the ionic radius being comparable to that of iron. Pu(IV) and Np(V) have similar ionic radii to Fe(III), and consequently can be taken up into the biological iron transport and storage systems of mammals.

In the United States, more than half of legacy Department of Energy (DOE) facilities contain radioactively contaminated soils, sediments, and groundwater.[1–3] At the Hanford Reservation, where the first industrial scale plutonium production occurred, more than 11,000 Ci* of Pu-239 and 55 Ci of Np-237 were disposed of as liquid waste in the near-surface environment.[4–6] More than 240,000 Ci of plutonium contamination (Pu-238, Pu-239, and Pu-240) and almost 50 Ci of Np-237 were deposited in the subsurface at the Nevada Test Site (NTS) as a result of underground tests.[7] At the Savannah River Site (SRS), 16 Ci of plutonium was released into streams, seepage basins, and the atmosphere, and up to 160,000 $m^3$ of liquid waste containing fission products and transuranic elements were directly discharged into the ground at the Oak Ridge Operations site.[8,9]

* In 1975, the General Conference on Weights and Measures declared the becquerel (Bq) as the SI unit of radioactivity, but the curie (Ci) is still widely used, and is the preferred unit for the experiments described in this work. 1 Ci = 3.7 x $10^{10}$ Bq

Actinide contamination is also a worldwide issue, ranging from accidents at nuclear reactors and transporting nuclear material. The 1986 reactor explosion at the Chernobyl Nuclear Power Plant released 23 kg of plutonium isotopes totaling 180 Ci into the surrounding area.[10] At the Mayak Production Association in Urals, Russia, Novikov *et al*. measured plutonium more than 4 km away from where waste effluent was discharged into Lake Karachai.[11] Other examples include an aircraft accident resulting in two damaged nuclear weapons in Palomares, Spain[12], the Sellafield nuclear fuel reprocessing plant in Great Britain, and releases into the nearby sea from the La Hague reprocessing plant in France[13].

These are just a few examples of radioactively contaminated sites that require reliable risk assessment. Additionally, the importance of understanding the reactions of actinides in the environment, especially processes at the solid/solution interface, which contribute to migration of contaminants is illustrated.

Today, there exists an urgent need for cleaner energies, and the use of nuclear power is a promising alternative to accomplish such. Spent nuclear fuel (SNF), fuel after it has been used and removed from commercial nuclear reactors, is a complex mixture of uranium and other radionuclides including strontium, cesium, plutonium, neptunium, and curium. A report by the National Academy of Sciences endorsed geological repositories for safely and securely isolating nuclear waste from humans and the environment.[14] Consensus of the international scientific community also agrees, and consequently, Sweden, Finland, Great Britain, and China are actively considering locations for geological repositories as the optimal method for dealing with nuclear waste.[15] Hence, most SNF is destined for long-term storage in a nuclear repository.

As time passes, the chemistry of SNF changes. The major contributors initially are the highly radioactive fission products, such as Cs-137 and Sr-90. With relatively short half-lives, these fission products will have decayed away in a few hundred years. After hundreds of thousands of years then, it is the long-lived radionuclides, such as Tc-99, I-129, Np-237, Pu-239, and Am-241, that will dominate. Also on that time scale, it is expected that the infrastructure of repositories will be subject to elevated temperatures. Figure 1.1 shows the activity of selected radionuclides in SNF after uranium separation as a function of time for a million years[16,17] and Figure 1.2 shows the expected temperature distribution after 1000 years in the proposed Yucca Mountain repository[18]. The radioactive decay of actinides such as Np-237, Pu-239, and Am-241 will generate heat for an extended period of time, and thus result in elevated temperatures (~80 °C) in a nuclear waste repository. Np-237 is the daughter product from α decay of Am-241, which also adds to the increasing radioactivity in SNF.

A main concern of emplacing nuclear waste in geological repositories is the possibility of radionuclide migration in the accessible environment via dissolved constituents in groundwater. Thus, the behavior of actinides in the environment must be considered for the safe management of SNF, and necessary to evaluate the conditions of elevated temperatures. Again, this emphasizes the need for the geochemical understanding of actinides in the environment.

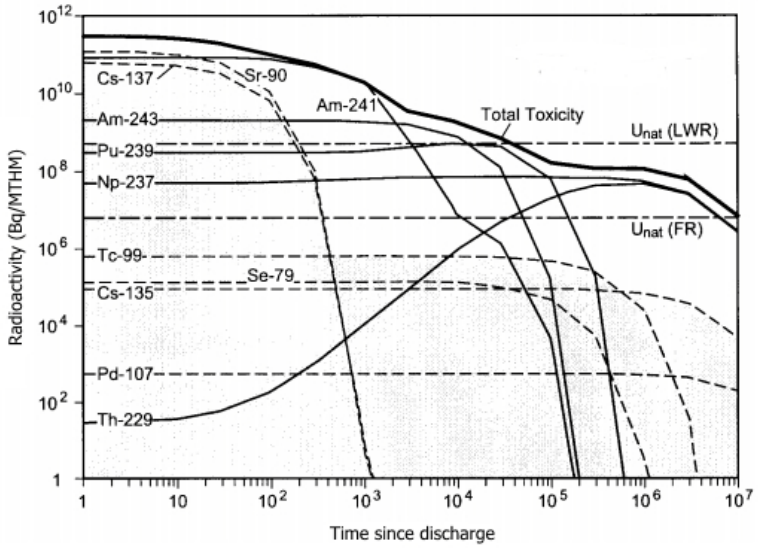


Figure 1.1: Activity of selected radionuclides in SNF as a function of time. Adapted from Bodansky[16] and Wydler and Baetslé[17].

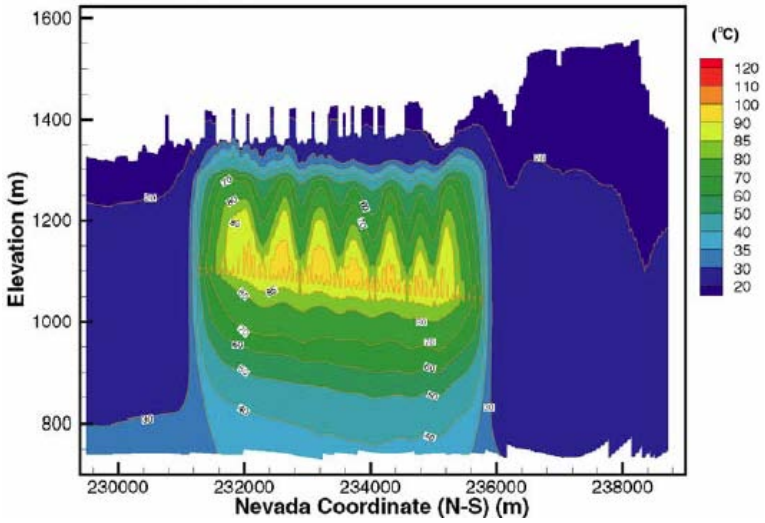


Figure 1.2: The expected temperature distribution of SNF after 1000 years in the proposed Yucca Mountain repository. Taken from the Yucca Mountain Science and Engineering Report: Technical Information Supporting Site Recommendation Consideration.[18]

Actinides can interact with the environment in a myriad of ways. Figure 1.3 shows the many potential interactions of a metal ion associated with aqueous and solid phases in the geosphere. These interactions include, and are not limited to, oxidation and reduction, formation and release of aqueous complexes, sorption and desorption of surface complexes, and precipitation and dissolution of solid phases. As seen, there are a multitude of variables that realistically comprise actinide interactions in the environment, but the specific aspect studied in this work is the sorption processes to mineral surfaces. Sorption of radionuclides on minerals

plays a key part in the retardation of contaminant migration through various environmental systems. It is generally assumed that a stronger affinity between the contaminant of concern and the environmental material will limit the mobility of the contaminant. Similarly, contaminants that interact weakly with minerals, clays, and rocks tend to migrate faster compared to the flow of groundwater. This complex behavior of radionuclides necessitates knowledge of actinide sorption in various environmental matrices under varying chemical conditions to better understand the interaction of actinides in the environment.

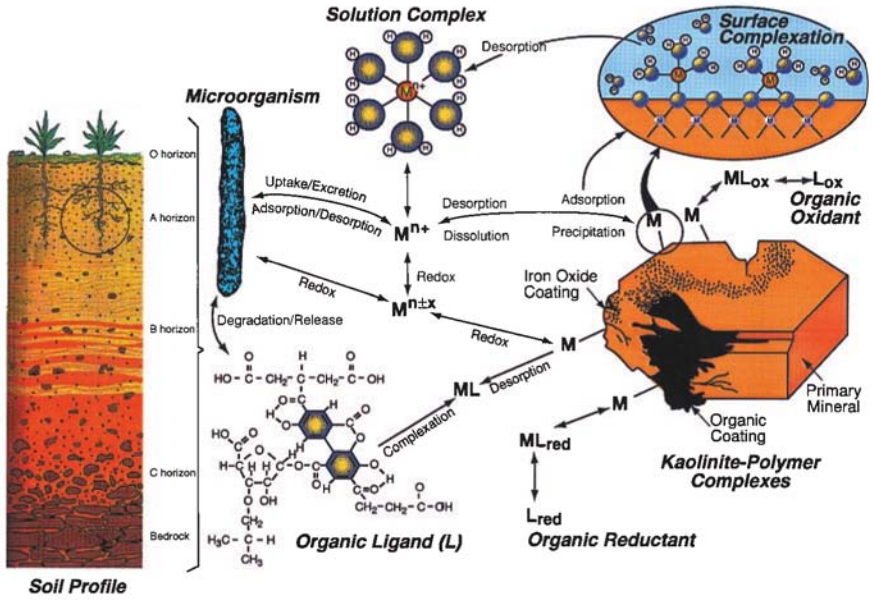


Figure 1.3: The myriad of environmental processes that can occur for a metal contaminant in soils and groundwater. Taken from Brown *et al.*[19]

Iron oxide minerals are ever-present in nature, especially so in soils and sediments. Goethite and hematite are the most thermodynamically stable iron oxides and thus two of the most common and widespread in the environment.[20] Expected to have high sorption capacity and a tendency to form coatings on mineral surfaces,[21] iron oxides play a critical part in regulating contaminant migration. In regards to nuclear waste repositories, the long-term stability of hematite[22] lends itself to be considered an additional barrier layer, because iron oxides are anticipated to be present from the unavoidable corrosion of steel containers that hold SNF.[23] Furthermore, the elevated temperatures associated with a sealed repository may enhance hematite formation, and by extension, minimize actinide migration.

Batch sorption experiments provide essential information of an actinide's sorption behavior to a mineral surface. Knowledge of how actinide ions are bound to a surface, particularly if bound as inner-sphere or outer-sphere complexes, is paramount to the sorption mechanism. Because sorption reactions in the environment generally occur at the solid/solution interface, drying sorption samples may cause changes to the surface species.[24] X-ray absorption spectroscopy (XAS) is a spectroscopic method that allows *in-situ* characterization of the surface complexes. X-ray absorption near-edge structure (XANES) measurements directly and unambiguously measures the oxidation state of an actinide ion associated with a mineral surface, and extended X-ray fine structure (EXAFS) gives information about the local coordination

environment of a specific element. In particular, EXAFS has been used to help elucidate the molecular-level binding structure of actinides on the surface of environmental minerals.[25]

To face the challenges of predicting contaminate migration in remediation efforts of contaminated sites and responsibly storing nuclear waste, a complete understanding of the interactions involved in actinide transport and migration in the environment is essential. A thorough knowledge of the mechanism behind sorption processes that occur at the mineral/water interface is particularly important to understand how actinides move through the geosphere. This work examined actinide interactions to mineral surfaces with the overarching objective to gain a fundamental understanding of the sorption processes that contribute to the transport, migration, and immobilization of actinides in the environment. Specifically, the sorption behaviors of Pu(VI) and Np(V) to iron oxide minerals goethite and hematite were investigated. To that end, this work can be described in the following manner:

- Chapter 2 and Chapter 3 provide an introduction to plutonium and neptunium chemistry, respectively. These chapters are far from exhaustive, but cover the relevant complexities of aqueous plutonium and neptunium chemistries. How the radionuclides were measured and characterized is also briefly described.

- Some background information about surface chemistry is given in Chapter 4, focusing on the pertinent information regarding reactions at the solid/solution interface.

- The iron oxide minerals, goethite, 1% Al-substituted goethite, and hematite, used in these studies are briefly described in Chapter 5. The experimental details as to the mineral syntheses are provided, as well as the subsequent characterization and determination of the point of zero charge (PZC).

- Chapter 6 presents a study of the interactions of Pu(VI) with goethite and 1% Al-substituted goethite. Batch sorption experiments were performed to examine sorption behavior of plutonium to the iron oxides. The oxidation state of plutonium was determined using XAS to elucidate if redox chemistry of plutonium occurred upon association with the mineral surface.

- Chapter 7 presents a study of the interactions of Np(V) with hematite. Batch sorption experiments and XAS measurements were used to determine the effects of elevated temperature and ionic strength on Np(V) sorption. XANES spectra confirmed the pentavalent oxidation state of the Np-hematite complex with varying temperatures and ionic strengths, and EXAFS spectra and fits support the suggestion that the sorption mechanism is via formation of inner-sphere complexes.

- In the final chapter, the important findings and conclusions of the studies are summarized.

The results presented in this work are a small but significant contribution towards a thorough understanding of actinide interactions in the environment.

# 2. PLUTONIUM CHEMISTRY

One of the primary focuses of this work is the investigation of the interactions between iron oxide mineral surfaces and aqueous plutonium species. Knowledge of plutonium behavior in solution is paramount for understanding how it will interact with a mineral surface at the solid/solution interface. This chapter gives an overview of plutonium, presents the complicated chemistry of aqueous plutonium, and describes how plutonium was measured and characterized. A comprehensive and excellent review of plutonium solution chemistry can be found in the authoritative text by Cleveland.[26]

Plutonium, element 94, is a fascinating element for its place in both the periodic table and in human political history. Along with the discovery of nuclear fission in 1939,[27] plutonium has tremendous importance in nuclear reactions. Its incorporation in nuclear weapons became a deciding factor of World War II. Important to also highlight is how the fissile nature of Pu-239 is used peacefully as a fuel source for power generation, both at nuclear power reactors and nuclear-powered naval vessels. The high decay heat of Pu-238 makes it the main power source for deep space exploration vehicles sent out by the National Aeronautics and Space Administration (NASA).

Positioned between the light actinides (Th-Pu) and the heavy actinides (Am-Lr), plutonium is one of the most chemically complex elements in the periodic table. The chemistry of the light actinides is more akin to that of transition metals while the heavy actinides exhibit chemistry more analogous to the lanthanide elements. (This similarity between the heavy actinides and lanthanides is what led Seaborg to first posit the introduction of an actinide series in the periodic table.[28]) For the light actinides, the electrons in the closed 6s and 6p shells shield the 5f electrons, and so many oxidation states are accessible. Conversely, the increased number of 5f electrons and relativistic effects result in the heavy actinides being chemically similar to the lanthanides. (This is what gives rise to the famous Actinide Contraction, wherein the ionic radii decrease moreso-than-expected going across the actinide series.) The heavy actinides typically exist in the trivalent oxidation states, like the lanthanides.

In solution, plutonium has seven different oxidation states available*, Pu(II) – Pu(VII), of which four of these oxidation states are accessible under environmental conditions. As a solid, plutonium exhibits seven different crystal phases and can form alloys and compounds with an array of other elements.[29] The rich yet complicated chemistry of plutonium consequently can be a blessing or a curse to the actinide chemist.

The synthesis of plutonium occurred at the Radiation Laboratory of the University of California, Berkeley. Professor Glenn T. Seaborg, Professor Joseph W. Kennedy, and graduate student Arthur C. Wahl bombarded a U-238 target with deuterons at the 60 inch cyclotron of E. O. Lawrence. This led to the second man-made transuranic element, Pu-238.[30]

$$^{238}_{92}U + ^{2}_{1}H \rightarrow ^{238}_{93}Np + 2\,^{1}_{0}n \qquad \text{Eq 2.1}$$

$$^{238}_{93}Np \rightarrow ^{238}_{94}Pu + \beta^{-} \qquad \text{Eq 2.2}$$

Chemical separations were performed to verify that a new element had indeed been produced,[31] and element 94 was named plutonium to follow the convention used in naming neptunium. This experiment was performed in December of 1940 and experiments investigating the properties of plutonium followed, leading to a number of publications submitted to journals in 1941. However, at the request of the U.S. government, they were withheld from publication for security reasons until the end of World War II.

## 2.1 Pu-239 Production and Decay

The more notable isotope of plutonium, Pu-239, was first produced in the spring of 1941, again at the 60 inch cyclotron, by neutron capture of U-238 and subsequent decay,[32] as shown in the nuclear reactions below:

$$^{238}_{92}U + ^{1}_{0}n \rightarrow ^{239}_{92}U \qquad \text{Eq 2.3}$$

$$^{239}_{92}U \rightarrow ^{239}_{93}Np + \beta^{-} \qquad \text{Eq 2.4}$$

$$^{239}_{93}Np \rightarrow ^{239}_{94}Pu + \beta^{-} \qquad \text{Eq 2.5}$$

Most of the isotopes of plutonium decay primarily by α emission. The half-lives, α decay energies, and decay intensities of selected plutonium isotopes are listed in Table 2.1. The radioisotope used in the studies presented in this work was Pu-239, which has a half-life of 24110 years[33] and decays by α emission to the daughter product U-235, as shown in Eq 2.6. The emitted α particles have an average energy of 5.105 MeV.[34] This radioisotope is convenient to work with because its half-life is long enough that decay corrections are not required on the experimental time scale and yet short enough to detect trace amounts (concentrations $\geq 10^{-9}$ M).

$$^{239}_{94}Pu \rightarrow ^{235}_{92}U + \alpha \qquad \text{Eq 2.6}$$

* The electronic ground state of Pu, $[Rn]7s^{2}5f^{6}$, suggests the Pu(VIII) oxidation state can be obtained under highly oxidizing conditions. However, no experimental evidence has yet been reported.

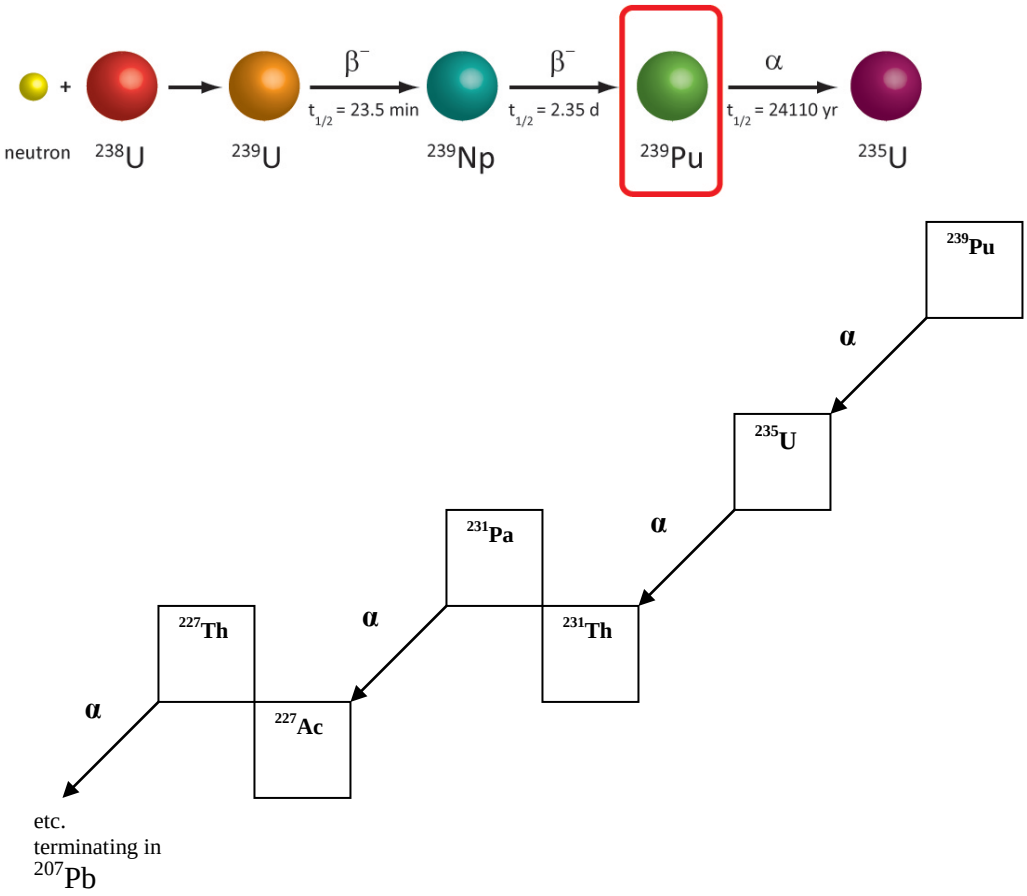


Figure 2.1: Production and partial decay scheme of Pu-239. Pu-239 is the mother nuclide to the U-235 decay series, also known as the Actinium series or the A = 4n + 3 series, which terminates in Pb-207.

| Isotope | half-life, $t_{1/2}$ | Decay Modes | α energy (MeV), Intensity (%) | α energy (MeV), Intensity (%) |
|---|---|---|---|---|
| Pu-236 | 2.858 y | α, SF | 5.768, 69.1 | 5.721, 30.8 |
| Pu-237 | 45.6 d | EC, α | 5.335, 0.002 | |
| Pu-238 | 87.7 y | α, SF | 5.499, 70.9 | 5.456, 29.0 |
| **Pu-239** | **24110 y** | **α, SF** | **5.157, 70.8** | **5.144, 17.1** |
| Pu-240 | 6561 y | α, SF | 5.168, 72.8 | 5.124, 27.1 |
| Pu-241 | 14.3 y | $\beta^-$, α, SF | 4.896, 0.002 | |
| Pu-242 | 373000 y | α, SF | 4.902, 76.5 | 4.858, 23.4 |
| Pu-243 | 4.956 h | $\beta^-$ | | |
| Pu-244 | $8.11 \times 10^7$ y | α, SF | 4.589, 80.5 | 4.546, 19.4 |

Table 2.1: Half-lives and most intense α emissions for selected isotopes of plutonium. The radioisotope used in the studies described in this work, Pu-239, is highlighted in **bold**. Values taken from the Evaluated Nuclear Structure Data File.[33]

A key nuclear property of Pu-239 stems from it being fissionable with thermal neutrons (0.025 eV). While Pu-239 has a small spontaneous fission branch ($\gamma = 3 \times 10^{-10}$), experiments by Kennedy *et al.* measured a neutron induced fission cross section almost 50% larger than that of U-235.[32,35] Figure 2.2 shows a log-log plot of the fission cross section for Pu-239 as a function of neutron energy, with a sharp increase in cross section for neutrons of energy ~0.25 eV.

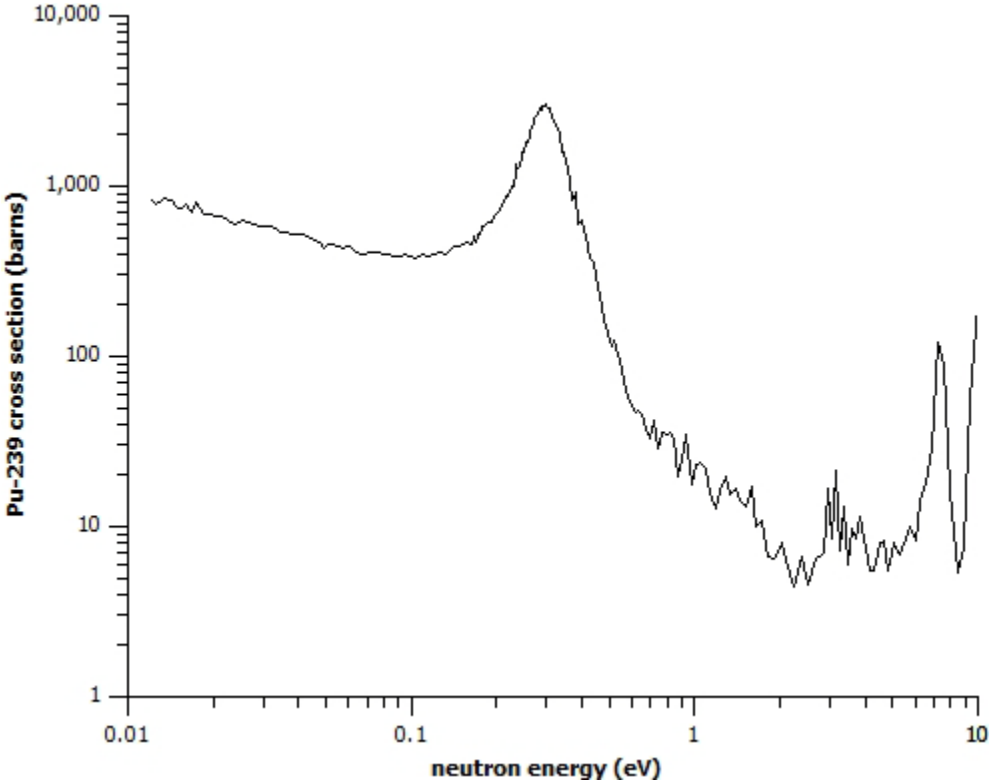


Figure 2.2: Log-log plot of Pu-239 fission cross section. Adapted from the Organisation for Economic Co-operation and Development (OECD) Nuclear Energy Agency (NEA) EXFOR database.[36]

Figure 2.3 shows a log plot of the distribution of fission products for the asymmetric fission of Pu-239, with a peak at A ~ 100 (Mo, Tc, Ru) and a peak at A ~ 140 (Cs, Ba, lanthanides). The fission products are often themselves radioactive with short half-lives and usually undergo β decay. In addition to the fission fragments, several neutrons (2-4) are also released.[37,38] Under certain conditions, these neutrons released during fission sustain or accelerate a chain reaction with Pu-239 or other fissile isotopes. This has led to Pu-239 being one of three main isotopes (U-235, U-238, and Pu-239) used as fuel in nuclear power, and used as the primary fissile isotope for the production of nuclear weapons.

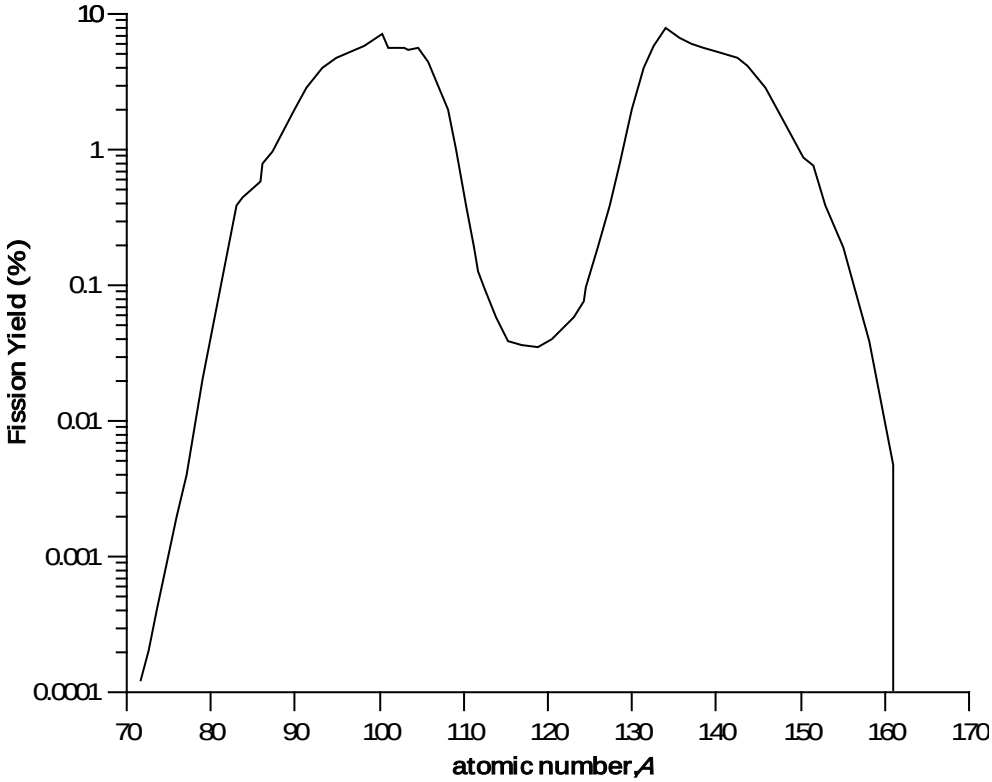


Figure 2.3: Log plot of the mass distribution for the thermal neutron-induced fission of Pu-239. Adapted from Seaborg and Loveland.[39]

## 2.2 Plutonium Aqueous Solution Chemistry

Plutonium exhibits extremely complex solution chemistry, and as such, knowing which plutonium species are present in aqueous environmental conditions is crucial to understanding plutonium interactions with a surface.

In solution, plutonium can exist as compounds or complexes in mainly four different oxidation states (III, IV, V, and VI). Changes in oxidation state readily occur due to the relatively similar standard potentials of ~1 V for the plutonium redox couples (Table 2.2). The similar redox couples also give rise to the coexistence of multiple oxidation states under environmental conditions, which further complicates the aqueous chemistry of plutonium. The four plutonium oxidation states can exist simultaneously under acidic conditions[26] but plutonium mainly exists as Pu(IV), Pu(V), and Pu(VI) in oxic waters; Pu(III) exists under anoxic conditions[40]. Pu(IV), Pu(V) and Pu(VI) are likely to be the predominant oxidation states found in mildly oxic environmental conditions, and thus are extremely relevant to environmental studies and understanding the interactions with a mineral surface. For this reason, and the higher solubility and stability under a wide range of pH conditions, hexavalent plutonium was the oxidation state used in the studies described in this work. While Pu(VI) will slowly undergo reduction to Pu(V) and then to Pu(IV), autoreduction* is significantly minimized for aqueous plutonium solutions kept in concentrated $HClO_4$, due to the oxidizing capabilities of perchloric acid.[26,41,42]

* The phenomenom of autoreduction is also referred to as alpha particle induced reduction due to alpha decay self-irradiation effects.

In noncomplexing acidic conditions such as perchloric acid, Pu(III) and Pu(IV) exist as simple hydrated cations $Pu^{+3}$ and $Pu^{+4}$, respectively. In contrast, Pu(V) and Pu(VI) exist in solution as the plutonyl moiety ($PuO_2^{n+}$) with two axial oxygen atoms bound to the central plutonium atom.[43] The spherically symmetric $Pu^{+3}$ and $Pu^{+4}$ cations and the plutonyl moieties of $Pu^{V}O_2^{+}$ and $Pu^{VI}O_2^{2+}$ are shown with ball-and-stick models in Figure 2.4. The aquo ions $Pu^{+3}$ and $Pu^{+4}$ have ionic radii of 1.123 Å and 0.962 Å, respectively, for an 8 coordinate system, though these ions may accommodate as many as 10 or 12 oxygen atoms in the first coordination shell, respectively.[44–46] As bare cations, $Pu^{+3}$ and $Pu^{+4}$ retain their overall formal charge. The dioxocations $PuO_2^{+}$ and $PuO_2^{2+}$ have Pu–O bond lengths of 1.81 Å and 1.74 Å, respectively[47]; the slightly shorter plutonyl bond distance for $PuO_2^{2+}$ is due to the higher cationic charge on the plutonium atom. Formation of the axial oxygen bonds of Pu(V) and Pu(VI), however, lowers their effective charges. Choppin and Rao report the effective charge of Pu(VI) to be $+2.9 \pm 0.1$[48], and the effective charge of Pu(V) is assumed to be analogous to that of Np(V), $+2.3 \pm 0.2$[26,49].

The effective charge of the plutonium cation drastically affects aqueous plutonium chemistry because of the ionic nature of the plutonium ions. The strength of the ionic bond between a plutonium cation and an anionic ligand is proportional to the effective charge of the plutonium cation. Generally, as effective charge increases, the ionic bonds that form become shorter and thus stronger. This leads to the trend of stronger bond formation, which follows the trend of effective charge: $Pu^{4+} > PuO_2^{2+} \approx Pu^{3+} > PuO_2^{+}$. (This trend of $An^{4+} > AnO_2^{2+} \approx An^{3+} > AnO_2^{+}$ often holds true for the early actinides, again based upon the effective charge of the cations.)

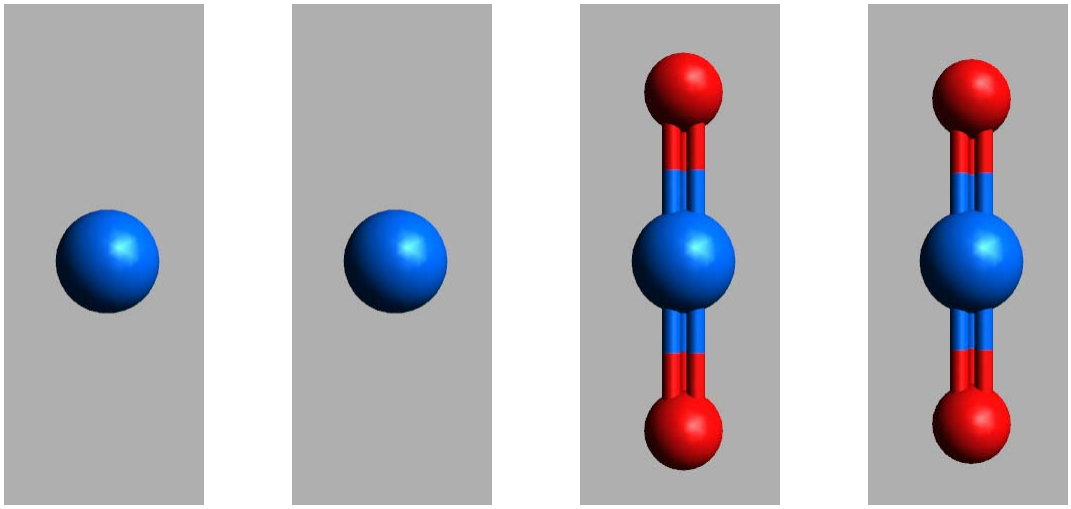

Figure 2.4: Ball-and-stick models of (a) $Pu^{3+}$ cation, (b) $Pu^{4+}$ cation, (c) plutonyl moiety $PuO_2^{+}$, and (d) plutonyl moiety $PuO_2^{2+}$ with plutonium shown in blue and oxygen shown in red. Relative bond distances are drawn accurately, but atomic radii are not. Notice the slightly shorter plutonyl bond distance for $Pu^{VI}O_2^{2+}$due to the higher cationic charge on the plutonium atom.

### 2.2.1 Oxidation-Reduction Chemistry

The solution chemistry of plutonium is heavily dependent upon oxidation state, which is further complicated by plutonium being extremely sensitive to redox changes.[50] Table 2.2 presents the reduction half-reactions that can occur in solution along with the standard reduction potentials for the reactions.* Of importance to highlight is how the redox couples between Pu(III), Pu(IV), Pu(V), and Pu(VI) all have similar reduction potentials of ~1 V. Oxidation state transformations readily occur for the cation Pu(III)/Pu(IV) pair and the plutonyl Pu(V)/Pu(VI) pair, as no gain or loss of oxygen is required but only a simple electron transfer.

The Pu(III)/Pu(IV) and Pu(V)/Pu(VI) couples are independent of solution pH. In both cases, there is no need to form or break the axial Pu–O bonds. In contrast, the other redox reactions exhibit pH dependence, as structural rearrangement is required in order to form or break the axial Pu–O bonds. Figure 2.5 shows the formal reduction potentials among common plutonium oxidation states and the metal in a Latimer diagram measured in acidic conditions.[26]

Under acidic conditions, all four plutonium oxidation states can coexist. As the pH of the system is raised, the reduction potential for the Pu(III)/Pu(IV) couple becomes negative, and Pu(III) is no longer stable in solution. However, the reduction potentials for the Pu(IV)/Pu(V), Pu(V)/Pu(VI), and Pu(IV)/Pu(VI) couples remain ~1 V, and thus Pu(IV), Pu(V), and Pu(VI) can exist simultaneously at neutral pH. Under alkaline conditions, the reduction potential for the Pu(IV)/Pu(V) couple becomes negative, so higher pH conditions favor Pu(V) and Pu(VI).

| Redox Reaction | Acidic | Neutral | Basic |
|---|---|---|---|
| $Pu^{4+} + e^- \rightleftharpoons Pu^{3+}$ | +0.982 | -0.39 | -0.96 |
| $PuO_2^+ + 4H^+ + 2e^- \rightleftharpoons Pu^{3+} + 2H_2O$ | | +1.076 | |
| $PuO_2^+ + 4H^+ + e^- \rightleftharpoons Pu^{4+} + 2H_2O$ | +1.170 | +0.70 | -0.67 |
| $PuO_2^{2+} + e^- \rightleftharpoons PuO_2^+$ | +0.913 | +0.60 | +0.12 |
| $PuO_2^{2+} + 4H^+ + 2e^- \rightleftharpoons Pu^{4+} + 2H_2O$ | +1.043 | +0.65 | +0.34 |

Table 2.2: Formal electrochemical potentials for plutonium redox couples in acidic, neutral, and basic solutions versus the standard hydrogen electrode (SHE). Values taken from Clark *et al.*[51]

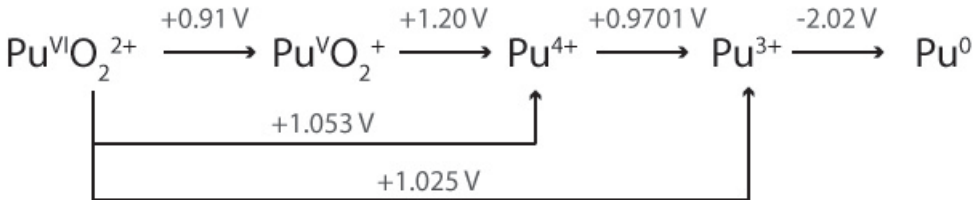


Figure 2.5: Latimer diagram that shows the formal reduction potentials among plutonium oxidation states Pu(III) – Pu(IV) and plutonium metal in 1 M $HClO_4$ at 25° C. Values taken from Cleveland.[26]

* The reduction potential is a measure of a species' ability to gain electrons to become reduced. Reduction potentials are given in comparison with the reduction of aqueous $H^+$, which is arbitrarily set as 0. The more positive the potential, the easier the species is reduced.

## 2.2.2 Disproportionation

The abilities of Pu(IV) and Pu(V) to disproportionate also contribute to the complexity of plutonium chemistry. These reactions are typically important to consider when aqueous plutonium concentrations exceed $10^{-6}$ M.[51] Connick[52] and Rabideau[53,54] studied plutonium disproportionation under acidic conditions and both determined the reactions to undergo a two-step process that does not rely on water oxidation or reduction or that of any other elements to act as electron shuttles.

The overall disproportionation of Pu(V) at pH < 1 is provided in Eq 2.7.

$$3PuO_2^+ + 4H^+ \rightleftharpoons Pu^{3+} + 2PuO_2^{2+} + 2H_2O \qquad \text{Eq 2.7}$$

Pu(V) disproportionation can occur two ways, depending on the presence of Pu(III).[52] If Pu(III) is present, the disproportionation reaction of Pu(V) proceeds in two separate steps:

$$PuO_2^+ + Pu^{3+} + 4H^+ \rightleftharpoons 2Pu^{4+} + 2H_2O \qquad \text{Eq 2.8}$$

$$PuO_2^+ + Pu^{4+} \rightleftharpoons Pu^{3+} + PuO_2^{2+} \qquad \text{Eq 2.9}$$

The first step is slow as it requires the axial Pu–O bond to be formed and broken, whereas the second step proceeds quickly, as it simply involves electron transfers. If there is little or no Pu(III) in solution and only Pu(V) species are available, Pu(V) disproportionation proceeds by:

$$PuO_2^+ + Pu^{4+} \rightleftharpoons Pu^{3+} + PuO_2^{2+} \qquad \text{Eq 2.10}$$

$$2PuO_2^+ + 4H^+ \rightleftharpoons Pu^{4+} + PuO_2^{2+} + 2H_2O \qquad \text{Eq 2.11}$$

The first step is assumed to reach equilibrium rapidly, followed by the rate-determining step. This reaction is initiated by cation-cation complex formation that undergo protonation followed by disproportionation. This reaction proceeds slower than the one above because it involves breaking the axial Pu–O bonds in the plutonyl moiety. Theoretical calculations of this system by Steele and Taylor support this mechanism.[55]

The overall disproportionation reaction of Pu(IV) proceeds by:

$$3Pu^{4+} + 2H_2O \rightleftharpoons 2Pu^{3+} + PuO_2^{2+} + 4H^+ \qquad \text{Eq 2.12}$$

Just as the disproportionation reaction for Pu(V) in the presence of Pu(III), the reaction appears to be tri-molecular, but proceeds through two separate steps:

$$2Pu^{4+} + 2H_2O \rightleftharpoons Pu^{3+} + PuO_2^+ + 4H^+ \qquad \text{Eq 2.13}$$

$$Pu^{4+} + PuO_2^+ \rightleftharpoons Pu^{3+} + PuO_2^{2+} \qquad \text{Eq 2.14}$$

The first step, the reverse of the slow step for Pu(V) disproportionation, is slow. Two Pu(IV) cations combine to form Pu(III) and Pu(V), requiring formation of the axial P–O bonds in

the plutonyl moiety. The second step proceeds quickly, as it simply involves a single electron transfer; the Pu(V) produced in the first step reacts with a third Pu(IV), yielding Pu(III) and Pu(VI). Disproportionation is complete when both steps have reached equilibrium.

Plutonium disproportionation is a function of both concentration and pH. Disproportionation increases as the plutonium concentration in a system increases. It can be inferred from Le Chatelier's Principle that as the pH decreases, Pu(IV) is favored, whereas Pu(V) is favored in high pH conditions. The reactions as written above tend to be favored under acidic to slightly acidic conditions. Studies on plutonium disproportionation were not conducted at neutral solution conditions, but in acidic conditions (pH < 1) and matrices not representative of environmental systems.[52–57] This further belies the need to understand plutonium chemistry as it becomes more complex under environmental conditions.

### 2.2.3 Ligand Complexation Chemistry

The f-block elements are generally considered hard Lewis acids, so most interactions with ligands are regarded as ionic bonds. However, due to relativistic effects, actinides can form bonds that are slightly covalent in nature. With high Z elements, the s and p orbitals contract and the d and f orbitals expand. The relativistic Dirac model predicts comparable energies of the 5f, 6d, 7s, and 7p orbitals with energy gaps similar to chemical bond energies, such that bonding may occur between these orbitals, depending on the chemical conditions.

In general, the trend of complex formation follows that of effective charge: $An^{4+} > AnO_2^{2+} \approx An^{3+} > AnO_2^{+}$. The complexation between a metal, M, and ligand, L, to form ML, $ML_2$, $ML_3$, etc… can be described in the reactions:

$$\mathrm{m}M + \mathrm{l}L \rightleftharpoons \mathrm{n}M_mL_l \qquad \text{Eq 2.15}$$

$$M + L \rightleftharpoons ML \qquad \text{Eq 2.16}$$

$$ML + L \rightleftharpoons ML_2 \qquad \text{Eq 2.17}$$

$$ML_2 + L \rightleftharpoons ML_3 \qquad \text{Eq 2.18}$$

The equilibrium constant is given by:

$$K = \frac{\{M_mL_l\}^n}{\{M\}^m\{L\}^l} \qquad \text{Eq 2.19}$$

The stability constant $\beta$ (also referred to as the formation constant) for the step-wise complexation reaction shown in Eq 2.18 is given by[*]:

$$\beta_{(1,3)} = K_1K_2K_3 \qquad \text{Eq 2.20}$$

$$\log\beta_{(1,3)} = \log K_1 + \log K_2 + \log K_3 \qquad \text{Eq 2.21}$$

[*] The number of the reaction is specified when expressing stability constants, as suggested by Lemier *et al.* and Guillaumont *et al.*[62,63] This is partially due to IUPAC not explicitly defining a standardized way of presenting equilibrium constants.

Common inorganic ligands present in natural fresh waters include hydroxide, carbonate, phosphate, sulfate, chloride, and fluoride. Because of the relatively high concentration of hydroxide and carbonate, [58] the discussion below will focus on the effect hydrolysis and carbonate complexation have on plutonium aqueous chemistry.

### 2.2.3.1 Hydrolysis

Aqueous actinide ions undergo hydrolysis according to the general chemical reaction:

$$An^{x+} + \mathrm{y}(H_2O) \rightleftharpoons An\left(OH\right)_{\mathrm{y}}^{+(x-\mathrm{y})} + \mathrm{y}H^{+} \qquad \text{Eq 2.22}$$

Mononuclear hydrolysis products form first, which subsequently form oligomers and polymers. Because of ion-dipole interactions, a hydration sphere surrounds all ions in solution. The greater the ionic charge, the more water molecules are attracted. For ions of the same charge, the smaller the ionic radius, the more charge density around the ion, and the more water molecules are attracted. Thus, a highly charged ion with small ionic radius has a large hydration radius in aqueous solutions.

All plutonium oxidation states readily undergo hydrolysis; this is especially so for Pu(V) and Pu(VI), which immediately hydrolyze to form the plutonyl moiety. During hydrolysis, the greater positive charge on the plutonium cation causes the ion to interact strongly with water, resulting in an acidic aquo acid. This Brønsted acid easily gives up a proton to form hydroxo complexes of plutonium. The plutonium hydroxo complexes form via the following general reaction:

$$\mathrm{z}Pu^{x+} + \mathrm{n}H_2O \rightleftharpoons Pu\left(OH\right)_{\mathrm{n}}^{(\mathrm{z}x-\mathrm{n})+} + \mathrm{n}H^{+} \qquad \text{Eq 2.23}$$

Table 2.3 shows the number of coordinating waters in the primary hydration sphere for the various plutonium hydroxo complexes and the corresponding Pu–O distance. A secondary hydration sphere is also present as a result of dipole-dipole interactions between the waters that comprise the primary hydration sphere and bulk water. Both primary and secondary hydration spheres influence how a metal ion in solution will interact with a mineral surface; that is, whether an inner-sphere or outer-sphere complex will form. The larger effective charge of Pu(IV) compared to Pu(V) and Pu(VI) means increased hydration. This is supported by spectroscopic data, which shows that $Pu^{4+}$ has 8 coordinating waters in its primary hydration sphere[59] and can even accommodate as many as 12 oxygen atoms in the first coordination shell.[45,46] In comparison, the aquo ions $PuO_2^{+}$ and $PuO_2^{2+}$ have 4-6 coordinating waters in their primary hydration spheres.[47,59,60]

| Oxidation State | General Formula | Number of Coordinating Waters (n) | Pu–O (Å) | Ref |
|---|---|---|---|---|
| Pu(III) | $Pu(OH_2)_n^{3+}$ | 9 | 2.48 | 59,61 |
| | | 10 | 2.51 | 45,61 |
| Pu(IV) | $Pu(OH_2)_n^{4+}$ | 8 | 2.39 | 59 |
| Pu(V) | $PuO_2(OH_2)_n^{+}$ | 4-5 | 2.47 | 59 |
| Pu(VI) | $PuO_2(OH_2)_n^{2+}$ | 4-5 | 2.41 | 59 |

Table 2.3: Number of coordinating waters in the primary hydration sphere of plutonium hydroxo complexes

Hydrolysis is dependent on pH. The effect of hydrolysis is important across the entire pH range for the Pu(III), Pu(IV), and Pu(VI) oxidation states, but Pu(V) does not hydrolyze until alkaline conditions. Compare Figure 2.6, Figure 2.7, and Figure 2.8. [*] The strength of plutonium hydrolysis decreases in the order $Pu^{4+} > PuO_2^{2+} \approx Pu^{3+} > PuO_2^{+}$, so hydrolysis is most pronounced for Pu(IV) and least so for Pu(V). Tetravalent plutonium is almost fully hydrolyzed at pH 1 and completely hydrolyzed to the $Pu(OH)_2^{2+}$ species by pH 2 (Figure 2.6). The solids formed by precipitation, $Pu(OH)_{4\,(s)}$, dominate at alkaline conditions. Pu(IV) is successively hydrolyzed to $Pu(OH)_2^{2+}$, $Pu(OH)_3^{+}$, and $Pu(OH)_4$. Compare, finally, to Pu(V), which remains as the free dioxo cation below pH 9 and hydrolyzes only in alkaline conditions. The pH effect on the extent of hydrolysis can be seen in the speciation diagrams of Pu(IV), Pu(V), and Pu(VI) in carbonate-free conditions (Figure 2.6, Figure 2.7, and Figure 2.8). Pu(V) exists as the free cation for the majority of the pH range whereas Pu(VI) begins to hydrolyze at neutral pH conditions. The formation constants for the plutonium hydroxo complexes are listed in Table 2.4. The formation constants were taken from the NEA database[62] including its update[63], with the exception of the Pu(IV) hydroxo species which were taken from Knopp *et al.*[64].

[*] Pu(III) also hydrolyzes, but the hydrolysis species are not shown. Studying the higher hydrolysis products of Pu(III) is complicated by the instability of Pu(III) at alkaline pH conditions and in the presence of complexing ligands such as hydroxyl groups.

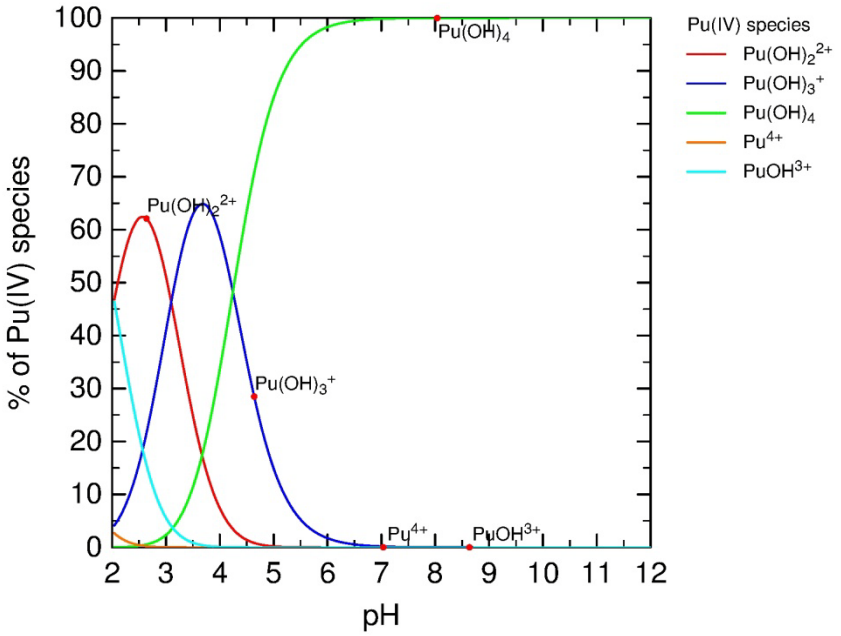


Figure 2.6: Hydrolysis of Pu(IV) in the absence of carbonate

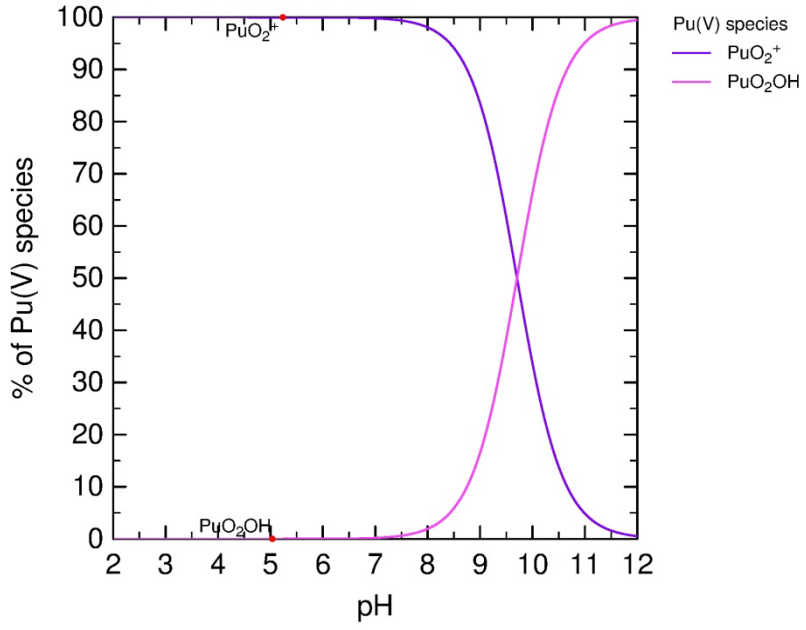


Figure 2.7: Hydrolysis of Pu(V) in the absence of carbonate

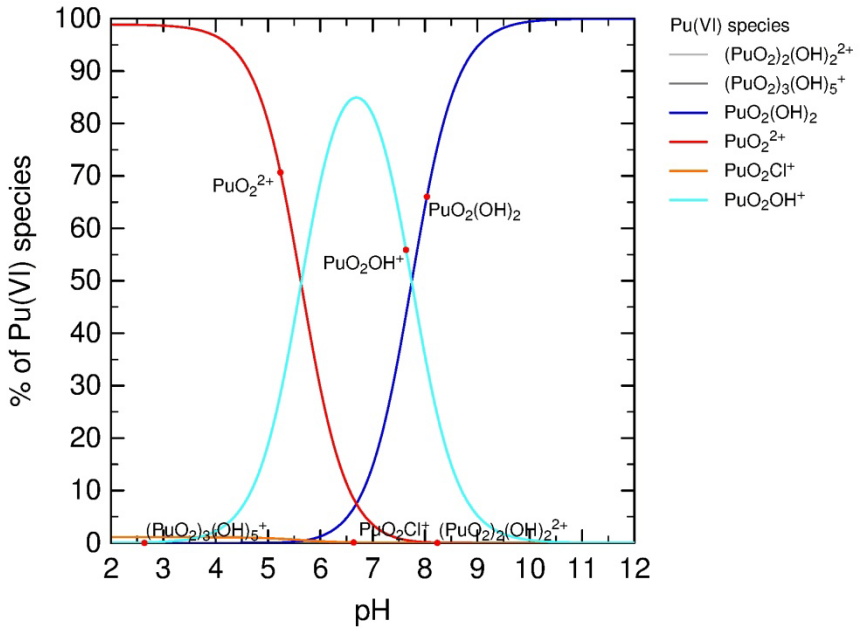


Figure 2.8: Hydrolysis of Pu(VI) in the absence of carbonate

| Chemical Reaction | log β° | Ref |
|---|---|---|
| $Pu^{4+} + H_2O \rightleftharpoons PuOH^{3+} + H^+$ | -0.45 | 64 |
| $Pu^{4+} + 2H_2O \rightleftharpoons Pu(OH)_2^{2+} + 2H^+$ | -1.2 | 64 |
| $Pu^{4+} + 3H_2O \rightleftharpoons Pu(OH)_3^{+} + 3H^+$ | -4.5 | 64 |
| $Pu^{4+} + 4H_2O \rightleftharpoons Pu(OH)_4 + 4H^+$ | -10.8 | 64 |
| $PuO_2^{+} + H_2O \rightleftharpoons (PuO_2)OH + H^+$ | ≤ -9.730 | 62,63 |
| $PuO_2^{2+} + H_2O \rightleftharpoons (PuO_2)OH^+ + H^+$ | -5.5 ± 0.5 | 62,63 |
| $PuO_2^{2+} + 2H_2O \rightleftharpoons (PuO_2)(OH)_2 + 2H^+$ | -13.2 ± 1.5 | 62,63 |
| $2PuO_2^{2+} + 2H_2O \rightleftharpoons (PuO_2)_2(OH)_2^{2+} + 2H^+$ | -7.5 ± 1.0 | 62,63 |

Table 2.4: Formation constants for the hydrolysis complexes of plutonium. Formation constants taken from the NEA database[62] including its update[63], with the exception of the Pu(IV) hydroxo species which were taken from Knopp *et al.*[64].

### 2.2.3.2 Carbonate Equilibrium

Due to the presence of $CO_{2(g)}$ in the atmosphere, bicarbonate and carbonate need to be considered for solutions open to air under near-neutral pH to alkaline conditions. From the $pK_a$ values listed in Table 2.5, bicarbonate and carbonate are present for pH conditions above pH 6 and pH 10, respectively. The dissolution of carbon dioxide in water results in aqueous carbonic acid and subsequent deprotonation reactions yield bicarbonate and carbonate. Henry's Law

expresses the relationship between the concentration of aqueous carbonic acid and the partial pressure of $CO_2$ in the atmosphere (Eq 2.24 and Eq 2.25).*

$$pCO_{2(g)} \rightleftharpoons CO_{2(aq)} \quad \text{Eq 2.24}$$

$$CO_{2(g)} + H_2O_{(l)} \rightleftharpoons H_2CO_3^*{}_{(aq)} \quad \text{Eq 2.25}$$

$$H_2CO_3^*{}_{(aq)} \rightleftharpoons H^+{}_{(aq)} + HCO_3^-{}_{(aq)} \quad \text{Eq 2.26}$$

$$HCO_3^-{}_{(aq)} \rightleftharpoons H^+{}_{(aq)} + CO_3^{2-}{}_{(aq)} \quad \text{Eq 2.27}$$

$$k_H = \frac{\left[H_2CO_3^*\right]}{pCO_2} \quad \text{Eq 2.28}$$

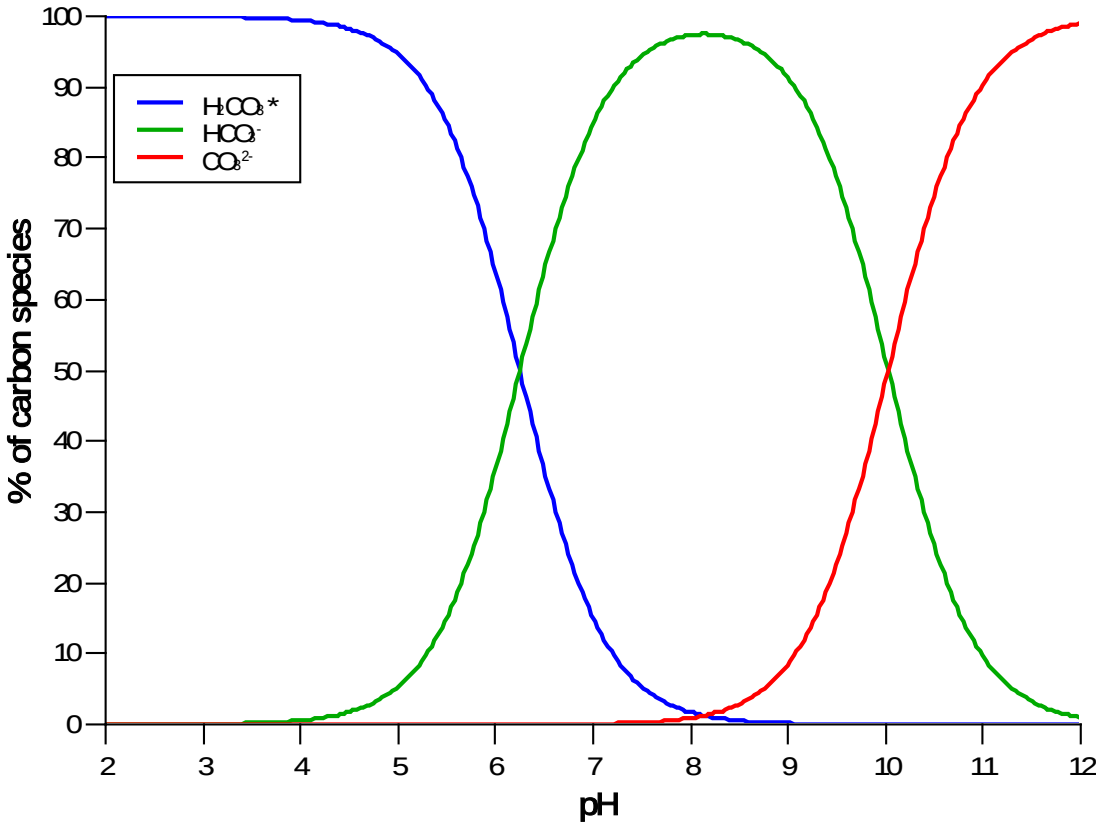


Figure 2.9: Carbonate speciation diagram in an aqueous system open to atmosphere

* When preparing sample solutions representative of environmental systems open to air, the presence of carbonate in solution must be taken into account. One option is to prepare solutions and leave them open to air, allowing the dissolution of $CO_{2(g)}$ from the atmosphere to come to equilibrium with the sample and then adjust the pH until the target pH is reached. This equilibrium process is slow and iterative as pH adjustment causes the equilibrium to shift and the sample then re-equilibrated. Another option, which was done for the studies described in this work, is to prepare samples and "rapidly equilibrate" these solutions by introducing the correct amount of $HCO_3^-$ and $CO_3^{2-}$ into the solution by addition of $NaHCO_3$ and $Na_2CO_3$ solutions.

| Chemical Reaction | $pK_a$ |
|---|---|
| $CO_{2(g)} + H_2O_{(l)} \rightleftharpoons H_2CO_{3(aq)}$ | 1.47 |
| $H_2CO_{3(aq)} \rightleftharpoons H^+_{(aq)} + HCO_3^-{}_{(aq)}$ | 6.35 |
| $HCO_3^-{}_{(aq)} \rightleftharpoons H^+_{(aq)} + CO_3^{2-}{}_{(aq)}$ | 10.33 |

Table 2.5: Dissolved carbonate equilibria. Equilibrium constants are given at 25° C and zero ionic strength, taken from Stumm and Morgan.[58]

Figure 2.9 shows the carbonate equilibrium for an aqueous system open to atmosphere; the speciation diagram is generated from the equilibrium constants given by Stumm and Morgan[58] (Table 2.5). Most scientific texts give the partial pressure of $CO_2$ in the atmosphere as $10^{-3.5}$ atm, or ~316 ppm by volume. Data from the National Oceanic and Atmospheric Administration (NOAA) indicates this value was most likely measured in the early 1960s. As of April 2017, the partial pressure of $CO_2$ in the atmosphere has reached above $10^{-3.39}$ atm, or ~404 ppm, by volume. Figure 2.10 shows the yearly average partial pressure of $CO_2$ from 1959-2016 measured at the Mauna Loa Observatory in Hawaii.

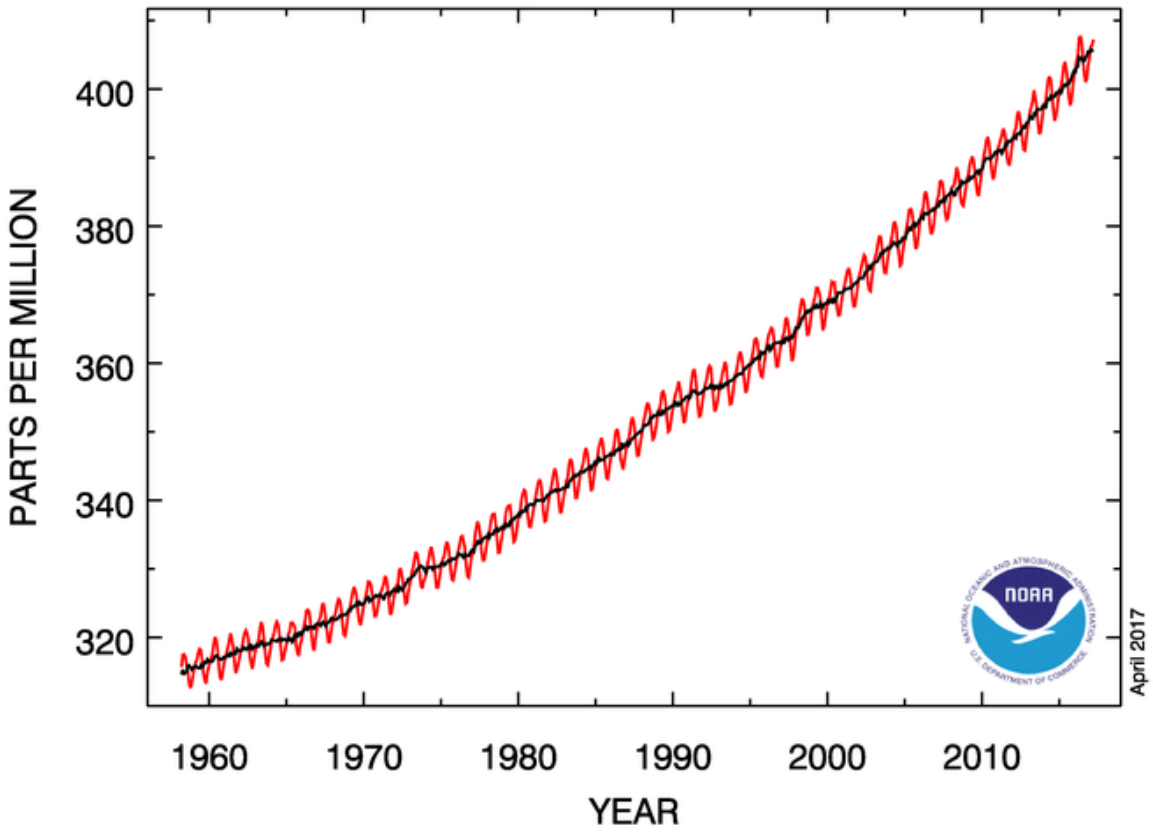


Figure 2.10: Yearly average partial pressure of $CO_{2\,(g)}$ in the atmosphere measured at Mauna Loa Observatory in Hawaii. Adapted from the Global Greenhouse Gas Reference Network.[65]

Formation of plutonium carbonate complexes are given by the following general chemical reaction:

$$Pu^{x+} + \mathrm{n}CO_3^{2-} \rightleftharpoons Pu(CO_3)_{\mathrm{n}}^{(x-2\mathrm{n})^+} \qquad \text{Eq 2.29}$$

The formation reactions of plutonium carbonato complexes and corresponding stability constants are shown in Table 2.6. Important to note is that the stability constants for plutonium carbonato complexes are greater than the hydrolysis stability constants, so plutonium carbonate complexation is favored over plutonium hydrolysis. The plutonium carbonato complexes formed that are negatively charged are expected to repel a negatively charged surface, even though the plutonium hydroxo species would otherwise be attracted to that same surface in the absence of carbonate. Thus, the presence of carbonate could cause lower amounts of plutonium to sorb to iron oxide mineral surfaces, which may ultimately increase plutonium mobility in the environment.

| Chemical Reaction | $\log_{10}\beta°$ | Ref |
|---|---|---|
| $Pu^{4+} + CO_3^{2-} \rightleftharpoons Pu(CO_3)^{2+}$ | 19.4 ± 0.7 | 66 |
| $Pu^{4+} + 2CO_3^{2-} \rightleftharpoons Pu(CO_3)_2$ | 33.5 ± 1.0 | 66 |
| $Pu^{4+} + 3CO_3^{2-} \rightleftharpoons Pu(CO_3)_3^{2-}$ | 42.7 ± 0.8 | 66 |
| $Pu^{4+} + 4CO_3^{2-} \rightleftharpoons Pu(CO_3)_4^{4-}$ | 45.3 ± 0.8 | 66 |
| $Pu^{4+} + 5CO_3^{2-} \rightleftharpoons Pu(CO_3)_5^{6-}$ | 44.5 ± 0.8 | 66 |
| $PuO_2^{+} + CO_3^{2-} \rightleftharpoons (PuO_2)CO_3^{-}$ | 5.1 ± 0.1 | 66 |
| $PuO_2^{+} + 3CO_3^{2-} \rightleftharpoons (PuO_2)(CO_3)_3^{5-}$ | 8.2 ± 2.1 | 66 |
| $PuO_2^{2+} + CO_3^{2-} \rightleftharpoons (PuO_2)CO_3$ | 9.5 ± 0.5 | 62,63 |
| $PuO_2^{2+} + 2CO_3^{2-} \rightleftharpoons (PuO_2)(CO_3)_2^{2-}$ | 14.7 ± 0.5 | 62,63 |
| $PuO_2^{2+} + 3CO_3^{2-} \rightleftharpoons (PuO_2)(CO_3)_3^{4-}$ | 18.0 ± 0.5 | 62,63 |

Table 2.6: Stability constants for plutonium carbonate complexes. Values of $\log_{10}\beta°$ taken from Clark *et al.*[66], with the exception of the Pu(VI)-carbonato species, which were taken from the NEA database[62] including its update[63].

A Pourbaix diagram shows the expected species of plutonium and thermodynamically stable oxidation state under various $E_h$ and pH conditions. An example Pourbaix diagram (Figure 2.11), taken from Choppin *et al.*,[67] shows the stability regions of the four plutonium oxidation states accessible under environmental conditions in a solution of low ionic strength, accounting for plutonium hydrolysis and carbonate complexation. Figure 2.12, taken from Runde,[68] shows a more detailed Pourbaix diagram for plutonium in aqueous solution with the presence of hydroxide, carbonate, and fluoride. The $E_h$ and pH conditions found in natural waters are also outlined.

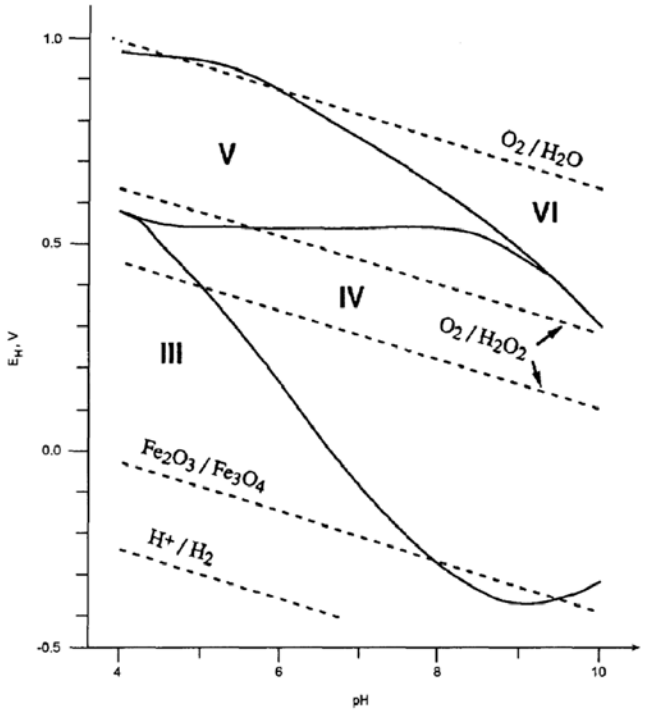


Figure 2.11: Pourbaix diagram for plutonium in solution, with low ionic strength and low plutonium concentration in equilibrium with atmospheric $CO_{2(g)}$. Taken from Choppin *et al.*[67]

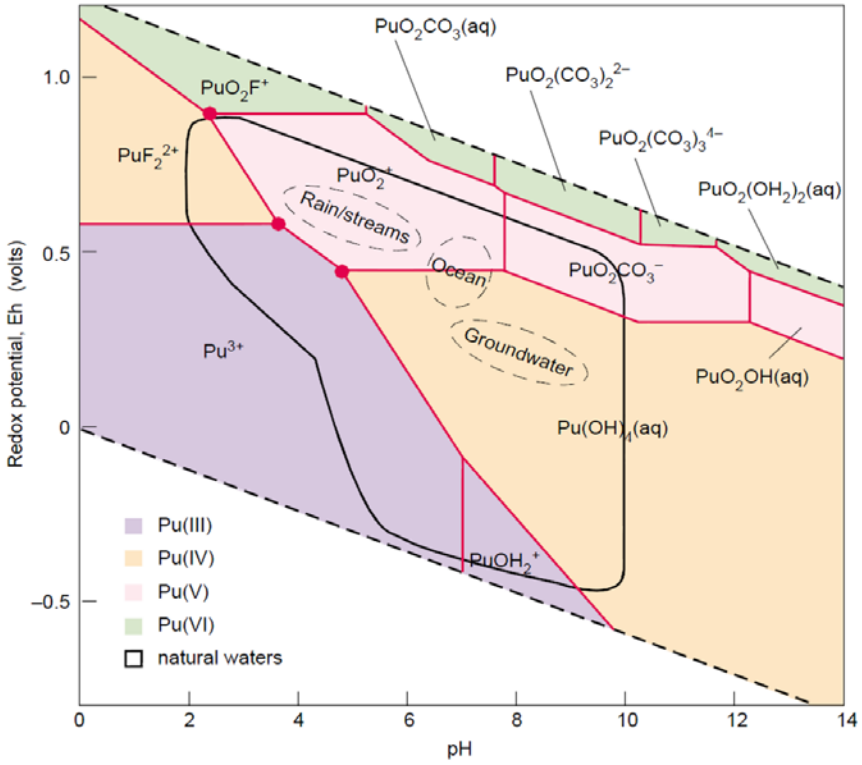


Figure 2.12: Pourbaix diagram for aqueous plutonium in the presence of hydroxide, carbonate, and fluoride. The $E_h$ and pH conditions found in natural waters are also outlined. Taken from Runde.[68]

## 2.2.4 Solubility and Precipitation

The solubility of plutonium is constrained by oxidation state, hydrolysis, presence of carbonate and other complexing ligands, and pH conditions of the aqueous solution. Table 2.7 lists the solubility products, log $K_{sp}$, for plutonium oxides, hydroxides, and carbonates complexes in aqueous solution. Oxidation state has a dramatic effect on plutonium solubility. Generally, solubility follows the trend of complexation formation ($An^{4+} > AnO_2^{2+} \approx An^{3+} > AnO_2^{+}$), so generally, An(IV) would be much less soluble than An(V). Indeed, the solubility of the more oxidized plutonium forms is greater than the reduced forms, especially so at higher pH conditions.[26,29,69] Pu(IV) is many orders of magnitude more insoluble than Pu(V) and Pu(VI).

Carbonate complexation increases plutonium solubility in alkaline conditions, where negatively charged carbonate species form. As mentioned previously, the formation constants for plutonium carbonato complexes are greater than the hydrolysis formation constants, so plutonium carbonato complexes form over the hydrolysis products, and thus control solubility. Though the solubility product indicates the insoluble $PuO_2CO_3$ species is favored, Pu(VI) solubility is decreased in neutral and slightly alkaline solutions, as the $K_{sp}$ for $PuO_2CO_3$ is lower than that for $PuO_2(OH)_2$. The Pu(VI) carbonato species is present in appreciable amounts above pH 10.

| Pu species | Chemical Reaction | log K°$_{sp}$ | Ref |
|---|---|---|---|
| Pu(III) | $Pu(OH)_{3(s)} + 3H^+ \rightleftharpoons Pu^{3+} + 3H_2O$ | 15.8 ± 0.8 | 70 |
| | $Pu(OH)_{3(s)} \rightleftharpoons Pu^{3+} + 3OH^-$ | -26.2 ± 1.5 | 62,63 |
| Pu(IV) | $PuO_{2(\text{am, hyd})} + 4H^+ \rightleftharpoons Pu^{4+} + 2H_2O$ | -2.33 ± 0.52 | 62,63 |
| | $PuO_{2(\text{am, hyd})} + 2H_2O \rightleftharpoons Pu^{4+} + 4OH^-$ | -58.33 ± 0.52 | 71 |
| | $PuO_{2(\text{am, hyd})} + 2H_2O \rightleftharpoons Pu(OH)_4$ | -10.4 ± 0.5 | 71 |
| Pu(V) | $(PuO_2)(OH)_{(\text{am})} + H^+ \rightleftharpoons PuO_2^+ + H_2O$ | 5.0 ± 0.5 | 62,63 |
| | $(PuO_2)(OH)_{(\text{am})} \rightleftharpoons PuO_2^+ + OH^-$ | -9.0 ± 0.5 | 62,63 |
| Pu(VI) | $(PuO_2)(OH)_2 \bullet H_2O_{(s)} + 2H^+ \rightleftharpoons PuO_2^{2+} + 3H_2O$ | 5.5 ± 1.0 | 62,63 |
| | $(PuO_2)(OH)_2 \bullet H_2O_{(s)} \rightleftharpoons PuO_2^{2+} + 2OH^- + H_2O$ | -22.5 ± 1.0 | 62,63 |
| | $(PuO_2)CO_{3(s)} \rightleftharpoons PuO_2^{2+} + CO_3^{2-}$ | -14.65 ± 0.47 | 62,63 |

Table 2.7: Solubility products, log K°$_{sp}$, for plutonium oxides, hydroxides, and carbonate complexes in aqueous solution.

Tetravalent plutonium is the least soluble plutonium oxidation state in the absence of complexing ligands. The two most insoluble forms of plutonium are $PuO_{2(s)}$ and amorphous $Pu(OH)_4$, both of which have $K_{sp} \approx -58$.[62,63] Under reducing conditions, the solubility controlling phase is $PuO_{2(s, hyd)}$, in equilibrium with aqueous Pu(III) and Pu(IV). In the absence of reducing and oxidizing agents, however, trace amounts of $O_{2\,(g)}$ lead to a mixed valent $PuO_{2+x(s, hyd)}$ phase

that controls solubility. The solubility of $PuO_{2+x(s, hyd)}$ can be increased by Pu(VI), especially at higher redox potentials caused by carbonate or radiolysis in chloride brines. These redox and solubility processes are illustrated in Figure 2.13. For a full treatment of plutonium hydroxide and plutonium hydrous oxide solubility, refer to the equations and derivations found in Neck *et al.*[70]

The formation of Pu(IV) colloids complicates the issue of plutonium solubility.[71,72] The concentration of plutonium nanocolloids in near-neutral solutions can far exceed the solubility limits of Pu(IV) hydroxide and oxide solids. Unlike U(IV) and Th(IV) colloids, the formation of Pu(IV) colloids is considered an irreversible reaction. This species readily forms in Pu(IV) solutions of dilute acid concentrations, and can also form in highly acidic concentrated plutonium solutions. Elevated temperatures also increase the rate of colloid formation.

The structure and composition of the Pu(IV) colloid has been debated in the literature. Traditionally, this species was considered an amorphous polymer of hydrous Pu(IV) oxide.[64] Using X-ray scattering techniques and transmission electron microscopy (TEM), however, some studies have suggested the structure and composition of plutonium colloids to actually be nanocrystalline $PuO_2$.[72,73]

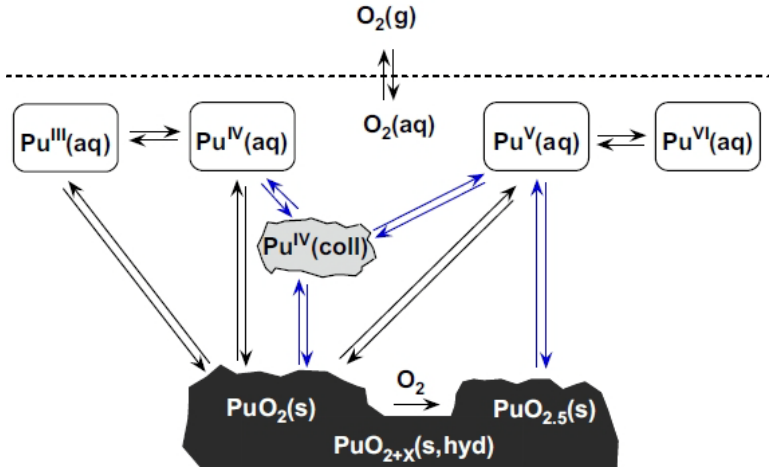


Figure 2.13: Illustration of plutonium solid-liquid and redox equilibria under reducing conditions, redox-neutral conditions, and in the presence of oxygen. Taken from Neck *et al.*[70]

## 2.2.5 Speciation

Plutonium speciation is extremely important in order to know what species are present in aqueous solutions at varying pH conditions. It is crucial that Pu(VI) sorption behavior be evaluated with regards to Pu(VI) aqueous speciation. Knowing which plutonium species are present in solution at a certain pH is necessary to identify what plutonium complexes are available for sorption to a mineral surface. A speciation diagram of Pu(VI) in 0.01 M $NaClO_4$ in the presence of atmospheric $CO_2$ ($pCO_2 = 10^{-3.5}$ atm) at 25 °C is presented in Figure 2.14. Speciation calculations were performed using the thermo.com.V8.R6.230 database[74] developed at Lawrence Livermore National Laboratory (LLNL), which was modified to include aqueous Pu(VI) species. Thermodynamic data for plutonium species used in the speciation calculations were taken from the NEA database[62] including its update[63] and are given in Table 2.8.

Speciation diagram was generated using PhreePlot, which contains an embedded version of PHREEQC.[75] PHREEQC is a free and open source program available from the United States Geological Survey (USGS). For more clarity, the PhreePlot input file used to generate the Pu(VI) speciation diagram is given in Appendix D.

Under atmospheric $CO_2$ conditions, the predominate Pu(VI) species for acidic conditions is $PuO_2^{2+}$. Hydroxide and carbonate species begin to form at near-neutral pH conditions. In a pH 8.5 solution, the Pu(VI) species present are neutral $PuO_2(OH)_2$ and $PuO_2CO_3$ and negatively charged $PuO_2(CO_3)_2^{2-}$ and $PuO_2(CO_3)_3^{4-}$. Above pH 9, the anionic Pu(VI) carbonate species dominate. The contributions of $(PuO_2)_2(OH)_2^{2+}$, $(PuO_2)_3(OH)_5^{+}$, and $PuO_2Cl^{+}$ are negligible (< 1% together) and not obviously visible in the speciation diagram. At alkaline conditions in the absence of carbonate, Pu(VI) speciation is dominated by the neutral second hydrolysis product $PuO_2(OH)_2$ (refer to Figure 2.8).

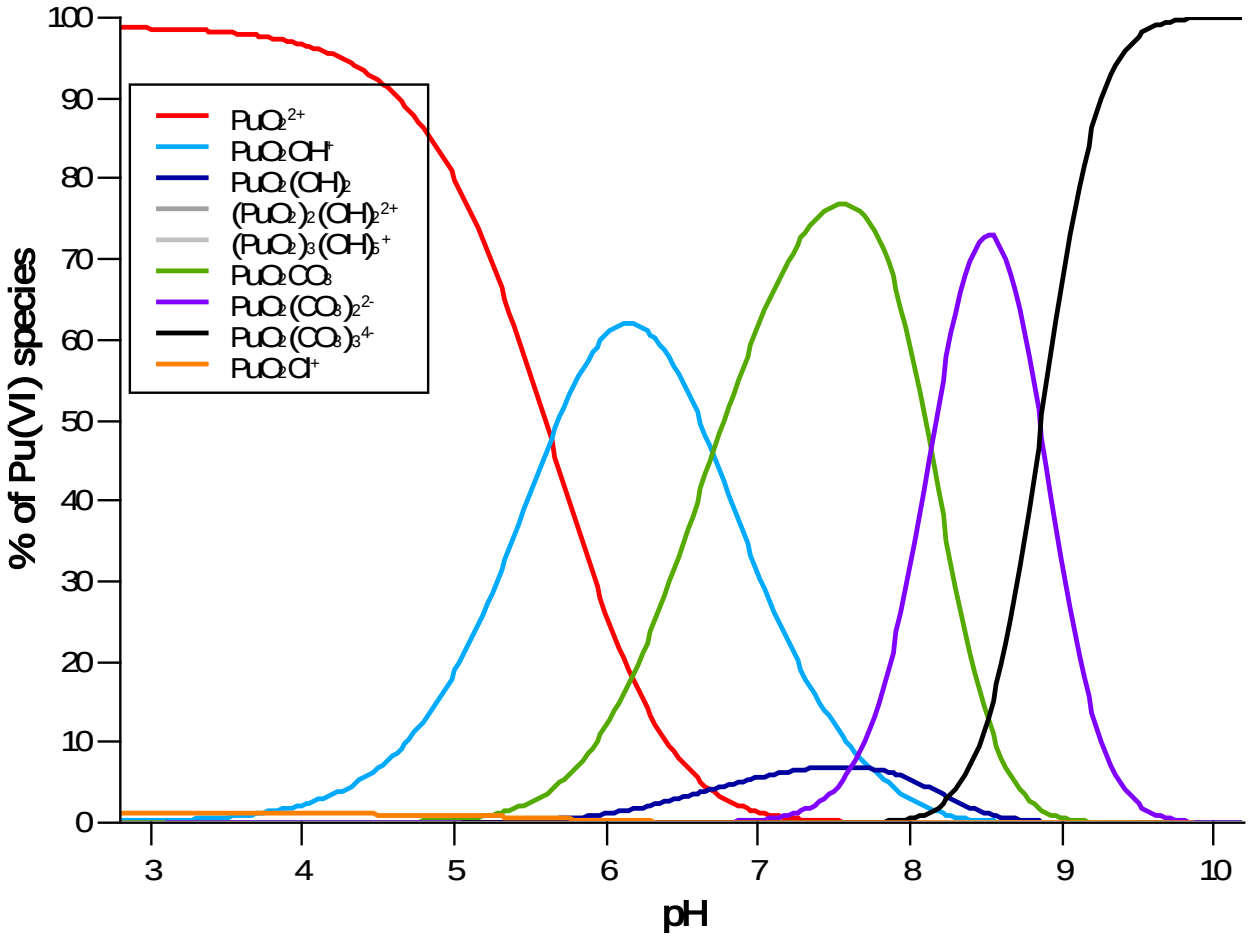


Figure 2.14: Complete speciation diagram of aqueous Pu(VI) in 0.01 M $NaClO_4$. Note the plutonium species $(PuO_2)_2(OH)_2^{2+}$, $(PuO_2)_3(OH)_5^{+}$, and $PuO_2Cl^{+}$ are plotted but are not clearly visible, as they did not exceed 1% of the total solution species. Thermodynamic data used to calculate this diagram is shown in Table 2.8.

| Chemical Reaction | log K° |
|---|---|
| $PuO_2^{2+} + H_2O \rightleftharpoons (PuO_2)OH^+ + H^+$ | -5.5 ± 0.5 |
| $PuO_2^{2+} + 2H_2O \rightleftharpoons (PuO_2)(OH)_2 + 2H^+$ | -13.2 ± 1.5 |
| $2PuO_2^{2+} + 2H_2O \rightleftharpoons (PuO_2)_2(OH)_2^{2+} + 2H^+$ | -7.5 ± 1.0 |
| $3PuO_2^{2+} + 5H_2O \rightleftharpoons (PuO_2)_3(OH)_5^{+} + 2H^+$ | -21.655 |
| $PuO_2^{2+} + HCO_3^{2-} \rightleftharpoons (PuO_2)CO_3 + H^+$ | -0.8288 |
| $PuO_2^{2+} + 2HCO_3^{2-} \rightleftharpoons (PuO_2)(CO_3)_2^{2-} + 2H^+$ | -5.9576 |
| $PuO_2^{2+} + 3HCO_3^{2-} \rightleftharpoons (PuO_2)(CO_3)_3^{4-} + 3H^+$ | -12.9864 |
| $PuO_2^{2+} + Cl^- \rightleftharpoons (PuO_2)Cl^+ + 2H^+$ | 0.23 ± 0.03 |
| $HCO_3^{2-} \rightleftharpoons CO_3^{2-} + H^+$ | -10.3288 |

Table 2.8: Thermodynamic data for the hydrolysis and formation of carbonate species and chloride species in aqueous solution for Pu(VI). Values taken from the NEA database[62] including its update[63].

## 2.3 Measurement and Characterization

The following sections briefly describe how plutonium was measured and characterized. Liquid scintillation counting (LSC) was used to quantitatively determine plutonium concentration. α and γ spectroscopy were essential to verify the purity of concentrated plutonium stock solutions after anion exchange columns were run, and optical absorbance spectroscopy in the visible and near-infrared (vis-NIR) range was used to ascertain the oxidation state of plutonium working stocks. XAS measurements provided information as to oxidation state. For the theory behind these spectroscopic measurements and characterization techniques, and how they pertain specifically to plutonium, refer to Appendix A.

### 2.3.6 γ Spectroscopy

A concentrated Pu-239 stock solution can contain trace amounts of Am-241, which stems from the β decay of Pu-241, and other transuranic impurities. Concentrated plutonium stock solutions were run through anion exchange resin (Appendix B) and the isotopic purity was confirmed using γ spectroscopy. The amplifier and multichannel analyzer (MCA) of the high purity germanium (HPGe) detector system were optimized for collection of low energy γ rays (< 100 keV). Figure 2.15 shows the γ ray energy spectrum of a concentrated plutonium stock solution. The three prominent photopeaks of Pu-239 (38.66 keV, 0.0104% intensity; 51.62 keV, 0.0272%; and 56.83 keV, 0.0012%) are visible, as well as the plutonium X-rays at low energy.[76] Am-241 has a strong γ line at 59.54 keV with 35.9% intensity, but is not seen in the spectrum, indicating anion exchange effectively purified the plutonium stock.

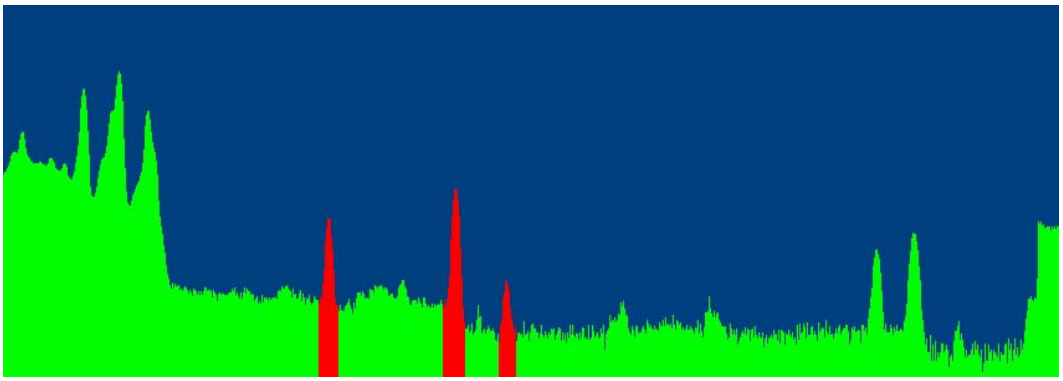

Figure 2.15: γ spectrum of a concentrated plutonium stock solution collected with a HPGe detector. The three photopeaks of Pu-239 at 38.66 keV, 51.62 keV, and 56.83 keV (highlighted in red) and absence of a Am-241 peak at 59.54 keV indicate the isotopic purity of the Pu-239 stock.

### 2.3.7 α Spectroscopy

Concentrated Pu-239 stock solutions were qualitatively characterized using α spectroscopy. Figure 2.16 shows the α spectrum of a concentrated plutonium stock solution with counts plotted on a log scale. The main peak corresponds to an α particle of 5.157 MeV (branching ratio of 70.8%), with shoulders corresponding to α particles with energy 5.105 MeV and 5.144 MeV with branching ratios of 11.5% and 17.1%, respectively. The small higher energy peak at ~5.4-5.5 MeV can be attributed to the 5.443 MeV or 5.486 MeV α particles from Am-241 or the 5.456 keV or 5.499 keV α particles from Pu-238. The presence of Am-241 can be ruled out from the absence of a 59.54 keV peak in the γ spectrum; this demonstrates the use of multiple spectroscopic methods for assessment of the chemical purity of stock solutions. Trace amounts of Pu-238 are assumed to be present. Though the smaller peak accounts for 0.02% of the entire activity in the α spectrum, even the smallest trace of Pu-238 in the sample creates a measurable signal because of its much shorter half-life ($t_{1/2}$ = 87.7 y) compared to that of Pu-239.

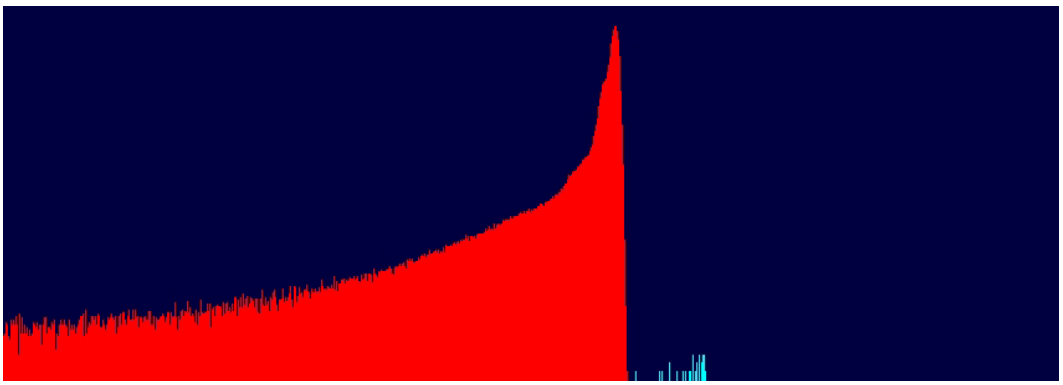

Figure 2.16: α spectrum of a concentrated plutonium stock solution collected with a surface barrier silicon diode detector. The main peak corresponds to the 5.157 MeV α-particle of Pu-239. The small higher energy peak at ~5.4-5.5 MeV is attributed to a Pu-238 impurity.

## 2.3.8 Liquid Scintillation Counting

As mentioned previously, Pu-239 emits an α particle with energy 5.157 MeV. With a high energy particle and absence of quenchers, the efficiency of LSC is considered to be 100%.[77] Solution aliquots of 5-10 μL were added to 5 mL Ecolume™ cocktail in a polyethylene (PE) vial. Inner LSC vials were doubly-contained with 20 mL transparent polyethylene terephthalate (PET) vials and shaken vigorously for at least 60 s to evenly disperse the analyte solution through the scintillation cocktail prior to counting. Plutonium samples, taken in duplicate, were counted for 300 s (Wallac 1414 liquid scintillation counter operating in α/β discrimination mode). A blank sample with no activity added but exposed to the same glovebox environment was counted with each sample set to give the background count rate, which was then subtracted. Almost all samples contained activity at least an order of magnitude greater than the background. Plutonium concentration was calculated from activity, determined from the count rate given from the liquid scintillation counter.

$$n = \frac{\text{count rate}}{60 N_A \lambda} \qquad \text{Eq 2.30}$$

$$\lambda = \frac{\ln 2}{t_{1/2}} \qquad \text{Eq 2.31}$$

where $N_A$ is Avogadro's number, λ is the decay constant for the radionuclide of interest, and $t_{1/2}$ is the half-life of the radionuclide of interest.

## 2.3.9 Optical Absorbance Spectroscopy

Optical absorbance spectroscopy using light with wavelength in the vis-NIR energy range was used to determine the oxidation states of aqueous plutonium. Cohen thoroughly characterized the ultraviolet, visible, and infrared absorbance spectra of Pu(III), Pu(IV), Pu(V), and Pu(VI).[78] The vis-NIR spectra of the Pu(III), Pu(IV), Pu(V) and Pu(VI) oxidation states are shown in Figure 2.17, Figure 2.18, Figure 2.19, and Figure 2.20, respectively, with the main peaks and extinction coefficients given in Table 2.9. While all four spectra are given for a solution of 1 M $HClO_4$, the spectra are vastly different from one another. This demonstrates the functionality of vis-NIR spectroscopy not only to determine plutonium concentration but to distinguish between oxidation states as well. At the lower wavelengths, the Pu(IV) spectrum exhibits what appears to be a large background absorption, but is historically attributed to light scattering in the solution, due to possible formation of the Pu(IV) colloid species. Pu(V) has the smallest extinction coefficients of the four plutonium oxidation states, meaning it is the species with the highest limit of detection. The large resonance peak of Pu(VI) spectrum at 830 nm has an extinction coefficient of ~550 $M^{-1}cm^{-1}$, and serves as an excellent indicator for the presence of aqueous Pu(VI). However, most spectrometers cannot properly resolve the sharp peak and so use of this truncated peak height is ill-advised to precisely quantify Pu(VI) concentration in solution.

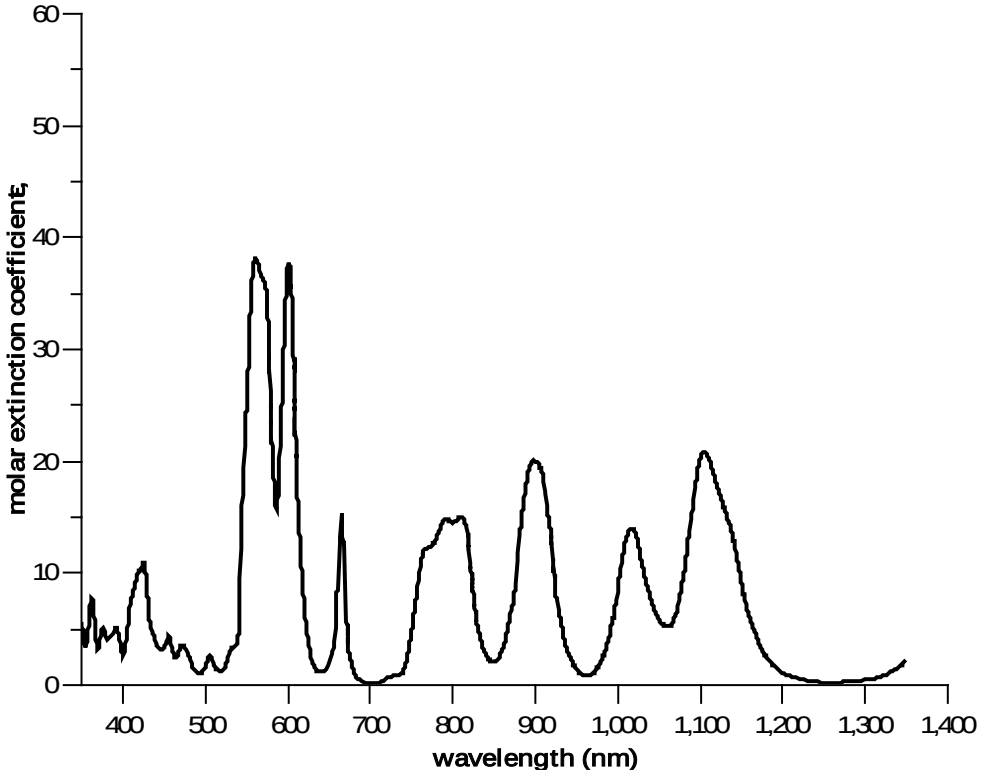


Figure 2.17: vis-NIR spectrum of Pu(III) in 1 M $HClO_4$. Adapted from Cohen.[78]

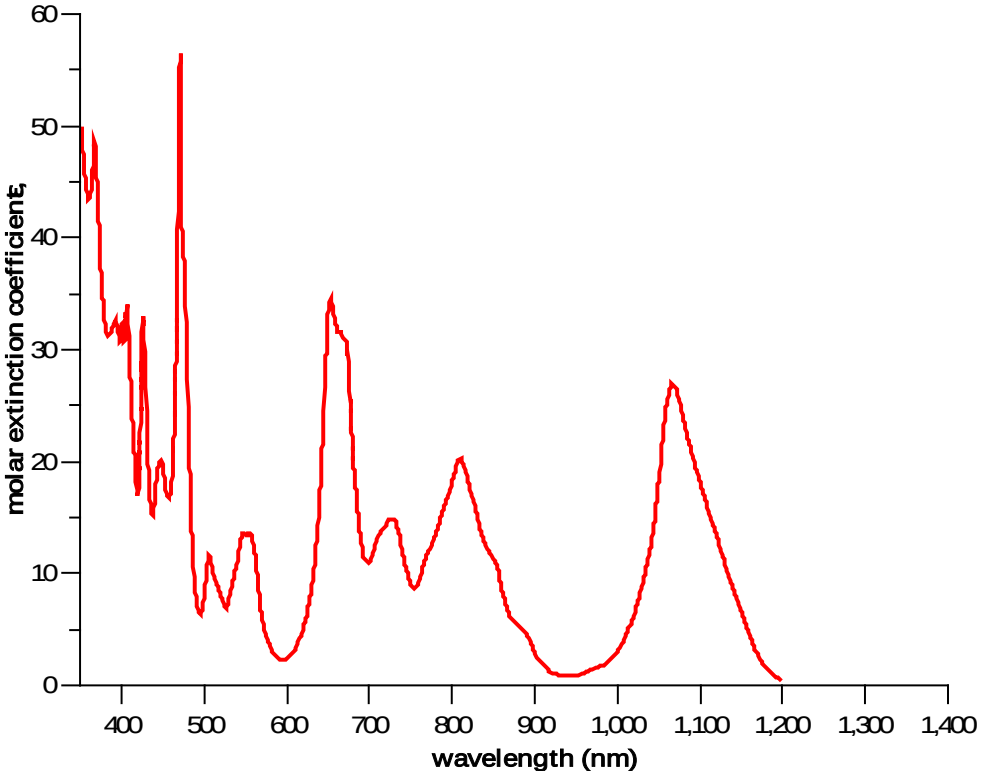


Figure 2.18: vis-NIR spectrum of Pu(IV) in 1 M $HClO_4$. Adapted from Cohen.[78]

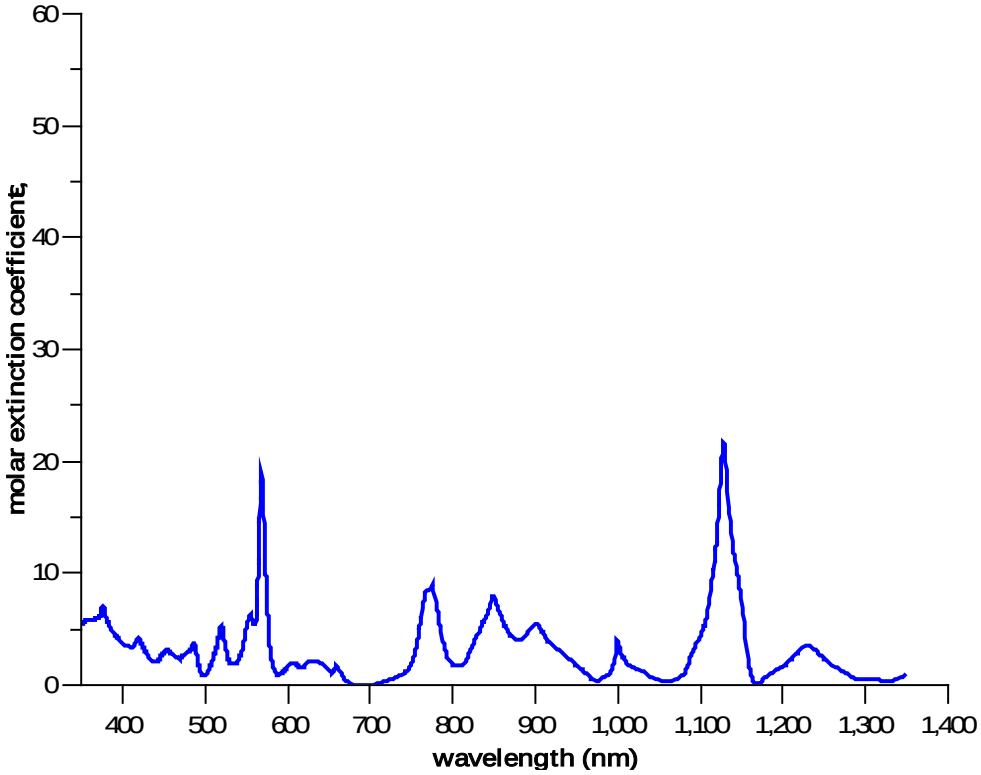


Figure 2.19: vis-NIR spectrum of Pu(V) in 1 M $HClO_4$. Adapted from Cohen.[78]

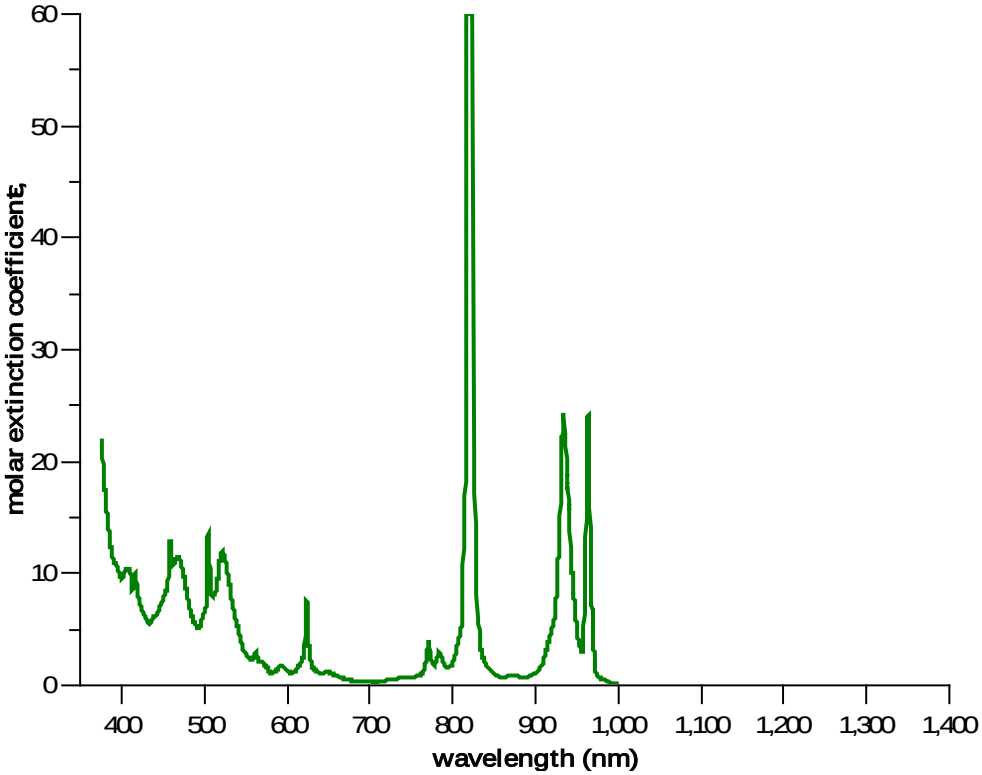


Figure 2.20: vis-NIR spectrum of Pu(VI) in 1 M $HClO_4$. Adapted from Cohen.[78]

| | wavelength (nm) | extinction coefficient, ε ($M^{-1}cm^{-1}$) |
|---|---|---|
| Pu(III) | 600 | 38 |
| Pu(IV) | 470 | 55 |
| Pu(V) | 568 | 19 |
| Pu(VI) | 830 | 550 |

Table 2.9: Wavelengths and molar extinction coefficients of the characteristic peaks in Pu(III), Pu(IV), Pu(V), and Pu(VI) spectra.[1,26,78]

## 2.3.10 X-ray Absorption Spectroscopy

XAS is a powerful technique to determine *in-situ* the electronic state of an atom.[25,79,80] XAS was used to probe the oxidation state of plutonium after sorption to iron oxide minerals.

XANES

A typical absorption spectrum of plutonium is given in Figure 2.21. The absorption edge for the $L_{III}$-edge is generally accepted at 18062.3 eV, but shifts in energy depending on oxidation state. Generally, samples are referenced to $PuO_2$ with a white line of 18062 eV, and the aquo ions in perchloric acid are shifted -2.3 eV, +0.9 eV, 0, and +2.6 eV for Pu(III), Pu(IV), Pu(V), and Pu(VI), respectively. Table 2.10 lists the $L_{III}$-edge energies for the plutonium oxidation states in various media matrices, as determined from the first inflection point of the absorption spectrum, and distances of nearest neighbors.[59] While the differences in energies for the absorption edges are minute, an obvious distinction between the more reduced plutonium forms [Pu(III) and Pu(IV)] from the more oxidized forms [(Pu(V) and PuVI)] is the feature on the higher energy side of the white line. Indicative of the plutonyl moiety, this shoulder is a result of multiple scattering along the linear Pu–O axial bond.

XANES spectra of pure Pu(IV), Pu(V), and Pu(VI) oxidation state standards are shown in Figure 2.22. Observe the characteristic plutonyl shoulder for Pu(V) and Pu(VI), while the feature is absent in the Pu(IV) spectrum. The spectra also show that a greater energy X-ray is needed to eject the core-level electron as the oxidation state of plutonium increases from Pu(V) to Pu(VI). Pu(IV) does not follow this trend though, as it exists as the bare cation. The two higher oxidation states Pu(V) and Pu(VI) exist as the plutonyl moiety and the presence of these plutonyl oxygens at short bond lengths (1.81 Å and 1.74 Å, respectively) increases the electron density around the plutonium atom and contributes to better shielding in a similar fashion as decreasing the oxidation state would. This causes the Pu(V) and Pu(VI) XANES spectra to shift to lower energies, resulting in overlap with the Pu(IV) spectra.

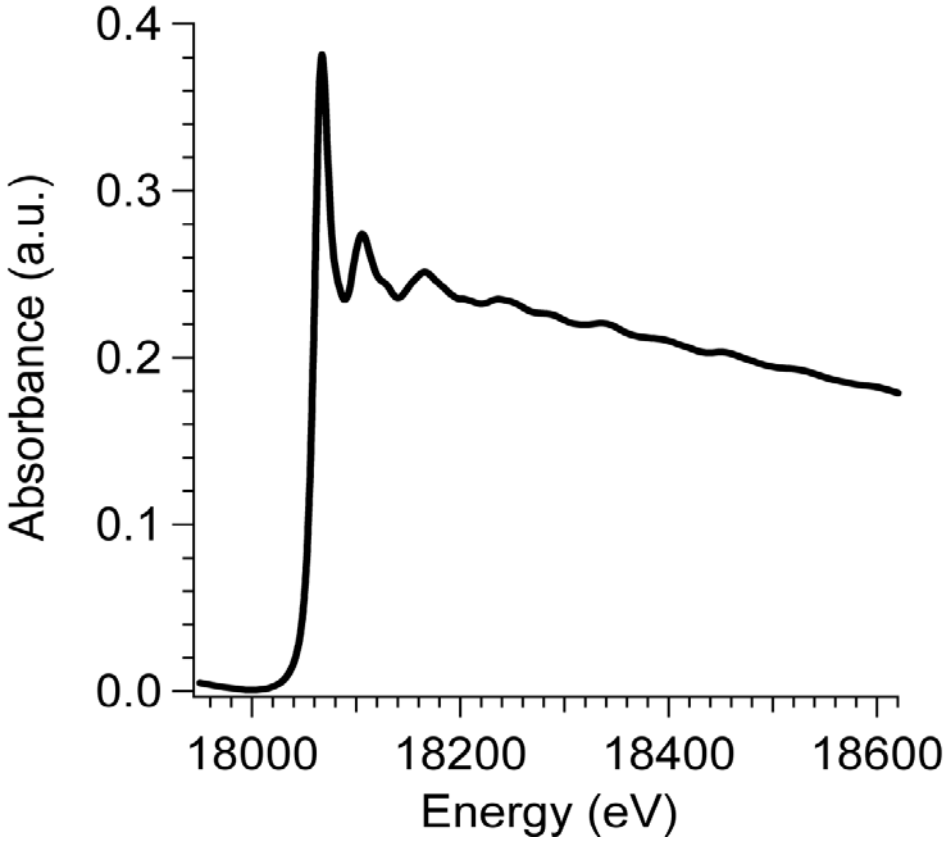


Figure 2.21: A typical absorption spectrum of plutonium at the $L_{III}$-edge

| Plutonium oxidation state | Edge Energy (eV) | Nearest Neighbor Distances (Å) |
|---|---|---|
| Pu(III) in 1M $HClO_4$ | 18060.0 | 2.48 |
| Pu(IV) in 1M $HClO_4$ | 18063.2 | 2.39 |
| Pu(V) in 1M $HClO_4$ | 18062.3 | 1.81, 2.47 |
| Pu(VI) in 1M $HClO_4$ | 18064.9 | 1.75, 2.41 |
| $PuO_{2\,(s)}$ | 18062.3 | 2.33 |
| $PuO_2(CO_3)_2^{4-}$ in 1M $HClO_4$ | 18064.7 | 1.75, 2.48 |
| $PuO_2(CO_3)_3^{5-}$ in 1M $HClO_4$ | 18062.9 | 1.84, 2.50 |

Table 2.10: The $L_{III}$-edge energies for plutonium, as determined from the first inflection point of the absorption spectrum, and nearest neighbor distances. Values taken from Conradson.[59]

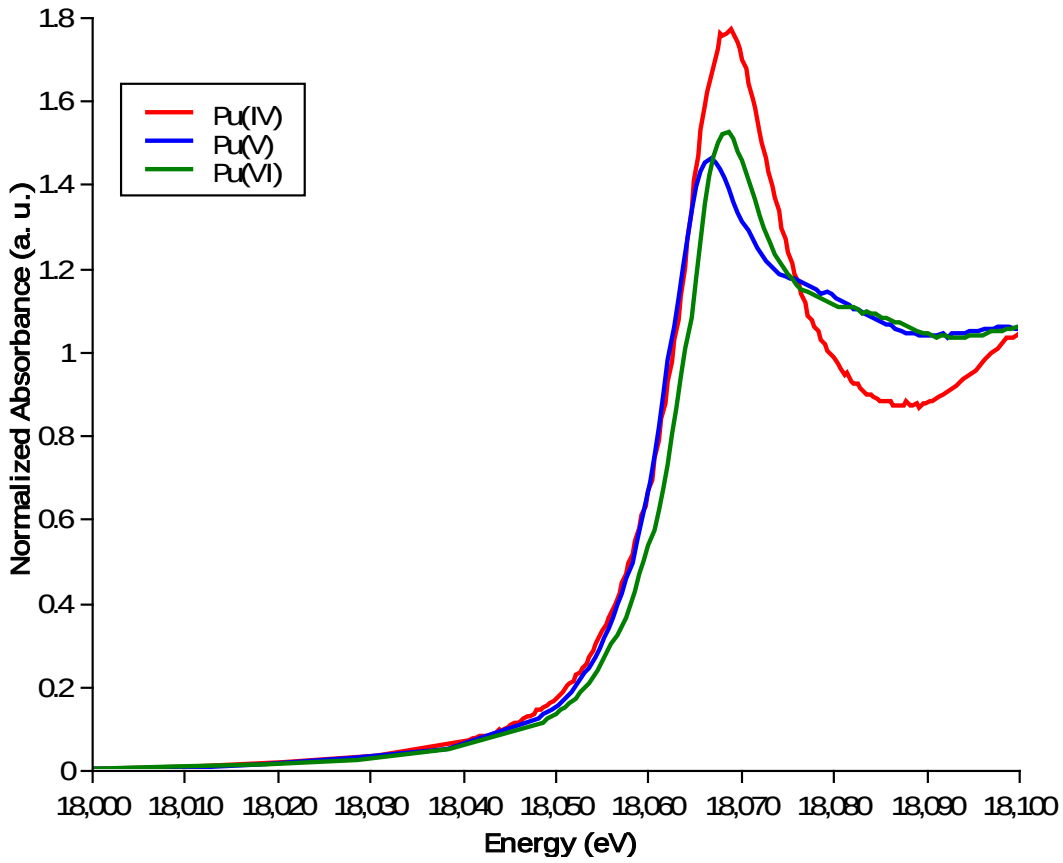


Figure 2.22: XANES spectra of the Pu(IV), Pu(V), and Pu(VI) solution standards used in fitting to determine plutonium oxidation state distribution. Note the characteristic shoulder for Pu(V) and Pu(VI), caused by scattering from the axial oxygens in the plutonyl moiety; this feature is absent for Pu(IV).

EXAFS

Figure 2.23 shows the structure of $PuO_{2(s)}$, and Figure 2.24 shows the EXAFS spectra of a $PuO_2$ reference in both *k*-space and the Fourier transform in *r*-space. Though the plots in *k*-space and *r*-space contain the same information, it is visually easier to see in *r*-space that there are 2 shells of atoms around each central plutonium atom in $PuO_{2(s)}$. The first shell at ~1.8 r + Δ (Å) is a shell of oxygen atoms and the second shell at ~3.8 r + Δ (Å) is a shell of plutonium atoms. The large peak at about 3.8 Å is indicative of Pu-Pu scattering.

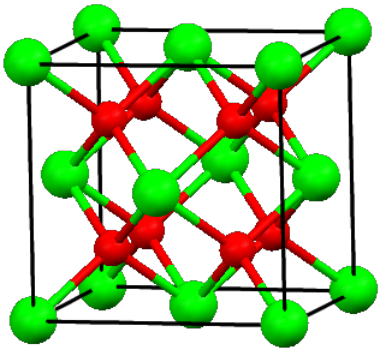

Figure 2.23: The structure of $PuO_2$ with plutonium atoms shown in green and oxygen atoms in red.

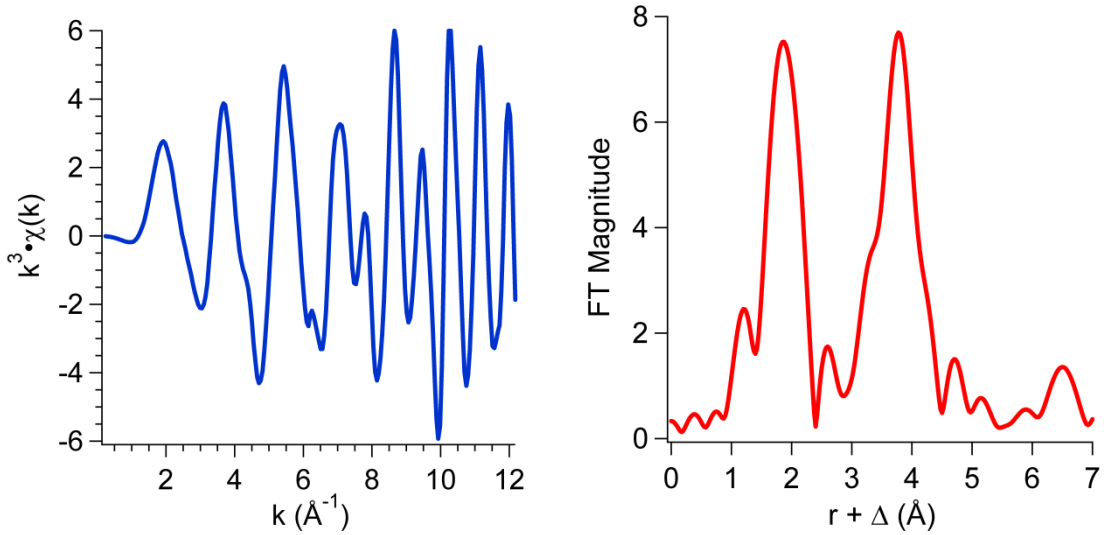


Figure 2.24: Plot of the EXAFS oscillations for $PuO_{2(s)}$ in (a) *k*-space and (b) the Fourier transform in *r*-space.

# 3. NEPTUNIUM CHEMISTRY

Another primary focus of this work is the investigation of the interactions of neptunium and hematite. Knowledge of aqueous neptunium chemistry is important for understanding how it will interact with a mineral surface at the solid/solution interface. This chapter gives an overview of neptunium, presents the solution chemistry of neptunium with particular focus on Np(V), and describes how neptunium was measured and characterized. A comprehensive compendium of neptunium solution chemistry can be found in the text by Yoshida *et al*.[81]

While there is no major commercial use of neptunium at present, Np-237 is vital for scientific research and exploratory work.[*] Np-237 is widely used as the precursor for various plutonium isotopes. (Pu-236 is useful as a chemical yield tracer for assessing plutonium in biological and environmental samples. Pu-236 is produced by irradiating Np-237 with bremsstrahlung (high energy photon ~25 MeV)[82] or 23.5 MeV protons[83] from a linear accelerator (LINAC). Pu-238 is the primary component of Radioisotope Thermoelectric Generators (RTGs) used to power NASA's deep space exploration vehicles. Pu-238 is produced by neutron irradiation of Np-237 in the core of the High Flux Isotope Reactor (HIFR) of Oak Ridge National Laboratory (ORNL).) Np-237 also serves as an important component in detectors of high-energy neutrons.

Neptunium, element 93, was the first ever transuranic element produced synthetically. In 1939 at the University of California, Berkeley, Professor Edwin M. McMillan irradiated uranium with slow neutrons from the 60 inch cyclotron. Neutron capture of U-238 and subsequent β decay resulted in an isotope of mass 239, shown in the nuclear reactions below (Eq 3.1 and Eq 3.2), with half-life of 2.3 days. The results were published but McMillan was hesitant to claim discovery of a new element.[84] Together with Professor Philip H. Abelson from the Carnegie Institute in Washington DC, the experiment was repeated in May 1940, and demonstrated conclusively that a new element had been discovered.[85] McMillan named element 93 neptunium after the planet Neptune, in recognition of its position beyond uranium, which was named after the planet Uranus.

[*] Neptunium is considered useable in nuclear weapons production, but no country has yet utilized it, given its critical mass of ~ 60 kg for Np-237's fissionability.

$$^{238}_{92}U + ^{1}_{0}n \rightarrow ^{239}_{92}U \quad \text{Eq 3.1}$$

$$^{239}_{92}U \rightarrow ^{239}_{93}Np + \beta^{-} \quad \text{Eq 3.2}$$

## 3.1 Np-237 Production and Decay

The most stable radioactive isotope of neptunium is Np-237. This radioisotope was first produced early in 1942 by Seaborg and Wahl, again at the University of California, Berkeley, as the daughter product of U-237, produced via an (n,2n) reaction of U-238.

$$^{238}_{92}U + ^{1}_{0}n \rightarrow ^{237}_{92}U + 2n \quad \text{Eq 3.3}$$

$$^{237}_{92}U \rightarrow ^{237}_{93}Np + \beta^{-} \quad \text{Eq 3.4}$$

Np-237 is routinely produced in nuclear reactors as a result of successive neutron capture of U-235 and U-236, two common constituents of nuclear fuel. U-235 is bombarded with an excess of neutrons to form metastable U-236. About 81% of the excited U-236 nuclei undergo fission, but the remainder decay to U-236. Further neutron capture forms U-237, which undergoes β decay to result in Np-237.

$$^{235}_{92}U + ^{1}_{0}n \rightarrow ^{236}_{92}U_{m} \rightarrow ^{236}_{92}U + \gamma \quad \text{Eq 3.5}$$

$$^{236}_{92}U + ^{1}_{0}n \rightarrow ^{237}_{92}U \quad \text{Eq 3.6}$$

$$^{237}_{92}U \rightarrow ^{237}_{93}Np + \beta^{-} \quad \text{Eq 3.7}$$

Np-237 is also formed from the α decay of Am-241.

$$^{241}_{95}Am \rightarrow ^{237}_{93}Np + \alpha \quad \text{Eq 3.8}$$

The half-lives, decay modes, and energies of emitted particles of select neptunium isotopes are listed in Table 3.1. The radioisotope used in the studies presented in this work was Np-237, which has a half-life of 2177000 years[33] and decays by α emission to the daughter product Pa-233, according to Eq 3.9. Pa-233 is a short-lived $\beta^-$ emitter, with a half-life of $t_{1/2}$ = 27 d, and rapidly ingrows in solutions of Np-237.

$$^{237}_{93}Np \xrightarrow{\alpha} ^{233}_{91}Pa + \quad \text{Eq 3.9}$$

$$^{233}_{91}Pa \rightarrow ^{233}_{92}U + \beta^{-} \quad \text{Eq 3.10}$$

$$^{233}_{92}U \rightarrow ^{229}_{90}Th + \alpha \quad \text{Eq 3.11}$$

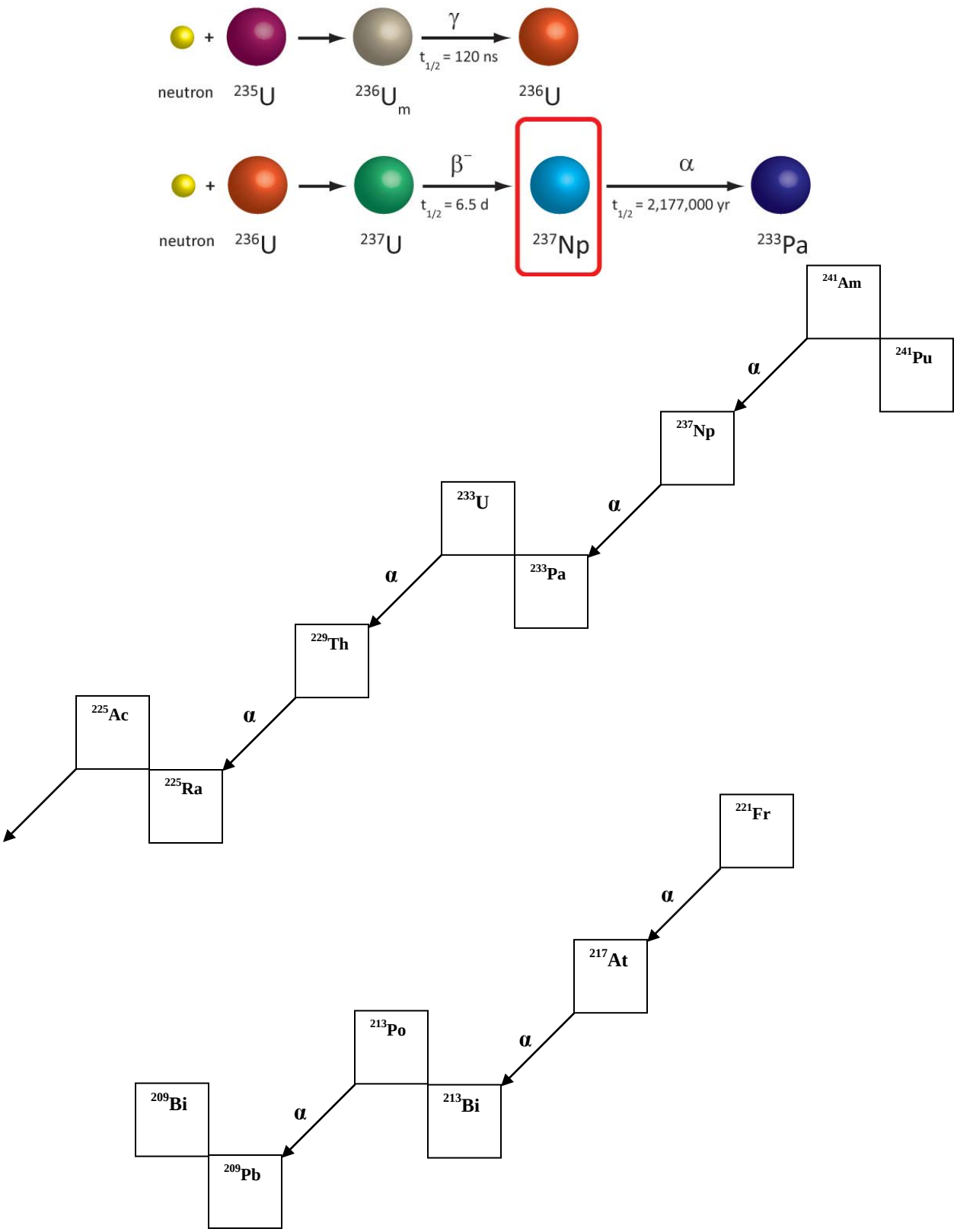


Figure 3.1: Production and decay scheme of Np-237, also known as the A = 4n + 1 series, which terminates in Bi-209.

| Isotope | half-life, $t_{1/2}$ | Decay Modes | energy of α-particle (MeV) | energy of β-particle (keV) | energy of γ-rays (keV) |
|---|---|---|---|---|---|
| Np-235 | 396 d | EC | | | 17.19 |
| Np-236 | 153000 y | EC, $\beta^-$, α | | 178, 163 | 44.6 |
| Np-236m | 22.5 h | EC, $\beta^-$ | | 46, 92 | 44.6, 45.2 |
| **Np-237** | **2177000 y** | **α** | **4.788** | | **29.37, 86.99** |
| Np-238 | 2.1 d | $\beta^-$ | | 60, 72, 412 | 44 |
| Np-239 | 2.4 d | $\beta^-$ | | 56, 93, 126 | 61 |

Table 3.1: Half-lives and decay information for select isotopes of neptunium. The radioisotope used in the studies described in this work, Np-237, is highlighted in **bold**. Values taken from the Evaluated Nuclear Structure Data File.[33]

## 3.2 Neptunium Aqueous Solution Chemistry

The solution chemistry of neptunium is very complex, given that neptunium can exist as compounds or complexes in five different oxidation states[*], and multiple oxidation states can be simultaneously present. As such, it is important to know what neptunium species are present in aqueous environmental conditions in order to understand neptunium interactions with the hematite surface.

The oxidation states of neptunium typically encountered in aqueous solutions are Np(III), Np(IV), Np(V), and Np(VI). In noncomplexing acidic conditions, Np(III) and Np(IV) exist as the aquo ions $Np^{3+}$ and $Np^{4+}$. In contrast, Np(V) and Np(VI) are unstable in aqueous solution and hydrolyze instantly to form the neptunyl moiety ($NpO_2^{n+}$) with two axial oxygen atoms bound to the central neptunium atom.[43] The aquo cations $Np^{3+}$ and $Np^{4+}$ have formal charge of +3 and +4, whereas the bonds between the axial oxygen atoms and neptunium atom causes the effective charge of the dioxocations $NpO_2^+$ and $NpO_2^{2+}$ to be $+2.3 \pm 0.2$ and $+3.3 \pm 0.1$, respectively.[48,49,86] Thus, the effective charge of neptunium cations is as follows: $Np^{4+} > NpO_2^{2+} \approx Np^{3+} > NpO_2^+$. Effective charge is correlated with an actinide's ionic character, so a higher effective charge results in a stronger, and thus shorter, bond. Accordingly, Np(V) and Np(VI) have Np–O bond lengths of 1.85 Å and 1.73 Å, respectively.[24,45,87–89] Spectroscopic data shows that Np(IV), with ionic radius of 0.98 Å[44], forms a spherically coordinated deca-aquo complex[90] and the aquo complexes of Np(V) and Np(VI) have 5 coordinating waters in their primary hydration spheres.[90]

### 3.2.1 Redox Chemistry and Disproportionation

Figure 3.2 shows the formal reduction potentials of the common neptunium oxidation states and the metal in a Latimer diagram measured in acidic conditions. Redox reactions between Np(III)/Np(IV) and Np(V)/Np(VI) occur rapidly and are electrochemically reversible, as only an electron is transferred. The reaction between Np(IV)/Np(V) has a slower reaction rate as the axial Np–O bond must be formed or broken, and as such is considered irreversible.

On the basis of redox potentials, Np(IV) and Np(V) are the oxidation states likely to be present in environmental conditions. Np(IV) will form under anoxic conditions; Np(V) is the

[*] The electronic ground state of Np is $[Rn]7s^2 6d^1 5f^4$, so five oxidation states (III-VII) are accessible.

expected dominant oxidation state under mildly oxic environmental conditions. However, oxidation state stability is strongly affected by factors such as acidity of the solution, presence of a complex forming ligand, and neptunium concentration. Np(V) is not easily complexed, so for this reason, pentavalent neptunium was the oxidation state used in the studies described in this work.

Np(VI) is stable in acidic solutions, and while autoreduction of Np(VI) to Np(V) does occur, it does so at a much lower rate than compared to other hexavalent actinides.[91] Only the Np(V) oxidation state undergoes appreciable disproportionation. Np(V) disproportionates to Np(IV) and Np(VI) through the following reaction:

$$2NpO_2^+ + 4H^+ \rightleftharpoons Np^{4+} + NpO_2^{2+} + 2H_2O \qquad \text{Eq 3.12}$$

Eq 3.12 shows that disproportionation is favored with high neptunium concentrations and in highly acidic solutions,[92] and as follows, the synproportionation reaction is promoted by a lower acidity of solution.

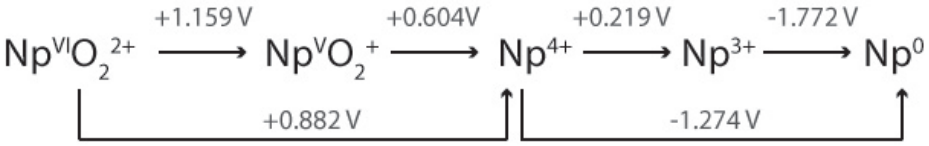


Figure 3.2: Latimer diagram that shows the standard redox potentials for neptunium oxidation states Np(III) – Np(VI) and neptunium metal in 1 M $HClO_4$. Values taken from Yoshida *et al.*[81]

## 3.2.2 Hydrolysis and Carbonate Complexation

The inclination of neptunium to form complexes is generally in the order $Np^{4+} > NpO_2^{2+} \approx Np^{3+} > NpO_2^{+}$, following the effective charge of the ions. Because of the ubiquitous presence of hydroxide ions and carbonate ions in the environment[58], the following discussion focuses on hydrolysis behavior and complexation with the inorganic carbonate ligand.

Hydrolysis is a particular case of complex formation that is common to all aqueous actinide ions. The formation constants for the neptunium hydroxo complexes, taken from the NEA database[62] including its update[63], are listed in Table 3.2. The relative tendency of neptunium to hydrolyze follows the general trend of complexation: $Np^{4+} > NpO_2^{2+} \approx Np^{3+} > NpO_2^{+}$. The degree of hydrolysis depends on the solution pH. Np(IV) exhibits a strong tendency towards hydrolysis. Even in moderately acidic solution, considerable hydrolysis occurs above pH 1. Np(VI) and Np(III) are hydrolyzed in solution at pH above 4-5 and 3-4, respectively, reflecting the larger effective charge of $NpO_2^{2+}$ than the $Np^{3+}$ ion. Np(V) is the most stable aqueous oxidation state, as $NpO_2^{+}$ is the predominant species for a wide pH range. Np(V) is only hydrolyzed appreciably at pH > 7 and the first hydrolysis product of Np(V) is not significantly present until above pH 9. This emphasizes the high mobility expected of Np(V) through the environment.

Formation of carbonate complexes is largely dependent on the aqueous speciation, which is also a strong function of pH. Consideration of the presence of bicarbonate and carbonate must

be taken for solutions open to air at conditions above pH 6 and pH 10, respectively. The higher oxidation states of neptunium form stable carbonate complexes, and are the prevailing species at higher pH conditions.[93] The formation reactions of neptunium carbonato complexes and corresponding stability constants are shown in Table 3.3, where the values are taken from the NEA database[62] including its update[63]. Important to note is that the formation of the neptunium carbonato complexes is favored over the hydrolysis products,[94] so carbonate complexation can competitively affect neptunium sorption on a mineral surface.

| Chemical Reaction | log β° |
|---|---|
| $Np^{3+} + H_2O \rightleftharpoons NpOH^{2+} + H^+$ | -6.8 ± 0.3 |
| $Np^{4+} + H_2O \rightleftharpoons NpOH^{3+} + H^+$ | 0.55 ± 0.2 |
| $Np^{4+} + 2H_2O \rightleftharpoons Np(OH)_2^{2+} + 2H^+$ | 0.35 ± 0.3 |
| $Np^{4+} + 4H_2O \rightleftharpoons Np(OH)_4 + 4H^+$ | -8.3 ± 1.1 |
| $NpO_2^+ + H_2O \rightleftharpoons (NpO_2)OH + H^+$ | -11.3 ± 0.7 |
| $NpO_2^+ + 2H_2O \rightleftharpoons (NpO_2)_2(OH)_2^- + 2H^+$ | -23.6 ± 0.5 |
| $NpO_2^{2+} + H_2O \rightleftharpoons (NpO_2)OH^+ + H^+$ | -5.1 ± 0.4 |
| $2NpO_2^{2+} + 2H_2O \rightleftharpoons (NpO_2)_2(OH)_2^{2+} + 2H^+$ | -6.27 ± 0.21 |
| $3NpO_2^{2+} + 5H_2O \rightleftharpoons (NpO_2)_3(OH)_5^+ + 5H^+$ | -17.12 ± 0.22 |

Table 3.2: Formation constants for the hydrolysis complexes of neptunium. Formation constants for the hydrolysis complexes of neptunium. Values taken from the NEA database[62] including its update[63], and error is the 95% confidence interval.

| Chemical Reaction | $\log_{10}\beta°$ |
|---|---|
| $NpO_2^+ + CO_3^{2-} \rightleftharpoons NpO_2(CO_3)^-$ | 4.962 ± 0.061 |
| $(NpO_2)(CO_3)^- + CO_3^{2-} \rightleftharpoons (NpO_2)(CO_3)_2^{3-}$ | 1.572 ± 0.083 |
| $(NpO_2)(CO_3)_2^{3-} + CO_3^{2-} \rightleftharpoons (NpO_2)(CO_3)_3^{5-}$ | -1.034 ± 0.11 |
| $NpO_2^{2+} + CO_3^{2-} \rightleftharpoons (NpO_2)(CO_3)$ | 9.32 ± 0.61 |
| $NpO_2^{2+} + 2CO_3^{2-} \rightleftharpoons (NpO_2)(CO_3)_2^{2-}$ | 16.516 ± 0.729 |

Table 3.3: Stability constants for mono-, bis-, and tris-carbonate complexes of neptunium. Values taken from the NEA database[62] including its update[63], and error is the 95% confidence interval.

### 3.2.3 Solubility and Precipitation

Neptunium solubility is dependent on oxidation state, extent of hydrolysis, presence of complexing ligands, and pH conditions of the aqueous solution. Oxidation state has a considerable effect on neptunium solubility, but solubility generally holds to the trend of effective charge ($Np^{4+} > NpO_2^{2+} \approx Np^{3+} > NpO_2^{+}$). Because Np(IV) has the highest effective charge, it forms the least soluble precipitates. The oxidized forms of neptunium [Np(V) and Np(VI)] form hydroxides in neutral and basic solutions that are much more soluble than that of the Np(IV) hydroxide. The reduced forms of neptunium [Np(III) and Np(IV)] form insoluble hydroxides in aqueous solutions of low acidity, and the Np(III) hydroxide species is readily oxidized to the Np(IV) hydroxide species in air. The solubility of Np(V), in $CO_2$-free conditions with only hydroxide as the complexing ligand, is controlled by the solubility product of amorphous $NpO_2OH_{(s)}$. Solubility increases in alkaline conditions due to formation of the second hydrolysis species, $NpO_2(OH)_2^-$. Solubility of neptunium also increases in the presence of carbonate, due to formation of the more soluble neptunium carbonato complexes.[95,96]

### 3.2.4 Speciation

It is crucial that Np(V) sorption behavior be evaluated with regards to Np(V) aqueous speciation. A speciation diagram of Np(V) in 0.01 M $NaClO_4$ in the presence of atmospheric $CO_2$ is presented in Figure 3.3, with a narrower pH range shown in Figure 3.4 to better distinguish the hydrolysis products and carbonate complexes. Speciation calculations were performed using the thermo.com.V8.R6.230 database[74], which was modified to include aqueous Np(V) species. Equilibrium constants of the reactions used in the speciation calculations were taken from the NEA database[62] including its update[63] and are given in Table 3.4. Speciation diagram was generated using PhreePlot, which contains an embedded version of PHREEQC.[75] Refer to Appendix D for the PhreePlot input file used to generate the Np(V) speciation diagram.

In the presence or in the absence of $CO_2$, Np(V) aqueous speciation is dominated by $NpO_2^+$ for acidic to neutral pH conditions. In the absence of $CO_2$, the stability of the Np(V)-hydroxyo complexes, $NpO_2OH$ and $NpO_2(OH)_2^-$, increases continuously with increasing pH, eventually dominating the neptunium speciation at high pH. Under atmospheric conditions, however, the presence of bicarbonate and carbonate must be considered above pH 6 and hydrolysis begins at pH 7. The stability of the neutral hydrolysis product, $NpO_2OH$ reaches a maximum near pH 8.5 and decreases with further increasing pH. Dissolved carbonate at higher pH leads to carbonate complexation of Np(V) species, and the negatively charged carbonato complexes ($NpO_2(CO_3)^-$, $NpO_2(CO_3)_2^{3-}$, and $NpO_2(CO_3)_3^{5-}$) are the prevailing solution species at pH > 8.5. The contributions of $NpO_2Cl_{(aq)}$ (due to the $O_2 + Cl_2$ reaction) and $NpO_2(OH)_2^-{}_{(aq)}$ are negligible (<0.5% together) and the two species are not visible in the speciation diagram.

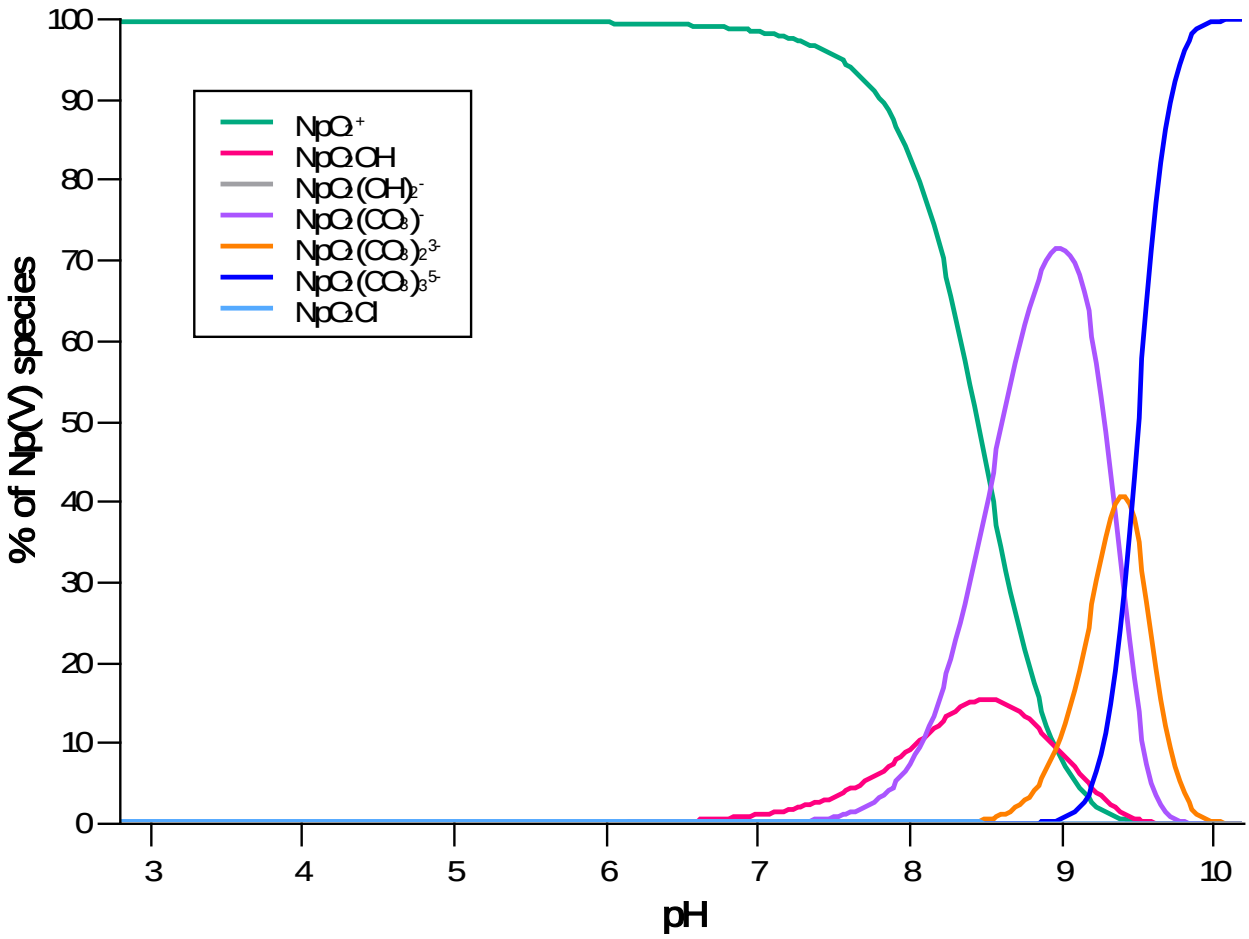


Figure 3.3: Speciation diagram of aqueous Np(V) in 0.01 M $NaClO_4$ from pH 3 to pH 10. Thermodynamic data used to calculate this diagram are shown in Table 3.4.

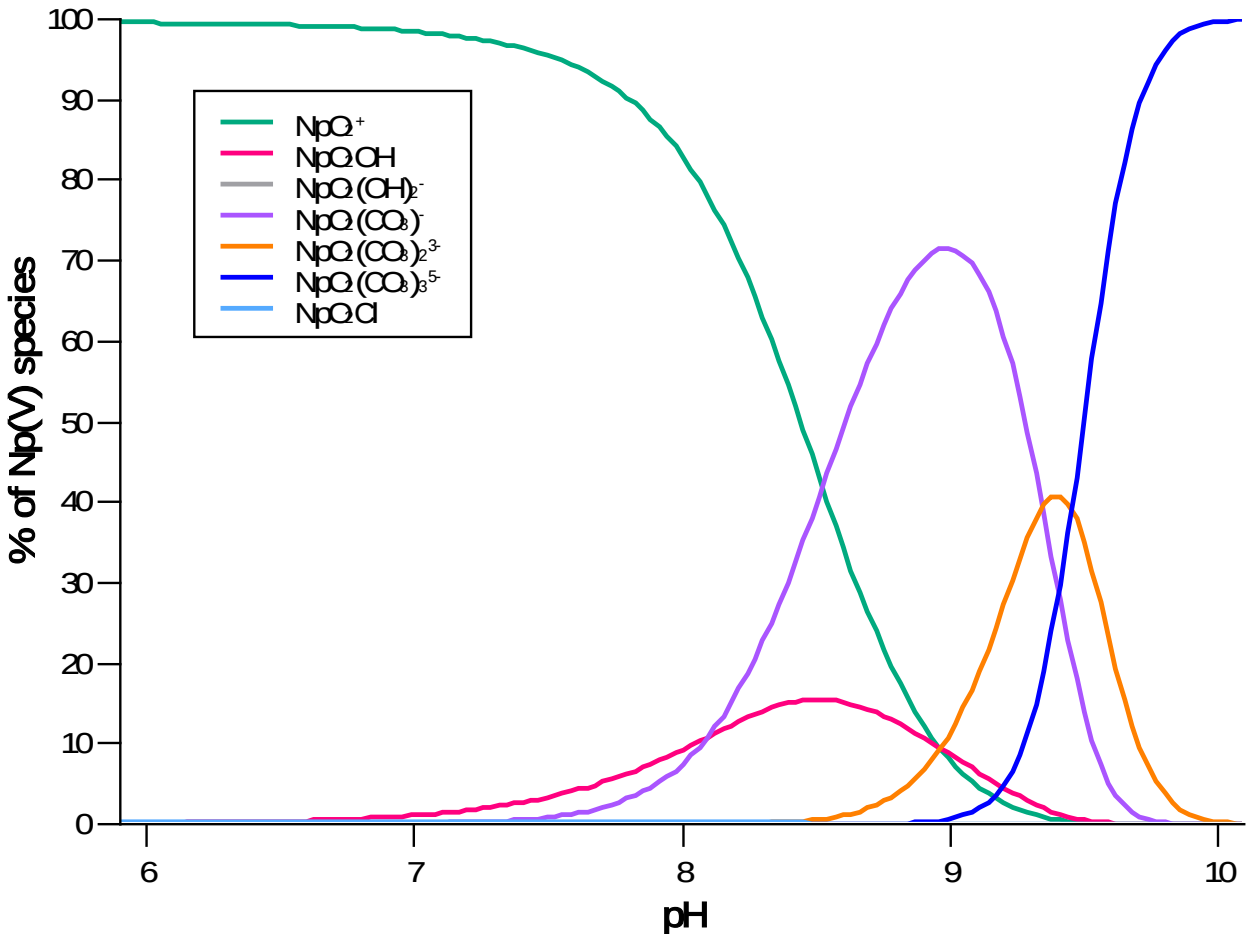


Figure 3.4: Speciation diagram of aqueous Np(V) in 0.01 M $NaClO_4$ from pH 6 to pH 10. Thermodynamic data used to calculate this diagram are shown in Table 3.4.

| Chemical Reaction | log K° |
|---|---|
| $NpO_2^+ + H_2O \rightleftharpoons (NpO_2)OH + H^+$ | -11.3 ± 0.7 |
| $NpO_2^+ + 2H_2O \rightleftharpoons (NpO_2)_2(OH)_2^- + 2H^+$ | -23.6 ± 0.5 |
| $NpO_2^+ + HCO_3^{2-} \rightleftharpoons (NpO_2)CO_3^- + H^+$ | -5.3668 |
| $NpO_2^+ + 2HCO_3^{2-} \rightleftharpoons (NpO_2)(CO_3)_2^{3-} + 2H^+$ | -14.1236 |
| $NpO_2^+ + 3HCO_3^{2-} \rightleftharpoons (NpO_2)(CO_3)_3^{5-} + 3H^+$ | -25.487 |
| $NpO_2^+ + Cl^- \rightleftharpoons (NpO_2)Cl + 2H^+$ | -0.4 |
| $HCO_3^{2-} \rightleftharpoons CO_3^{2-} + H^+$ | -10.3288 |

Table 3.4: Thermodynamic data for the hydrolysis and formation of carbonate species and chloride species in aqueous solution for Np(V). Values taken from the NEA database[62] including its update[63].

## 3.3 Measurement and Characterization

The following sections briefly describe how neptunium was measured and characterized. LSC was used to quantitatively determine neptunium concentration. α and γ spectroscopy were used to qualitatively characterize the concentrated neptunium stock solution after anion exchange, and optical absorbance spectroscopy in the vis-NIR range was used to verify the oxidation state of pentavalent neptunium working stocks. XAS measurements provided information as to oxidation state and local coordination of the neptunium ion. Refer to Appendix A for the theory behind these spectroscopic measurements and characterization techniques.

### 3.3.1 γ Spectroscopy

A concentrated neptunium stock solution can contain trace amounts of plutonium and other transuranic impurities. Additionally, the immediate daughter of Np-237 is the short-lived β emitter Pa-233, which rapidly ingrows in Np-237 solutions. To reduce the β activity and transuranic impurities, anion exchange columns were run (Appendix B) and the concentrated neptunium stock solution was qualitatively characterized with γ spectroscopy. The amplifier and MCA of the HPGe detector system were optimized for collection of low energy γ rays (< 100 keV). Figure 3.5 shows the γ ray energy spectrum of a concentrated neptunium stock solution. The two prominent photopeaks of Np-237 (29.36 keV, 14.12% and 86.48 keV, 12.4%) are visible, as well as the neptunium X-rays at low energy.

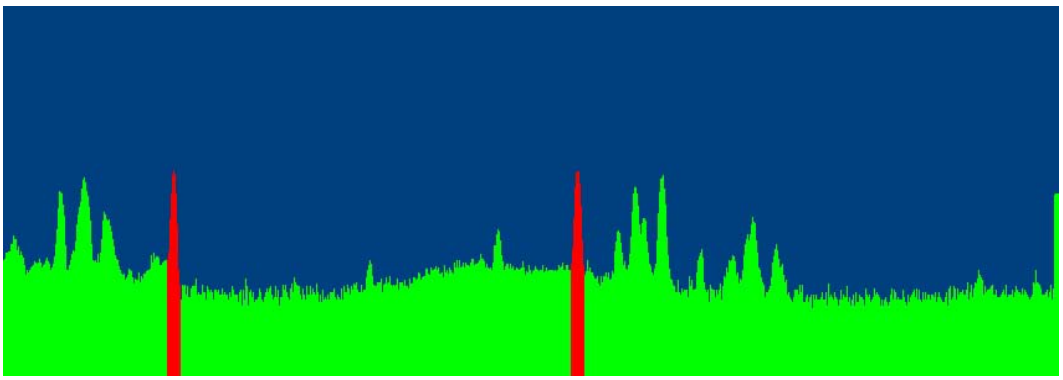

Figure 3.5: γ spectrum of a concentrated neptunium stock solution collected with a HPGe detector. The two major photopeaks of Np 237 at 29.36 keV and 86.48 keV are highlighted in red.

### 3.3.2 α Spectroscopy

α spectroscopy was used to complement γ spectroscopy in qualitatively characterizing the concentrated neptunium stock solution. Figure 3.6 shows the α spectrum with counts plotted on a log scale of a concentrated neptunium stock solution. The main peak corresponds to an

α particle of 4.788 MeV (branching ratio of 47.6%), with shoulders corresponding to α particles with energy 4.767 MeV and 4.771 MeV with branching ratios of 9.3% and 23.2%, respectively. The small higher energy peak at ~5.4-5.5 MeV can be attributed to the 5.443 MeV or 5.486 MeV α particles from Am-241 or the 5.456 keV or 5.499 keV α particles from Pu-238. The presence of Am-241 can be ruled out from the absence of a 59.54 keV in the γ spectrum, so trace amounts of Pu-238 are assumed to be present.

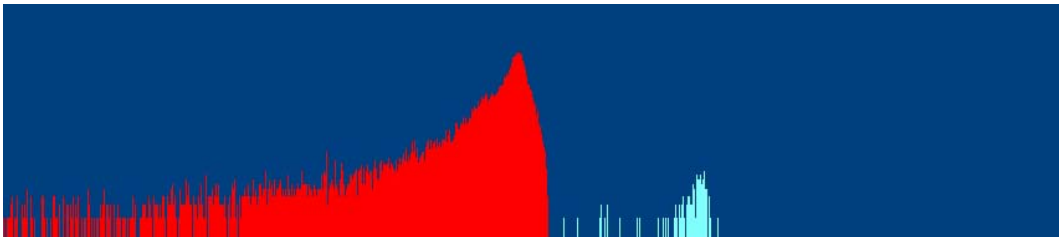

Figure 3.6: α spectrum of a concentrated neptunium stock solution collected with a surface barrier silicon diode detector. The main peak corresponds to the 4.788 MeV α-particle of Np-237. The small higher energy peak at ~5.4-5.5 MeV is attributed to a Pu-238 impurity.

### 3.3.3 Liquid Scintillation Counting

Neptunium α activity was counted using a Wallac 1414 liquid scintillation counter operating in α/β discrimination mode. The short-lived Pa-233 is the daughter of Np-237. Pa-233 emits β particles with average energies high enough (~100 keV) to interfere with the α decay spectrum measured by a liquid scintillation counter (~1-4 MeV). Therefore, α and β decay events were discriminated during counting by optimizing the pulse decay discriminator (PSA settings) with pure α and β emitters. Once optimized, the same PSA setting was used for all subsequent analyses of Np-237 α activity. Solution aliquots of 5-50 μL were added to 5 mL Ecolume$^{TM}$ cocktail in a PE vial. Inner LSC vials were doubly-contained with 20 mL transparent PET vials and shaken vigorously for at least 60 s to evenly disperse the analyte solution through the scintillation cocktail prior to counting. Neptunium samples, taken in triplicate, were counted for 3600 s. A blank sample with no activity added but exposed to the same radioactive environment was counted with each sample set to give the background count rate, which was then subtracted. Almost all samples contained activity at least an order of magnitude greater than the background. Neptunium concentration of the samples was determined from the count rate using Eq 2.30 and Eq 2.31.

### 3.3.4 Optical Absorbance Spectroscopy

vis-NIR spectroscopy was used to determine the oxidation states of aqueous neptunium. The absorbance spectra of Np(III), Np(IV), Np(V), and Np (VI) have been thoroughly characterized in perchloric acid[97–99] and nitric acid[100,101]. The vis-NIR spectra of the Np(III), Np(IV), Np(V) and Np(VI) oxidation states in 2 M $HClO_4$ are shown in Figure 3.7[81], and the wavelengths and extinction coefficients of the characteristic peaks presented in Table 3.5[1,91]. The large peak at 980 nm, with extinction coefficient of ~395 $M^{-1}cm^{-1}$, signifies the presence of aqueous Np(V).

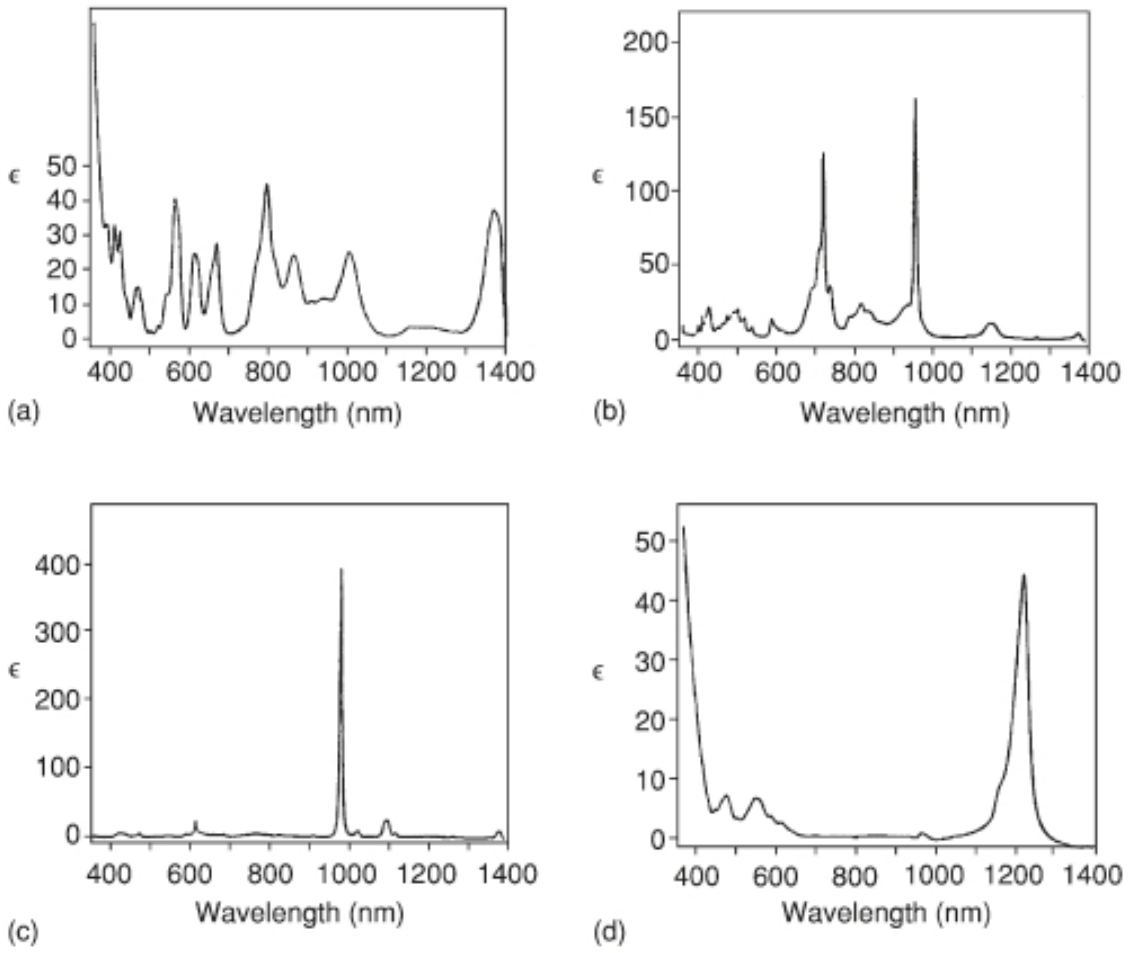


Figure 3.7: The vis-NIR spectra of neptunium oxidation states in 2 M $HClO_4$: (a) Np(III), (b) Np(IV), (c) Np(V), and (d) Np(VI). Taken from Yoshida *et al.*[81]

| | wavelength (nm) | extinction coefficient, ε ($M^{-1}cm^{-1}$) |
|---|---|---|
| Np(III) | 786 | 44 |
| Np(IV) | 723 | 127 |
| | 960 | 162 |
| Np(V) | 617 | 22 |
| | 980 | 395 |
| Np(VI) | 1223 | 45 |

Table 3.5: Wavelengths and molar extinction coefficients of the characteristic peaks in Np(III), Np(IV), Np(V), and Np(VI) spectra. Values taken from Burney and Harbour.[91]

### 3.3.5 X-ray Absorption Spectroscopy

The absorption spectra of neptunium at the $L_{III}$-edge were well characterized by Soderholm *et al.*[102] Figure 3.8 shows the XANES spectra of Np(III), Np(IV), Np(V), and Np(VI) with primary absorption peaks at ~17610 keV due to the $2p_{3/2} \rightarrow 6d$ transition. Note the different shapes between the reduced forms (Np(III)/Np(IV)) and the oxidized forms (Np(V)/Np(VI)). The characteristic shoulder to the high energy side of the white line at 17.62 keV is due to the multiple scattering effects of the photoelectron off of the two axial oxygens present in the neptunyl moiety. The relative energy shift between Np(V) and Np(VI) was determined to be +2.5 eV by Reich *et al.*[103]

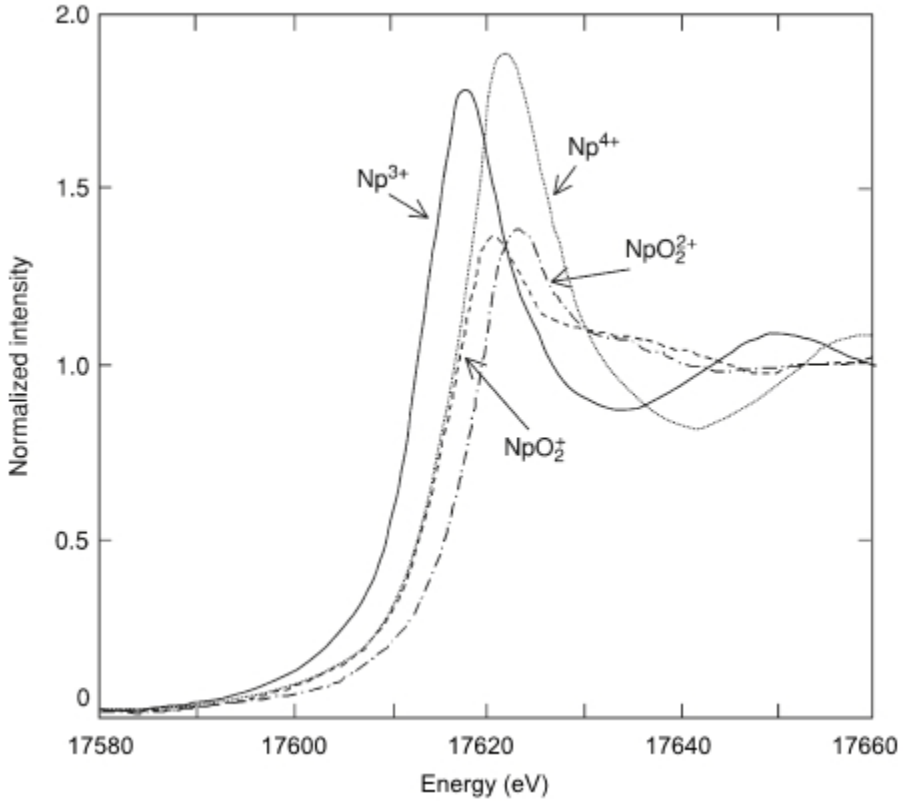


Figure 3.8: XANES spectra of Np(III), Np(IV), Np(V), and Np(VI) oxidation states. Note the characteristic shoulder for Np(V) and Np(VI), which is absent for Np(III) and Np(IV). Adapted from Soderholm *et al.*[102]

# 4. SURFACE CHEMISTRY

To understand the interactions between aqueous actinide species and iron oxide minerals, knowledge of the reactions that occur at the solid/solution interface is essential. This encompasses both the properties of the solid surface and the nature of its interactions with aqueous species. The following chapter describes some key concepts, definitions, and descriptions of surface chemistry that are relevant to understanding the reactions at mineral surfaces in solution.

## 4.1 Surface Complexation

The term "sorption" is an overarching term used to describe interactions that occur between a solid phase and an aqueous solution phase, generally referring to the loss of ions from solution to a surface. Adsorption is the net accumulation of chemical species at the solid/solution interface, whereas absorption specifically refers to an aqueous species being taken up and incorporated into a pure mineral phase. Adsorption includes both chemisorption and physisorption. Chemisorption is chemical adsorption where there is an actual chemical bond between the interacting species. In contrast, physisorption involves only weak intermolecular forces, such as van der Waals interactions or hydrogen bonding between the species.

When a surface functional group (adsorbent) reacts with a molecule or ion dissolved in solution (adsorptive) to form a stable complex (adsorbate), this is termed "surface complexation". Examples of surface functional groups include hydroxyl groups that protrude from the surface of hydrous metal oxides or clay minerals and carboxyl or phenol groups on surfaces of colloidal organic matter. Surface complexation can occur through three mechanisms: inner-sphere complexation, outer-sphere complexation, and the diffuse-ion swarm. An inner-sphere surface complex has no water molecule interposed between the surface and the complexed ion. If at least one water molecule is interposed between the surface and the complexed ion, the complex is outer-sphere. The covalent or ionic interactions of inner-sphere complexation lead to considerable stability of the complex, whereas outer-sphere complexation is a result of electrostatic interactions. As such, inner-sphere complexes are generally much more stable than outer-sphere complexes. Ions in the diffuse swarm are fully dissociated from the surface. These solvated ions are not involved in a surface complex, and accordingly remain free to move about nearby in the solution, neutralizing surface charge through their proximity to

the charged solid surface. Figure 4.1 shows the three mechanisms of surface complexation described above.

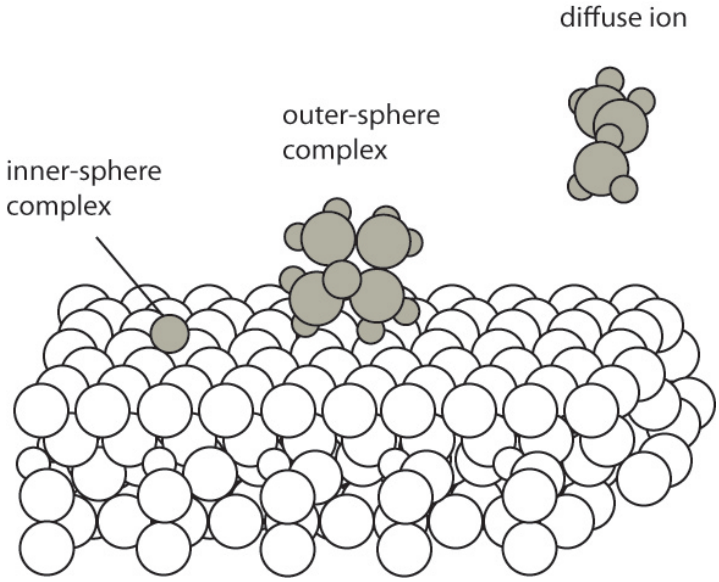


Figure 4.1: A schematic of the three types of surface complexes that can form: an inner-sphere complex, an outer-sphere complex, and a diffuse ion floating in solution. Adapted from Sposito.[104]

The generic term "specific adsorption" occurs when ions have a high affinity for the surface in contrast to "nonspecific adsorption" which is dominated by electrostatic attraction. (Here, nonspecificity refers to the weak dependence on the electron configuration of the surface group and adsorbed ion to be expected for the interaction of solvated species.) Specific adsorption is often used to describe inner-sphere complexes formed between surface functional groups on minerals and ions in solution, while nonspecific adsorption often describes outer-sphere complexation and diffuse-ion association.

In regards to actinides, inner-sphere complexation occurs when the actinide ion becomes covalently bonded to a surface. The actinide ion, a hard Lewis acid, accepts electron pairs from the surface. Formation of an inner-sphere complex involves the release of protons from surface functional groups and loss of a water molecule from the hydration sphere of the actinide.[105,106] This would be an irreversible endothermic process, as the actinide ion goes from a disordered state (aqueous phase) to a more ordered state (solid phase). Outer-sphere complexation is a result of electrostatic attraction between an actinide ion and a charged surface, and the interaction is typically considered reversible.

## 4.2 Surface Complexation Models (SCM)

Sorption models provide a simplified description of the adsorption process. A number of models for the sorption of ions to surfaces, both cations and anions, have been developed. These adsorption models begin with hypotheses about the interactions between an adsorbent and an adsorptive, but the accuracy of the models can only be verified through experimental spectroscopic data. Surface complexation models (SCM) are based on the assumption that surfaces are composed of functional groups that can form complexes with ions in solution.

Using this approach, surface functional groups are treated analogous to complexing ligands in solution. SCMs take into account surface species, chemical reactions, equilibrium constants, mass balances, charge balances, and the consideration of charge on both the adsorptive ion and the solid adsorbent surface. Three of the more common SCMs include the constant capacitance model, the diffuse-layer model, and the triple-layer model. These three models are based on the well-known electrical double layer (EDL) theory proposed by Guoy and Chapman, where there is one layer of surface charges, another diffuse layer of counterions in solution, and the two layers balance each other's electrostatic charge. The models differ most notably in the structural representation of the solid/solution interfacial region and distinguishing between the types of surface complexation that takes place. For both the diffuse-layer model and the constant capacitance model, all surface complexes are inner-sphere; conversely, the triple-layer model considers inner- as well as outer-sphere complexes. A brief overview of the three SCMs will be given below; an in-depth review by Goldberg[107] provides more detailed descriptions of the models that involve surface site density, capacitance densities, and surface complexation constants.

Perhaps the simplest SCM, the diffuse-layer model was proposed by Stumm *et al.*,[108,109] and expanded further into the generalized two-layer model by Dzombak and Morel.[110] In the diffuse-layer model, the solid/solution interface comprises two planes of charge density: a surface layer and a diffuse layer. The model assumes all surface complexes are inner-sphere and no surface complexes are formed with ions from the background electrolyte. All reactions occur only at the one surface layer, referred to as the "o-plane". These reactions include protonation-deprotonation of surface hydroxyl sites in addition to surface complexation reactions. The background electrolyte ions reside in the diffuse layer, referred to as the "d-plane", and the d-plane is given by the Gouy-Chapman model. Figure 4.2a shows the surface complexation and two planes of charge density of the solid/solution interface as described with the diffuse-layer model.

Schindler *et al.*[111,112] developed the constant capacitance model, where the solid/solution interface is modeled as a parallel plate capacitor. The two plates represent the solid and solution sides with charges $\sigma$ and zero, respectively, and a constant capacitance between the two plates. The constant capacitance model also assumes all surface complexes are inner-sphere, no surface complexes are formed with ions from the background electrolyte, all reactions (protonation, deprotonation, and complexation) occur at the o-plane, and background electrolyte ions reside a certain distance away from the surface where the net charge is zero. The constant capacitance model is applicable for conditions of high ionic strength and/or low potential, unlike the diffuse-layer model that is primarily valid under low ionic strength conditions. Figure 4.2b gives an illustration of the constant capacitance model.

The triple-layer model was developed by Davis and Leckie *et al.* as an extension of the diffuse-layer model.[113–115] In this SCM, the solid/solution interface comprises three planes of charge density: the o-plane (which corresponds to the surface), the d-plane (which corresponds to the diffuse layer), and the $\beta$-plane located between the two. This additional layer of bound water makes it such that the diffuse layer begins even farther from the surface. The assumptions of this model are: protons and hydroxyl ions form inner-sphere complexes, ion adsorption reactions form both inner- or outer-sphere complexes, and ions from the background electrolyte form outer-sphere complexes. Protonation and deprotonation of surface hydroxyl groups occur at the o-plane, whereas background electrolyte ions reside in the $\beta$-plane. Using the triple-layer model, sorption can occur through strongly bound inner-sphere complexes at the o-plane or weakly

bound outer-sphere complexes at the β-plane. Figure 4.2c shows the surface complexation and three planes of charge density of the solid/solution interface as described within the triple-layer model.

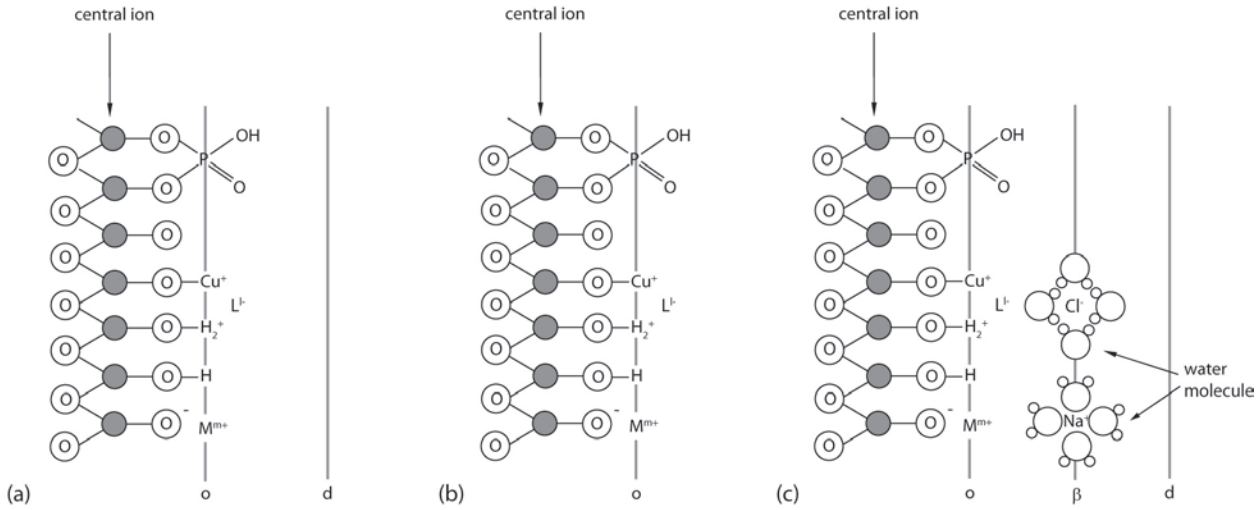


Figure 4.2: Two-dimensional depth profiles of the (a) diffuse-layer model, (b) constant capacitance model, and (c) triple-layer model. Vertical gray lines designate specific planes that are parallel to the surface, with depth into the surface increasing from right to left. The o-plane represents the surface where inner-sphere complexes form, the β-plane represents the boundary for outer-sphere complexes, and the d-plane represents the diffuse layer.

## 4.3 Surface Charge

Mineral surfaces in solution can have electrical charge, either from isomorphic substitutions or reactions of surface functional groups with ions in solution. To assist in understanding the balance of surface charge in a soil, a few definitions of surface charge density are needed. The net total particle charge, $\sigma_P$, represents the net surface charge on the solid particles in a mineral, and comprises of four different types of surface charge. First, there is the permanent structural charge of a soil, $\sigma_0$, which arises from isomorphic substitutions in minerals. Using iron oxide minerals as an example, substitution of the Fe(III) ion by another metal without the same charge will result in a charge imbalance. The sign of $\sigma_0$ is almost always negative because of the negative charge deficits from isomorphic substitution.[116] Second, the net proton charge, $\sigma_H$, of a soil is the difference between the moles of protons and the moles of hydroxide ions complexed by the surface (Eq 4.1). This term represents interactions between surface functional groups and ions (apart from $H^+$ and $OH^-$) that were originally in the soil solution. Note protons and hydroxide ions adsorbed in the diffuse-ion swarm are not included in $\sigma_H$.

$$\sigma_H = q_H - q_{OH} \qquad \text{Eq 4.1}$$

In addition to the adsorption of protons and hydroxide ions, adsorption of other cations or anions can also occur at the mineral surface and will contribute to the net particle charge. The inner-sphere complex charge, $\sigma_{IS}$, is the net total charge of ions apart from $H^+$ and $OH^-$ that form

inner-sphere complexes with the surface functional groups. Similarly, $\sigma_{OS}$, is the net total charge of ions that interact through water or in outer-sphere complexes. Combining this third and fourth type of surface charge contributes to the Stern layer. The net total particle charge, $\sigma_P$, can then be represented as the sum of the four different types of surface charges:

$$\sigma_P = \sigma_0 + \sigma_H + \sigma_{IS} + \sigma_{OS} \qquad \text{Eq 4.2}$$

While mineral particles can bear electrical charge, the total charge of the mineral must be electrically neutral. When $\sigma_P$ is nonzero, the countering component comes from the contribution of charge from the diffuse-ion swarm. The disassociated surface charge term, $\sigma_D$, represents ions that are fully dissociated from the mineral surface and can move freely in the soil solution while remaining near enough to the mineral surface.

$$\sigma_P + \sigma_D = 0 \qquad \text{Eq 4.3}$$

The condition of surface charge balance for a soil in solution can be expressed as the sum of these five surface charge densities:

$$\sigma_0 + \sigma_H + \sigma_{IS} + \sigma_{OS} + \sigma_D = 0 \qquad \text{Eq 4.4}$$

It states that any electrical charge a soil particle bears must always be balanced by a charge in the diffuse swarm of ions in solution near the surface, and maintains the overall electroneutrality of a soil in aqueous solution.

## 4.4 Points of Zero Charge (PZC)

Points of zero charge are pH values where one or more of the surface charge components of Eq 4.4 is zero. The surface charge densities are used to define several points of zero charge for minerals. The various points of zero charge are summarized in Table 4.1.

The most general point of zero charge (PZC) is conventionally considered the pH value at which the total positive charges are equal to the total negative charges.[117] Sposito further defined this to be where the net total particle charge vanishes, $\sigma_P = 0$.[118] This represents the pH when there is no surface charge contribution to be balanced by ions in the diffuse swarm.

If the PZC is determined by measuring the pH where the difference between $H^+$ and $OH^-$ adsorbed on the mineral surface is zero, it is specifically the point of zero net proton charge (PZNPC). The PZNPC is the pH value where $\sigma_H = 0$. This represents the pH when absorbed ions, other than $H^+$ and $OH^-$ contributing to $\sigma_H$, balance the permanent structural charge.

The isolectric point (IEP) occurs where the zeta potential ($\zeta$) of the surface equals zero. This value corresponds to the situation when mineral particles do not move in an electric field (electrophoresis measurement) or when a suspension of soil particles settles (flocculation measurement). The PZC equals the IEP if no adsorption of ions other than $H^+$ or $OH^-$ occurs; that is, when the coverage of $H^+$ equals the coverage of $OH^-$.

The net proton charge, $\sigma_H$, is usually measured by titration in the presence of an indifferent background electrolyte at several ionic strengths. The point of zero salt effect (PZSE) is the pH value when $\sigma_H$ is independent of ionic strength of the soil solution. PZSE is often taken from the common intersection point (CIP) of three potentiometric titration curves carried

out at different ionic strengths. This represents the pH when ionic strength does not influence the mineral surface.

Analogously to the PZNPC, the point of net zero charge (PZNC) is the pH value where the net adsorbed charge is zero. This condition is met when the cation exchange capacity (CEC) equals the anion exchange capacity (AEC) of a soil. The difference (CEC – AEC) is proportional to the sum ($\sigma_{OS} + \sigma_D$) and also proportional to $-(\sigma_o + \sigma_H + \sigma_{IS})$.[116] This represents the pH when the total positive charges are equal to the total negative charges.

$$\sigma_{IS} + \sigma_{OS} + \sigma_D = 0 \qquad \text{Eq 4.5}$$

| Acronym | Points of Zero Charge | Defining Condition |
|---|---|---|
| PZC | zero point of charge | $\sigma_P = 0$ |
| PZNPC | point of zero net proton charge | $\sigma_H = 0$ |
| IEP | isoelectric point | $\sigma_H = 0$<br>$\sigma_o = \sigma_{IS} = \sigma_{OS} = 0$ |
| PZSE | point of zero salt effect | $\frac{\Delta\sigma_H}{\Delta I} = 0$ |
| PZNC | point of zero net charge | $\sigma_{OS} + \sigma_D = 0$ |

Table 4.1: Defining conditions for various points of zero charge

There are instances when these different points of zero charge are equal to one another. If there is no structural charge, then the PZNPC equals the PZNC. The PZNPC and the IEP coincide when the terms contributing to the balance of surface charge in Eq 4.4 are only $\sigma_H$ and $\sigma_D$.[116] That is, the PZNPC equals the IEP when the only contributors to the surface charge are the proton and dissociated charges. It was shown by Sposito that the PZSE does not necessarily coincide with a zero surface charge.[104] Because the PZSE is taken from the CIP, where the mineral surface is not influenced by the ionic strength of the solution, the PZSE equals the PZC when the sum of ($\sigma_{IS} + \sigma_{OS}$) remains invariant under a change in ionic strength of the soil solution. This occurs if the mineral is pure, no inner-sphere adsorption occurs, and there is no contribution from either outer-sphere or diffuse swarm ions (that is, if the net surface charge densities of both inner-sphere and outer-sphere complexes are independent of ionic strength). Thus, the PZSE and the PZC coincide when the mineral is pure and there is no influence from ionic strength. And finally, the PZNC and the PZC coincide only when $\sigma_{OS} = 0$. That is, the PZNC equals the PZC only if the net surface charge density of outer-sphere complexes in the soil vanishes.

When the pH of the solution in contact with the mineral is below the PZC, surface functional groups become completely protonated, resulting in a positively charged mineral surface. Above the PZC, the mineral surface becomes negatively charged. The surface

functional groups can undergo both protonation, deprotonation, and dissociation reactions, represented by the following reactions:

$$M-OH + H^+ \rightleftharpoons M-OH_2^+ \quad \text{Eq 4.6}$$

$$M-O^- \rightleftharpoons M-OH + OH^- \quad \text{Eq 4.7}$$

$$M-OH \rightleftharpoons M-O^- + H^+ \quad \text{Eq 4.8}$$

where MOH represents the surface functional groups, $MOH_2^+$ represents the positive surface sites, and $MO^-$ represents the negative surface sites.

The surface hydroxyl groups of iron oxide minerals, represented as FeOH, are amphoteric hydroxyl groups. $FeOH_2^+$ groups would be present at the surface in acidic medium (pH < PZC), while the FeOH groups would deprotonate to $FeO^-$ groups in alkaline medium (pH > PZC). A schematic of this is shown in Figure 4.3. Note that because protonation and deprotonation of surface functional groups begin at a pH far from the PZC, the surface charge of a mineral continually changes as a function of pH.

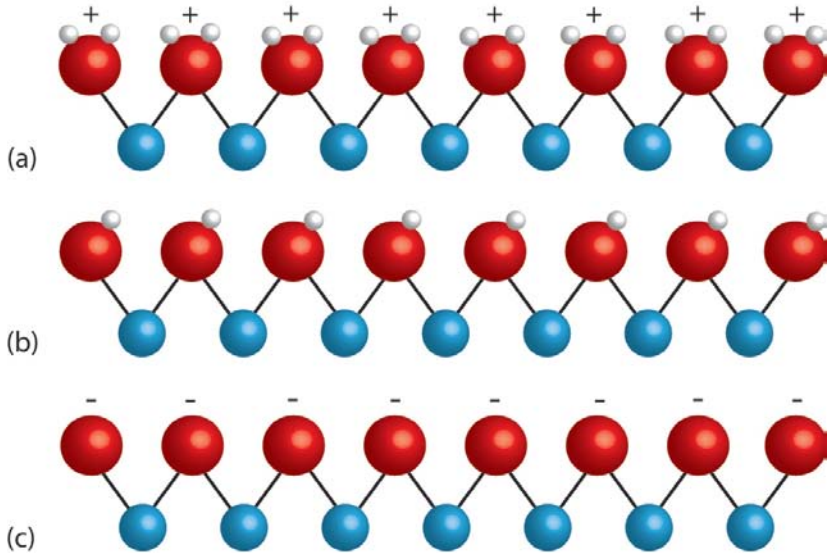


Figure 4.3: Surface charge of an iron oxide mineral (a) below the pH of the PZC is negative where the surface oxygen groups are doubly protonated, (b) at the pH of the PZC is neutral with singly protonated surface oxygen groups, and (c) above the pH of the PZC is negative with deprotonated surface oxygen groups.

## 4.5 PZC Determination

The point of zero charge of the iron oxide minerals measured in this work is specifically the PZNPC. The PZNPC is commonly determined by acid/base titration[119] and can also be measured by mass titration or powder addition. The three methods employed, potentiometric

titration, mass titration, and powder addition, will be described further below. For ease of reference, PZNPC will be referred to simply as the PZC.

Potentiometric titration is a widely used method to measure the PZC, and is described well by Parks and de Bruyn[117] and Cristiano *et al.*[120]. The mineral acts as a weak diprotic acid or base and is titrated with small additions of a strong acid or base in the presence of a background electrolyte. The PZC can be estimated as the average between the two acidity constants, $pK_1$ and $pK_2$ (Eq 4.9). Potentiometric titrations are performed on both a blank and the mineral suspension at a minimum of three different background electrolyte ionic strengths. The blank curve is subtracted from the mineral curves, and the CIP of the three resulting curves is considered the PZC.

$$PZC = \frac{pK_1 + pK_2}{2} \qquad \text{Eq 4.9}$$

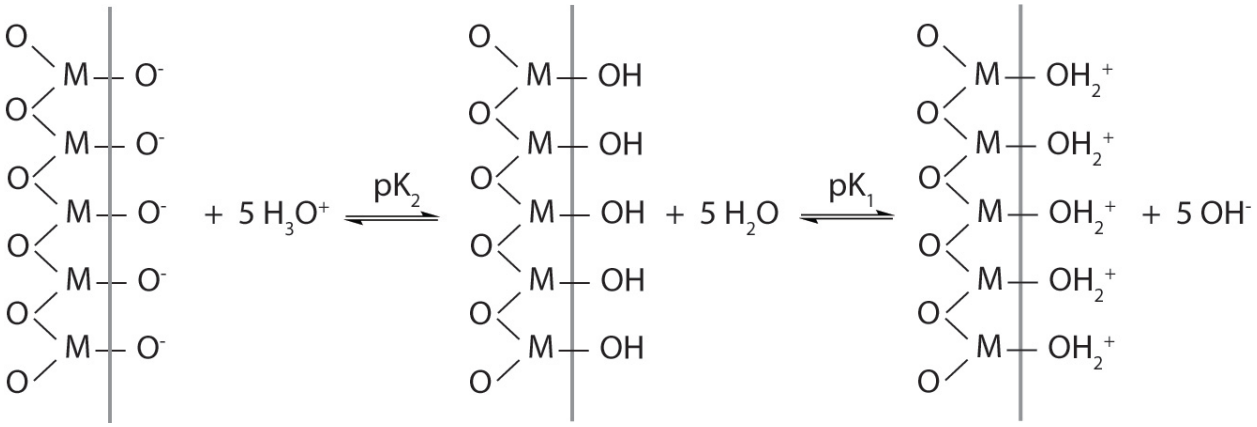


Figure 4.4: pH-dependent protonation and deprotonation of hydroxyl groups on a mineral surface. Adapted from Parks and de Bryun[117] and Tourinho *et al.*[121].

Some disadvantages of this method is that the background electrolyte added can be adsorbed to a certain degree on the mineral surface, requires that the mineral have a large surface area, and curves must be collected at a minimum of three different background electrolyte concentrations.

Developed to estimate the PZC of simple amphoteric oxides, the mass titration method is a variation of the pH drift method. The mass titration method assumes the dry oxide is a pure mineral and uncharged. Varying amounts of mineral is added to pure water, causing the pH of the mineral suspension to change. It is expected that the pH will be buffered toward the mineral's PZC. The solution reaches a steady pH value after the addition of an excess of solid. This limiting pH value, called the "acidity of infinite mass" should approach $\frac{1}{2}(pK_1 + pK_2)$, and just as in potentiometric titration, this value is considered the PZC.[122]

This limiting pH value can be interpreted as a function of the oxide concentration:

$$N_t = \frac{\left(C_{OH^-} - C_{H^+}\right) \times \left(\left[MOH\right] + \left[MOH_2^+\right] + \left[MO^-\right]\right)}{\left[MOH_2^+\right] - \left[MO^-\right]} \qquad \text{Eq 4.10}$$

where $N_t$ is the total number of ionizable sites on the mineral surface (representative of the mass of the solid), ($C_{OH^-}$ - $C_{H+}$) is the difference between the concentration of $OH^-$ and $H^+$ in the mineral suspension (representative of the pH of the solution), and [*MOH*], [$MOH_2^+$] , [$OH^-$] are the concentrations of positive, neutral, and negative sites, respectively.

As $N_t$ approaches infinity and if ($C_{OH^-}$ - $C_{H^+}$) ≠ 0, then [$MOH_2^+$] – [$OH^-$] approaches zero. Under these conditions, the net surface charge of the solid is zero. In the case when ($C_{OH^-}$ - $C_{H^+}$) = 0, the mineral suspension pH is equal to that of pure water and is independent of the mineral mass $N_t$; the PZC of the mineral is 7. The PZC is essentially considered the pH value at the "acidity of infinite mass".[122]

The main advantage of this method is its ease: it can be performed in pure water, without the risk of specific sorption by background electrolytes. The limitations, however, include the need for the mineral to be insoluble in solution and the restriction of the mineral:water ratio to be less than 20% (difficulties arise in measuring pH when the solution density increases).

The powder addition method is to add a constant amount of mineral to a set of solutions, which are at the same ionic strength but vary in pH. Addition of the mineral changes the pH of each mineral suspension based on the mineral's PZC. For example, if the initial pH is lower than the PZC of the mineral, the mineral surface sorbs protons and the final pH of the mineral suspension will be higher. Conversely, if $pH_i$ is higher than the mineral's PZC, the mineral surface will desorb protons, and $pH_f$ will be lower. The $pH_f$ values are measured 24 h after addition of the mineral. The change in pH ($pH_f$ – $pH_i$) is plotted versus $pH_i$, and the PZC is determined from the value where ΔpH = 0.[123]

The main advantages to this method are the ease in dealing with just one ionic strength (compared to potentiometric titration) and that it does not require minerals to have a large surface area.

# 5. IRON OXIDE MINERALS: GOETHITE, 1% AL-SUBSTITUTED GOETHITE, AND HEMATITE

Iron oxides and oxyhydroxides are an important class of minerals due to their ubiquitous presence in the environment.[20] There are sixteen known iron oxides, iron oxide hydroxides, and iron hydroxides, listed below in Table 5.1. (For simplicity, the family of iron oxides, hydroxides/oxyhydroxides, and hydroxides will be referred to collectively as "iron oxides".) All iron oxides consist of Fe, O, and/or OH, but differ in composition, valence of iron, and most importantly, in crystal structure. For most iron oxides, iron is in the trivalent state. Iron oxides consist of close-packed arrays of $O^{2-}$ or $OH^-$ anions, slightly distorted hexagonally close-packed (hcp) or cubic close-packed arrangements (ccp). (The hcp structures are deemed α-phases whereas the ccp structures are γ-phases.) There are twice as many interstices between the sheets of anions as there are anions in a layer. The iron atom fits into the octahedral interstices (six-fold coordination) or the smaller tetrahedral interstices (four-fold coordination). The iron oxides differ mainly in the arrangement of the iron cation in the interstices as well as, to a lesser extent, variations in the stacking of sheets of anions.

The basic structural unit of iron(III) oxides is an octahedron, where each iron cation is surrounded by six $O^{2-}$ and $OH^-$ ions such as $Fe(O)_6$ or $FeO_3(OH)_3$. A tetrahedron, where iron is surrounded by four $O^{2-}$ ions such as $Fe(O)_4$, is also possible, but much less common. These structural units are linked by their corners, edges, or faces, shown in Figure 5.1, and various combinations of these linkages results in the different iron oxides.

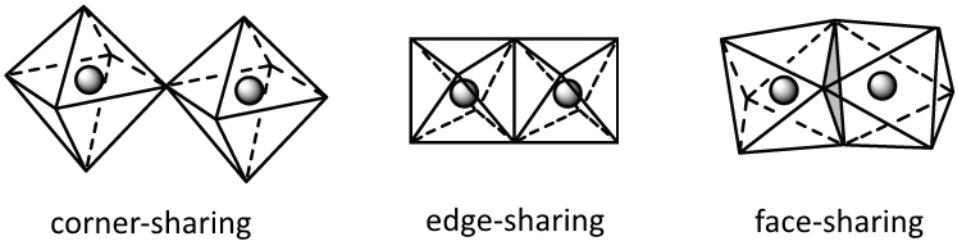


Figure 5.1: Different ways Fe octahedra can be linked: (a) corner-sharing, (b) edge-sharing, and (c) face-sharing.

| Iron Oxides | | Iron Oxyhydroxides | |
|---|---|---|---|
| Mineral | Formula | Mineral | Formula |
| Hematite | $\alpha$-$Fe_2O_3$ | Goethite | $\alpha$-FeOOH |
| Maghemite | $\gamma$-$Fe_2O_3$ | Akaganéite | $\beta$-FeOOH |
| Magnetite | $Fe_3O_4$ | Lepidocrocite | $\gamma$-FeOOH |
| | $\beta$-$Fe_2O_3$ | Schwertmannite | $Fe_{16}O_{16}(OH)_y(SO_4)z \cdot n\ H_2O$ |
| | $\varepsilon$-$Fe_2O_3$ | | $\delta$-FeOOH |
| Wüstite | FeO | Feroxyhyte | $\delta'$-FeOOH |
| | | | high pressure FeOOH |
| | | Ferrihydrite | $Fe_5HO_8 \cdot 4H_2O$ |
| | | Bernalite | $Fe(OH)_3 \cdot 3H_2O$ |
| | | | $Fe(OH)_2$ |

Table 5.1: The iron oxides and iron oxyhydroxides

## 5.1 Goethite, α-FeOOH

Goethite (named after the famous German poet J. W. von Goethe) is one of the most prevalent iron oxide minerals found in nature,[124–126] with a yellow color when finely ground and dark brown in massive crystal aggregates. Goethite has an orthorhombic crystal system. The structure is based on an approximately hcp array of $O^{2-}$ and $OH^-$ anions with $Fe^{3+}$ cations occupying half the octahedral interstices. The iron atoms are arranged in double chains of $FeO_3(OH)_3$ octahedra, linked by edge-sharing through an $O^{2-}$ and an $OH^-$. The chains run parallel to *c* and are linked to adjacent double chains through corner-sharing of $O^{2-}$ anions. This arrangement leads to double chains separated by vacant double rows.

The crystal structure of goethite was first determined by Goldsztaub[127] and Hoppe[128] using X-ray diffraction photographic techniques. Szytula *et al.* examined the magnetic structure of goethite with neutron powder diffraction to find it is anti-ferromagnetic below ~373 K (the Néel point)[129], and Gualtieri and Venturelli investigated the structural behavior of goethite as a function of temperature and pressure using synchrotron X-ray powder diffraction[130]. Detailed structural information for goethite was determined by Yang *et al.* by means of single-crystal X-ray diffraction.[131]

There are two different types of oxygen atoms in the goethite structure, classified $O_I$ and $O_{II}$. The $O_I$ atom is shared between two different chains of octahedra, forming the corner linkages between the parallel chains. The $O_{II}$ atom is shared by octahedra of the same chain and is also linked to the proton. The $O_I$-$O_{II}$ bond distance is 2.747 Å and the $O_{II}$-H bond distance is 0.88 Å.[131] The hydrogen bond joins an $O_{II}$ atom of one octahedron to an $O_I$ atom of an octahedron in a chain diagonally opposite, helping to link the parallel chains of octahedra. Figure 5.2 shows the crystal structure of goethite in an isometric view.

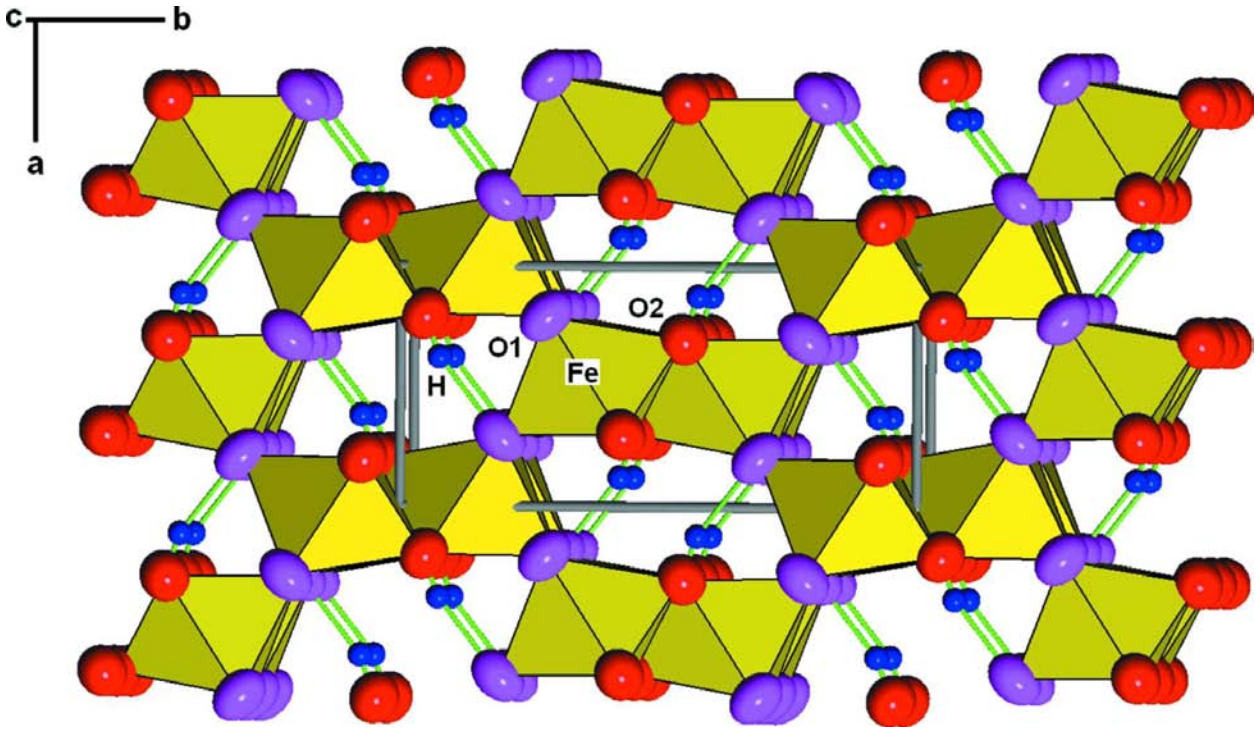


Figure 5.2: The crystal structure of goethite, α-FeOOH. Fe atoms occupy octahedral interstices, $O_I$ atoms in purple, $O_{II}$ atoms in red, protons in blue, and hydrogen bonding indicated with green lines. Taken from Yang *et al.*[131]

### 5.1.1 Synthesis

Goethite can be synthesized from either Fe(III) or Fe(II) systems. In alkaline media, synthesis involves holding freshly prepared ferrihydrite in NaOH at pH > 12 for several days. Ferrihydrite dissolves to release soluble Fe(III) species ($Fe(OH)_4^-$) from which the less soluble goethite forms.

Goethite was prepared with ferric solutions in alkaline media, using a method adapted from Böhm[132] to ensure that nitrates were not present in the final mineral.* To minimize silica contamination, all synthesis steps were carried out using plastic labware. A 1 M $Fe(NO_3)_3$ solution was rapidly added with 5 M NaOH to precipitate 2-line ferrihydrite. The red-brown suspension was immediately diluted and held in a closed polyethylene bottle at 70 °C for 60 h, converting red-brown ferrihydrite to a yellow-brown goethite precipitate. The cooled product was dialyzed to remove residual salts with dialysis tubing (SnakeSkin Pleated Dialysis Tubing 3500 MCWO) and 18.2 MΩ $H_2O$ (Milli-Q water) until the conductivity of the exchange solution was < 2.0 μS, which took approximately 10 days. The Milli-Q water was replaced every day during this period. The washed goethite suspension was dried at 110 °C for several days. The resulting yellow-brown solid was gently ground using a mortar and pestle and size fractionated using a range of sieves. This method yielded ~9 g of goethite.

* This precaution was taken to ensure nitrate complexation with plutonium would not occur, which may influence the plutonium redox chemistry,

## 5.1.2 Characterization

Surface Area Determination by $N_2$ Adsorption

The surface area of the synthesized goethite was determined to be 32.8 $m^2/g$, measured by BET $N_{2(g)}$ adsorption (Micromeritics ASAP 2010 physisorption analyzer).

X-ray Powder Diffraction

Powder X-ray diffraction (XRD) was taken of the synthesized goethite using a Pananalytical X'Pert Pro diffractometer with Cu $K_{\alpha 1}$ radiation and a Ni filter. Generator settings were 40 kV, 35 mA. Divergence, scattered, and receiving slits were 1°, 1°, and 0.2 mm, respectively. The ground mineral sample was placed on a zero background plate atop a thin layer of immersion oil. Data were collected over 2θ angle from 10.0° to 70.0°, with scanning step of 0.025° and a counting time of 15 s per point. The Bragg peaks were indicative of the goethite structure (Figure 5.3), identifying goethite as the sole product. The synthesized mineral was also crystalline and no evidence of significant impurities was observed.

Scanning Near-Field Microscopy

Using optical microscopy, goethite shows the expected morphology of acicular (needle-shaped) crystals with particle sizes of ~80-100 μm (Figure 5.4). This also confirms that sieving isolates the proper mineral size fraction. Imaging was conducted with a WITec near-field scanning optical microscope.

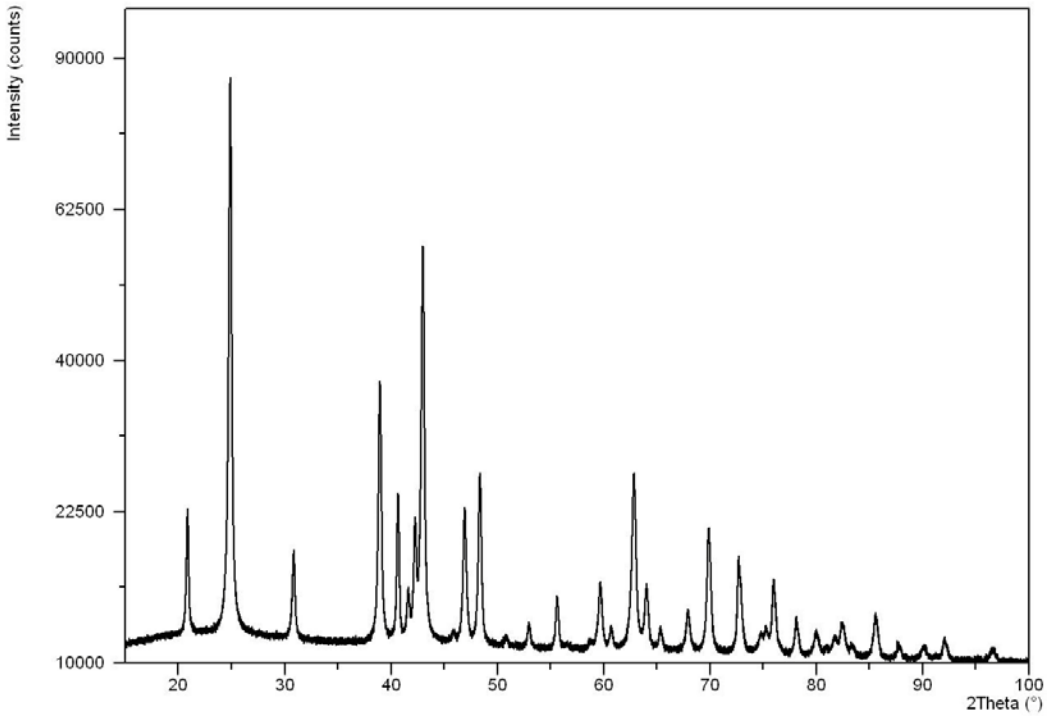


Figure 5.3: X-ray diffractogram of synthesized goethite

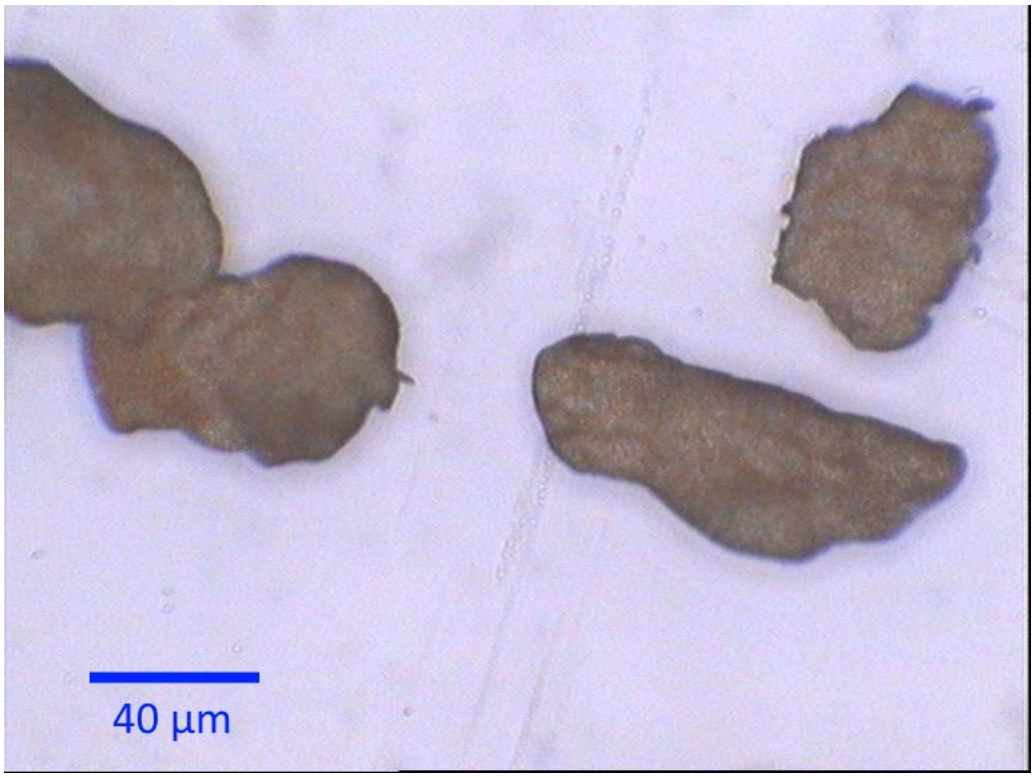


Figure 5.4: Microscopy image of synthesized goethite particles from the 75-150 µm size fraction.

### 5.1.3 Point of Zero Charge

Measurements of the PZC were conducted on goethite using the potentiometric titration method, mass titration method, and the powder addition method.

Potentiometric titrations of goethite were performed under $CO_2$-free argon atmosphere using an automatic titrator (751 GPD Titrino, Metrohm). The minerals were added to 12 mL of $NaClO_4$ at concentrations of 0.01, 0.1, and 1 M. The solid:liquid ratio was fixed at 5 g/L. The suspension was equilibrated for 20 min under argon blanketing and the pH was measured. Before the analysis, a predetermined amount of NaOH was added to increase the pH environment to pH 11. The titrations were carried out from high to low pH by adding 0.0773 M $HClO_4$ at 25 °C. The titration parameters were 1 µL as the minimum volume increment at the beginning and near the equivalence point; outside these ranges, the increment was constrained between 5-50 µL. Each small volume of titrant was added as soon as a 1 mV/min signal drift criterion was met. Blank titrations were performed under the same conditions.

Unfortunately, attempts to measure the PZC of goethite using the potentiometric titration method proved unsuccessful. No CIP was found for the three ionic strengths measured (0.01 M $NaClO_4$, 0.1 M $NaClO_4$, and 1 M $NaClO_4$). Additionally, there was a great deal of difficulty in successfully excluding carbonate. Due to the time-consuming nature of the potentiometric titrations, the future determinations of mineral PZC were measured using the

other two simpler methods. This decision is supported by the findings of Cristiano *et al.* that demonstrated mass titration yields an equivalent PZC as potentiometric titrations for goethite.[120]

The mass titration method was performed following the procedure described by Noh and Schwarz.[122] Varying amounts of mineral was added to 5 mL of $CO_2$-free Milli-Q water in acid-washed polycarbonate tubes and backfilled with $Ar_{(g)}$ before sealing. The mineral:water ratios were 0.1%, 1%, 5%, 10%, and 20% by weight. The samples were placed on a rocker and allowed to equilibrate for 24 h. The pH of the mineral suspension was then measured using a glass pH electrode (8103BNUWP, Orion; fill solution 3 M NaCl), and the equilibrium pH at 20% was taken as the PZC. Solution pH was checked every week for the following month, of which the values remained constant during this period.

The powder addition method was performed using a procedure described by Mustafa *et al.*[123] A set of 0.01 M $NaClO_4$ solutions were adjusted to pH 3 – 10 using $CO_2$-free NaOH and $HClO_4$ in acid-washed polycarbonate tubes. The initial pH ($pH_i$) was measured and a constant amount of mineral added to each solution in a solid:liquid ration of 1 g/L. The polycarbonate tubes, backfilled with argon, were allowed to equilibrate on a rocker. As recommended by Mustafa *et al.*, the final pH ($pH_f$) was measured soon after the addition of the mineral, about 24 h. The $\Delta pH$ ($pH_f - pH_i$) was plotted versus $pH_i$, and the value where $\Delta pH = 0$ was taken to be the PZC. Solution pH was regularly checked for 30 days, of which the values remained constant during this period.

## 5.2 1% Al-substituted Goethite, $Fe_{1-x}Al_xOOH$

The Fe(III) cation in the octahedral position may be partially replaced by other trivalent metal cations of similar size without modifying the goethite structure. Isomorphous substitution of iron in iron oxides is often observed in nature,[125,133] where metal cations such as Mn(III), Al(III), and Cr(III) partially replace the octahedrally-coordinated Fe(III) ion. The substitution of aluminum for iron in goethite is well documented.[124,126,133–143] Norrish and Taylor originally demonstrated the existence of Al-substitution in natural goethites using chemical analysis and XRD line shifts.[134] The extent of aluminum for iron substitution spans from 0 to 33 mol%.[20,124,134,135,140,143] The Al(III) cation is slightly smaller than the Fe(III) cation, 0.53 Å compared to 0.645 Å;[126] thus when aluminum substitutes for iron in the goethite structure, the average size of the unit cell decreases.[124,134,143,144]

### 5.2.1 Synthesis

A common method of synthesizing metal-substituted iron oxides is to precipitate mixed metal-iron salt solution by base addition. Al-substituted goethite forms from soluble Fe and Al species released by dissolution of the coprecipitate, and corporation of Al in the goethite structure is preceded by adsorption of the soluble Al species on the growing nuclei of goethite.[20]

As a model to environmental minerals, 1% Al-substituted goethite was synthesized using a method adapted from Schwertmann and Cornell.[144] An aluminate solution was prepared by addition of 0.1 M $Al(NO_3)$ to 5 M NaOH with constant stirring. A 1 M $Fe(NO_3)_3$ solution was rapidly added with the aluminate solution to precipitate ferrihydrite. The suspension was immediately diluted and held in a closed polyethylene bottle at 70 °C for 14 days to allow complete transformation to goethite. The bottle was gently shaken once a day. The cooled product was dialyzed to remove residual salts with dialysis tubing and Milli-Q water until the conductivity of the exchange solution was < 2.0 μS, which took approximately 10 days. The

Milli-Q $H_2O$ was replaced every day during this period. The washed Al-substituted goethite suspension was dried at 110 °C for several days. The resulting yellow-brown solid was gently ground using a mortar and pestle and size fractionated using a range of sieves. This method yielded ~9 g of 1% Al-substituted goethite.

### 5.2.2 Characterization

Surface area was not determined for the synthesized 1% Al-substituted goethite. However, literature shows an increase of aluminum substitution in goethite contributes to the decrease in surface area.[139]

XRD was collected of the synthesized 1% Al-substituted goethite in the same manner mentioned above. The XRD pattern (Figure 5.5) revealed that the synthesized mineral remained a goethite-like structure, as no significant shifts were observed in the Bragg peaks from that of goethite. While XRD is not sensitive enough for trace elements smaller than 3-5%,[133] peak shifts to lower d-values (due to the shrinking of the a- and c-crystallographic parameters and the expansion of the b-parameter with increasing aluminum substituted into the goethite crystal lattice) are expected for >5% aluminum substitution.[143,144] Also, an increase in the aluminum substitution results in the peaks broadening.[142]

Using optical microscopy, 1% Al-substituted goethite was observed to highly aggregated, slightly smaller, and more spherical particles (Figure 5.6) compared to goethite. The shorter particles with increasing aluminum substitution has been observed previously.[134,137,142,143] A decrease in crystal size is expected with increasing aluminum substitution[124,134,135,144] due to the reduction in unit cell size. Imaging was conducted with a WITec near-field scanning optical microscope.

### 5.2.3 Point of Zero Charge

PZC measurement of the 1% Al-substituted goethite was conducted using the powder addition method. This method was chosen over potentiometric titration and mass titration for two main advantages: the process is quick and requires a small amount of solid. The PZC of the synthesized mineral is similar to that of pure goethite.

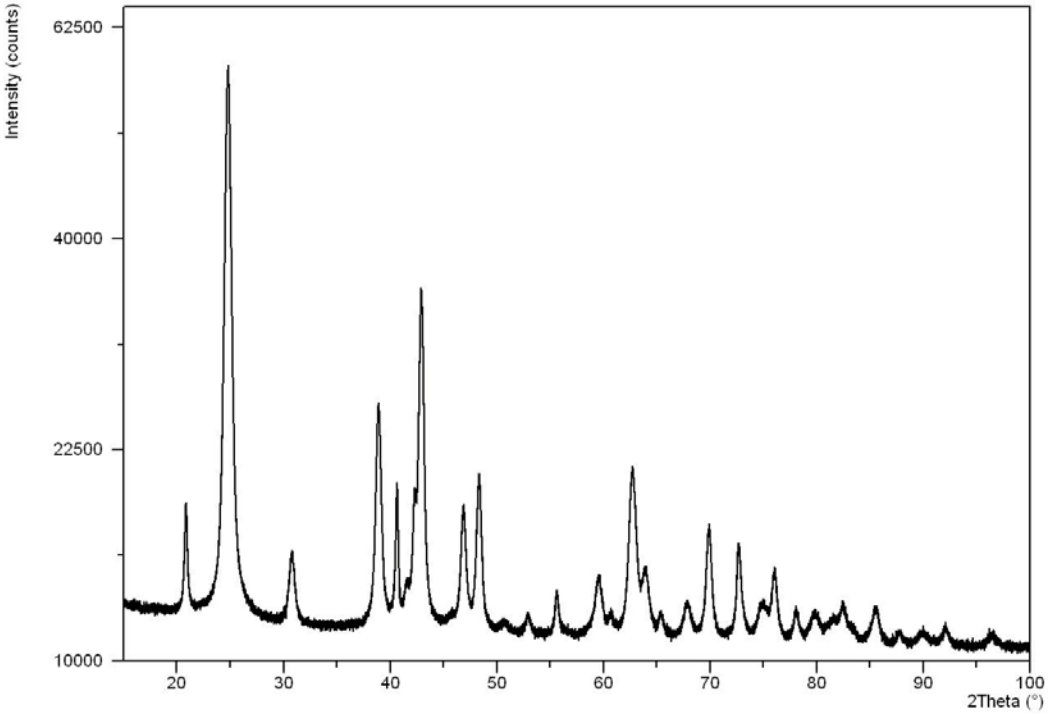


Figure 5.5: X-ray diffractogram of synthesized 1% Al-substituted goethite

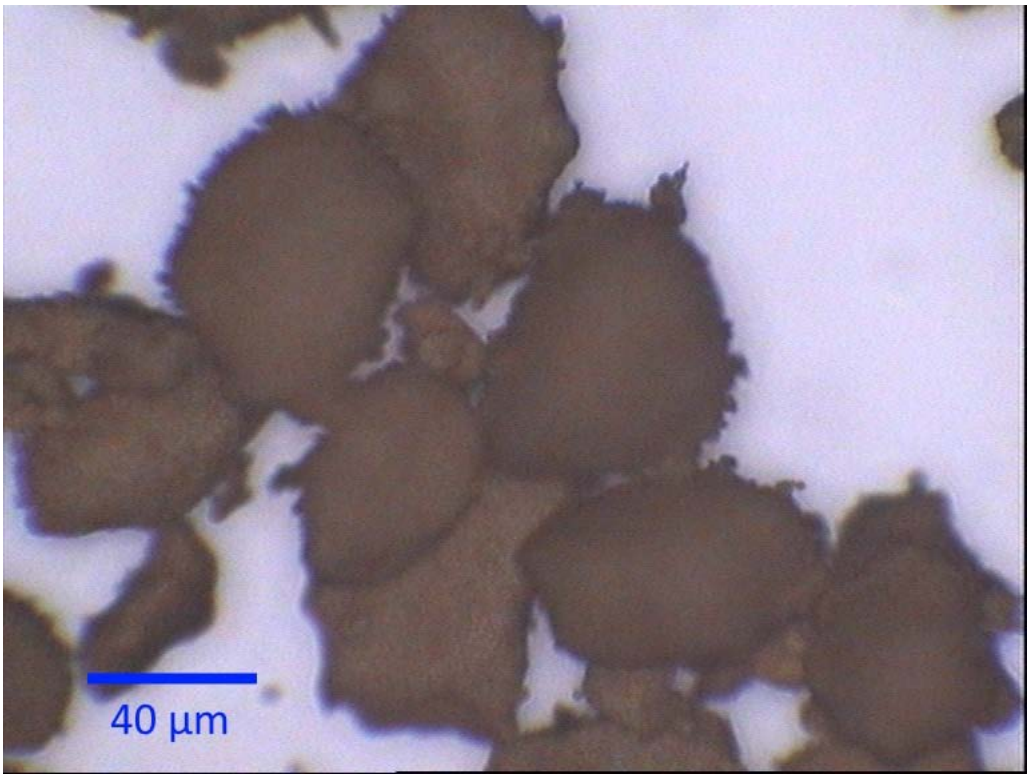


Figure 5.6: Microscopy image of synthesized 1% Al-substituted goethite particles from the 75-150 µm size fraction.

## 5.3 Hematite, α-$Fe_2O_3$

Hematite (named from the Greek word "αἷμα" for "blood") is the oldest known iron oxide mineral, with a red color when finely ground and sparkling black when coarsely crystalline. Hematite has a trigonal crystal system. The structure is based on hcp anions; planes of parallel $O^-$ anions with $Fe^{3+}$ cations are distributed in the octahedral interstices. Two-thirds of the octahedral interstices are filled with Fe(III) atoms. The $Fe(O)_6$ octahedra are linked by edge-sharing and face-sharing; each octahedron shares edges with three neighboring octahedral in the same plane and one face with an octahedron in an adjacent plane. The face-sharing is accomplished by a slight distortion of the octahedral which results in a regular displacement of the iron ions. The distortion and absence of H-bonds yields a compact structure, evident in the high density of 5.26 g/$cm^3$.

### 5.3.1 Synthesis

Hematite can be prepared in a variety of ways; one common synthetic route is the transformation of ferrihydrite in aqueous suspension. Hematite is produced by precipitating 2-line ferrihydrite which is then converted into hematite in aqueous suspension by a short-range crystallization process within the ferrihydrite aggregates.

Hematite was synthesized using a method adapted from Schwertmann and Cornell.[144] 40 g of $Fe(NO_3)_3 \cdot H_2O$ was dissolved in 500 mL of Milli-Q water at 90 °C. This 0.198 M $Fe(NO_3)_3$ solution was carefully mixed with 500 mL of 1.0 M KOH (also preheated to 90 °C) to precipitate ferrihydrite. 50 mL of a 1 M $KHCO_3$ solution was added to the voluminous brown ferrihydrite suspension to give ~ pH 8. The solution was then heated to 100 °C for ~72 h to allow complete transformation to hematite. The cooled product was dialyzed to remove residual salts with dialysis tubing and Milli-Q water until the conductivity of the exchange solution was < 2.0 μS, which took approximately 10 days. The Milli-Q water was replaced every day during this period. The washed hematite suspension was dried at 110 °C for several days. The resulting red solid was gently ground using a mortar and pestle and size fractionated using a range of sieves. This method yielded ~7 g of hematite.

### 5.3.2 Characterization

Hematite was identified as the sole product by the Bragg peaks of an X-ray diffractogram. Powder XRD was collected using a Rigaku Ultima IV diffractometer (Cu $K_{\alpha 1}$ radiation). Surface area analysis by $N_2$ adsorption using a Micrometrics ASAP 2010 gave a BET surface area of 30.7 $m^2$/g, and optical microscopy identifed the mineral as having a rhombohedral morphology with particles ~100-150 μm in size.

### 5.3.3 Point of Zero Charge

PZC measurement was again conducted using the powder addition method. Although the PZC of the synthesized hematite measured is slightly lower than the value given by Schwertmann and Cornell, it is within the range of ~6.2-8.8 given by Kosmulski.[145,146]

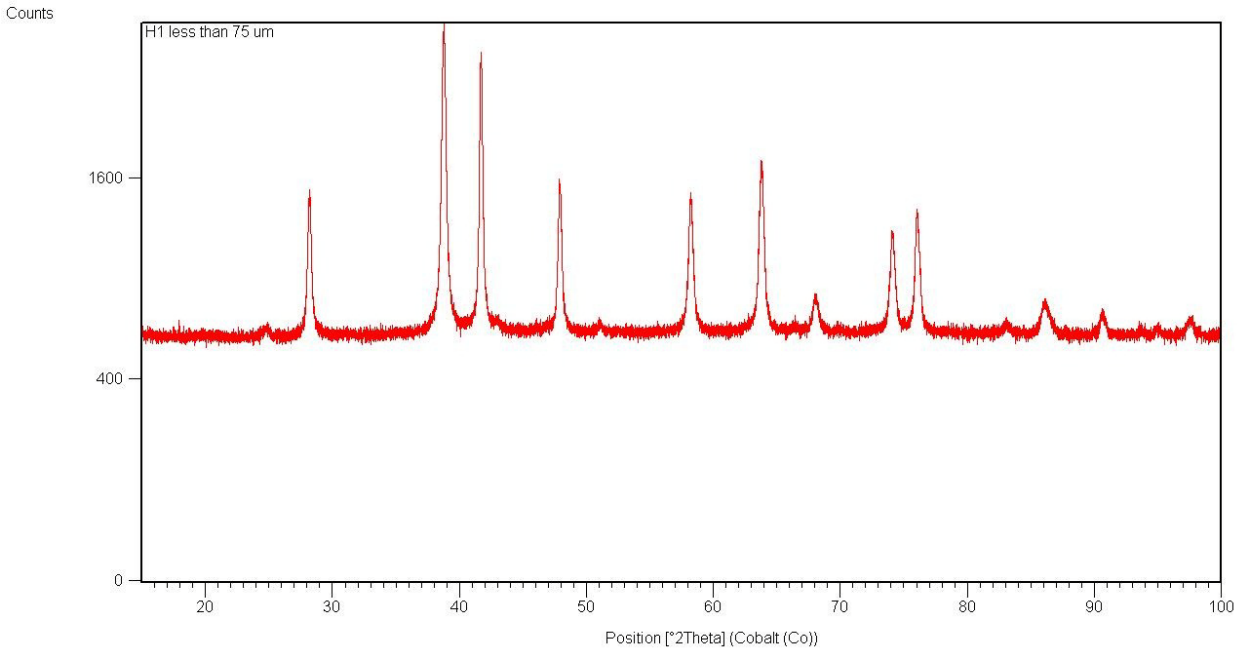


Figure 5.7: X-ray diffractogram of synthesized hematite

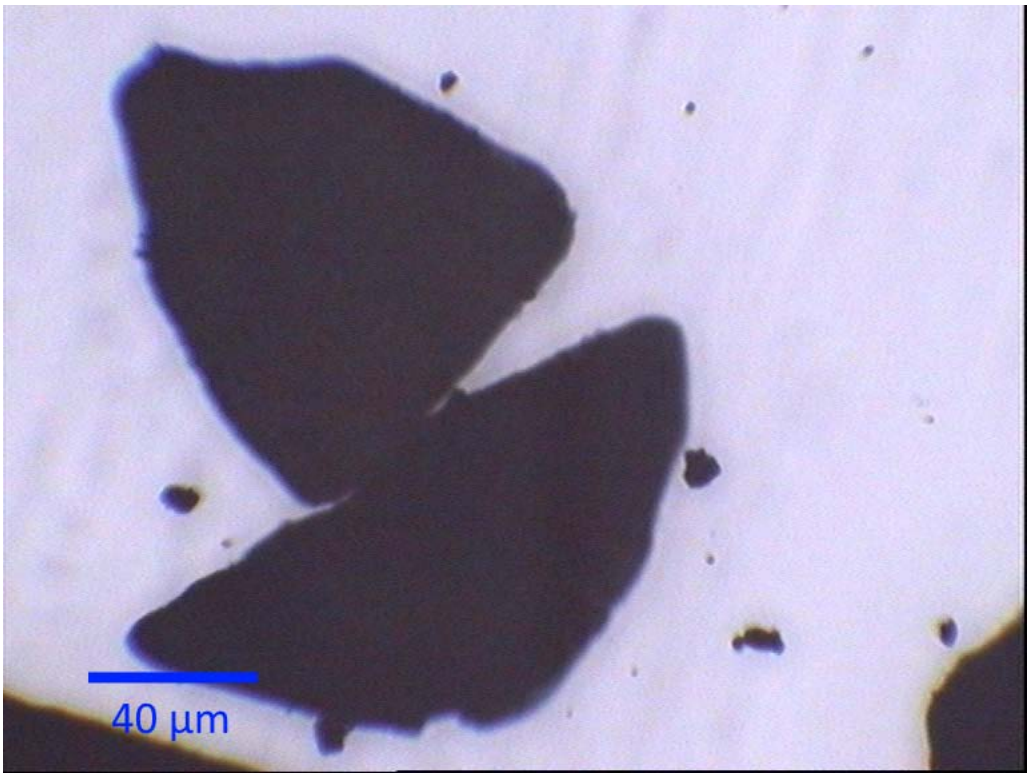


Figure 5.8: Microscopy image of synthesized hematite particles from the 75-150 µm size fraction.

# 6. PU(VI) SORPTION ON GOETHITE AND 1% AL-SUBSTITUTED GOETHITE

The presence and migration of plutonium in the environment is a major concern due to its radiotoxicity and long-lived isotopes. There are several locales within the U.S. with considerable plutonium contamination, such as the Hanford Reservation, the SRS, and the NTS, and elsewhere globally, including the Mayak Production Association in Russia and the Windscale reprocessing facility (Sellafield) in England. In particular, migration of plutonium over a distance of more than 4 km from Lake Karachai was reported. Sorption onto soils, sediments, and rock surfaces constitute a large aspect of controlling actinide migration in nature, which leads to the importance of understanding plutonium interactions with environmental matrices. This aids in the development of actinide transport models and improving risk assessment concerning actinide behavior. Additionally, this demonstrates good stewardship at radioactively contaminated sites and nuclear waste storage sites.

In oxic environmental conditions, plutonium is present predominantly in the Pu(V) and Pu(VI) oxidation states, which are highly soluble and thus more mobile. Because plutonium is extremely redox active, contact with minerals found in nature could reduce Pu(V)/Pu(VI) to the less soluble Pu(IV) oxidation state, thus limiting plutonium mobility in the environment. Despite the many studies of plutonium sorption to various iron, manganese, silica minerals and clay materials, many questions still remain regarding plutonium behavior in the environment. The objective of this study is to investigate the interactions of plutonium with the surface of iron oxide minerals to gain additional insight of the mechanism behind plutonium sorption reactions. Batch sorption experiments were conducted of Pu(VI) on goethite and 1% Al-substituted goethite as a function of pH; sorption behavior was also monitored with time. Goethite was chosen due to its prevalence in the environment. Minor elemental substitutions often occur, as goethite is rarely found as a pure mineral phase, so 1% Al-substituted goethite was synthesized as an example of naturally-occurring iron oxide mineral. XAS measurements were taken to determine whether redox chemistry occurred between Pu(VI) and the associated mineral surfaces.

## 6.1 Methods and Materials

Unless stated otherwise, distilled deionized water (Milli-Q, 18 MΩ·cm resistivity) and ACS grade chemicals was used in all experiments.

Pu(VI) working stock preparation

A concentrated stock solution of Pu-239 was purified using anion exchange resin (BioRad AG 1-X8, 100-200 mesh) to remove Am-241 and any other transuranic impurities (refer to Appendix B). The concentrated plutonium stock solution was qualitatively characterized using γ spectroscopy and α spectroscopy to be free of Am-241 (refer to Appendix A). The concentrated stock solution was refluxed several times with concentrated $HClO_4$ for at least 3 hours to ensure complete oxidation to Pu(VI). The concentrated plutonium stock was kept in concentrated $HClO_4$ to maintain the hexavalent oxidation state.

To prepare a plutonium working stock, an aliquot was removed from the concentrated stock solution and diluted in 1 M $HClO_4$. The hexavalent oxidation state of the working stock was verified with vis-NIR spectroscopy prior to beginning each experiment. The final plutonium concentration of the working stock was determined with LSC (Wallac 1414 LSC, Ecolume cocktail). The plutonium working stocks were freshly prepared prior to each batch sorption experiment and XAS experiment.

Mineral synthesis and characterization

Goethite was synthesized using the method of Schwertmann and Cornell.[144] Briefly, 1 M $Fe(NO_3)_3$ was added to 5 M NaOH and held at 70° C for approximately 60 hours. As a model to environmental minerals, 1% Al-substituted goethite was synthesized using a method adapted from Schwertmann and Cornell.[144] Briefly, an aluminate solution in alkaline conditions was added to a 1 M $Fe(NO_3)_3$ solution to precipitate ferrihydrite. The resulting suspension was diluted and heated at 70 °C for 14 days to allow complete transformation to goethite. The goethite and 1% Al-substituted goethite products were both dialyzed with Milli-Q water until the conductivity of the outer solutions were < 2 μS. The synthesized goethite has a surface area of 32.8 $m^2/g$, and the 62-212 μm size fraction was used for batch sorption studies. The 75-150 μm size fraction of the synthesized 1% Al-substituted goethite was used for batch sorption studies. The synthesis and characterization of goethite and 1% Al-substituted goethite are covered in-depth in Section 5.1 and Section 5.2, respectively.

Batch sorption experiments: mineral suspension preparation

Mineral suspensions of 10 mg of mineral (goethite or 1% Al-substituted goethite) in 0.1 M $NaClO_4$ were prepared in acid-washed polypropylene vials. The total volume of the suspension was ~10 mL, resulting in a solid:liquid ratio of 1 g/L. Samples ranged between pH 4 and pH 9. Centrifuge tubes were left open to air to allow solutions to equilibrate with atmospheric $CO_2$ ($pCO_2 = 10^{-3.5}$ atm); no effort to exclude carbonate was made. Samples were spiked with sufficient plutonium from the plutonium working stock to reach the desired concentration of 50 μM. Solution pH was quickly adjusted with small volumes of $HClO_4$ or NaOH. pH was measured with a pH meter (Model 8025, VWR) equipped with a combination pH electrode (Orion 8103, Ross) calibrated with standard pH buffers. The original electrode filling solution (3 M KCl) was replaced with 3 M NaCl to avoid clogging the electrode frit glass septum due to the precipitation of $KClO_4$. No pH adjustments were made during the course of the experiment, but the pH was monitored over time to ensure minimal drift due to goethite buffering. The aqueous Pu(VI) was contacted with the mineral slurry by mixing the sample end-over-end on a rocker (Vari-Mix, Thermo Scientific) for various contact times.

After known time intervals, the samples were allowed to settle, solution pH was measured, and a 40 μL aliquot of supernatant was removed for filtration through a 30,000 MWCO regenerated cellulose filter (Vivacon) centrifuged at an RCF of ~3000 x g for 5 minutes. Aliquots were taken in duplicate from the filtrate and measured using LSC to determine the amount of plutonium remaining in solution. The percent of plutonium sorbed to the mineral surface was calculated from the difference between the initial amount of plutonium spiked into the sample and the amount left in solution.

XAS experiments: sample preparation

Samples for measurement by XAS were prepared in a similar fashion to the batch sorption samples. Mineral suspensions of 25 mg of mineral (goethite or 1% Al-substituted goethite) in 0.1 M $NaClO_4$ were prepared in acid-washed polypropylene vials. The total volume of the suspension was ~4 mL, resulting in a solid:liquid ratio of 6.25 g/L. All samples were open to air and no effort to exclude carbonate was made. Mineral suspensions of goethite or 1% Al-substituted goethite were spiked with the plutonium working stock to reach the desired concentration of 250 μM; acquiring high-quality XAS data requires the relatively high plutonium concentrations compared to the batch sorption studies. Samples were prepared at pH values of pH 6, pH 8, and pH 9, which represent solution conditions that are below, at, and above the PZC of the minerals. Solution pH was quickly adjusted with small volumes of $HClO_4$ or NaOH. The aqueous Pu(VI) was contacted with the mineral slurry by mixing the sample end-over-end on a rocker (Vari-Mix, Thermo Scientific) for various contact times. Solution pH was monitored over time to ensure minimal drift due to buffering from the iron oxide mineral. Measurement of pH over the course of the experiment indicated pH drift was less than 0.2 pH units.

Following equilibrium, the samples were allowed to settle, the pH of the solution measured, and the mineral slurry was carefully transferred into Kapton tubes and sealed with parafilm and epoxy. The Kapton tube was triply contained in nesting aluminum sample holders with Kapton windows and indium wire seals in the packaging method described by Hu *et al*.,[147] and then transported to the synchrotron for measurement.

XAS experiments: spectroscopy conditions and details

Plutonium $L_{III}$-edge XAS spectra were collected at SSRL on wiggler beamline 11-2 or beamline 4-1. X-ray wavelength was selected using a Si(220) Φ-0° double crystal monochromator. Higher harmonics were removed by applying a 50% detuning to the second crystal. The vertical aperture of the beam was held at 0.5 mm. Energy calibration was performed in transmission mode with a Zr metal foil reference or a $^{242}PuO_2$ powder reference. All samples were run at approximately 30 K using a specially engineered liquid helium cryostat (Janis) by Dr. Corwin Booth to mitigate the risk of beam-induced chemical changes during the experiment. Data were collected in fluorescence mode using a 32-element Ge detector or a 100-element Ge detector with a sample orientation of 45° to the incident beam. A deadtime correction was applied to the spectra.

The XANES spectra were energy calibrated to a $^{242}PuO_2$ reference by setting the first inflection point for the Pu $L_{III}$-edge to be 18062.3 eV.[148] Plutonium oxidation state percentages were determined through least-squares fitting of normalized Pu(IV), Pu(V), and Pu(VI) standards.[149] Errors to the fits are estimated through inversion of the covariance matrix. Raw data were pre-edge subtracted and normalized using the real-space X-ray analysis package

(RSXAP), software created by Dr. Corwin Booth for XAS data analysis.[150,151] Plutonium EXAFS spectra were obtained also with RSXAP using standard procedures.[151,152]

## 6.2 Plutonium Batch Sorption Experiments

Batch sorption experiments were conducted to investigate the sorption behavior of plutonium to goethite and to 1% Al-substituted goethite. Sorption behavior was measured as a function of pH and monitored with time. Plutonium was added initially as Pu(VI) and a calculation of Pu(VI) speciation at the highest concentration used in presence of carbonate shows that the solubility limit is approached, but not exceeded. In addition, concern for $PuO_2$ precipitation is not taken, as precipitation is not evidenced in the EXAFS data (to be addressed in Section 6.3).

Plutonium sorption on goethite and 1% Al-substituted goethite, as a function of pH

The sorption curve of plutonium to goethite after 7 days of contact time as a function of pH is presented in Figure 6.1. The plot shows that aqueous plutonium sorbs to goethite. The sorption curve of plutonium to 1% Al-substituted goethite as a function of pH is presented in Figure 6.2, and shows plutonium also sorbs to 1% Al-substituted goethite with a sorption behavior similar to/comparable to that of goethite. The sorption profiles are as expected for a cation sorbing to an oxide surface: low sorption in acidic conditions, increasing sorption as the solution pH increases until reaching a sorption maximum, and decreasing sorption as the solution pH further increases. Important to note is that the sorption profiles are in agreement with previous studies of plutonium to iron oxide minerals performed by Keeney-Kennicutt and Morse, Sanchez *et al*., and Powell *et al*.[153–155]

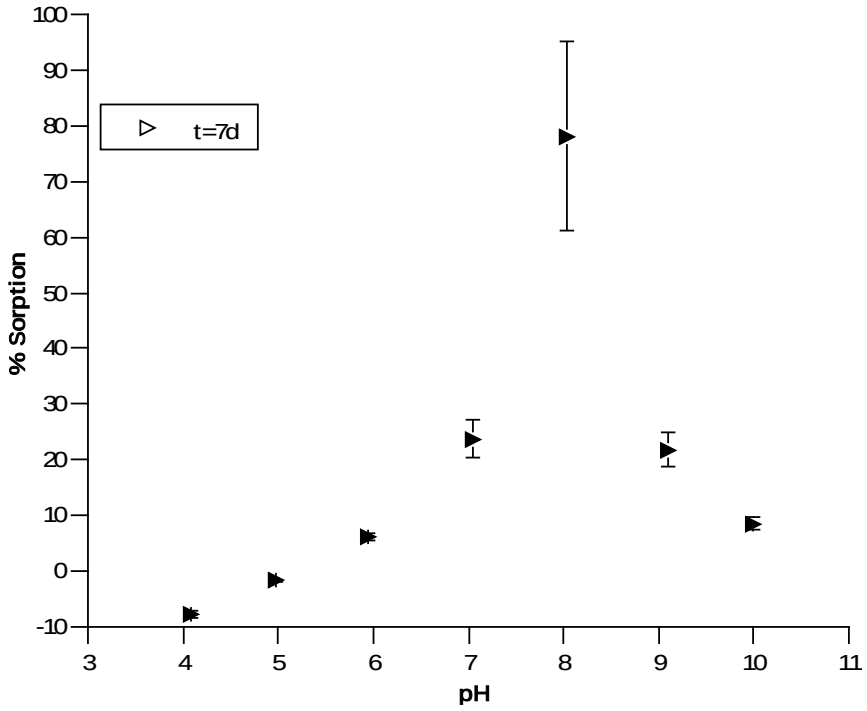


Figure 6.1: Sorption curve of plutonium to goethite after equilibration time of 7 days.

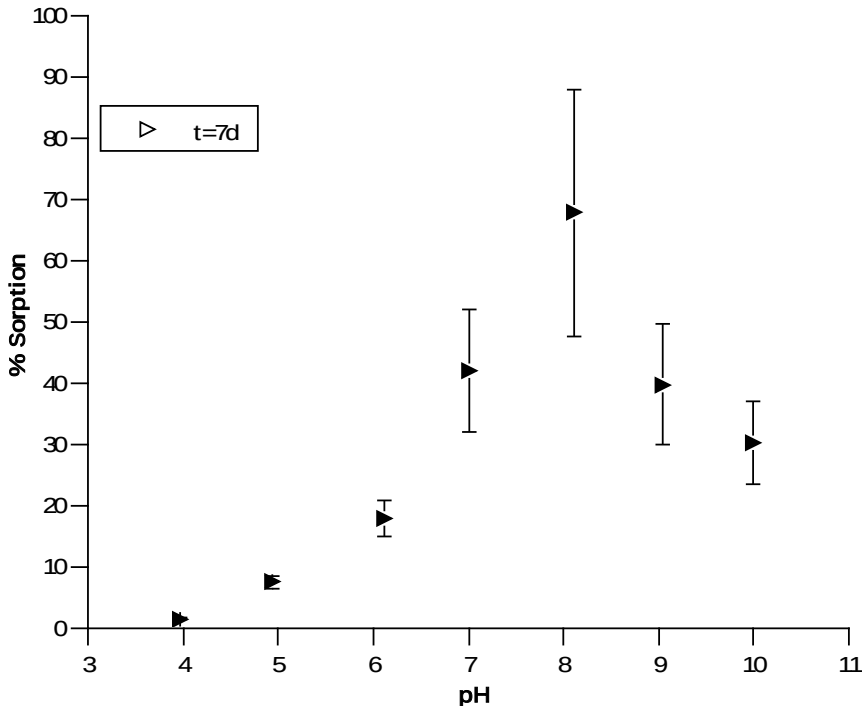


Figure 6.2: Sorption curve of plutonium to 1% Al-substituted goethite after equilibration time of 7 days.

The sorption profiles can be explained given the Pu(VI) species that are present at certain pH conditions and the iron oxide minerals' PZC of ~8.5. Recall that when solution pH is below the PZC, surface hydroxyl groups are double-protonated and so the mineral surface is positively charged. When pH is above the PZC, the deprotonated surface hydroxyl groups result in a negatively charged surface. Under the conditions of the batch sorption experiments (low ionic strength and open to atmosphere), $PuO_2^{2+}$ is the predominant aqueous species in low pH conditions. As the pH increases, plutonium hydrolyzes, and so there is the introduction of Pu(VI) hydrolysis products, and the increasing carbonate concentration gives rise to the Pu(VI)-carbonato complexes. Below the pH 8.5 value, it is likely that the positively charged $PuO_2^{2+}$ and $PuO_2OH^+$ species are electrostatically repelled from the net positive surface charge. A similar argument can be made for electrostatic repulsion between the negatively charged $PuO_2(CO_3)_3^{4-}$ species and the net negative surface charge when solution pH is above 8.5. (The competition of carbonate ions for the mineral surface is not considered for these pH conditions, again due to an anion attempting to sorb to a negatively charged surface.) The increase in sorption corresponds to negatively charged ($PuO_2(CO_3)_2^{2-}$) and neutral ($PuO_2CO_3$ and $PuO_2(OH)_2$) species interacting favorably with a positive and neutral surface, as the solution pH increases to or is at the PZC. Sorption decreases as the pH further increases with the formation of the more negatively charged carbonate ($PuO_2(CO_3)_3^{4-}$) species.

Figure 6.3 shows the sorption profile of plutonium to 1% Al-substituted goethite superimposed with the calculated fractional component of Pu(VI) species unlikely to sorb to the mineral surface: $PuO_2^{2+}$, $PuO_2OH^+$, and $PuO_2(CO_3)_3^{4-}$; Figure 6.4 shows the same sorption curve with $PuO_2CO_3$, $PuO_2(CO_3)_2^{2-}$, and $PuO_2(OH)_2$ overlaid, the Pu(VI) species expected to sorb to the mineral surface.

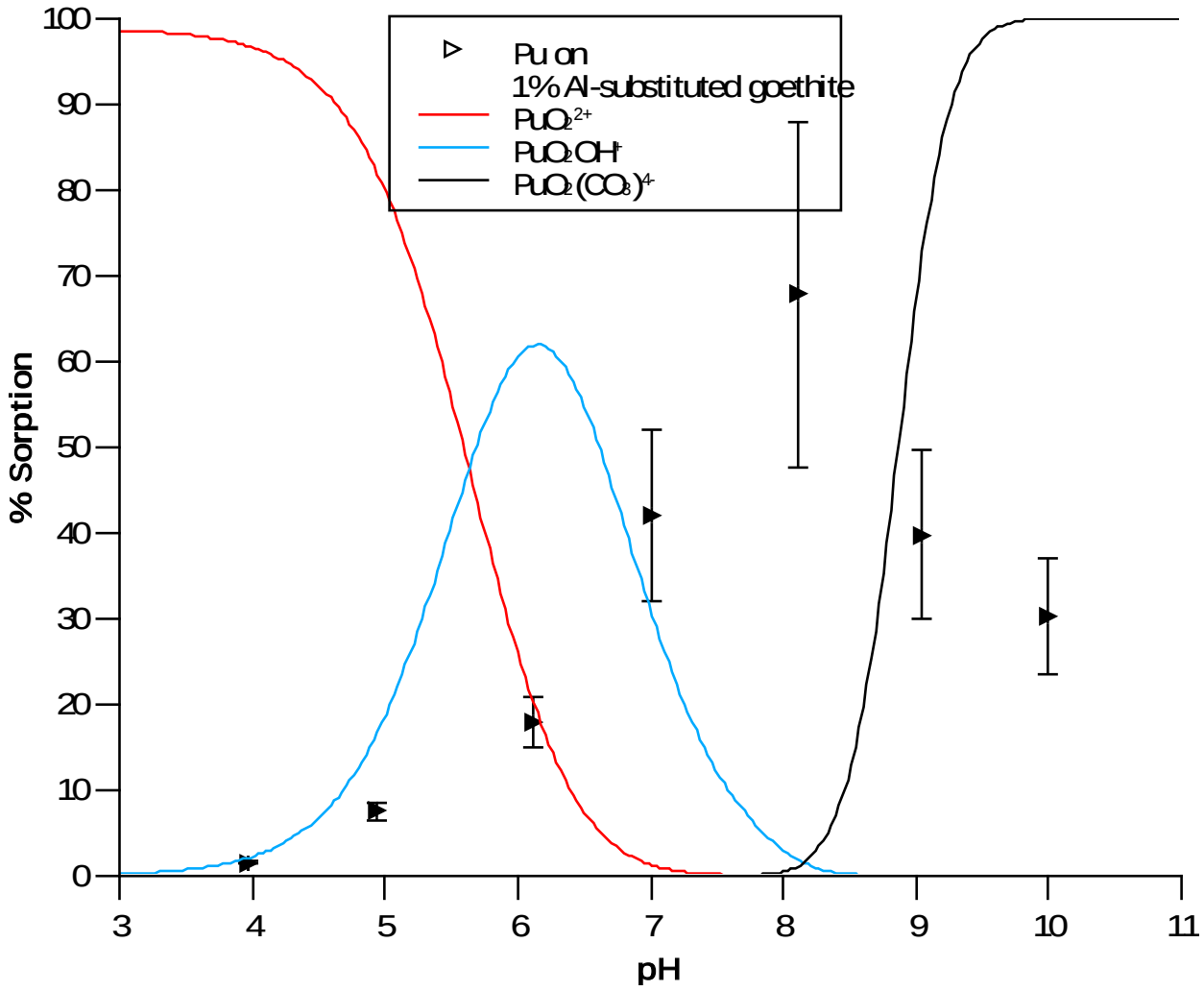


Figure 6.3: Sorption profile of plutonium on the surface of 1% Al-substituted goethite as a function of solution pH at an ionic strength of 0.1 M $NaClO_4$ and open to air. The fractional Pu(VI) species (see Figure 2.14) unlikely to sorb to the mineral surface are overlaid.

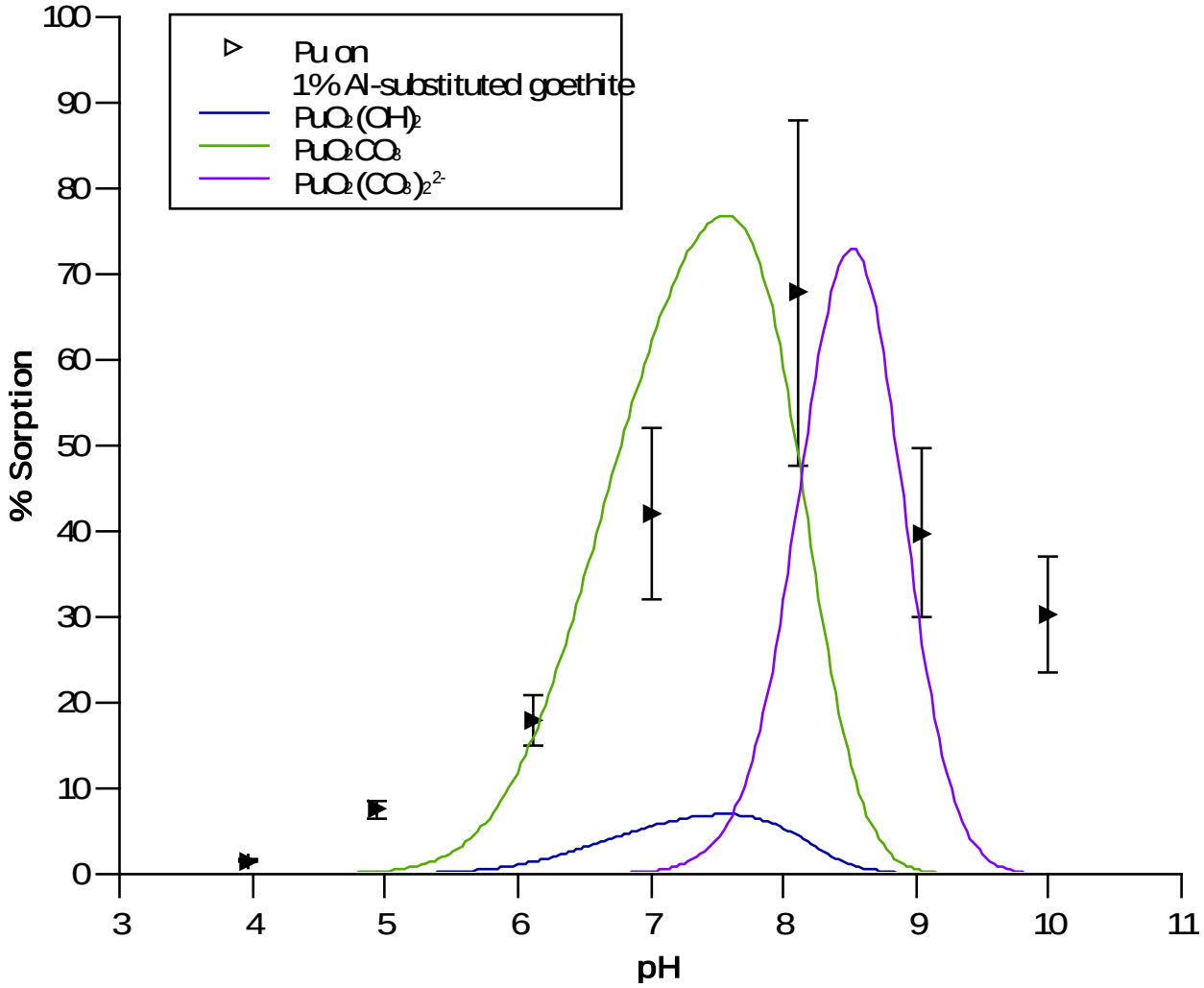


Figure 6.4: Sorption profile of plutonium on the surface of 1% Al-substituted goethite as a function of solution pH at an ionic strength of 0.1 M $NaClO_4$ and open to air. The fractional Pu(VI) species (see Figure 2.14) likely to sorb to the mineral surface are overlaid.

Plutonium sorption on goethite and 1% Al-substituted goethite, as a function of contact time

The sorption behavior of plutonium on goethite and 1% Al-substituted goethite between pH 4 to pH 10 was also monitored with time. To determine when plutonium sorption equilibrium is reached, sorption to the mineral surface was measured daily for 7 days. The sorption of plutonium on goethite as a function of pH over the course of 7 days shows a complex sorption behavior (Figure 6.5). For visual ease, see Figure 6.6, as error bars are not shown and lines are added to guide the eye. Throughout the 7 days, little or no change in sorption occurs below pH 5; similarly, no significant change in sorption is observed above pH 9. Plutonium sorption behavior between pH 5 and pH 9, however, is not straightforward. For pH conditions pH 5-7, sorption decreases during the first three days and then no further change in plutonium uptake is observed (Figure 6.7). Thus, for pH conditions pH < 7, sorption equilibrium is reached after 3 days. Around pH 8, sorption seemingly reaches equilibrium within the first day, as no change in sorption is observed during the first three days, but additional uptake of plutonium occurs after the fourth day (Figure 6.8).

Plutonium also exhibits a complex sorption behavior with 1% Al-substituted goethite. Plutonium sorption as a function of pH over the course of 7 days is shown in Figure 6.9; Figure 6.10 shows the same data but without errors bars and with guiding lines. Again, during the entire 7 days, no significant change in sorption is observed for pH conditions below pH 5, but sorption behavior between pH 5 and pH 7 is somewhat complicated. For pH conditions pH 5-7, sorption decreases during the first three days and then remains constant (Figure 6.11). In contrast to goethite, sorption does not significantly change across the entire pH range beyond the fourth day (Figure 6.12). Thus, for pH conditions pH 4-10, a sorption equilibrium for 1% Al-substituted goethite seems to be established after 3 days.

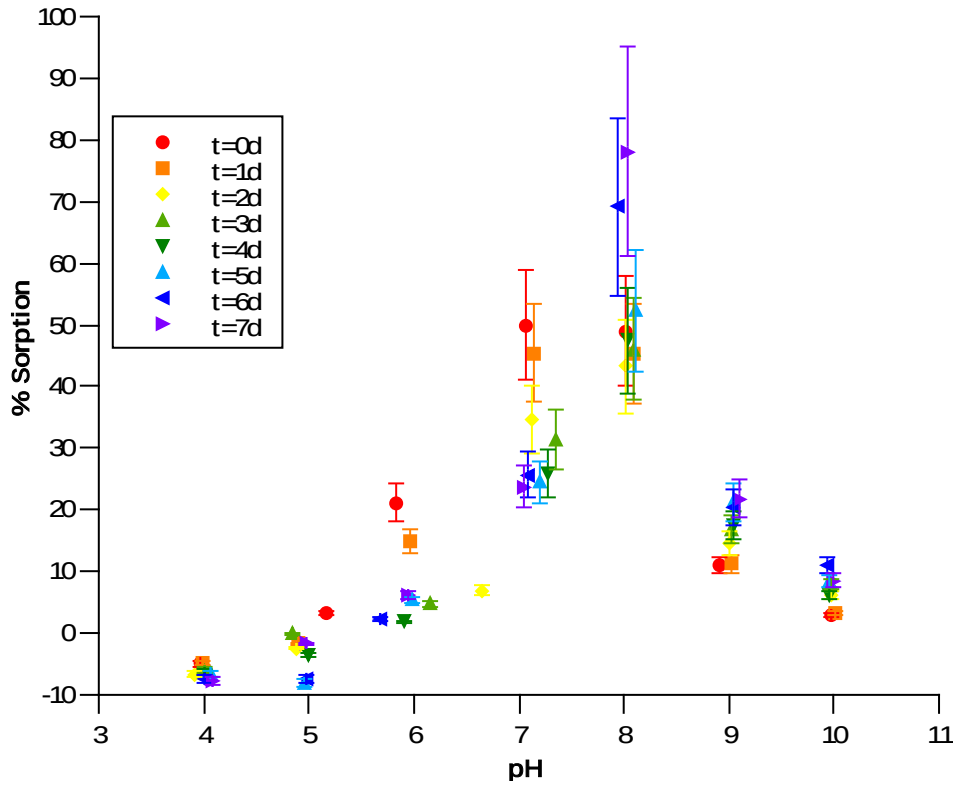


Figure 6.5: Sorption profile of plutonium to goethite as a function of pH on a daily basis over the course of 7 days.

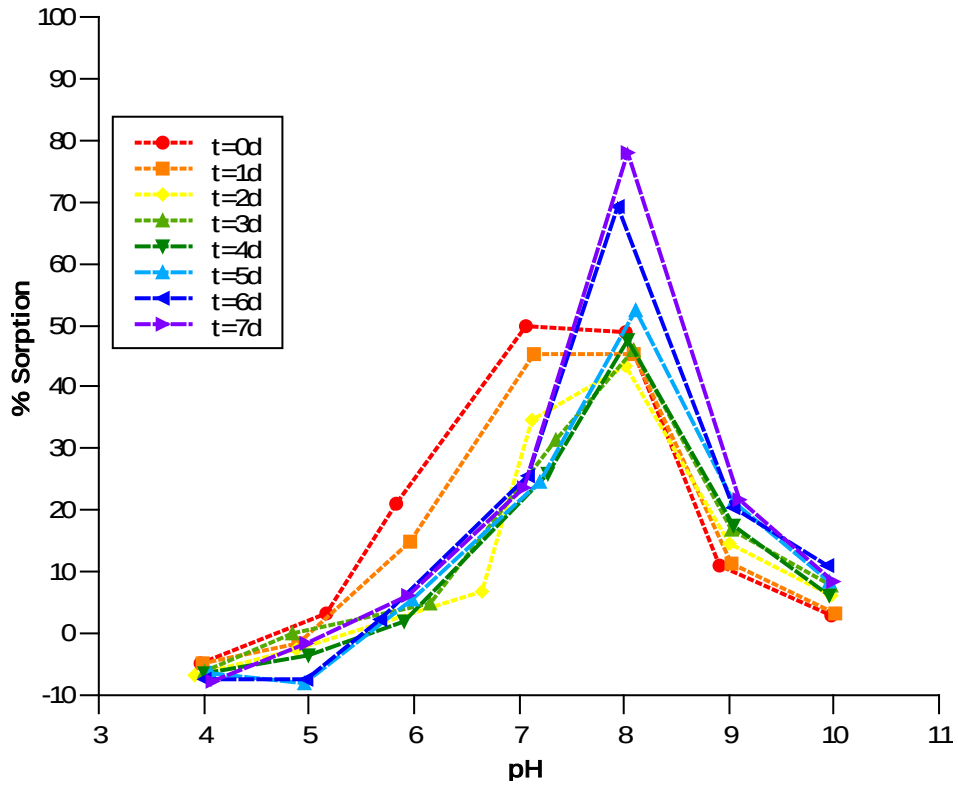


Figure 6.6: Sorption profile of plutonium to goethite as a function of pH on a daily basis over the course of 7 days. For clarity, error bars are not shown, and lines are added to guide the eye.

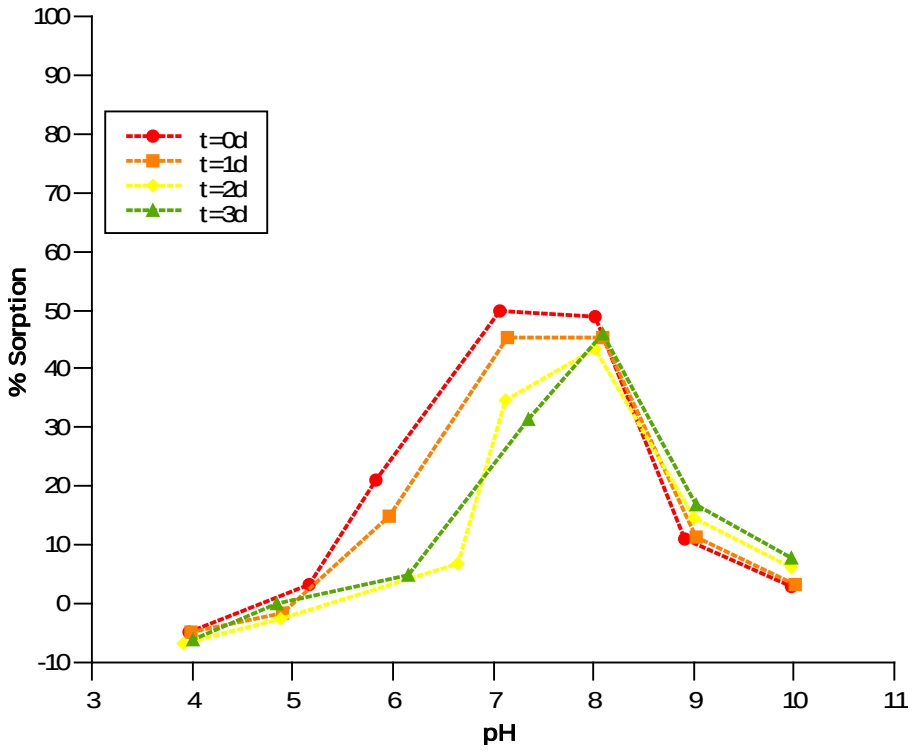


Figure 6.7: Sorption profile of plutonium to goethite as a function of pH on a daily basis for the first 3 days. For clarity, error bars are not shown, and lines are added to guide the eye.

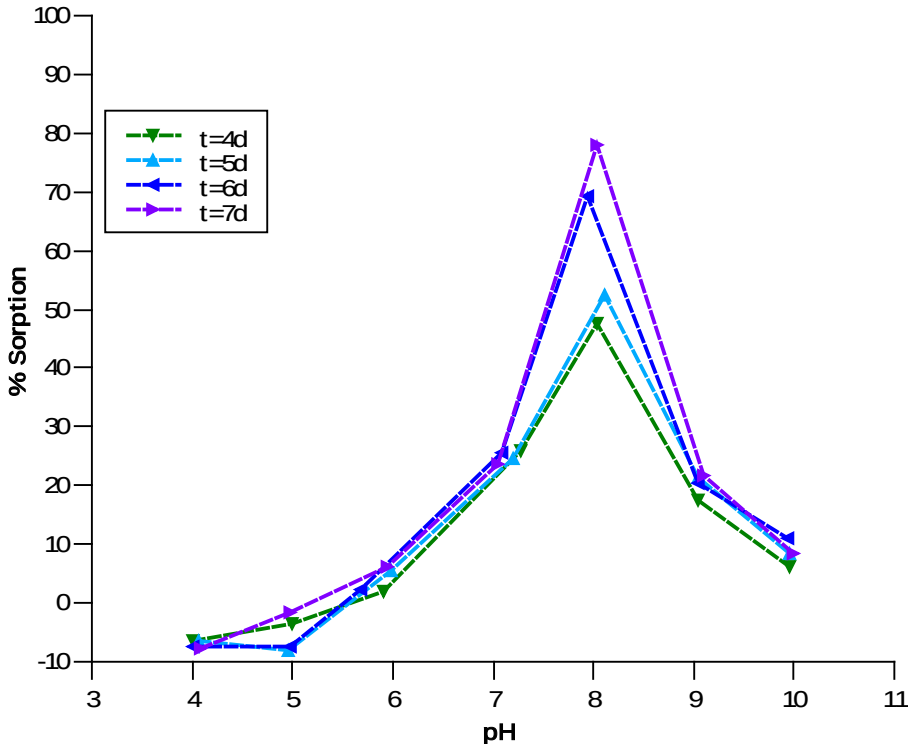


Figure 6.8: Sorption profile of plutonium to goethite as a function of pH on a daily basis after 3 days. For clarity, error bars are not shown, and lines are added to guide the eye.

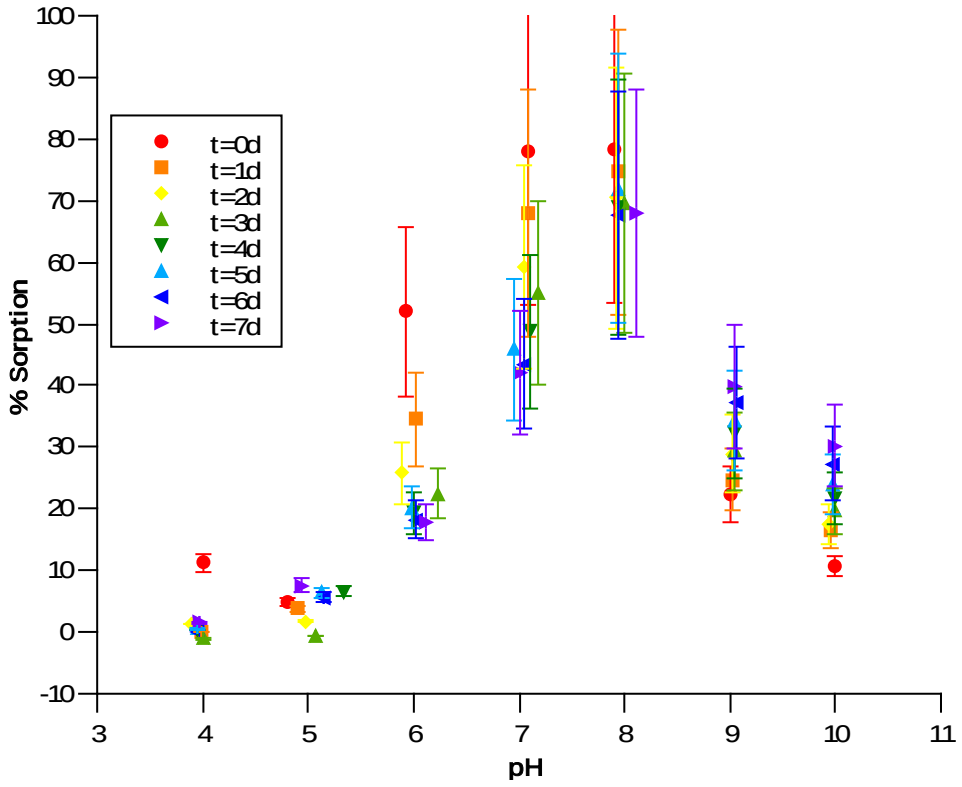


Figure 6.9: Sorption profile of plutonium to 1% Al-substituted goethite as a function of pH on a daily basis over the course of 7 days.

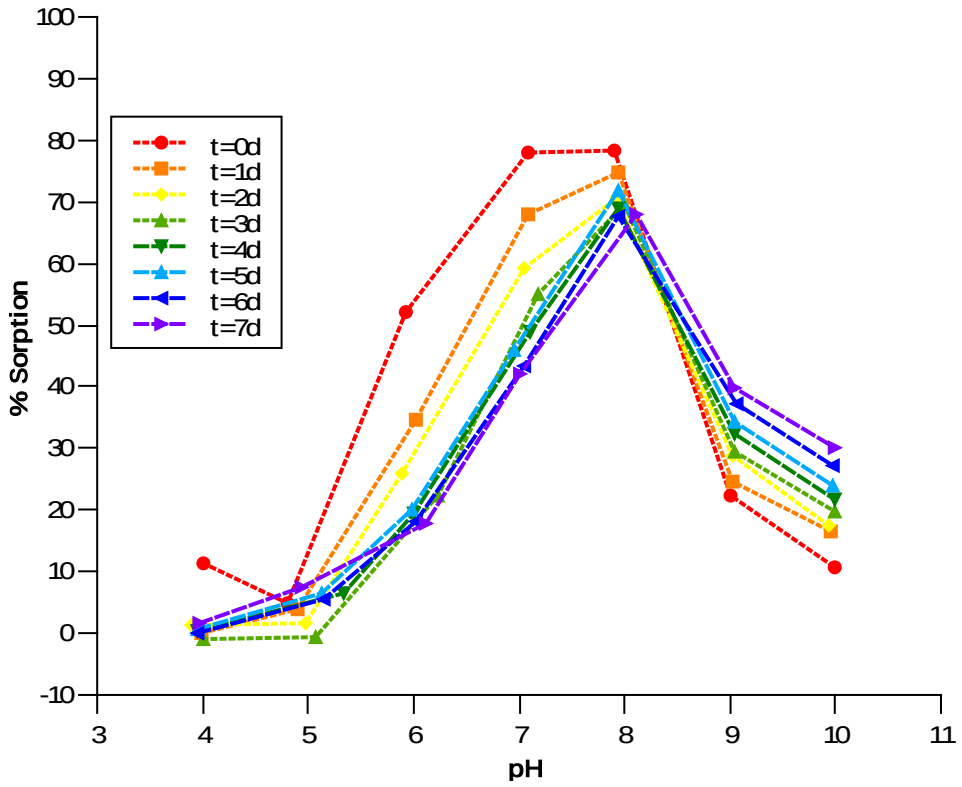


Figure 6.10: Sorption profile of plutonium to 1% Al substituted goethite as a function of pH on a daily basis over the course of 7 days. For clarity, error bars are not shown, and lines are added to guide the eye.

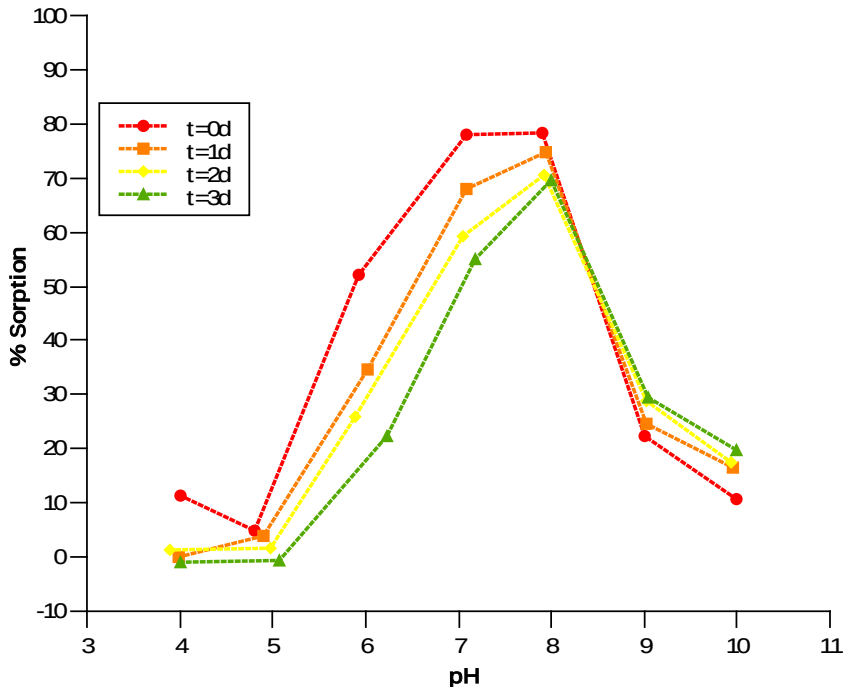


Figure 6.11: Sorption profile of plutonium to 1% Al-substituted goethite as a function of pH on a daily basis for the first 3 days. For clarity, error bars are not shown, and lines are added to guide the eye.

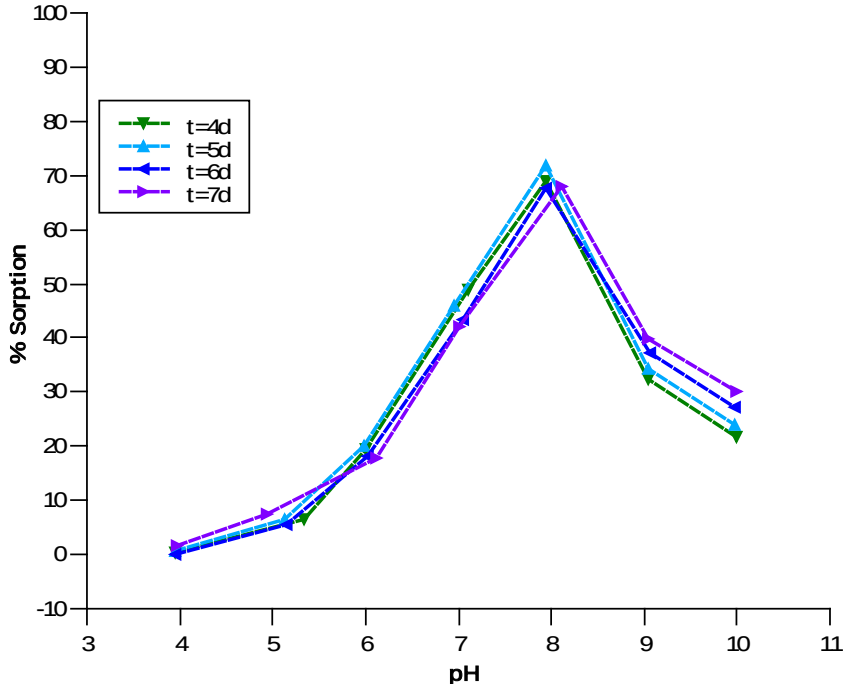


Figure 6.12: Sorption profile of plutonium to 1% Al-substituted goethite as a function of pH on a daily basis after 3 days. For clarity, error bars are not shown, and lines are added to guide the eye.

## 6.3 Plutonium XAS Experiments

To garner additional information about the plutonium complex sorbed on the mineral surface, XAS measurements were carried out for the plutonium-goethite system and the plutonium-1% Al-substituted goethite system. The use of XAS allows for element-specific, nondestructive, *in-situ* determination of oxidation state. XANES was used to directly determine the oxidation state of plutonium sorbed to the mineral surface.

X-ray beam-induced chemistry

As mentioned previously, the oxidation states of plutonium are extremely sensitive to the solution conditions. Exposure to intense X-ray beams, such as those present at synchrotrons, can result in radiolytic reactions within the system. X-ray beams affecting everyday operations of water-cooled nuclear reactors have been long observed.[156] This unwanted effect complicates measurements when the focus of the work is to determine the exact oxidation state of an element, and especially a concern when working with highly redox sensitive samples like plutonium.

To demonstrate the effect of intense X-ray beams, XAS measurements of a sample representative of the plutonium-goethite system were taken at a cryogenic temperature and at room temperature. The sample was first cooled to 30 K and then exposed to the X-ray beam to collect XANES measurements. The same sample was then warmed to 300 K, exposed to the X-ray beam again, and additional measurements were subsequently collected at 300 K. Figure 6.13 shows the normalized XANES spectrum of plutonium sorbed on goethite measured at 30 K and the fits. The spectrum clearly shows the characteristic plutonyl shoulder, indicating presence of Pu(V)/(Pu(VI). Compare to Figure 6.14, which shows the normalized XANES spectrum of the sample measured at 300 K. Because the loss of the characteristic plutonyl shoulder at ~18090 eV and an increase in the white-line peak of the plutonium $L_{III}$ edge at ~18065 eV may be difficult to discern by visual inspection, XANES spectra were fit to a linear combination of standards. The least-squares fits (Table 6.1) provide quantitative information that the sample underwent reaction in the presence of the X-ray beam at room temperature, indicating plutonium reduction to Pu(IV). While it is more important to compare the amount of oxidized plutonium (Pu(V) and Pu(VI) components) to the amount of reduced plutonium (Pu(IV)) between the two samples, notice there is no Pu(VI) present in the sample measured at 300 K, as all the Pu(VI) has reduced to either Pu(V) or even Pu(IV). Also note the spectrum is much nosier compared to the spectrum collected at 30 K; taking measurements at cryogenic conditions significantly enhances the signal-to-noise ratio.

While autoreduction is a possible explanation for the observed reduction of plutonium, it is unlikely autoreduction is playing a major role in the samples, as the plutonium activity is relatively low. Romanchuk *et al.* ruled out autoreduction and disproportionation mechanisms at trace plutonium concentrations.[157] In a recent study by Hixon *et al.*, plutonium sorption to a quartz surface was compared between two different isotopes, Pu-238 and Pu-242, such that the two systems had equal plutonium concentrations but different radioactivites. Reduction of Pu(V) to Pu(IV) was observed despite no significant differences in sorption or kinetics, suggesting that α radiolysis was not the cause.[158] Furthermore, it is evident that the reduction is correlated with exposure to the X-ray beam. This beam-induced chemistry was also observed by Wilk *et al.* for neptunium sorbed to manganese oxides[159] and by Drs. Tashi Parsons-Moss, Kestrel Brogan, and Yung-Jin Hu for plutonium sorbed to silica samples[160,161].

Beam-induced chemistry is unwanted, as one of the principal goals of XAS measurements is the direct determination of plutonium oxidation state in the sample. To

minimize the effect of X-ray beam-induced chemistry, all subsequent XAS measurements were conducted at cryogenic temperatures.

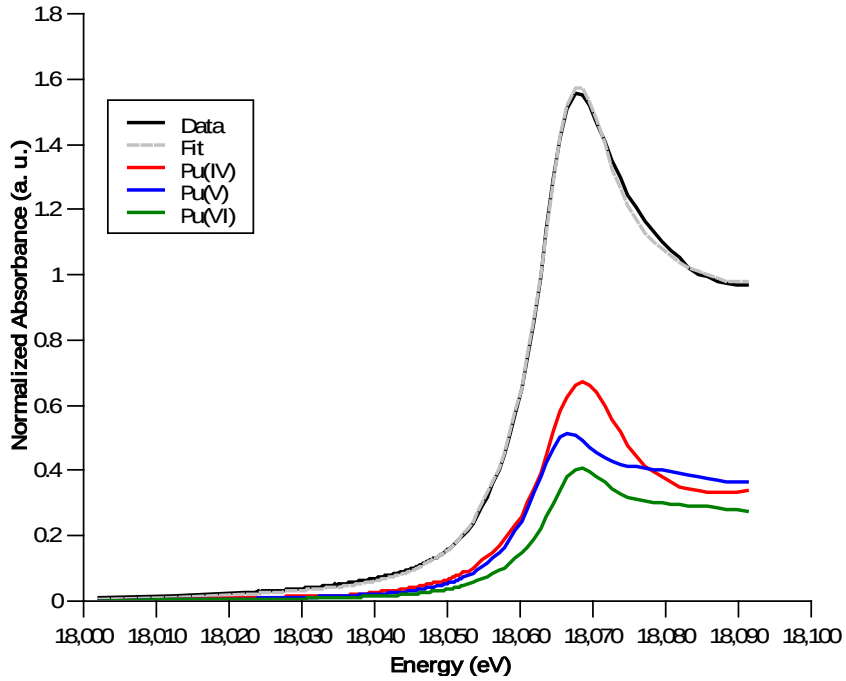


Figure 6.13: Normalized XANES spectrum and the least-squares fits of plutonium sorbed on goethite, measured when exposed to the X-ray beam at 30 K.

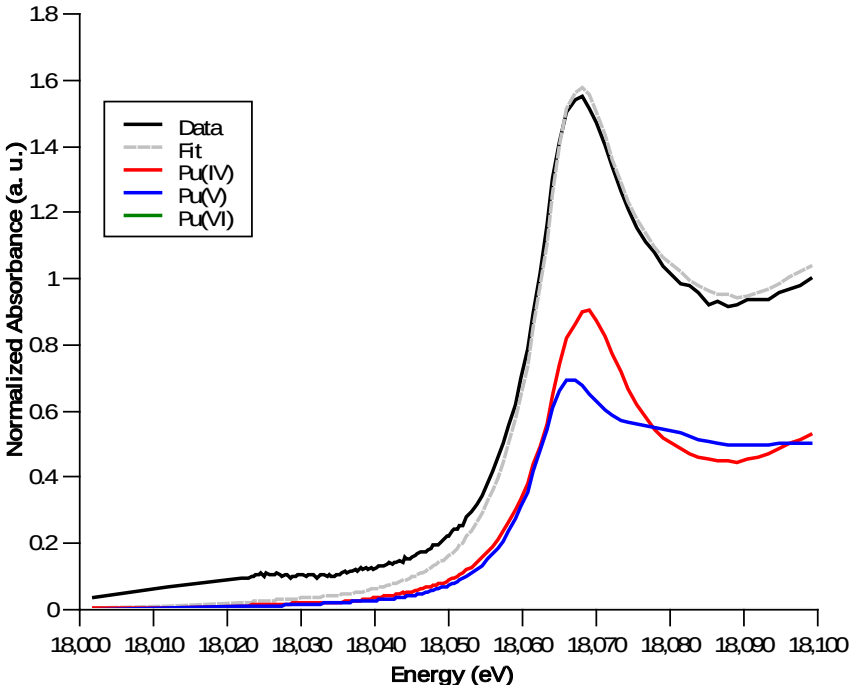


Figure 6.14: Normalized XANES spectrum and the least-squares fits of the same sample of plutonium sorbed on goethite, measured when exposed to the X-ray beam at 300 K

| Sample | % Pu(IV) | % Pu(V) | %Pu(VI) |
|---|---|---|---|
| plutonium-goethite, measured at T=30 K | 38.01 ± 4.11 | 35.10 ± 6.58 | 26.73 ± 6.80 |
| plutonium-goethite, measured at T=300 K | 51.23 ± 21.56 | 47.62 ± 33.99 | 0.03 ± 35.24 |

Table 6.1: Percentage of Pu(IV), Pu(V), and Pu(VI) determined from least-squares fits of plutonium $L_{III}$-edge XANES data. Error is 1σ.

Evidence of plutonium reduction in presence of goethite and 1% Al-substituted goethite

XAS experiments were carried out to garner additional information about the plutonium complex sorbed on the mineral surface. The initial focus was to compare the plutonium-goethite and the plutonium-1% Al-substituted goethite systems. Only a single solution condition was evaluated instead of the entire pH range of solution conditions used in the batch sorption studies. pH 8 was chosen because maximum sorption was observed at that solution condition for both systems. Figure 6.15 shows the normalized XANES spectrum of plutonium sorbed on goethite at pH 8 and Figure 6.16 shows the spectrum of plutonium sorbed on 1% Al-substituted goethite at pH 8. The characteristic plutonyl shoulder is not clearly evident in either spectra, indicating Pu(V) nor Pu(VI) is not the dominant oxidation state, but rather, it is Pu(IV). The presence of Pu(IV) was highly unexpected. The percentages of Pu(IV), Pu(V), and Pu(VI) were determined through least-squares fits (Table 6.2). The oxidation state distribution of the plutonium-goethite is: 82.19 ± 3.12% Pu(IV), 15.22 ± 4.24% Pu(V), and 5.35 ± 4.21% Pu(VI). For the plutonium-1% Al-substituted goethite, 81.63 ± 6.24% of the plutonium is Pu(IV), 23.02 ± 8.36% is Pu(V), and 0.01 ± 8.43% is Pu(VI). From the numbers, the extent of Pu(VI) reduction seems to be greater for 1% Al-substituted goethite than for goethite, but the amount of oxidized plutonium [Pu(V) and Pu(VI)] compared to the amount of reduced plutonium is not statistically different between the two minerals. Furthermore, the important take-away point is observed reduction of Pu(VI) to Pu(IV). The XANES data clearly show reduction of Pu(VI) to Pu(IV) is occurring in the presence of goethite and 1% Al-substituted goethite.

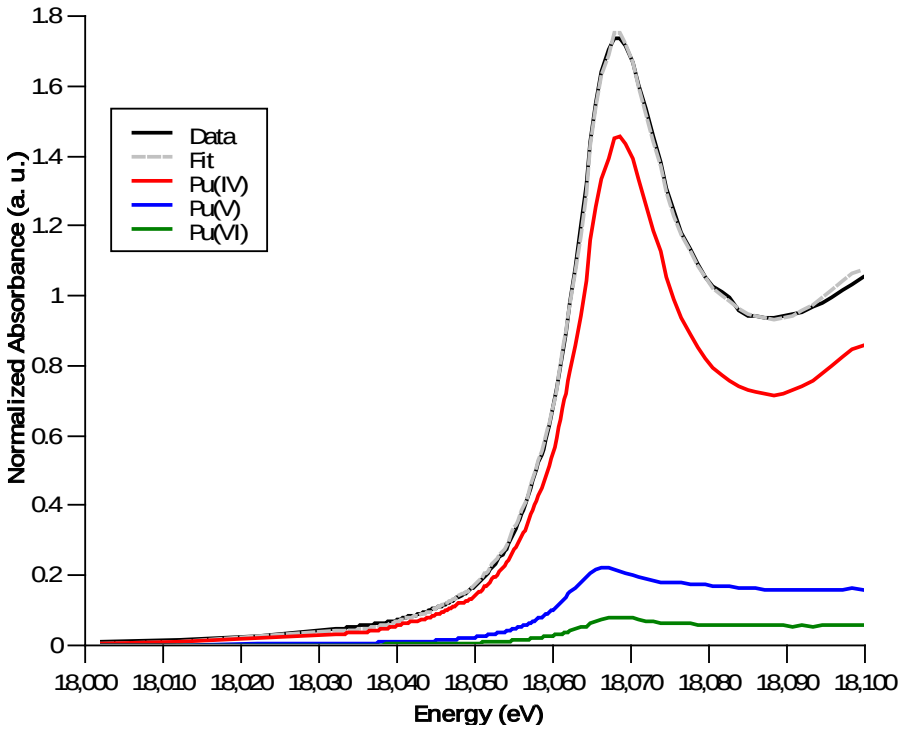


Figure 6.15: Normalized plutonium $L_{III}$-edge XANES spectra for plutonium sorbed on goethite. Approximately 82% of the plutonium is Pu(IV) and 20% is Pu(V)/ Pu(VI).

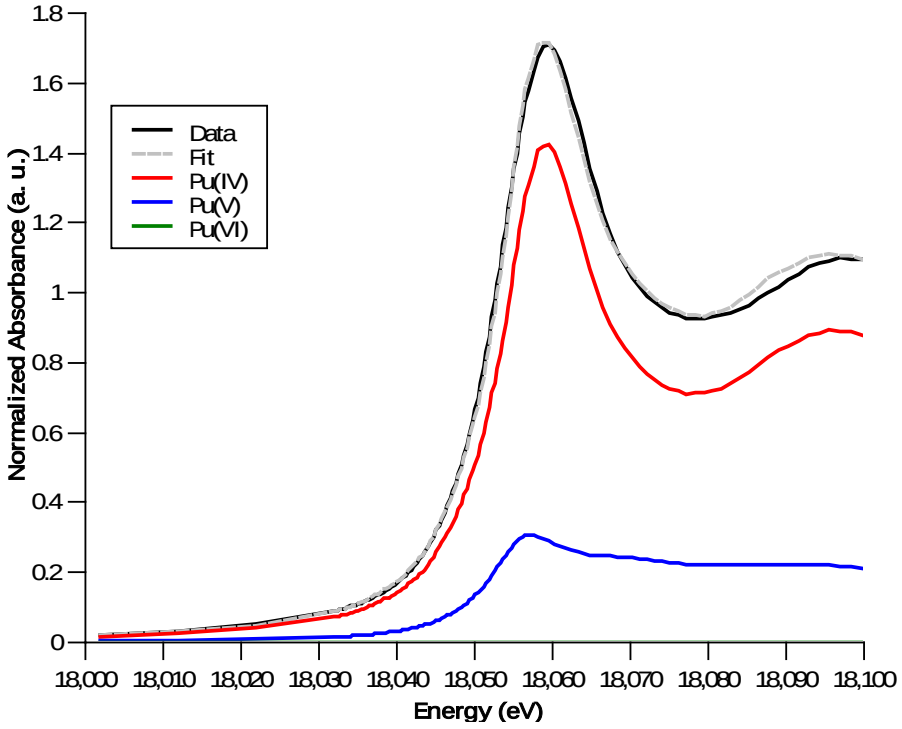


Figure 6.16: Normalized plutonium $L_{III}$-edge XANES spectra for plutonium sorbed on 1% Al-substituted goethite. Approximately 82% of the plutonium is Pu(IV) and 23% is Pu(V)/ Pu(VI).

| Sample | % Pu(IV) | % Pu(V) | %Pu(VI) |
|---|---|---|---|
| plutonium-goethite at pH 8 | 82.19 ± 3.12 | 15.22 ± 4.24 | 5.35 ± 4.21 |
| plutonium-1% Al-substituted goethite at pH 8 | 81.63 ± 6.24 | 23.02 ± 8.36 | 0.01 ± 8.43 |

Table 6.2: Percentage of Pu(IV), Pu(V), and Pu(VI) determined from least-squares fits of plutonium $L_{III}$-edge XANES data. Error is 1σ.

Plutonium reduction is pH dependent

Subsequent XAS experiments focused on the plutonium-goethite system. Three samples were prepared at pH 6, pH 8, and pH 9, representative of solution conditions below, at, and above the PZC of goethite. The XANES spectra collected for the plutonium-goethite sample at pH 6 (Figure 6.17) clearly show a plutonyl type structure. This is expected, as plutonium was spiked into the system as Pu(VI). However, the characteristic plutonyl shoulder is seemingly absent in the spectra of the pH 8 and pH 9 samples (Figure 6.18 and Figure 6.19). Though highly unexpected, the XANES spectra suggest presence of Pu(IV). Least-squares fits for the plutonium-goethite samples at pH 6, pH 8, and pH 9 were calculated (Table 6.3). The data show the presence of Pu(VI), Pu(V), and Pu(IV), with the amount of Pu(IV) increasing with solution pH conditions. Particularly important to note, there is a clear pH dependence for reduction. Table 6.3 shows that a difference in solution pH gives a significantly different Pu(IV) amount. Increasing the solution pH from 6 to 8, there is a 40% increase in reduction of Pu(VI) to Pu(IV). The change in pH coincides with the transition of the solution pH across goethite's PZC. Remember that positively charged or neutral species are at an electrostatic disadvantage for sorption onto the mineral surface at pH conditions lower than the PZC, but as the solution pH increases, the electrostatic interaction between the plutonium species and the goethite surface is favored, and maximum sorption occurs around and above pH 8.5. The significant increase in plutonium reduction with increasing solution pH which is correlated with increasing sorption suggests that plutonium reduction occurs through a surface-mediated mechanism.

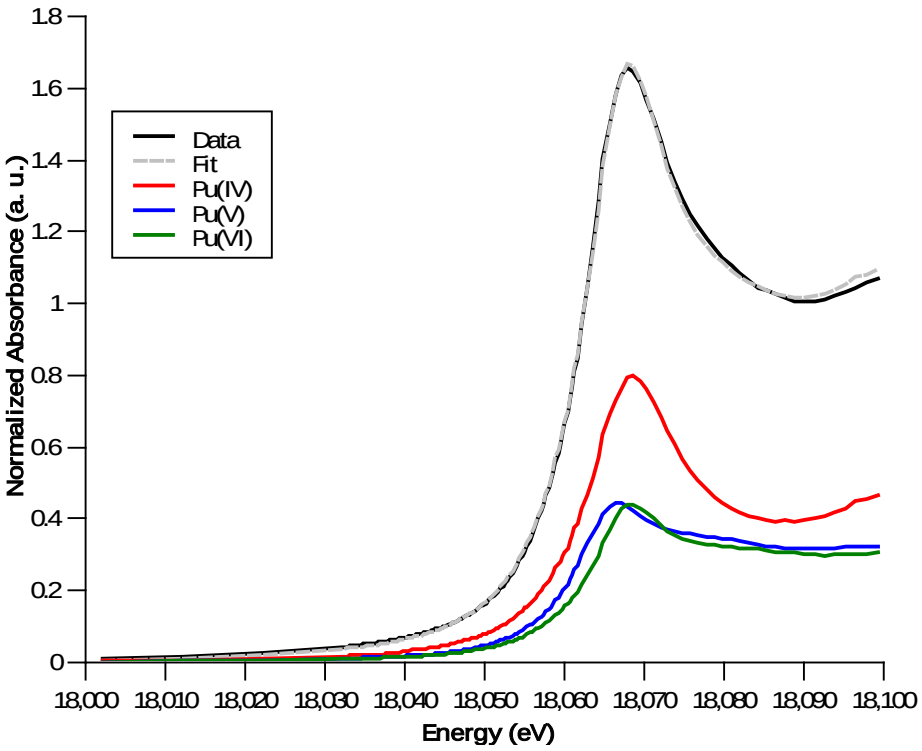


Figure 6.17: Normalized XANES spectrum of plutonium sorbed on goethite at solution condition of pH 6

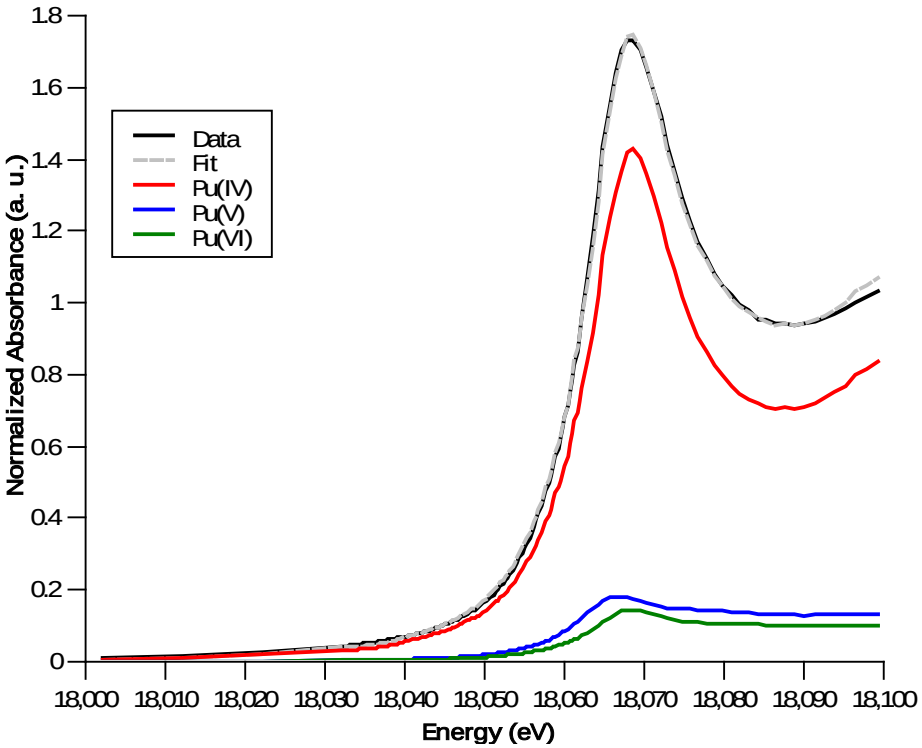


Figure 6.18: Normalized XANES spectrum of plutonium sorbed on goethite at solution condition of pH 8

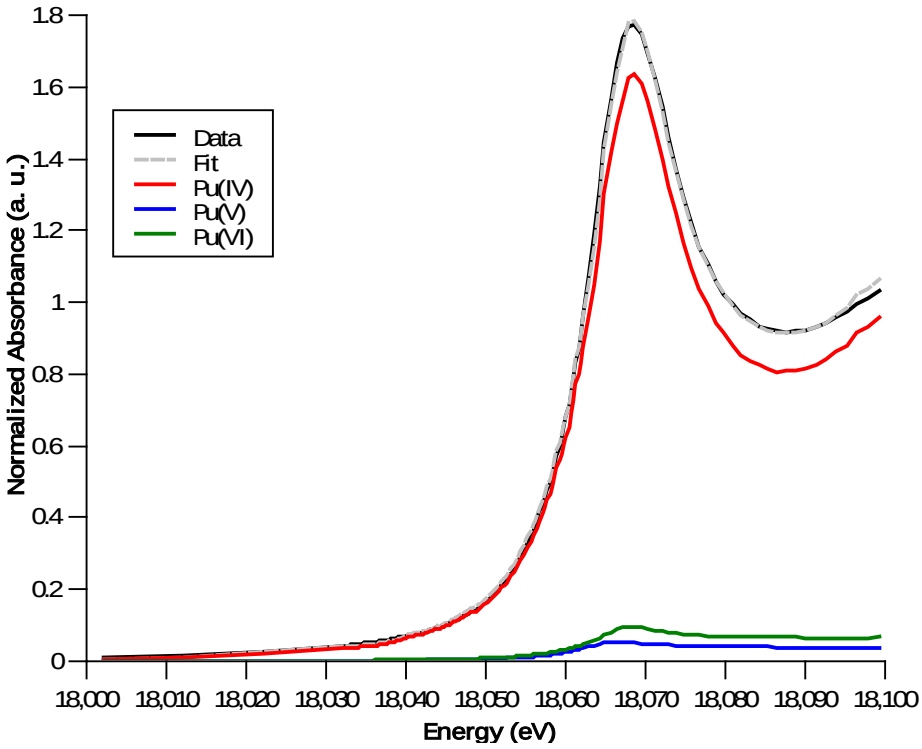


Figure 6.19: Normalized XANES spectrum of plutonium sorbed on goethite at solution condition of pH 9

| Sample | % Pu(IV) | % Pu(V) | % Pu(VI) |
|---|---|---|---|
| plutonium-goethite at pH 6 | 45.01 ± 3.16 | 30.43 ± 4.40 | 28.90 ± 4.42 |
| plutonium-goethite at pH 8 | 80.54 ± 3.54 | 12.46 ± 4.93 | 9.52 ± 4.95 |
| plutonium-goethite at pH 9 | 92.28 ± 3.82 | 3.73 ± 5.31 | 6.28 ± 5.34 |

Table 6.3: Percentage of Pu(IV), Pu(V), and Pu(VI) determined from least-squares fits of plutonium $L_{III}$-edge XANES data. Error is 1σ.

Abridged EXAFS analyses of the collected XAS measurements were carried out; complete analyses were not performed because the presence of multiple oxidation states of plutonium exceedingly complicates analyses. The EXAFS spectrum for the sample representative of the plutonium-goethite system at pH 6 is shown in Figure 6.20. The spectrum exhibits the split-oxygen shell associated with the plutonyl moiety. This distinguishing feature arises from interference between the EXAFS oscillations of the axial and equatorial oxygens of actinyl moiety.[162] This spectral feature suggests plutonium is in the oxidized form, which agrees with the XANES fits.

The EXAFS spectra for the samples representative of the plutonium-goethite system and the plutonium-1% Al-substituted goethite system at pH 8 are shown in Figure 6.21 and Figure 6.22. Inspection of the spectra show no split-oxygen shell, signifying the oxidized forms of plutonium (Pu(V) and Pu(VI)) are not the dominant species, but rather the reduced Pu(IV), agreeing with the XANES fit.

The EXAFS spectra were also of use to check for $PuO_2$ precipitation. There is the possibility that the presence of Pu(IV) is from $PuO_2$ precipitation during sample preparation. When adjusting the pH condition, addition of too much base too quickly after the plutonium spike can cause immediate precipitation of $PuO_2$. Recall the EXAFS spectrum of $PuO_2$ in *r*-space (Figure 2.24), which exhibits a large and distinct Pu-Pu scattering peak at about 3.9 Å. The characteristic Pu-Pu scattering peak is absent in the EXAFS spectra of the plutonium-goethite and plutonium-1% Al-substituted goethite systems (Figure 6.20, Figure 6.21, and Figure 6.22) and absent for all the other samples presented above (spectra not shown). Thus, there is no evidence of $PuO_2$ precipitation occurring on the mineral surface, and the observed plutonium reduction is not attributed to experimental error.

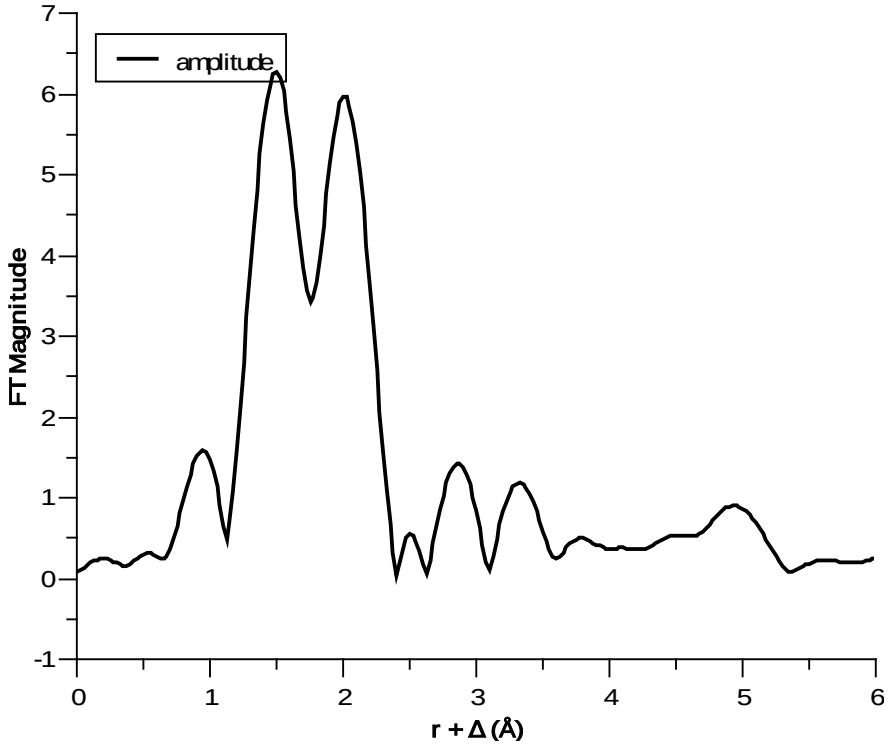


Figure 6.20: Fourier-transformed EXAFS spectrum in *r*-space of plutonium sorbed on goethite at pH 6

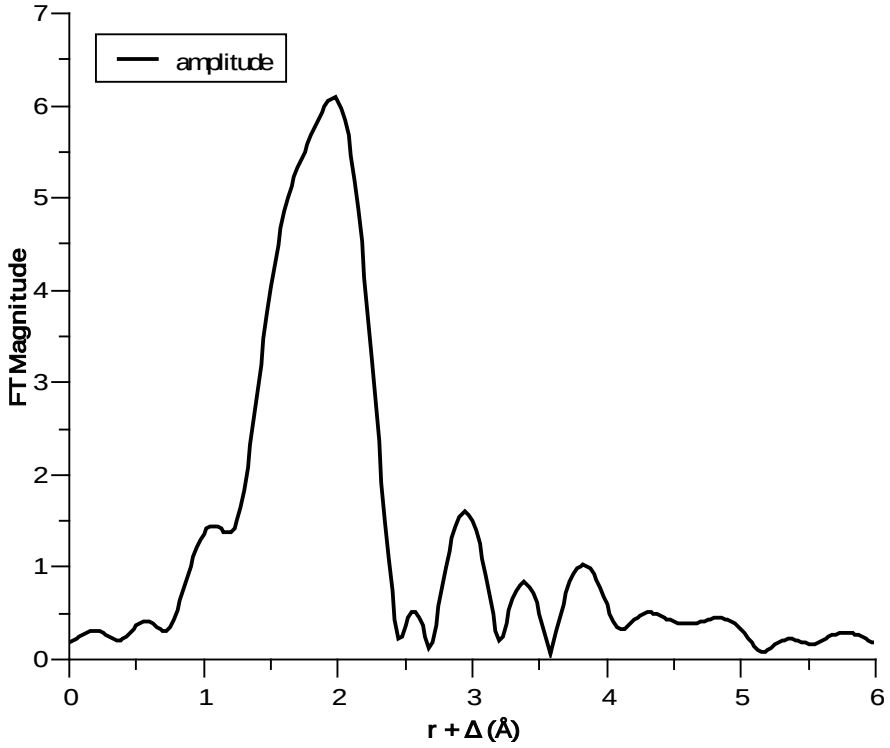


Figure 6.21: Fourier-transformed EXAFS spectrum in *r*-space of plutonium sorbed on goethite at pH 8

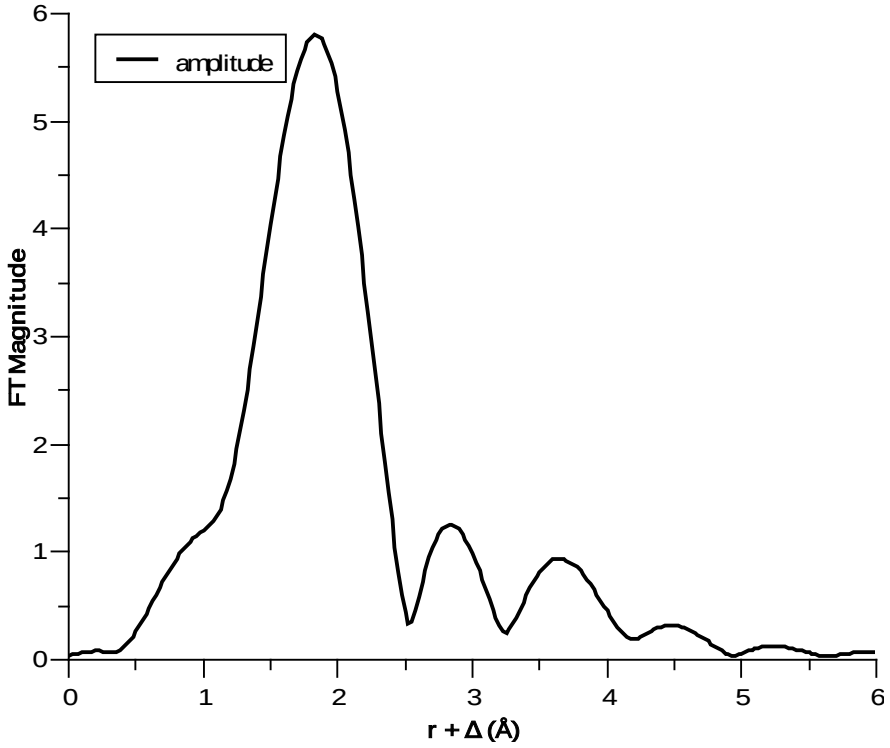


Figure 6.22: Fourier-transformed EXAFS spectrum in *r*-space of plutonium sorbed on 1% Al-substituted goethite at pH 8

## 6.4 Discussion

Evident from the batch sorption experiments, plutonium exhibits a complex sorption behavior to both the iron oxide minerals goethite and 1% Al-substituted goethite. Changes in sorption were observed at varying solution pH conditions over the course of 7 days. The data suggest sorption equilibrium is reached after 7 days of contact time for the goethite and 1% Al-substituted goethite.

The complex plutonium sorption behavior also indicates the sorption mechanism is a two-step process. The secondary sorption step may be due to a redox transformation, as put forward by Sanchez *et al*.[154] Reduction to Pu(IV) was indeed observed with XAS measurements. Two possibilities for where the redox transformation of plutonium occurs is either in solution or when bound to the iron oxide surface. A possible mechanism would be reduction of the anionic Pu(VI)-carbonate species to the neutral Pu(V)-hydroxo species, followed by subsequent sorption to the mineral surface. If this were the case, plutonium would be slowly released from the anionic carbonate complex to the neutral hydroxo complex and available for sorption. However, neither Sanchez *et al.* nor Keeney-Kennicutt and Morse observed redox transformation of plutonium in the solution phase.[153,154] Additionally, the results from batch sorption experiments in this study clearly indicate Pu(VI) is present in solution, as plutonium sorption is inhibited in the carbonate-rich solutions above pH 8.

XAS experiments were conducted to investigate the redox transformation of plutonium when bound to the mineral surface. A significant increase in plutonium reduction was observed with increasing solution pH conditions. The change in pH is correlated with increasing sorption and coincides with the transition across goethite's PZC. The sorption and reduction data lend further support to the hypothesis that plutonium reduction occurs through a surface-mediated mechanism.

Plutonium reduction could come about due to easily mobile electrons from small amounts of Fe(II) impurities. Williams and Scherer used Mössbauer spectroscopy to show that Fe(II) reacted with hematite resulted in electron transfer between sorbed Fe(II) and structural Fe(III). They also observed formation of an Fe(III) layer on the hematite surface that was capable of reducing nitrobenzene.[163] At 250 μM Pu(V), an equivalent of $2 \times 10^{-6}$ moles of electrons would be needed to reduce Pu(VI) to Pu(IV). At 6.25 g/L goethite, there is approximately $2.81 \times 10^{-4}$ moles of total iron. Therefore, approximately 0.70% of the iron in goethite would need to be present as Fe(II) in order for this to be the mechanism behind the plutonium reduction. In this study, no experiments were conducted to determine the fraction of Fe(II) in the synthesized minerals, because the low percentage of Fe(II) is below the detection limit of Mössbauer spectroscopy, and so this hypothesis cannot be discounted. However, while there may be small amounts of Fe(II) present, this is unlikely to be the primary cause of the reduction, as both goethite and 1% Al-substituted goethite were synthesized with 99.99% pure iron nitrate. Thus, the presence of Fe(II) is doubtful to be the cause of plutonium reduction from Pu(VI) all the way to Pu(IV).

Based on these discussions, there is a possibility that the plutonium reduction on iron oxide minerals is a combination of the presence of trace Fe(II) and Pu(V) disproportionation. Trace amounts of Fe(II) could account for reduction of Pu(VI) to Pu(V). With Pu(V), a plausible explanation for plutonium reduction at the solution-mineral interface could be the accumulation of Pu(V) at the surface, followed by Pu(V) disproportionation to Pu(IV) and Pu(VI). If such a combination mechanism controlled the redox chemistry at the solution-mineral surface, the extent of plutonium reduction would be expected to change as a function of the total amount of

plutonium sorbed onto the mineral surface. Subsequent experiments could be carried out with varying plutonium concentrations. An observed correlation between the amount of sorbed plutonium and extent of plutonium reduction might suggest this mechanism is likely. Also, several researchers have observed Pu(V) reduction to Pu(IV) with various pure and mixed mineral phases,[153–155,158] suggesting the presence of Pu(IV) may be the result of the thermodynamic favorability of aqueous Pu(V).

Another possible mechanism behind the plutonium reduction could be electron transfers from a semiconductor material due to light-induced photocatalysis. N-type semiconductors are electron donors, meaning electrons migrate across the depletion region at the solid/solution interface to react with holes from the electrolyte or electroactive species in solution. Upon the electrons and holes recombining, the semiconductor material will have positively charged ions remaining while the aqueous electroactive species will have gained electrons, having acted as a counter electrode.[164] Light of a particular wavelength matching the semiconductor band gap would have sufficient energy to excite electrons from the valence band into the conduction band. In a study by Powell *et al.*, sorption of Pu(V) to hematite was investigated at low concentrations ($10^{-8}$ M). Exposure to light resulted in the reduction of sorbed Pu(V) to Pu(IV), and the electron transfer mechanism was hypothesized to be the cause of reduction.[155] In a similar fashion, the photocatalytic behavior of iron oxide minerals behaving as semiconductors[165] could contribute to electron transfers. Light of sufficient energy could produce electron-hole pairs in goethite and cause reduction of Pu(VI) sorbed to the mineral surface. Especially given that plutonium redox potentials are on the order of ~1 V, a band gap above 1 V would be required of goethite for electron transfers to be thermodynamically possible. While the semiconductor properties of goethite have not been well characterized, crystalline iron oxides are generally considered to have band gaps in the 1.9-2.5 eV range. [164,166–169] Sorption studies conducted in the presence and absence of light could verify goethite's photocatalytic abilities and illuminate whether the electron transfers are the mechanism behind plutonium reduction.

## 6.5 Conclusions

Additional studies are recommended to further examine Pu(VI) sorption to goethite, especially in order to identify the reducing agent behind plutonium reduction. Nonetheless, overall, the data and analyses presented in this study support the following statements:

- Presence of goethite and 1% Al-substituted goethite in the environment can considerably retard plutonium migration, as sorption was observed at environmentally-relevant conditions.

- Plutonium exhibits a complex sorption behavior to goethite and 1% Al-substituted goethite.

- Sorption of Pu(VI) to goethite and 1% Al-substituted goethite results in reduction to the more insoluble Pu(IV) oxidation state.

- The sorption mechanism of Pu(VI) to goethite or 1% Al-substituted goethite surface is postulated to be a surface-mediated reduction to Pu(IV).

# 7. Np(V) Sorption on Hematite

Most SNF is destined for long-term storage in a nuclear waste repository. Understanding the interactions of actinides is crucial in developing accurate transport models and predicting actinide behavior in the storage of nuclear waste, and especially so under repository conditions. In the storage of nuclear waste, which extends to hundreds of thousands of years, elevated temperatures and ionic strengths are likely to be encountered, due to the heat of radioactive decay and high salt content, respectively.[18,170,171]

A major component of SNF is Np-237 because of its long-lived half-life, and hence is the radioisotope of focus for this study. Furthermore, Np(V) serves as a stable chemical analog to Pu(V), as working with neptunium provides a somewhat simpler aqueous and redox chemistry than compared to plutonium. Hematite was chose as the solid phase because of its prevalence in nature and has been extensively studied. Additionally, hematite is representative of corrosion by-products expected to occur in future nuclear waste repositories where SNF will be emplaced in steel containment drums.

There are many studies on the interactions of neptunium with a multitude of mineral surfaces, so there is a fairly robust understanding of Np(V) sorption to iron oxides. However, few studies have examined neptunium sorption apart from ambient laboratory temperatures (~20-25 °C), so there is relatively little information regarding actinide sorption processes above ambient temperature. This is despite the varying temperatures encountered in natural systems and elevated temperatures (~80 °C) expected in nuclear waste repositories. Therefore, to improve ability to model and predict actinide transport in both natural and engineered systems, it is important to investigate actinide sorption over a range of temperatures.

The objective of this study was to investigate the interactions of neptunium with iron oxide hematite, with particular emphasis on the effect of elevated temperature and ionic strength upon Np(V) sorption behavior. Batch sorption experiments were performed on the Np(V)-hematite system at pH conditions ranging from pH 3 to pH 10, at variable temperatures of 25 °C, 35 °C, 50 °C, and 75 °C , and ionic strengths of 0.01 M $NaClO_4$, 0.1 M $NaClO_4$, and 1 M $NaClO_4$. The Np(V)-hematite surface complex was further characterized with XAS. The oxidation state of neptunium was determined with XANES measurements and EXAFS spectra and fits provided additional information about the coordination of neptunium associated with the hematite surface.

## 7.1 Methods and Materials

Unless stated otherwise, distilled deionized water (Milli-Q, 18 MΩ·cm resistivity) and ACS grade chemicals was used in all experiments.

Np(V) working stock preparation

A concentrated stock solution of Np-237 was purified using anion exchange resin (BioRad AG 1-X4, 50-100 mesh) to reduce the amount of daughter product Pa-233 and remove any transuranic impurities (refer to Appendix B). The concentrated neptunium stock solution was qualitatively characterized with γ spectroscopy and α spectroscopy (refer to Appendix A). The concentrated neptunium stock was kept in 1 M $HClO_4$ to hold the pentavalent oxidation state.

To prepare a neptunium working stock, an aliquot was removed from the concentrated stock solution and diluted in 0.01 M $HClO_4$. The pentavalent oxidation state of the working stock was verified with vis-NIR spectroscopy prior to beginning each experiment. The final neptunium concentration of the working stock was determined with LSC (Wallac 1414 LSC running in α/β discrimination mode, Ecolume cocktail). Fresh neptunium working stocks were prepared prior to each batch sorption experiment and XAS experiment.

Mineral synthesis and characterization

Hematite was synthesized using a method adapted from Schwertmann and Cornell.[144] Briefly, a 0.198 M $Fe(NO_3)_3$ solution was heated to 90° C and mixed with a 1 M KOH solution, also at 90 °C, to precipitate ferrihydrite. A 1 M $KHCO_3$ solution was added to raise the pH to ~pH 8 and the solution was then heated to 100 °C for 72 h to allow complete transformation to hematite. The hematite was dialyzed with dialysis tubing and Milli-Q water until the conductivity of the exchange solution was < 2.0 μS. The synthesized hematite has a surface area of 30.7 $m^2/g$, and the 75-150 μm size fraction was used for batch sorption studies. The synthesis and characterization of hematite is covered in-depth in Section 5.3.

Batch sorption studies: mineral suspension preparation

Samples were prepared with low neptunium concentrations to avoid the complicating effects of neptunium precipitation. Calculations show the solutions remained undersaturated with respect to solubility data for $Np_2OH_{(s)}$, $Np_2O_5$, and Na-neptunyl-carbonato complexes.[172–177] All samples were prepared in duplicate.

Mineral suspensions of 6 mg of hematite in 0.01 M, 0.1 M, or 1 M $NaClO_4$ solutions were prepared in acid-washed polycarbonate vials. (For future reference, the nominal terms "low ionic strength" refers to μ = 0.01 M $NaClO_4$, "medium ionic strength" of μ = 0.1 M $NaClO_4$, and "high ionic strength" of μ = 1 M $NaClO_4$.) The total volume of the suspension was ~12 mL, resulting in a solid:liquid ratio of 0.5 g/L. Samples ranged between pH 3 and pH 10. All samples were open to air and no effort to exclude carbonate was made. Samples were spiked with sufficient Np(V) from the neptunium working stock for a concentration of 10 μM. Solution pH was quickly adjusted with small volumes of $HClO_4$ or NaOH. pH was measured with a pH meter (Model 8025, VWR) equipped with a combination pH electrode (Orion 8103, Ross; 3 M NaCl fill solution) calibrated with standard pH buffers. No pH adjustments were made during the course of the experiment, but the pH was measured over time in an attempt to quantity the number of protons released per sorption of neptunyl ion. The

aqueous Np(V) was contacted with the hematite slurry by mixing the sample end-over-end in an incubated rocker (Enviro-Genie, Scientific Industries) for 7 days at 25 °C.

After a contact time of 7 days, the samples were centrifuged for 30 minutes, the pH of the solution measured, and a 50 μL aliquot was removed from the clear supernatant. Aliquots were taken in triplicate and measured using LSC to determine the amount of neptunium remaining in solution. The percent of neptunium sorbed to hematite was calculated from the difference between the initial amount of neptunium spiked into the sample and the amount left in solution.

Upon completion of this sampling protocol, the samples were returned to the incubated rocker for an additional 7 days. The same sampling technique was repeated and sorption equilibrium was assumed if there was no significant difference between the two sampling events. The reaction temperature was increased and the sampling protocol continued as described above. Temperature increased from 25 °C to 35 °C to 50 °C to 75 °C every 14 days, unless otherwise noted.

Blanks (vials containing only neptunium) were run in parallel to determine the extent of neptunium sorption to the container walls. Blanks also served as a way to verify neptunium precipitation did not occur as the temperature was increased. The mineral-free samples were prepared in the same manner as described above.

XAS experiments: sample preparation

Samples for measurement by XAS were prepared in a similar fashion to the batch sorption samples. Mineral suspensions of 25 mg of hematite were placed in polycarbonate vials with 12 mL of solution (0.01 M $NaClO_4$ or 1 M $NaClO_4$), resulting in a solid:liquid ratio of 6.25 g/L. All samples were open to air and no effort to exclude carbonate was made. Mineral suspensions were spiked with the neptunium working stock to bring the total Np(V) concentration to 100 μM; acquiring high-quality XAS data requires the relatively high neptunium concentrations compared to the batch sorption studies. Because higher Np(V) concentrations could result in precipitation rather than sorption, samples were prepared at pH 6, where no hydrolysis products or carbonate complexes are expected to form. The pH of each sample was quickly adjusted with small volumes of $HClO_4$ or NaOH. Measurement of pH over the course of the experiment indicated pH drift was less than 0.2 pH units. The aqueous Np(V) was contacted with the mineral slurry for 7 days by mixing samples end-over-end on a rocker (Vari-Mix, Thermo Scientific) at room temperature or by mixing samples end-over-end in an incubated rocker (Enviro-Genie, Scientific Industries) at 75 °C. No pH adjustments were made to the samples during the course of the experiment. Following equilibration, samples of the mineral slurry were carefully transferred into Kapton tubes and sealed with parafilm and epoxy. The Kapton tube was triply contained in nesting aluminum sample holders with Kapton windows and indium wire seals in the packaging method described by Hu *et al*.,[147] and then transported to the synchrotron for measurement.

XAS experiments: spectroscopy conditions and details

Neptunium $L_{III}$-edge XAS spectra were collected at SSRL on wiggler beamline 11-2. X-ray wavelength was selected using a Si(220) Φ-90° double crystal monochromator. Higher harmonics were removed by applying a 30% detuning to the second crystal. The vertical aperture of the beam was held at 0.5 mm. Energy calibration was performed in transmission mode by setting the first inflection point at the K-edge absorption spectrum of a Zr metal foil reference run in transmission mode to 17997.6 eV.[178] All XAS measurements were collected at

approximately 30 K using a specially engineered liquid helium cryostat (Janis) to mitigate the risk of beam-induced chemical changes during the experiment. Data were collected in fluorescence mode using a 100-element Ge detector with a sample orientation of 45° to the incident beam. A deadtime correction was applied to the spectra.

The XANES spectra were energy calibrated to a $^{237}NpO_2$ powder reference, where the first inflection point for the neptunium $L_{III}$-edge was defined as 17610 eV.[178] EXAFS data were analyzed by Dr. Daniel Olive according to the standard EXAFS analysis procedures;[179,180] data reduction including alignment, summation, calibration, and error correction were done using Athena[181] and SixPack[182]. Spectral fitting to determine structural parameters was performed using Artemis[181] with theoretical EXAFS paths created with the *ab-initio* code FEFF6[183–186]. Uncertainties of the fitting parameters were determined by inversion of the covariance matrix.[187]

## 7.2 Np(V) Batch Sorption Experiments

Neptunium sorption on polycarbonate vials

Blanks (vials with no hematite) of 10 μM Np(V) were run for the low, medium, and high ionic strength systems, in order to determine the extent of neptunium sorption to the container walls. The results of the mineral-free experiments are shown in Figure 7.1, Figure 7.2, and Figure 7.3. These blanks demonstrate that, under the experimental conditions for the batch sorption studies, sorption of Np(V) onto polycarbonate vials was negligible. Additionally, the blanks indicated neptunium precipitation did not occur as the temperature was increased.

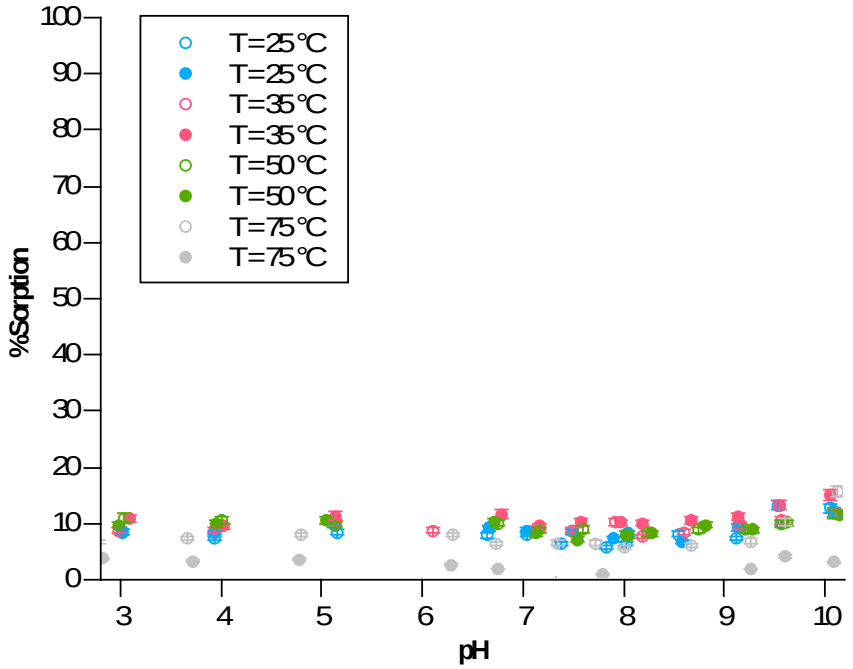


Figure 7.1: Blanks of 10 μM Np(V) for the low ionic strength system (μ = 0.01 M $NaClO_4$) were measured at varying temperatures as a function of pH to verify neptunium sorption to polycarbonate vials was negligible.

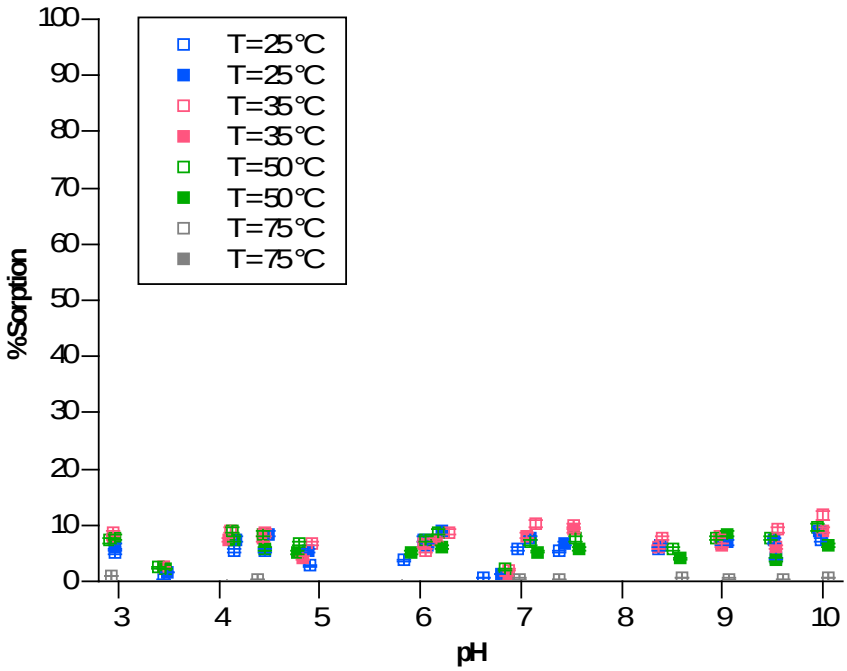


Figure 7.2: Blanks of 10 μM Np(V) for the medium ionic strength system ($\mu$ = 0.1 M $NaClO_4$) were measured at varying temperatures as a function of pH to verify neptunium sorption to polycarbonate vials was negligible.

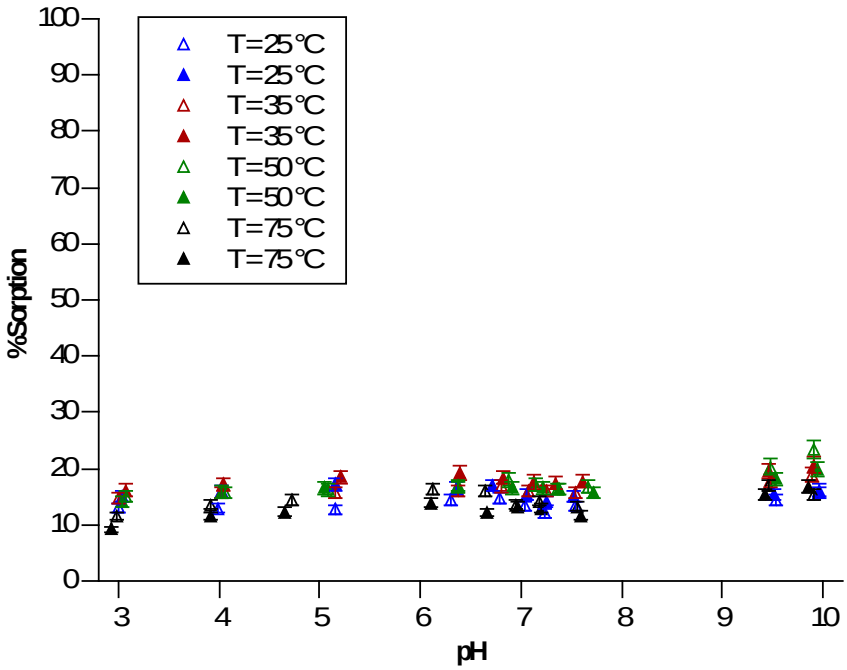


Figure 7.3: Blanks of 10 μM Np(V) for the high ionic strength system ($\mu$ = 1 M $NaClO_4$) were measured at varying temperatures as a function of pH to verify neptunium sorption to polycarbonate vials was negligible.

Neptunium sorption on hematite, as a function of pH

The sorption curve of Np(V) to hematite in 0.1 M $NaClO_4$ after 7 days of contact time shows that aqueous neptunium sorbs to hematite (Figure 7.4). For the pH range considered and in the presence of $CO_2$, Np(V) sorption is less than the sorption onto iron oxide minerals observed for U(VI).[188,189] The overall lower sorption is not unexpected though, given the effective charge for Np(V) of +2.2. The sorption edge is very broad and peaks around pH 8.5, then sorption decreases with further increasing pH. The sorption behavior of Np(V) to hematite is typical for cation sorption to an oxide surface: low sorption in acidic conditions, increasing sorption as the solution pH increases until reaching a sorption maximum, and decreasing sorption as the solution pH further increases. Overall, the neptunium sorption profile is consistent with that observed in previous studies.[190–194] The sorption profile can be explained by the PZC of hematite at ~7.5 and which Np(V) species are present. Recall that the mineral surface is positively charged when solution pH is below the PZC, and negatively charged when above the PZC. In acidic conditions, sorption to hematite is low, likely due to electrostatic repulsion of the positively charged $NpO_2^+$ species to a positive surface charge. Above pH 6, sorption gradually increases as the pH increases, which corresponds to positive $NpO_2^+$ ions interacting favorably with the decreasing surface charge. This is especially so as the solution pH increases beyond the PZC, and the surface becomes negatively charged. Decreased sorption at alkaline conditions is due to the increasing carbonate concentration and formation of carbonate complexes. The negatively charged $NpO_2(CO_3)^-$, $NpO_2(CO_3)_2^{3-}$, and $NpO_2(CO_3)_3^{5-}$ species would be electrostatically repelled from the negative surface charge. This matches previous studies where the presence of carbonate was found to decrease sorption in high pH conditions.[190–194] Neptunium hydrolysis does not greatly affect sorption. While sorption to the hematite surface is not hindered for the neutrally charged $NpO_2OH$ species, the hydroxo complex is present only for a narrow pH range (~pH 7-9) and accounts for a small fractional component of the Np(V) species.

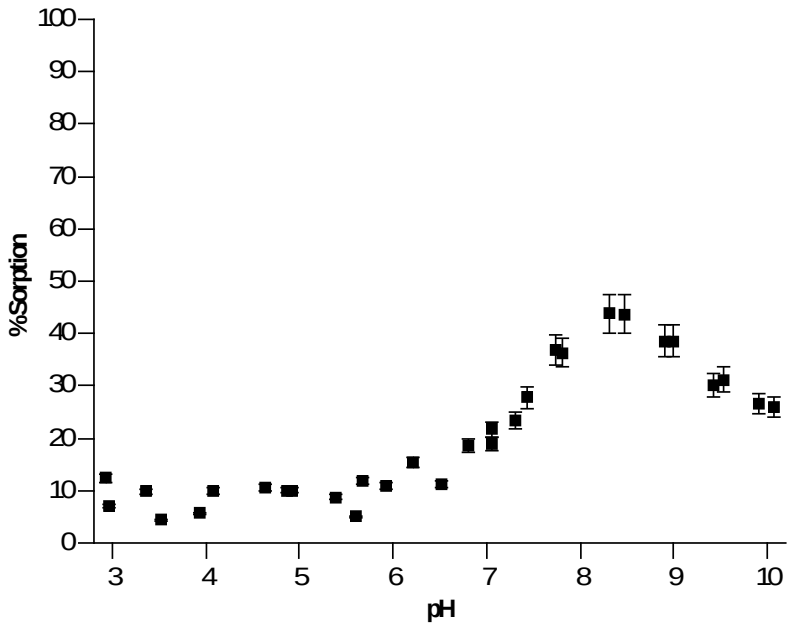


Figure 7.4: Sorption profile of neptunium on the surface of hematite in 0.1 M $NaClO_4$ after equilibration time of 7 days.

Neptunium sorption on hematite, investigated with regards to time

Based on the results from the batch sorption experiments of plutonium on goethite and 1% Al-substituted goethite (Section 6.2), the sorption of neptunium on hematite was also monitored with time. Sorption was measured at 3 days and 7 days. The sorption profile of Np(V) on hematite in 0.01 M $NaClO_4$ measured at 3 days and then 7 days for sequentially increasing temperatures of 25 °C, 35 °C, 50 °C, and 75 °C is shown in Figure 7.5, where open and closed symbols represent the first and second sampling events, respectively. This plot illustrates that for the low ionic strength system, sorption equilibrium has not been reached after 3 days, as the 7 day measurement indicated additional neptunium uptake occurred. Similar to the results at 25 °C, differences between the first and second sampling events were observed at 35 °C, 50 °C, and 75 °C. Next, sorption was measured at 7 days and 14 days. No significant difference in sorption was measured between 7 days and 14 days for all temperature conditions, indicating neptunium sorption equilibrium is reached within 7 days. The Np(V) sorption on hematite in 1 M $NaClO_4$ measured at 3 days and then 7 days for sequentially increasing temperatures of 25 °C, 35 °C, 50 °C, and 75 °C is shown in Figure 7.6. Contrastingly to the low ionic strength system, no significant difference in sorption was observed between the first and second sampling events, and so sorption equilibrium is considered to be reached within 3 days for all temperature conditions.

Because the goal was to study sorption under equilibrium conditions, sampling times were chosen to assure completion of sorption and to avoid kinetic effects. A contact time of 7 days was used for consistency across the low, medium, and high ionic strength systems. This agrees with what was observed for plutonium sorption on iron oxide minerals presented previously in this work (Section 6.2), and is also in line with the 10 day neptunium-montmorillonite equilibration time reported by Turner *et al.*, attributed to the relatively slow mass transfer of $CO_2$ between the gas and aqueous phase.[195]

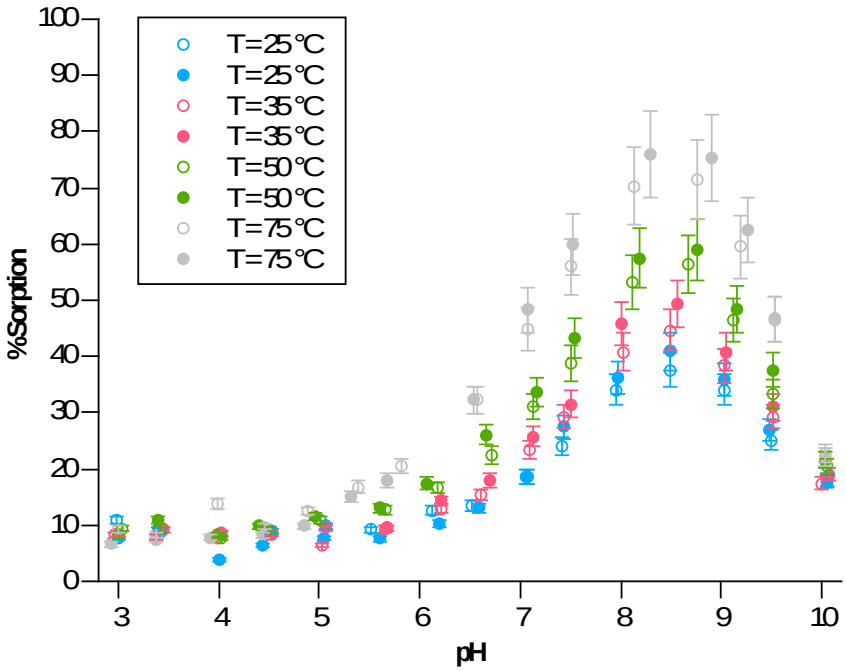


Figure 7.5: Np(V) sorption to hematite as a function of pH and temperature at low ionic strength ($\mu$ = 0.01 M $NaClO_4$). Open and closed symbols represent measurements from the first and second sampling events at 3 days and 7 days, respectively.

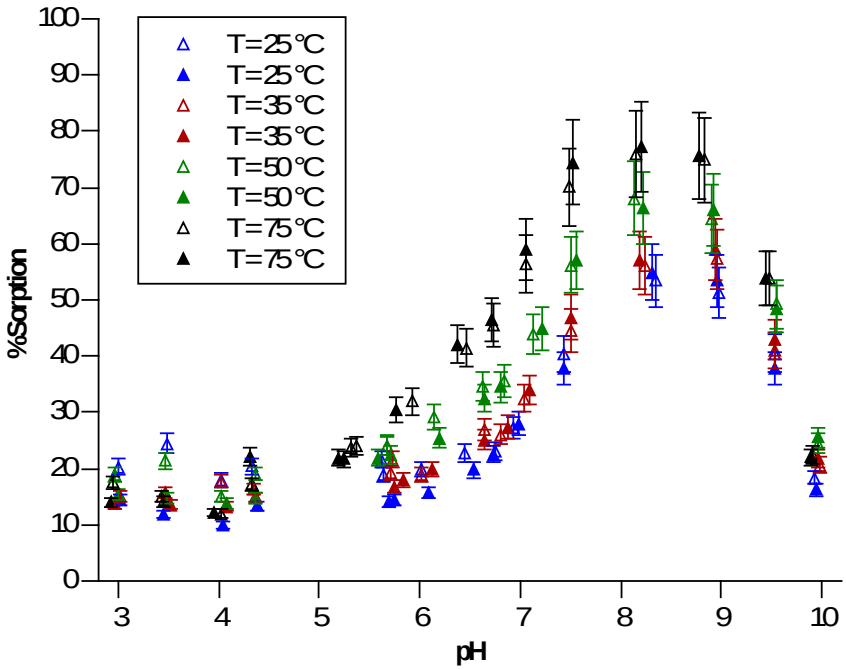


Figure 7.6: Np(V) sorption to hematite as a function of pH and temperature at high ionic strength ($\mu$ = 1 M $NaClO_4$). Open and closed symbols represent measurements from the first and second sampling events at 3 days and 7 days, respectively.

Neptunium sorption on hematite, as a function of temperature

To investigate the effect of temperature, batch sorption experiments of Np(V) on hematite were conducted from pH 3 to pH 10 at sequentially increasing temperatures of 25 °C, 35 °C, 50 °C, and 75 °C for ionic strengths of 0.01 M $NaClO_4$, 0.1 M $NaClO_4$, and 1 M $NaClO_4$. Np(V) sorption to hematite as temperature is sequentially increased in the low, medium, and high ionic strength systems are shown in Figure 7.7, Figure 7.8, and Figure 7.9, respectively. For the low ionic strength system ($\mu$ = 0.01 M $NaClO_4$), an increase in Np(V) sorption to hematite was observed with increasing temperature. Similarly, Np(V) sorption increased with increasing temperature for the medium and high ionic strength systems ($\mu$ = 0.1 M and 1 M $NaClO_4$).

Sorption increases with temperature for all ionic strengths, but the extent of increase varies based on ionic strength, however. A significant increase of sorption is observed going from 25 °C to 75 °C for the low ionic strength system (Figure 7.7), whereas the increase of sorption from ambient to elevated temperature is less so for the high ionic strength system (Figure 7.9). The range of the temperature effect also varies based on ionic strength. For the low ionic strength system, the increase of sorption occurs from 25 °C all the way up to 75 °C. In contrast, increased sorption is observed in the high ionic strength system only from 50 °C to 75 °C.

Also of note, the sorption edge shifts to lower pH as the reaction temperature is increased to 75 °C, regardless of ionic strength. However, no shift in the sorption edge is observed when increasing temperature from 25 °C to 35 °C or from 35 °C to 50 °C. Because $K_w$ varies with temperature,[196] the observed shift in the sorption edge might be misleading and not necessarily indicate increased sorption. To effectively eliminate temperature dependence in the abscissa axis, data was replotted as a function of "pH – 1/2p$K_w$" and the sorption edge shift is still evident (Figure 7.10, Figure 7.11, and Figure 7.12).

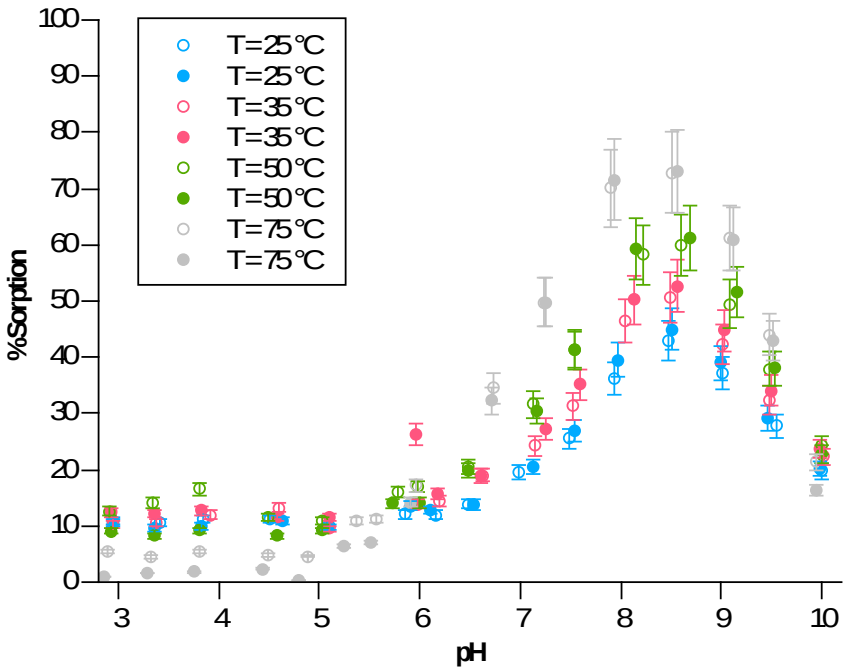


Figure 7.7: Np(V) sorption to hematite as a function of pH and temperature at low ionic strength ($\mu$ = 0.01 M $NaClO_4$). Open and closed symbols represent measurements from the first and second sampling events at 7 days and 14 days, respectively.

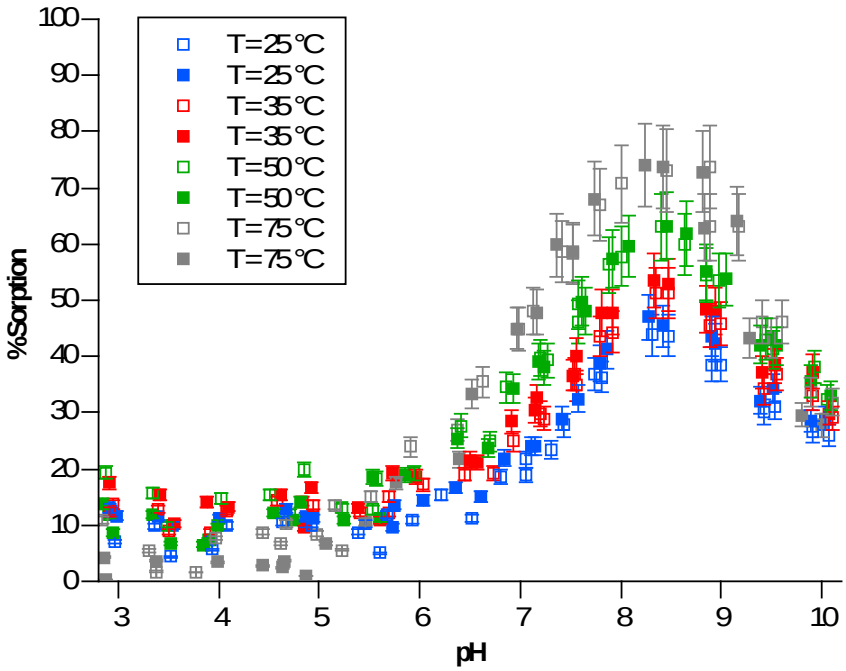


Figure 7.8: Np(V) sorption to hematite as a function of pH and temperature at medium ionic strength ($\mu$ = 0.1 M $NaClO_4$). Open and closed symbols represent measurements from the first and second sampling events at 7 days and 14 days, respectively.

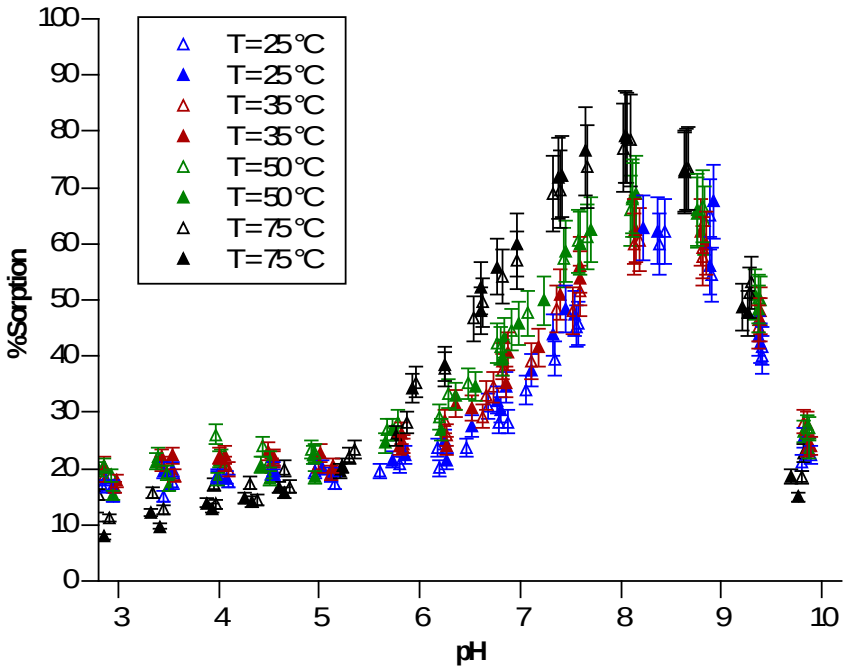


Figure 7.9: Np(V) sorption to hematite as a function of pH and temperature at high ionic strength ($\mu$ = 1 M $NaClO_4$). Open and closed symbols represent measurements from the first and second sampling events at 7 days and 14 days, respectively.

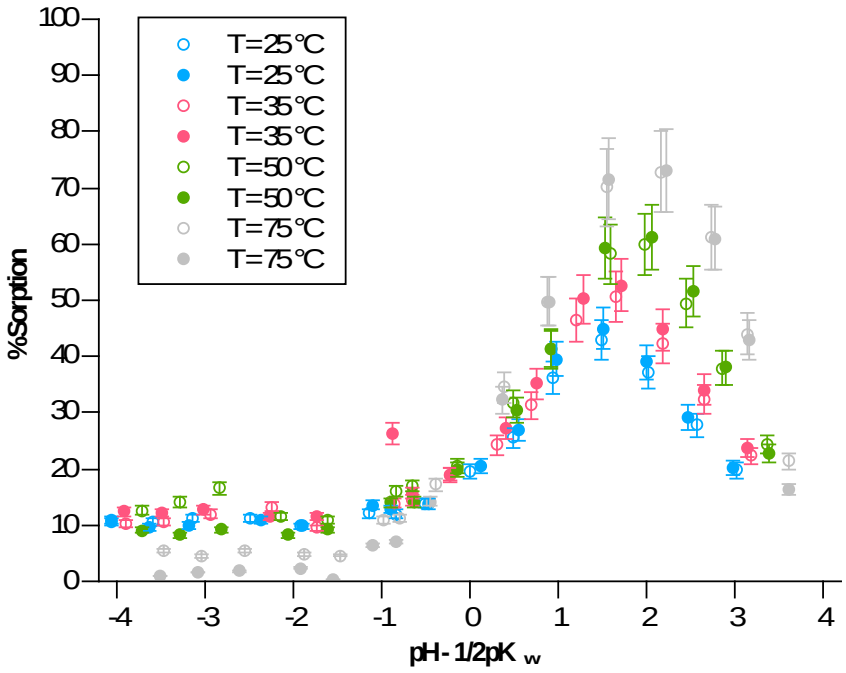


Figure 7.10: Np(V) sorption to hematite as a function of pH – 1/2p$K_w$ and temperature at low ionic strength (μ = 0.01 M $NaClO_4$). Open and closed symbols represent measurements from the first and second sampling events at 7 days and 14 days, respectively.

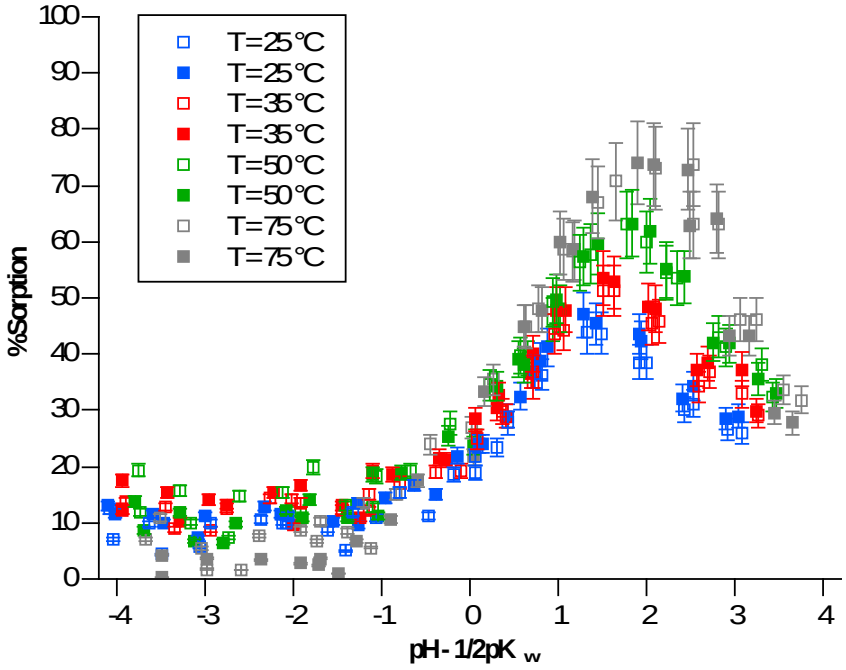


Figure 7.11: Np(V) sorption to hematite as a function of pH – 1/2p$K_w$ and temperature at medium ionic strength (μ = 0.1 M $NaClO_4$). Open and closed symbols represent measurements from the first and second sampling events at 7 days and 14 days, respectively.

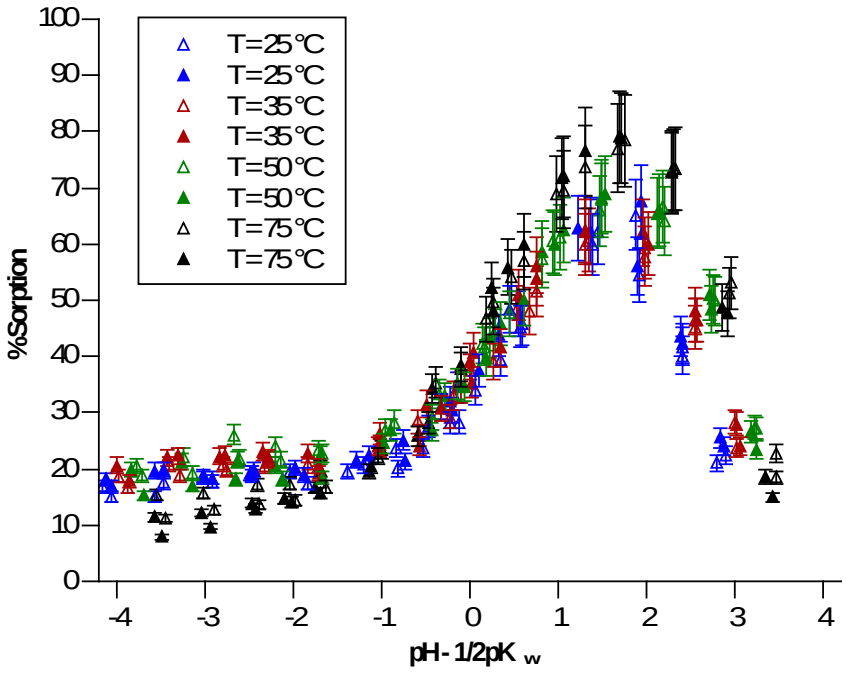


Figure 7.12: Np(V) sorption to hematite as a function of pH – 1/2p$K_w$ and temperature at high ionic strength (μ = 1 M $NaClO_4$). Open and closed symbols represent measurements from the first and second sampling events at 7 days and 14 days, respectively.

To verify that the increase of sorption is an effect of increasing temperature, batch sorption studies were performed to compare sorption at 25 °C and 75 °C for the Np(V)-hematite systems in 0.01 M $NaClO_4$, 0.1 M $NaClO_4$, and 1 M $NaClO_4$. Samples were mixed end-over-end for 14 days at 25 °C, and measurements at 7 days and 14 days confirmed sorption equilibrium at ambient temperature was reached. The temperature was then increased to 75 °C, samples were mixed end-over-end for 14 days, and measurements at 7 days and 14 days confirmed sorption equilibrium at the elevated temperature was also reached. Samples ranged from pH 6 to pH 10, as sorption was negligible in acidic conditions for the previous batch sorption studies where temperature was increased sequentially from 25 °C to 75 °C. Sorption of Np(V) on hematite as temperature increases from 25 °C to 75 °C in the low, medium, and high ionic strength systems (Figure 7.13, Figure 7.14, and Figure 7.15, respectively) confirm sorption increases with temperature. The sorption edge shift as the temperature increases is also clearly noticeable. To account for the temperature dependence of the ionization constant of water, data were replotted as a function of "pH – 1/2p$K_w$" and the sorption edge shift is still evident (Figure 7.16, Figure 7.17, and Figure 7.18).

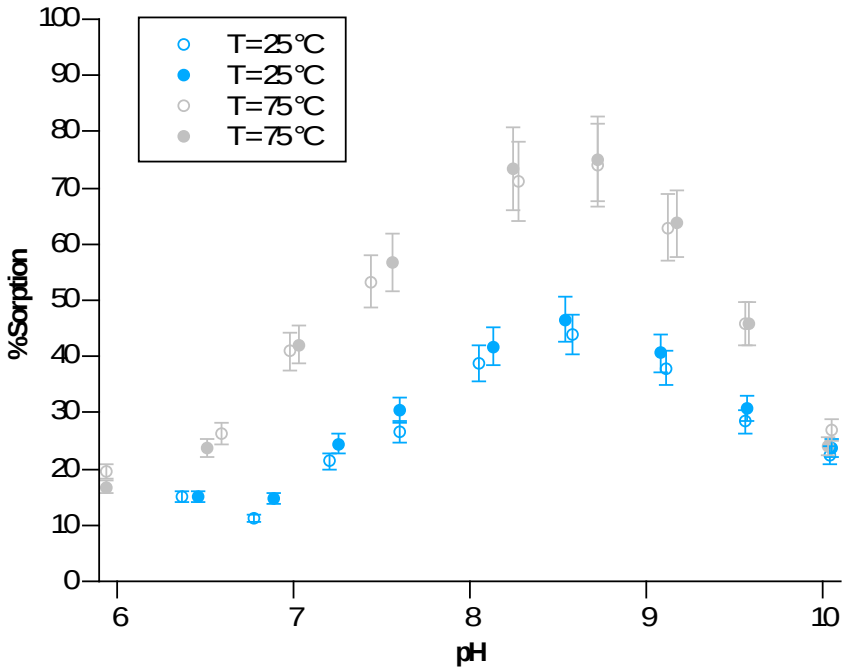


Figure 7.13: Np(V) sorption to hematite as a function of pH at temperatures T = 25 °C and at T = 75 °C at low ionic strength (μ = 0.01 M $NaClO_4$). Open and closed symbols represent measurements from the first and second sampling events at 7 days and 14 days, respectively.

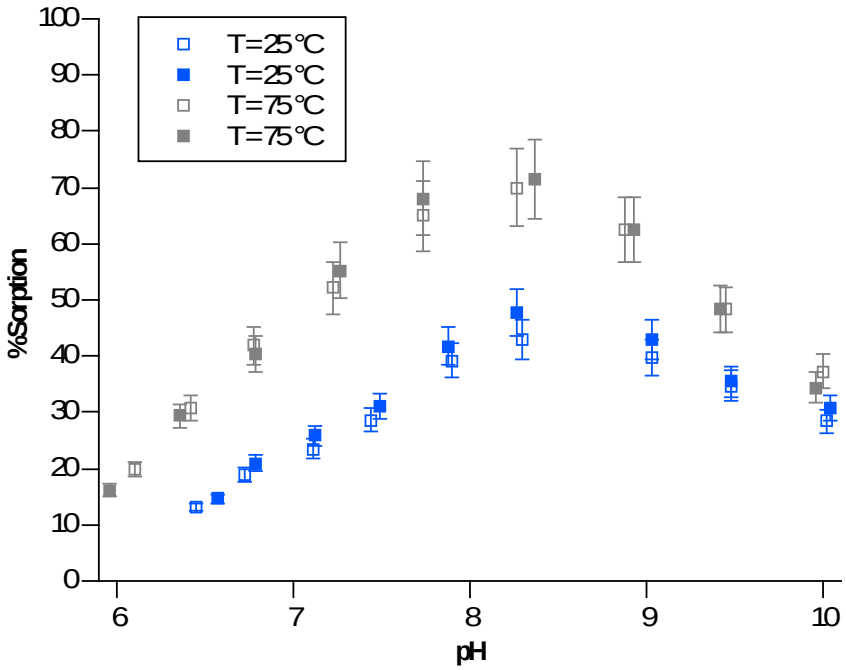


Figure 7.14: Np(V) sorption to hematite as a function of pH at temperatures T = 25 °C and at T = 75 °C at medium ionic strength (μ = 0.1 M $NaClO_4$). Open and closed symbols represent measurements from the first and second sampling events at 7 days and 14 days, respectively.

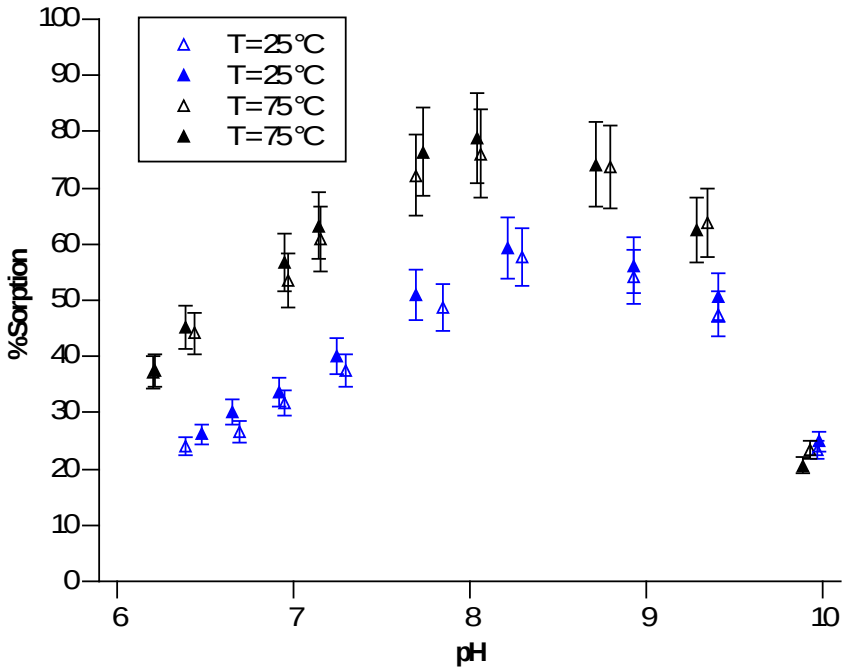


Figure 7.15: Np(V) sorption to hematite as a function of pH at temperatures T = 25 °C and at T = 75 °C at high ionic strength (μ = 1 M $NaClO_4$). Open and closed symbols represent measurements from the first and second sampling events at 7 days and 14 days, respectively.

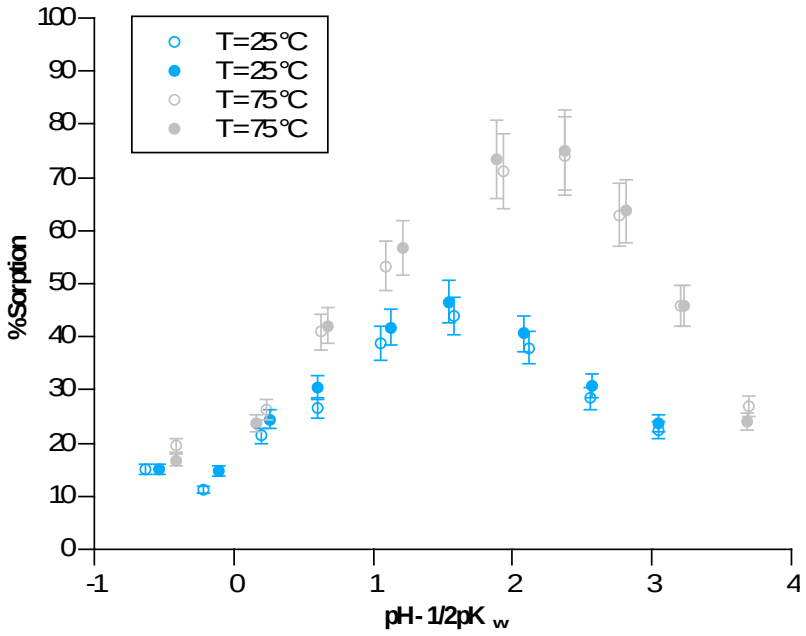


Figure 7.16: Np(V) sorption to hematite as a function of pH – 1/2p$K_w$ at temperatures T = 25 °C and at T = 75 °C at low ionic strength (μ = 0.01 M $NaClO_4$). Open and closed symbols represent measurements from the first and second sampling events at 7 days and 14 days, respectively.

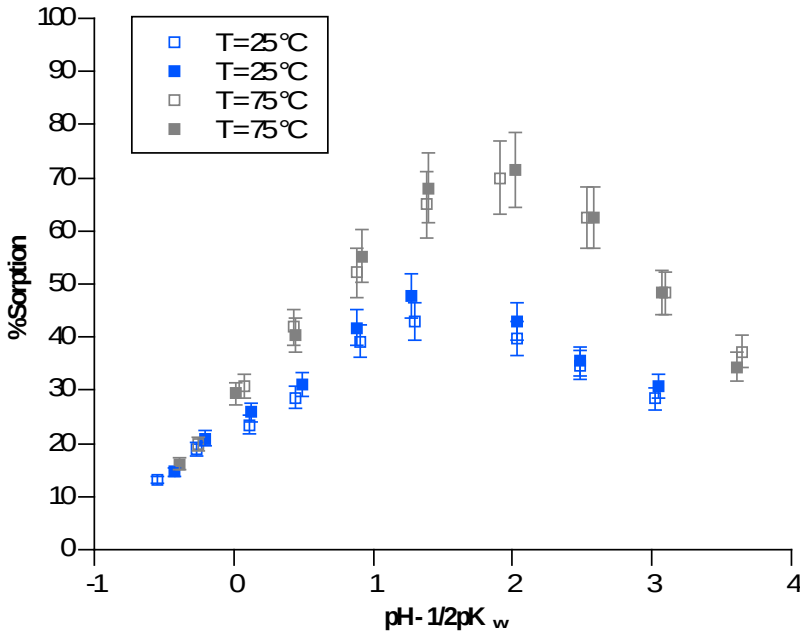


Figure 7.17: Np(V) sorption to hematite as a function of pH – 1/2p$K_w$ at temperatures T = 25 °C and at T = 75 °C at medium ionic strength (μ = 0.1 M $NaClO_4$). Open and closed symbols represent measurements from the first and second sampling events at 7 days and 14 days, respectively.

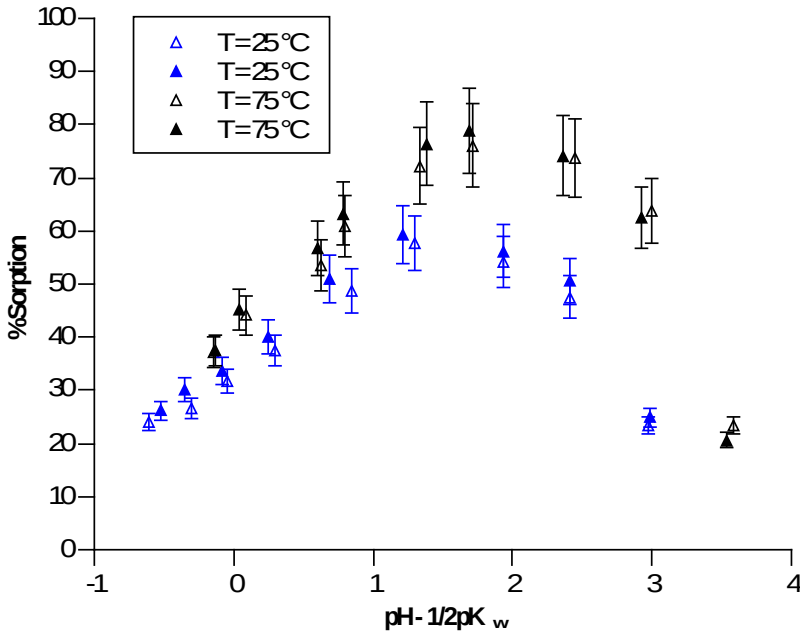


Figure 7.18: Np(V) sorption to hematite as a function of pH – 1/2p$K_w$ at temperatures T = 25 °C and at T = 75 °C at high ionic strength (μ = 1 M $NaClO_4$). Open and closed symbols represent measurements from the first and second sampling events at 7 days and 14 days, respectively.

Neptunium sorption on hematite, as a function of ionic strength

For a more direct comparison of the effect of ionic strength, the neptunium sorption data are replotted and shown at 25 °C, 35 °C, 50 °C, and 75 °C (Figure 7.19, Figure 7.20, Figure 7.21, and Figure 7.22). The influence of ionic strength on Np(V) sorption is not clearly evident. For all temperature conditions, there is no difference in sorption between low and medium ionic strengths. Only at 25 °C (Figure 7.19) is a difference in sorption observed between low and high ionic strengths.

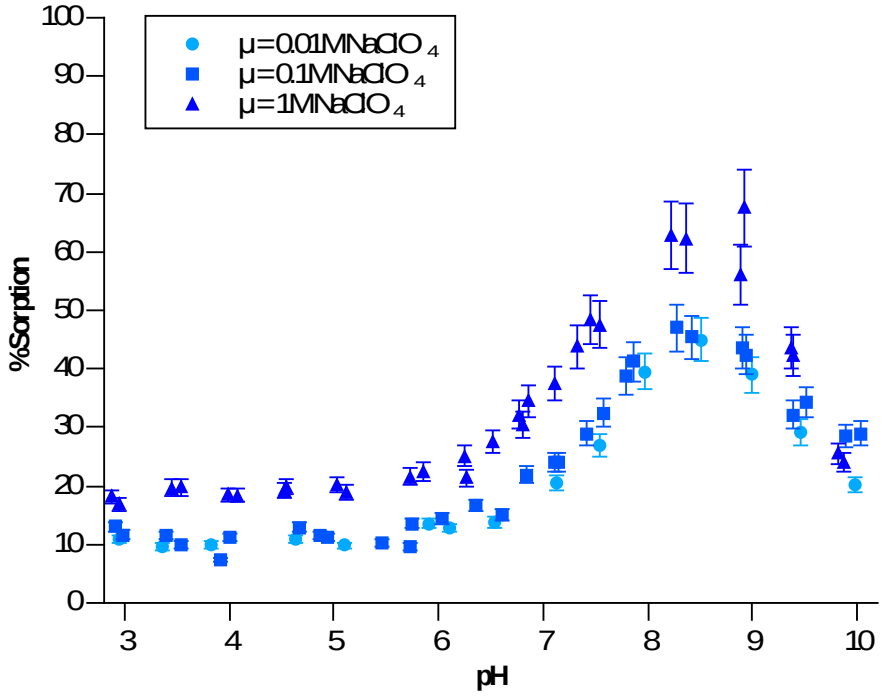


Figure 7.19: Np(V) sorption to hematite as a function of pH at T = 25 °C for 0.01 M $NaClO_4$, 0.1 M $NaClO_4$, and 1 M $NaClO_4$.

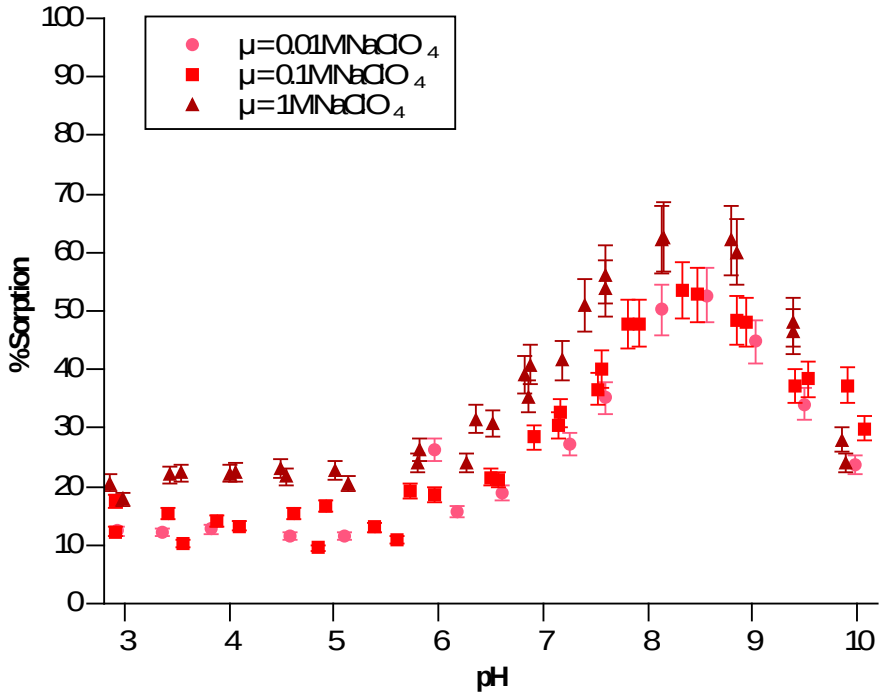


Figure 7.20: Np(V) sorption to hematite as a function of pH at T = 35 °C for 0.01 M $NaClO_4$, 0.1 M $NaClO_4$, and 1 M $NaClO_4$.

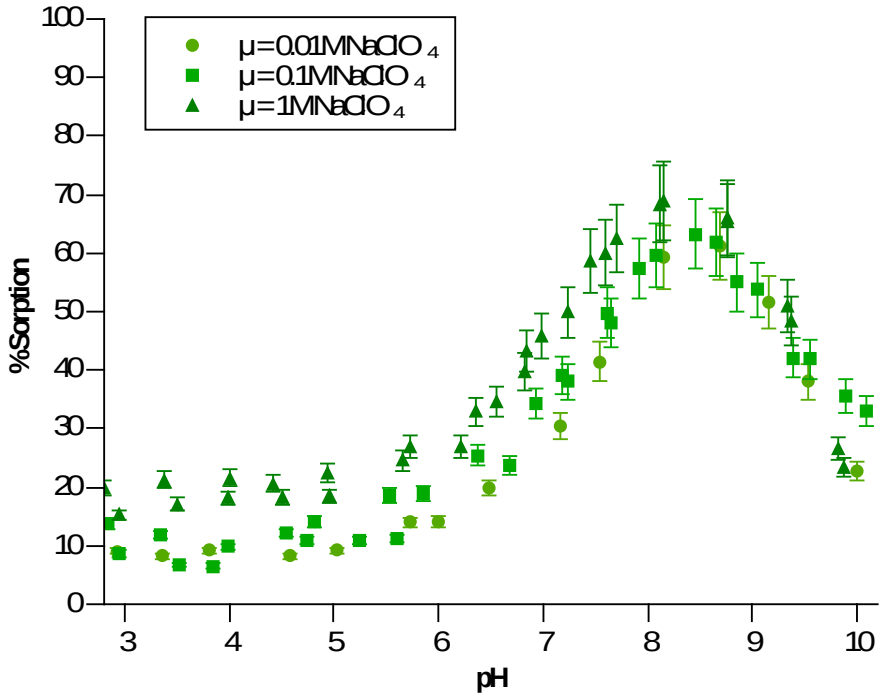


Figure 7.21: Np(V) sorption to hematite as a function of pH at T = 50 °C for 0.01 M $NaClO_4$, 0.1 M $NaClO_4$, and 1 M $NaClO_4$.

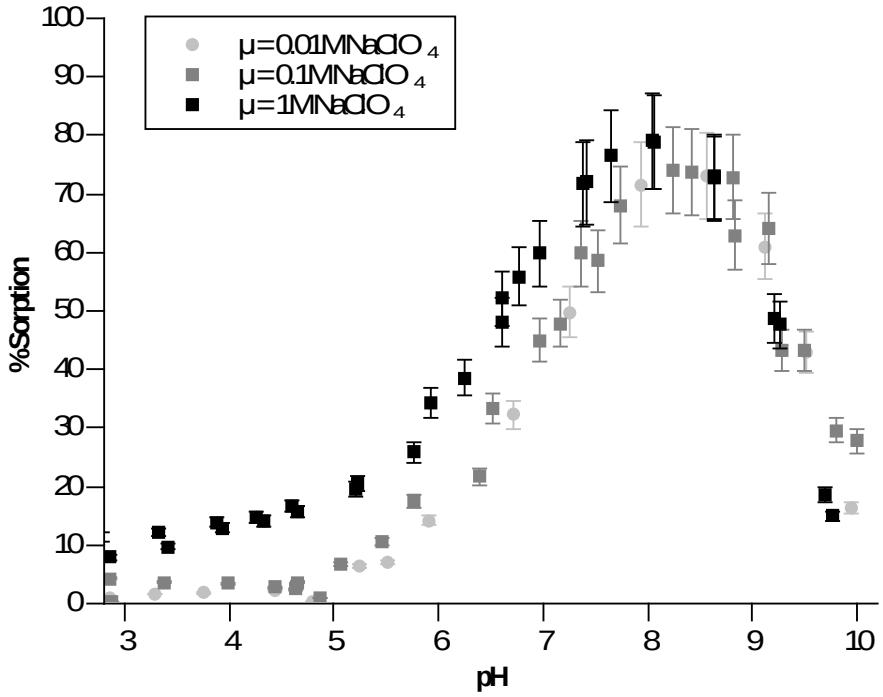


Figure 7.22: Np(V) sorption to hematite as a function of pH at T = 75 °C for 0.01 M $NaClO_4$, 0.1 M $NaClO_4$, and 1 M $NaClO_4$.

Determining the number of protons released per neptunyl ion sorbed could provide further information on the stoichiometry of the sorption mechanism. An effort was made to obtain this quantity in a manner similar to Hsi and Langmuir by carefully measuring the pH shift during the experiment.[197] However, because of uncertainties associated with pH measurements and inconsistencies of electrode calibration, it was not possible to determine the proton release during sorption.

## 7.3 Np(V) XAS Experiments

For more insight into the effect of elevated temperature and ionic strength on Np(V) sorption to hematite, XAS measurements were taken. Samples of Np(V) sorbed to hematite were prepared at various ionic strengths and at room temperature and 75 °C. The oxidation state of neptunium was determined with XANES, and the coordination environment of the Np(V)-hematite complex was analyzed with EXAFS. As was the case with plutonium, the XAS measurements were collected at cryogenic temperatures of 30 K to avoid beam-induced chemistry from the intense X-ray beam.

A series of Np(V)-hematite samples were prepared at room temperature with ionic strengths ranging from 0.001 M $NaClO_4$ to 1 M $NaClO_4$. The normalized absorption edge spectra for the Np(V)-hematite samples of varying ionic strength are shown in Figure 7.23. Also plotted is the XANES spectrum of a $NpO_2$ powder reference, which is used as a Np(IV) standard. The edge energies of the samples, as determined by the peak of the first derivative of the normalized absorption spectrum, are shifted 0.8-1.4 eV higher than the Np(IV) spectrum, which is consistent with a higher oxidation state. The peak positions, as measured by the white line

maximum, are also shifted slightly higher by 0.2-0.7 eV compared to the Np(IV) standard. These parameters are listed in Table 7.1. This confirms that neptunium is present in the samples as Np(V). This result is unsurprising, as no redox chemistry is expected to occur with sorption to the hematite surface. Also visible in the spectra is the characteristic neptunyl shoulder at 17625 eV, the feature that arises from the presence of short axial Np–O bonds found in the oxidized forms of neptunium.

Figure 7.24 shows the Fourier transforms (FT) of the EXAFS spectra of the four samples along with the corresponding fits. (In the following discussion of EXAFS data, the FT positions are reported in units of Å with no correction for phase shift ($r + \Delta$). In contrast, bond lengths are reported as actual distances in units of Å.) Strong scattering contributions are visible in the plot at 1.5 Å and 1.95 Å, due to the two axial oxygen atoms, $O_{ax}$, and the oxygen atoms in the equatorial plane of the neptunyl moiety, $O_{eq}$, respectively. The minor peaks around 3 Å could be attributed as the scattering contribution of iron atoms in a radial Np-Fe distance of 3.73-3.74 Å stemming from binary edge-sharing Np(V) sorption complexes.[198] Little structure at higher R values is seen, suggesting there is no evidence for bulk-like precipitates which would exhibit Np-Np scattering at higher R values, or other neighbors at regular distances common to the neptunium in the sample. The EXAFS spectra show $NpO_2$ precipitation did not occur, which would have been indicated by a Np-Np interaction at 4.2 Å.[89] The similarity of the EXAFS data suggests little difference in the sorption mechanism as ionic strength varies, implying an inner-sphere Np(V)-hematite complex.

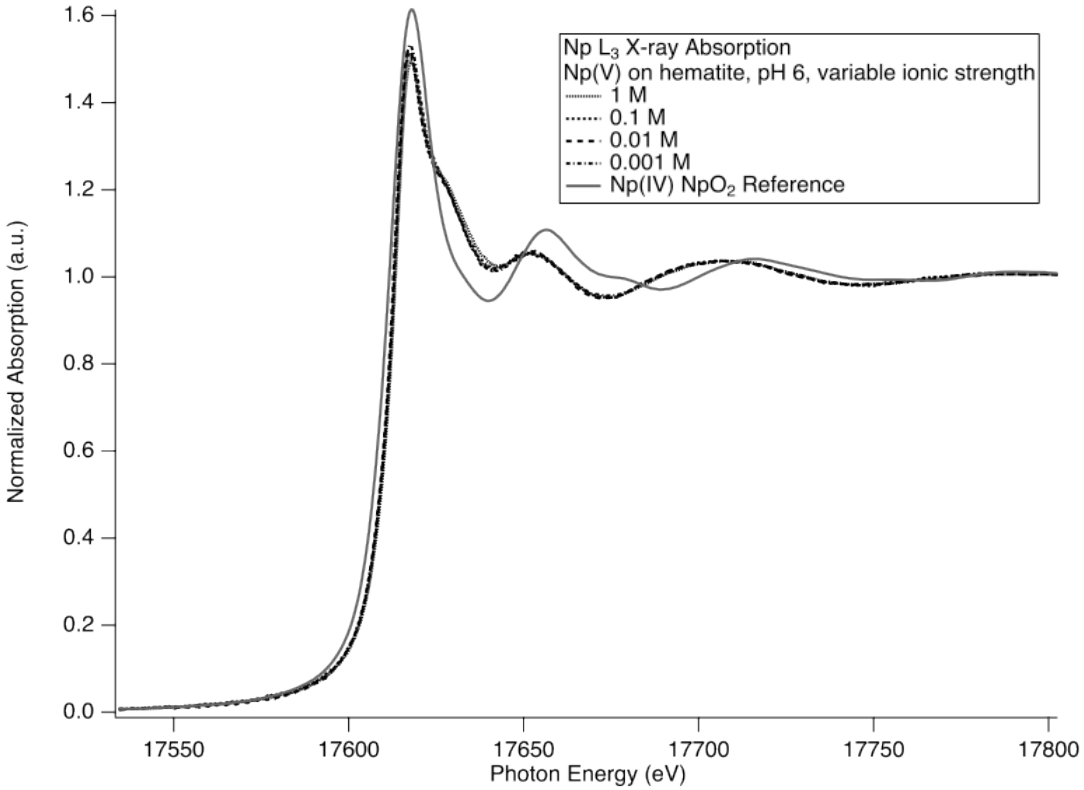


Figure 7.23: Normalized neptunium $L_{III}$-edge XANES spectra for Np(V) sorbed to hematite at pH 6 at ionic strengths of 0.001-1 M $NaClO_4$. A Np(IV) reference spectrum of $NpO_2$ is also shown in comparison.

| Background electrolyte | Edge Energy (eV) | Peak Position (eV) |
|---|---|---|
| 1 M | 17613.8 ± 0.5 | 17617.8 ± 0.5 |
| 0.1 M | 17613.3 ± 0.5 | 17617.3 ± 0.5 |
| 0.01 M | 17613.2 ± 0.5 | 17617.3 ± 0.5 |
| 0.001 M | 17613.8 ± 0.5 | 17617.6 ± 0.5 |
| $NpO_2$ | 17612.4 ± 0.5 | 17618.0 ± 0.5 |

Table 7.1: XANES parameters for Np(V) sorbed to hematite, Figure 7.23, at pH 6 at varying ionic strengths. The edge position is determined using the first derivative and locations of the white line maxima are indicated.

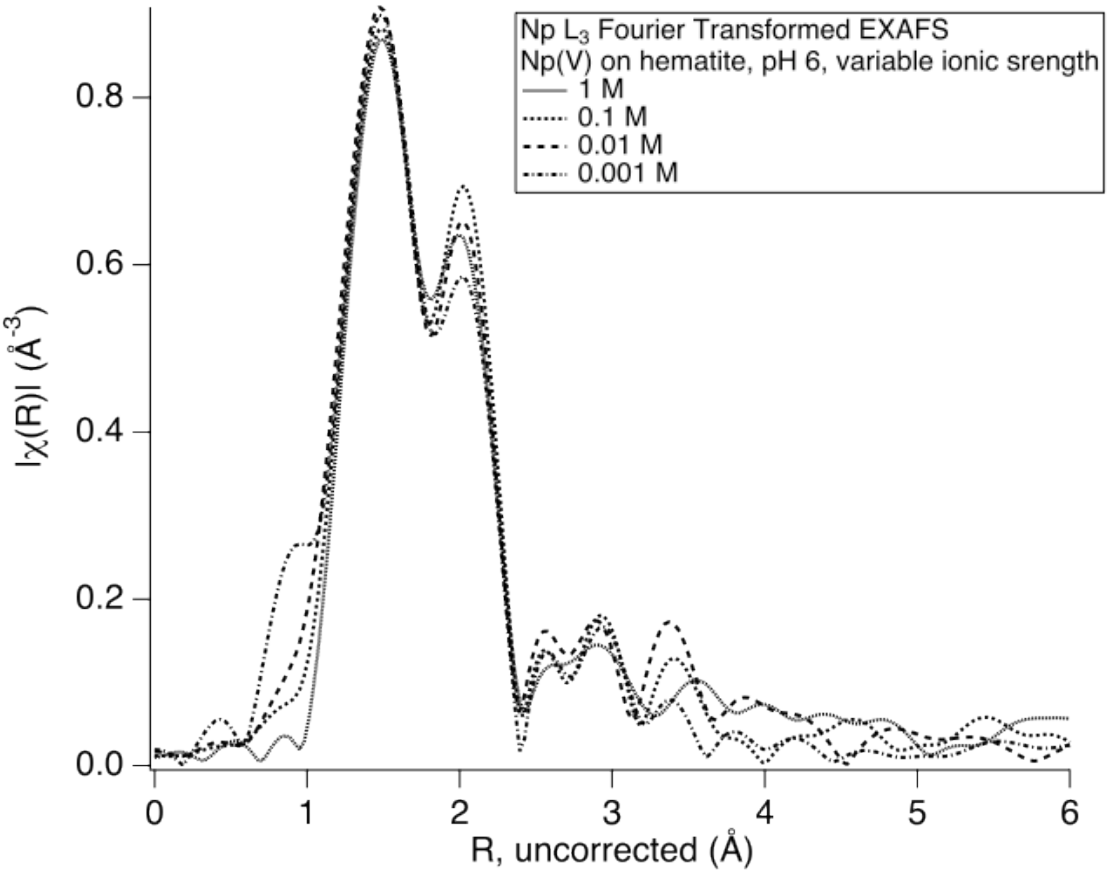


Figure 7.24: Fourier-transformed EXAFS spectra and fits Np(V) sorbed to hematite at pH 6 at ionic strengths of 0.001-1 M $NaClO_4$.

XAS measurements were taken of Np(V)-hematite samples prepared in pairs of room temperature and 75 °C and low and high ionic strength ($\mu$ = 0.01 M $NaClO_4$ and 1 M $NaClO_4$). The measured edge positions of the samples are higher in energy than that of the Np(IV) standard and are assigned to Np(V). The edge positions and shape of the XANES spectra of the four samples (Figure 7.25) show neptunium sorbed to hematite remained as Np(V). Although technical problems precluded satisfactory measurement on the room temperature/low ionic strength sample, high quality data was collected on the remaining three combinations (Figure 7.26).

Fitting of the EXAFS equation[180,199]

$$\chi(k) = \sum_i \frac{N_i S_0^2 F_i(k)}{kR_i^2} \sin\left(2kR_i + \varphi_i(k)\right) e^{(-2\sigma_i^2 k^2)} e^{\frac{-2R_i}{\lambda(k)}} \qquad \text{Eq 7.1}$$

to the measured $\chi$(k) involved performing a non-linear least-squares fit summing over each scattering path used, *i*, in order to find the best values for the amplitude of each path, $N_i$, scattering half-path length, $R_i$, energy shift, $\Delta E_0$\$, and mean squared displacement, $\sigma_i^2$, also known as the EXAFS Debye-Waller factor. The values for the effective scattering amplitude, $F_i(k)$, effective scattering phase shift, $\phi_i(k)$, and mean free path, $\lambda(k)$, were taken from the FEFF6 calculations.

Fitting of the EXAFS data was performed using the structure for $Np_2O_5$ as the basis for a model,[200] setting up the geometry of the two axial and five radial oxygen single scattering paths. Recall the axial bond distance in $NpO_2^+$ is 1.85 Å, and as such, two oxygen single scattering paths at a distance of 1.86 Å and 5 oxygen single scattering paths at a distance of 2.41 Å were used as the initial model. In the fitting model, the number of axial oxygen atoms was set to two, as those bonds in Np(V) are not easily changed. To allow for the possibility that slight changes in the radial oxygen peaks seen in Figure 7.26 are real and not within experimental variation, those amplitudes were allowed to float in the fitting process. Because the amplitude and EXAFS Debye-Waller factors are highly correlated, all three data sets were refined simultaneously in ARTEMIS using the same $\sigma^2$, $\Delta R$, $E_0$ values, while the radial oxygen amplitudes were allowed to float. Fitting results are summarized in Table 7.2. The fits to the first shell of the data encompassing the axial oxygen bond give bond distances consistent with $NpO_2^+$ (1.88 Å). The equatorial bond distances of 2.47 Å and 2.45 Å are also consistent with Np(V) complexes. The small Debye-Waller factors are consistent for low temperature measurements. The fits show no significant differences between the room temperature and 75 °C sorption samples, suggesting inner-sphere sorption mechanism at work.

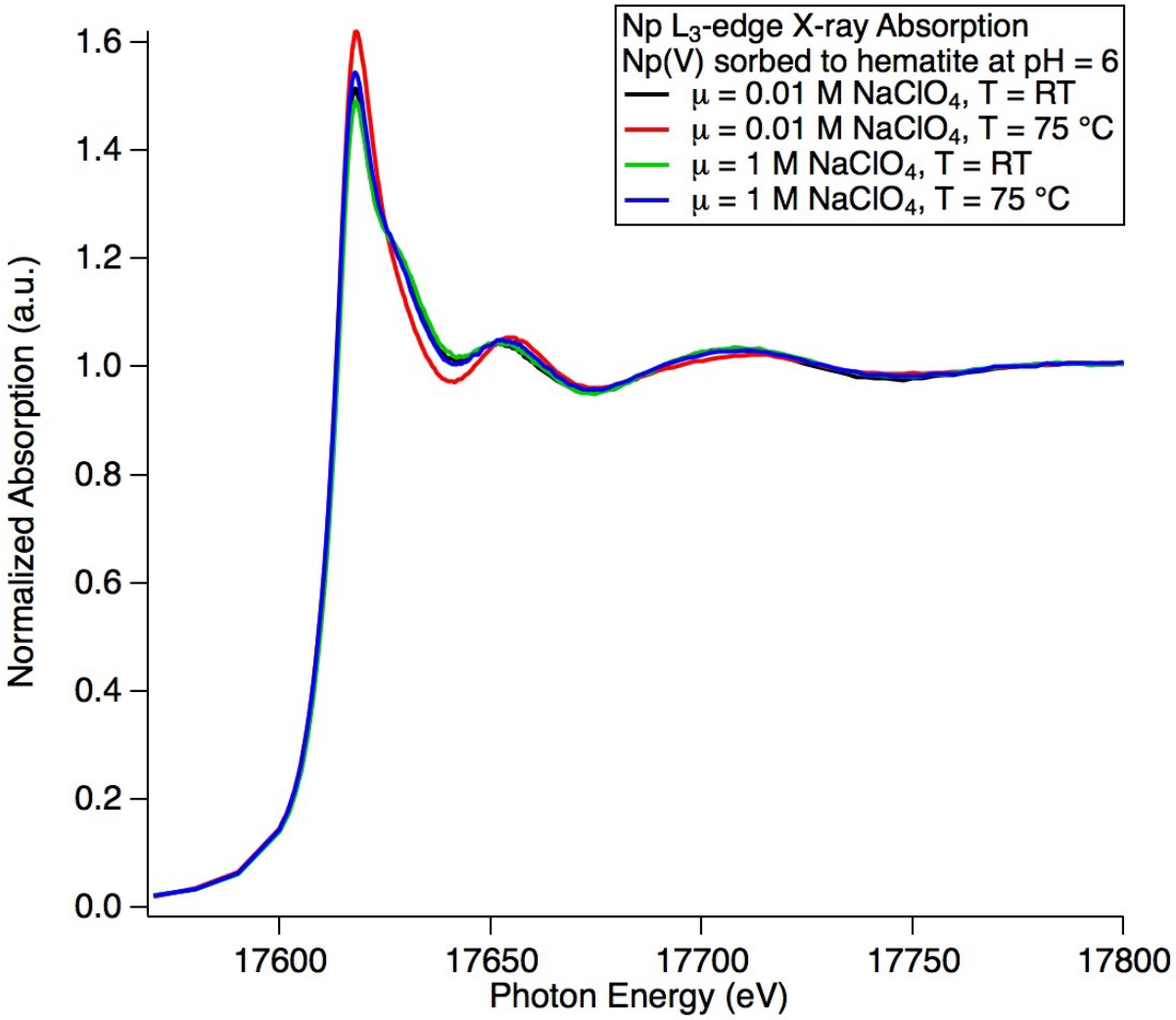


Figure 7.25: Normalized neptunium $L_{III}$-edge XANES spectra for Np(V) sorbed to hematite at pH 6 at room temperature and 75 °C and ionic strengths of 0.01 N $NaClO_4$ and 1 M $NaClO_4$.

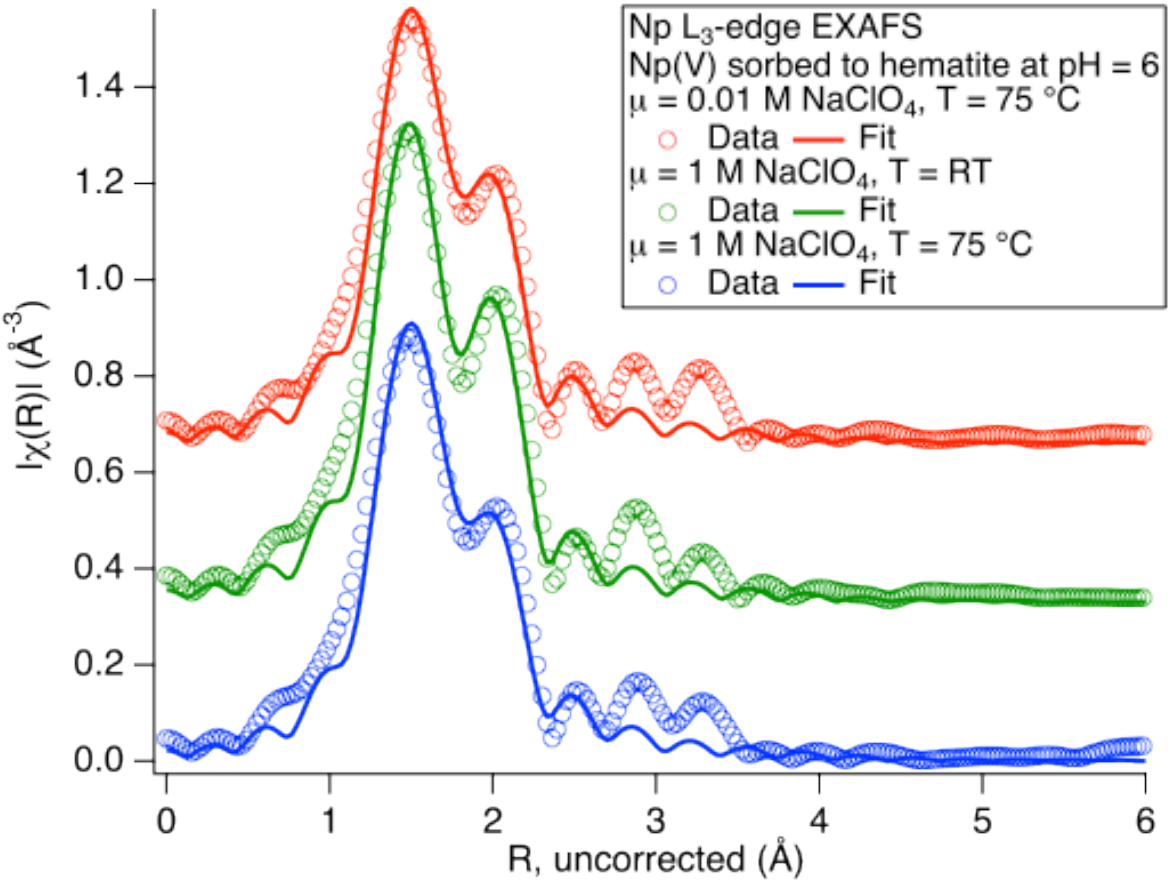


Figure 7.26: Fourier-transformed EXAFS spectra and fits of Np(V)-hematite samples at room temperature and 75 °C and low and high ionic strength. The data and best-fit models of the inner oxygen shells are shown for each set, offset for clarity.

| Parameter | μ = 0.01 M $NaClO_4$, T = RT | μ = 0.01 M $NaClO_4$, T = 75 °C | μ = 1 M $NaClO_4$, T = 75 °C |
|---|---|---|---|
| Energy shift, $E_0$ (eV) | 9.4 ± 2.2 | 8.3 ± 1.9 | 8.5 ± 2.2 |
| Axial oxygen amplitude | 2.0 ± 0.3 | 1.9 ± 0.3 | 2.0 ± 0.3 |
| Axial oxygen distance (Å) | 1.88 ± 0.01 | 1.88 ± 0.01 | 1.88 ± 0.01 |
| Axial oxygen, $\sigma^2$ ($Å^2$) | 0.0002 ± 0.0010 | 0.0004 ± 0.0015 | 0.0008 ± 0.0018 |
| Radial oxygen amplitude | 4.7 ± 1.0 | 5.0 ± 0.9 | 5.3 ± 1.2 |
| Radial oxygen distance (Å) | 2.47 ± 0.02 | 2.45 ± 0.02 | 2.45 ± 0.03 |
| Radial oxygen, $\sigma^2$ ($Å^2$) | 0.0066 ± 0.0034 | 0.0078 ± 0.0029 | 0.0098 ± 0.0040 |
| Goodness-of-fit, R-factor | 0.015 | 0.011 | 0.014 |

Table 7.2: Fitting results for the Np(V) hematite data sets shown in Figure 7.26. There were 12 independent points, and 7 variables in each fit. Uncertainties determined by inversion of the covariance matrix.

## 7.4 Discussion

The results from the batch sorption experiments of Np(V) on hematite show sorption increases as temperature increases. The correlation of increasing sorption with temperature has been reported for other actinides and lanthanides to mineral and clay surfaces. For example, Turner examined Np(V) sorption to montmorillonite, and experimental results and surface complexation modeling showed enhanced Np(V) at higher temperatures.[195] Lu *et al.* studied the interaction of plutonium with montmorillonite in J-13 well water from the proposed Yucca Mountain repository. An increase of ~40% in Pu(V) sorption to montmorillonite was observed as temperature increased from 20 °C to 80 °[201]. Greater sorption of Eu(III) to hematite was observed by Estes *et al.*[202] The effect of temperature for increased sorption could be attributed to a favorable entropy change as the hydrating waters around the neptunium cation are displaced.[203] Reactions that increase the disorder of a system are entropically-favored. Water in the bulk phase is less ordered than water molecules coordinated to an aqueous ion, so entropy would be gained during sorption as the hydrating waters are released from the ordered neptunium hydration sphere to the disordered bulk phase. Therefore, as temperature increases, entropy of the system increases, and so sorption is favored.

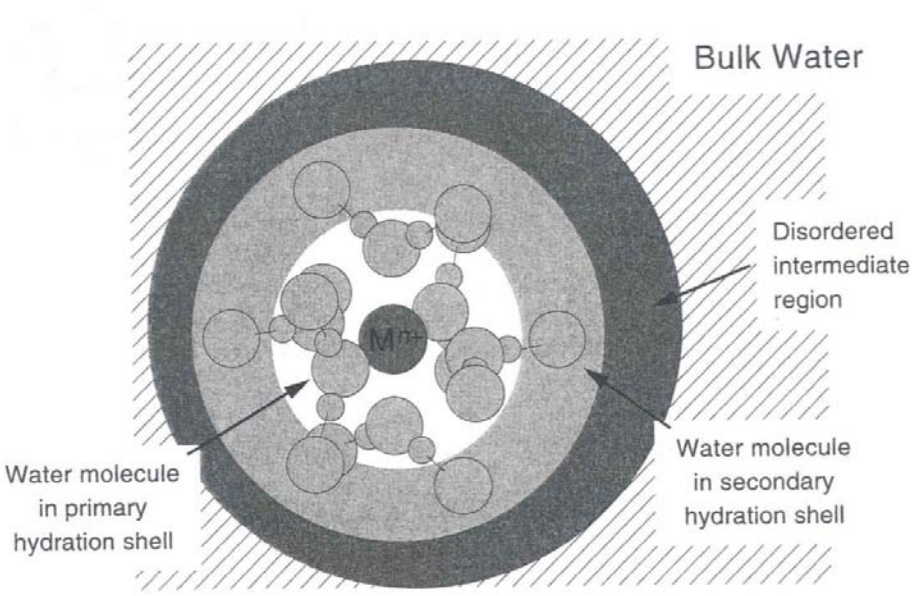


The increasing sorption of Np(V) on hematite with increasing temperature suggests the sorption reaction is endothermic. Additional studies to determine the thermodynamic parameters of the sorption reaction are strongly recommended. Knowledge of these parameters, such as the reaction enthalpies and entropies, would be greatly beneficial not only to fully understand the Np(V) sorption mechanism, but also for refinement of actinide sorption models and predicting actinide transport processes in the environment.

Sorption experiments conducted in solutions of different background ionic strengths is a method to differentiate between inner- and outer-sphere mechanisms.[204] The rationale behind this is that outer-sphere complexes are sensitive to changes in background electrolyte concentrations whereas inner-sphere complexes are not.[205] The sorption of weakly bound outer-sphere complexes can be reduced substantially, or even entirely suppressed, by an increase of ionic strength. Increasing a solution's ionic strength results in shielding the charged surface, this then disrupts the outer-sphere complexation, and thus causes outer-sphere complexes to become unbound ions in solution. On the other hand, inner-sphere complexes have no interaction with the background electrolytes and as such are not affected by changes in ionic strength.

Results from the batch sorption experiments presented in this study do not show ionic strength has an effect on Np(V) sorption to hematite, which suggests the Np(V)-hematite complex is an inner-sphere complex. This finding confirms a previous study by Kohler *et al.* where ionic strength was varied from 0.005 M $NaClO_4$ to 0.1 M $NaClO_4$ but no significant change in sorption was observed.[191] Hayes and Leckie also concluded that the insensitivity of cation sorption to differences in ionic strength is consistent with model calculations assuming inner-sphere surface complex formation.[206]

Lützenkirchen, in contrast, cautioned against drawing conclusions from the variation of sorption behavior with changes in ionic strength as an indication of inner-sphere or outer-sphere complexation.[207] Suggesting that the variation in sorption behavior with ionic strength is due to promotive effects, these are species in the aqueous or solid phase that are not taken into consideration in SCMs. If included in the model, these species might predict the increased

sorption with increasing ionic strength. As they are not accounted for, though, some sorption behavior may be deemed as outer-sphere complex formation when in fact inner-sphere complex formation is occurring. Also, a search of the literature did not find any spectroscopic evidence to support the theory that a change in sorption behavior with changing ionic strength is due to outer-sphere complex formation. While the results presented in this work so far suggest that Np(V) sorption to hematite occurs via an inner-sphere mechanism, outer-sphere complexation cannot be definitively excluded.

However, the increase of sorption as temperature increases, driven by positive changes in entropy, supports the assumption of inner-sphere complexation for Np(V) sorption to hematite. Changes within the primary hydration sphere of metal ions are associated with inner-sphere complexation on mineral surfaces. Release of coordinated water molecules from the hydration sphere of the metal ion is expected in order to accommodate space within the coordination shell for direct bonding to the mineral surface.[208]

Additionally, the assumption of inner-sphere complexation is strengthened by the XAS data presented in this study. EXAFS fits of Np(V)-hematite samples at room temperature and 75 °C and low and high ionic strength show no significant differences, suggesting inner-sphere sorption mechanism at work. Inner-sphere complexes have also been identified in previous neptunium studies. Kohler *et al*. investigated Np(V) sorption on hematite over a range of ionic strengths, pH conditions, Np(V) concentrations, and $CO_2$ partial pressures.[191] Similar to the results obtained in this study, the Np(V) sorption edge was observed at ~pH 7. Using the triple-layer model, which differentiates between inner- and outer-sphere surface species, Kohler *et al.* suggested that the dominant species below pH 8 is the inner-sphere surface complex, $\equiv FeONpO_2$, in the presence or absence of atmospheric $CO_2$. An additional second inner-sphere surface complex, $\equiv FeOHNpO_2^+$, was needed to accurately model the surface data at higher Np(V) sorption densities. Wang *et al.* modeled Np(V) sorption on hematite[189] using data published in a previous study by Nakayama and Sakamoto.[209] The modeling results suggested that two surface complexes best described the sorption data, $\equiv FeOHNpO_2^+$ and $(\equiv FeO)_2NpO_2^-$. Arai *et al.* investigated the interaction between Np(V) and hematite with EXAFS and suggested that both outer-sphere and bidentate inner-sphere surface complexes are present in the sorption samples at pH 7-9.[210] Using attenuated total reflectance Fourier-transform infrared spectroscopy (ATR FTIR), SCM, and EXAFS experiments, Müller *et al.* suggested that Np(V) forms inner-sphere bidentate complexes on the hematite surface, based on the large observed redshift of ~30 $cm^{-1}$ in the antisymmetric vibrational mode of the neptunyl ion. [211]

Desorption studies could reveal whether the sorption mechanism is based on inner- or outer-sphere complexation. Outer-sphere complexation is a result of electrostatic attraction between an ion and a charged surface, and the interaction is typically considered reversible. Formation of an inner-sphere complex is generally considered an irreversible process, as the ion becomes covalently bonded to the surface. An actinide ion, a hard Lewis acid, accepts electron pairs from anionic surface functional groups, consequently involving the release of protons from surface functional groups and the loss of a water molecule from the actinide's hydration sphere.[105,106] This is supported by previous plutonium studies to iron oxide minerals where sorption was ascribed to inner-sphere complexation. Desorption experiments revealed only a small fraction of plutonium was removed from the surface.[153,154,158,212–214] This suggests that desorption studies could determine whether Np(V) sorption to hematite is indeed via inner-sphere complexation, and future experiments focusing on the desorption behavior are recommended.

## 7.5 Conclusions

Additional studies are needed to further examine the Np(V) sorption process to hematite, especially focusing on the influence of temperature and ionic strength. This will provide necessary information of actinide migration through the environment and in geological repositories for nuclear waste. Nonetheless, overall, the data and analyses presented in this study support the following statements:

- Np(V) sorption to hematite is temperature dependent, as greater sorption was observed with increasing temperature.
- Sorption is hypothesized to be an entropy-driven reaction due to displacement of water molecules from the primary hydration sphere of the neptunium cation.
- Ionic strength does not have a significant effect on Np(V) sorption to hematite.
- Np(V)-hematite surface complex remains unchanged between room temperature and elevated temperature, as well as varying ionic strength.
- The sorption mechanism of Np(V) to hematite surface is assumed to be via inner-sphere complexation.

# 8. CONCLUSIONS

The primary focuses of this work was to investigate the sorption processes of plutonium and neptunium to goethite and hematite minerals, with the overarching objective to better understand actinide interactions in the environment. The combination of batch sorption experiments and XAS experiments, especially at variable temperatures and ionic strength, serve as an effective means to examine actinide sorption processes. Overall, this work has demonstrated the following:

- Plutonium exhibits a complex sorption behavior to both goethite and 1% Al-substituted goethite, with sorption equilibrium reached after 7 days of contact time. As plutonium sorbed to a mineral surface will be less mobile in the subsurface, the results highlight that the presence of goethite in the environment can minimize plutonium migration.

- Sorption of Pu(VI) to goethite and 1% Al-substituted goethite results in reduction to the more insoluble Pu(IV) oxidation state. Extent of plutonium reduction increased as solution pH increased, which is correlated with the transition across the PZC of the mineral. The complex sorption behavior and redox transformation suggest the sorption mechanism is surface-mediated reduction of Pu(VI) to Pu(IV) on the surface of iron oxide minerals goethite and 1% Al-substituted goethite.

- Np(V) sorption to hematite is temperature dependent, as greater sorption was observed with increasing temperature. This indicates that conditions of elevated temperature can contribute significantly to the retardation of Np(V) in geochemical environments where hematite is a major component. By extension, this suggests actinide sorption to iron oxide minerals will be favored at elevated temperatures, and the ubiquitous presence of iron oxide minerals in nature and presence of iron corrosion by-products in nuclear waste repositories may result in decreased migration of radionuclides through the environment.

- Displacement of the hydrating waters may be the driving force behind the increased sorption. This hypothesis is based on removal of water molecules from the primary hydration sphere to bulk water being an entropy driven reaction. The positive entropy change that occurs during the sorption reaction is due to the increased disorder in the system as water molecules move from a fully coordinated state in the neptunium hydration sphere to the more disordered state of bulk water.

- The effect of ionic strength on Np(V) sorption is not obviously apparent, indicating the sorption mechanism of Np(V) to hematite surface is based on the formation of inner-sphere Np(V)-hematite complexes. Spectroscopic measurements the Np(V) surface complex remains unchanged as temperature and ionic strength is varied, further supporting inner-sphere complexation.

The results presented in this work represent a step toward understanding the interactions of Pu(VI) and Np(V) with goethite and hematite, particularly the sorption processes at the solid/water interface. However, it is still evident that additional studies are needed to fully understand the sorption reactions. In particular is the case of plutonium reduction. Although many researchers have studied that sorption of plutonium to iron oxide minerals, and several studies have demonstrated the sorption may result from the stabilization of Pu(IV) surface species, the mechanism (or mechanisms) behind the Pu(VI) reduction upon sorption to goethite has not yet been identified. Future research efforts should also focus on examining the influence of temperature on sorption reactions across a wide range of experimental conditions, including, but not limited to, ionic strength, environmental material, and actinide. Studies to measure the thermodynamic and kinetic aspects are also recommended. Development of transport models through the environment and in nuclear waste repositories requires a thorough knowledge of the sorption mechanism coupled with thermodynamic and kinetic information. A comprehensive understanding of the plutonium and neptunium sorption processes to iron oxide minerals will improve the development of flow and transport models, which in turn will lead to a more reliable prediction of actinide migration in the environment.

This work is by no means a complete study of actinide behavior in the environment. It is, however, a significant contribution towards a thorough understanding of the interactions of plutonium and neptunium to iron oxide minerals goethite and hematite.

# A. RADIATION DETECTION AND MEASUREMENT TECHNIQUES

The following sections introduce and briefly explain the techniques used to measure and characterize actinides. For the quantitative determination of plutonium or neptunium concentration from solution aliquots, liquid scintillation counting was used. α and γ spectroscopy were essential to verify the purity of plutonium stock solutions and neptunium stock solutions after anion exchange columns were run, and optical absorbance spectroscopy in the visible and near-infrared (vis-NIR) range was used to verify oxidation state of working stocks prepared for batch sorption studies. X-ray absorbance spectroscopy (XAS) measurements provide information as to oxidation state and local coordination environment.

## A.1 γ Spectroscopy

γ spectroscopy

Similar to atomic levels, nuclei have discreet energy levels. Transitions between the nuclear energy levels produce the emission of photons in the energy range of ~10 keV to 10 MeV. When these emissions are detected, a γ ray energy spectrum can be produced, where the peaks correspond to the emitted γ ray from the transition between nuclear energy levels. A γ spectrum is characteristic of the individual radioisotopes present. For a comprehensive discourse on γ spectroscopy and γ ray detectors, refer to the textbooks by Tsoulfanidis and Landsberger[215], Knoll[77], and Leo[216].

Only a fraction of γ rays from a radioactive source interact with matter; many do not interact at all and simply pass right through. When a γ ray does interact with a detector, it is via one of three main mechanisms: photoelectric absorption, Compton scattering, and pair production. In photoelectric absorption, the incident γ ray deposits all its energy into the detector material, causing a bound electron from an inner shell to be ejected. The ejected electron has kinetic energy equal to the energy of the incoming γ ray minus the binding energy of the electron:

$$KE = E_{\gamma} - BE \qquad \text{Eq A.1}$$

where KE is the kinetic energy of the ejected electron, $E_\gamma$ is the photon energy, and BE is the binding energy of the electron. The photopeak of a γ spectrum is a result of the full γ ray energy being deposited.

Compton scattering is another way γ rays can interact with matter. This occurs when the incident γ ray does not deposit all its energy in the detector material. When the γ ray elastically scatters, only a portion of its energy is transferred to an electron. The energy loss to the electron during scattering is given by the Compton scattering equation:

$$\lambda' - \lambda = \frac{h}{m_e c}\left(1 - \cos\theta\right) \qquad \text{Eq A.2}$$

where λ and λ' are the wavelengths of the photon before and after scattering, *h* is Planck's constant, $m_e$ is the rest mass of an electron, *c* is the speed of light, and θ is the scattering angle of the photon. After collision, the scattered photon and recoil electron proceed in different directions. The scattered photon, which is greatly reduced in energy, produces the backscatter peak. It is also possible that the scattered photon escapes the detector. The maximum energy that can be transferred occurs if θ = 180°, which corresponds to the Compton edge in the γ spectrum. The energy of the recoil electron varies from a maximum at the Compton edge (when the photon backscatters) to zero (when the photon is scattered in the forward direction).

If a γ ray has sufficient energy, it can interact with the detector material through pair production. In this process, a γ ray with energy greater than 1.022 MeV can create an electron-positron pair (1.022 MeV being the rest mass energy of an electron and positron). Any γ energy in excess of this becomes kinetic energy of the electron and positron. With an abundance of electrons in any given system, the positron annihilates with an electron, producing two 511 keV γ rays. The creation, energy loss, and annihilation effectively occur instantaneously. These two annihilation γ rays can both be absorbed, one can escape the detector, or both can escape the detector. When both annihilation γ rays are detected, the total energy absorbed will be the original γ ray energy and the event would contribute to the photopeak. When one annihilation γ ray escapes, a single escape peak will appear 511 keV below the photopeak and is referred to as a "single escape peak". And when both annihilation γ rays escape, a double escape peak will appear 1.022 MeV below the photopeak.

Because of the different interactions of γ rays with the detector material, numerous features appear in a γ ray energy spectrum. Considering the fact that most radionuclides emit multiple γ rays, and samples may contain multiple radioisotopes, γ spectra can become very complex and interpretation of the spectra is often not straightforward.

γ ray detectors

The two main types of detectors used in γ spectroscopy are scintillation detectors and semiconductor detectors. Selection of which detector type to use depends on whether efficiency or resolution is sought after, as a detector with both high efficiency and high resolution is uncommon. The probability that a γ ray will interact with the detector and produce a count is the efficiency of the detector. Efficiency is mostly a function of crystal size and atomic number, Z, of the detector material. Efficiency increases with crystal size, as there is more area for ionizing radiation to interact with the detector material. However, large crystals of the required purity are difficult to grow and very costly. Detector materials with higher Z have higher efficiency, as the probability of a γ ray interacting with matter increases with Z. In contrast, resolution varies based on detector type and the particular properties of the detector material.

The most common scintillation detectors are thallium-doped sodium iodide detectors, often referred to as NaI detectors. Light is emitted when ionizing radiation, either a γ ray or X-ray, interacts with the NaI crystal, where the intensity of light produced is proportional to the energy deposited by the γ ray. The emitted photons are collected by a photomultiplier tube (PMT) that converts the light into electrons and then amplifies the electrical signal. The main advantage of NaI detectors is the high efficiency, due to the ability to produce large NaI crystals and the high Z of iodine (Z=53). Other benefits of this detector type include its relatively inexpensive cost and robustness, making NaI detectors ideal for field work. However, NaI detectors have poor energy resolution (~7% for a 661 keV γ ray).[77]

Semiconductor detectors, also called solid state detectors, are able to measure individual photons and the associated photon energy. For a solid state detector, the crystal is a semiconductor material, usually germanium or silicon. Because of the narrower band gap in a semiconductor compared to an insulator, electrons are easily excited into the conduction band, and subsequently produce an equal number of positive charge, or "holes", in the valence band. Semiconductors can be electron rich (n-type) or hole rich (p-type) materials, usually germanium or silicon. Semiconductor detectors operate on the basis of p-n junctions. When n-type and p-type materials are brought into contact, a small electric field is formed. A depleted region is created at the junction, and this depleted region is the active region of the detector. High voltage can be applied across the junction, increasing the width of the depletion region, and thus an increased active region means a higher efficiency (Figure A 1). When ionizing radiation, either a γ ray or X-ray, passes through the depleted region, it interacts with the detector crystal and generates electron-hole pairs. Diffusion of the charge carriers begins, as electrons are attracted to the positive side and holes to the negative side. The applied bias sweeps these charges from the crystal to the pre-amplifier and the resulting electrical signal is amplified and registered as a single count. The amplitude of the pulse is proportional to the charge collected, which is proportional to the energy deposited by the ionizing radiation into the depleted region of the detector. Figure A 2 shows a schematic diagram of a p-n junction in a semiconductor detector.[215]

The efficiency of semiconductor detectors increase with crystal size, but large crystals of the required purity are difficult to grow and very costly. Small Ge and Si crystals limit the amount of detector material available for ionizing radiation to interact with, meaning semiconductor detectors have relatively low efficiency. The efficiency decreases non-linearly with photon energy. Additionally, the lower Z of the germanium (Z=32) and silicon (Z=16) lowers the probability of γ ray interaction. In spite of the low efficiency, semiconductor detectors have high resolution (~0.2% for a 661 keV γ ray)[77], significantly higher energy resolution in comparison to NaI detectors. The resolution of a semiconductor detector is related to the number of charges collected, and so the small band gap of semiconductors (0.75 eV for Ge, 1.2 eV for Si) results in high resolution because there are more ionizations per photon interaction. (The resolution also increases with photon energy, but is superior to that of solid scintillator detectors at all γ energies.) Because of the small band gap, however, cryogenic temperatures are required to operate high purity germanium (HPGe) detectors. HPGe detectors are held near 77 K (usually achieved with liquid nitrogen) to minimize detector noise caused by thermal fluctuations. Additionally, formation of charge carriers can permanently destroy the resolution of semiconductor detectors; HPGe detectors easily become damaged if allowed to warm up to room temperature while high voltage is applied.

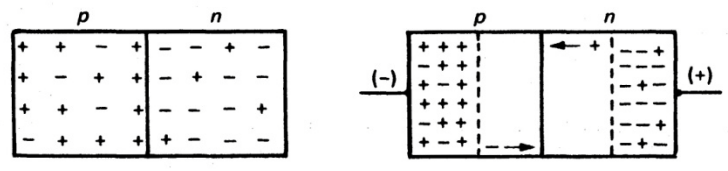


Figure A 1: A p-n junction without applied voltage and a p-n junction with applied voltage that results in the depleted region. Taken from Tsoulfanidis and Landsberger.[215]

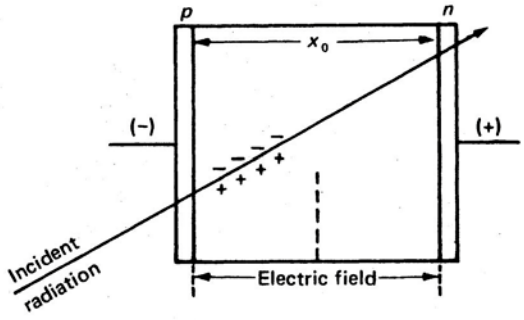


Figure A 2: A diagram of a p-n junction in a semiconductor detector, with applied voltage that results in the depleted region. Taken from Tsoulfanidis and Landsberger.[215]

## A.2. α Spectroscopy

α decay is the most common mode of decay for heavy radioisotopes (Z > 82). α spectroscopy is used to identify radioisotopes based on their emitted α particles.

By far, the most commonly used semiconductor detectors used for α spectroscopy are surface barrier silicon diode detectors. Semiconductor detectors were described previously in Appendix A.1. Silicon diode detectors are named as such because the p-n junction acts as a diode. Current is readily conducted if high voltage is applied in the forward direction, little if applied in the reverse direction. Applying a reverse bias at the p-n junction gives the depleted region. This depletion region, only a few millimeters thick (<5 mm)[216], is the active region of the detector. Because of the larger band gap (1.2 eV) than germanium, silicon detectors do not require cryogenic cooling. However, the resolution is slightly lower than HPGe detectors, but is still superior to that of scintillator detectors.

Surface barrier detectors consist of a pure n-type silicon crystal with a thin gold contact. It is necessary to allow the silicon surface to oxidize slightly before depositing gold. The gold and oxide layers make up a dead layer that forms the p-n junction. Having the depleted region right at the surface of the detector is ideal for detection of α particles, which do not travel far through any medium. Additionally, only a thin layer of gold is deposited to reduce the amount of energy lost by the α particle before it enters the depleted region.

One of the disadvantages of surface barrier detectors is their sensitivity to light. During operation, these detectors must be shielded from visible light as electron-hole pairs can be created by photons that interact with the silicon crystal. Also, surface barrier detectors are held under vacuum. Because of the short range of α particles in air, vacuum is applied to minimize α particles being readily absorbed. This allows for more efficient detection of α particles and increases detector resolution. Incomplete vacuum, loss of α energy during movement through the sample material or dead layer, and incomplete charge collection all result in detection of a lower energy than the actual α energy. This explains why the peaks of α spectra are not Gaussian but have a tail on the low energy side.

The following procedure describes how α plates were prepared for the experiments described in this work. A stainless steel plate is cleaned with acetone and heated on a hot plate. (Platinum will yield nicer spectrum and are the preferred substrate, but is costly.) A small volume (2-10 μL) of the sample solution is dropcast onto the center of the plate and evaporated.

The plate is heated for an additional few minutes on the hot plate to burn off other constituents in the sample. The drop cast method works well for solutions of low ionic strength and low acid concentration, so solutions with high salt and/or acid content were diluted prior to taking the aliquot.

## A.3 Liquid Scintillation Counting

Liquid scintillation counting (LSC) is a technique to measure radioactive elements that decay by α or β emission. Compared to the other radiation detection methods mentioned above, there are many advantages to using LSC: high efficiency, ease of sample preparation, and relatively short count times required (5-60 mins). Reference the textbooks by McDowell & McDowell[217] and Tsoulfanidis and Landsberger[215] for a complete treatment of LSC.

For LSC samples, an aliquot of radioactive solution is mixed with a scintillation cocktail in a translucent vial. Though the exact contents of scintillation cocktails are proprietary, they contain solvent, phosphor molecules (scintillators), and sometimes wavelength shifters (secondary scintillators). The solvent absorbs the energy of the emitted particle, either α particle or β particle, and then passes that energy to the phosphors and the scintillator then converts the captured energy to light. Typical solvents used in LSC are planar aromatic molecules such as toluene or anthracene. The high conjugation of the solvent molecule provides good absorption of the particle's energy and is also usually passed between solvent molecules until passed to a neighboring phosphor molecule. Due to the short distance the α or β particle travels in solution (on the order of mm) before encountering a solvent molecule, and the continual passing of energy between solvent molecules to a phosphor molecule is what gives the high efficiency of LSC, as it is highly unlikely the energy will be lost. The phosphor molecules undergo electronic excitations and release photons as they deexcite. The converted light usually has wavelength ~400 nm or less, so secondary scintillators absorb the fluorescence of the primary scintillators and re-emit it at a longer wavelength to be better measured by the PMT. A simplified schematic of LSC is shown in Figure A 3.

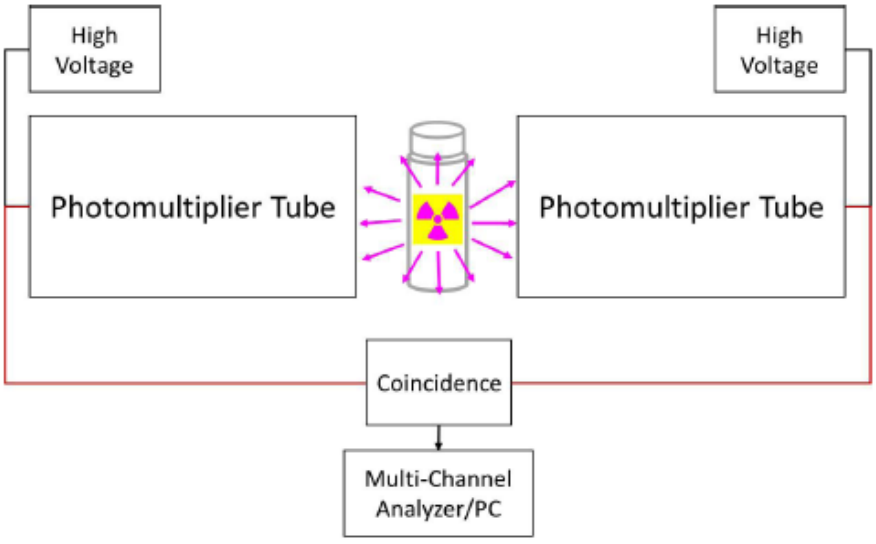


Figure A 3: Schematic of a liquid scintillation counter. Provided by Dr. Jennifer Shusterman.

Though the energy of an α or β particle will excite more than one solvent molecule, because of the short mean path of the particle ( 1 mm), all the energy is lost to solvent molecules contained to a very small area. The solvent molecules pass the energy to surrounding scintillators in a very small area, and each scintillator emits only a single photon characteristic of the phosphor molecule, and so all excitations originating from the α or β particle will be measured with sufficient simultaneity to register as just a single pulse of light that has the number of photons proportional to the path length of the emitted particle, which is in turn proportional to the energy of the particle. Ultimately, the response of the PMT can be correlated to the energy of the original radiation.

LSC efficiency is based on how well the emitted energy of the α or β particle is converted to light, which depends on the scintillation cocktail, sample solution, and type and energy of radiation. Low energy β particles have low efficiency (< 1%), but in the case of higher energy α particles, efficiency is generally considered to be 100%.[77] Though the PMT will not be able to measure all the produced photons, the energy of the α particle is sufficient to create enough photons that the signal will not be diminished. Efficiency can be lowered if other substances are present in the sample that absorb the energy of the radiation before being converted to light or the light is absorbed before it reaches the PMT. These processes are known as chemical quenching and color quenching, respectively. The reduced number of photons measured at the PMT results in a shift in the spectrum. Correcting for quenching can be achieved by use of an internal standard, external standard, or by using the amount the spectrum shifts. Fortunately, quenching is usually not an issue for samples that α decay due to their high particle energy relative to that of β particles.

To differentiate between α and β particles in LSC, pulse shape analysis (PSA) is applied.[77,218] While energy discrimination alone can be used, issues can occur when high energy β particles are mistakenly detected as α particles. In LSC, when an α or β particle is detected, there are two components to the pulse: 1) prompt and 2) delayed. Depending on the particle type, the relative duration of each of these components varies and can thus pulse duration is used to differentiate the type of particle. For β emissions, the prompt component lasts about 2-8 ns, and the delayed can last up to 900 ns, whereas α particles have a longer delayed component.[219] Additionally, PSA can be employed to discriminate between actual signals as opposed to background from cosmogenic sources interacting with the vials; however it is far more effective for α discrimination.

## A.4 Optical Absorbance Spectroscopy

Optical absorbance spectroscopy, often referred to as UV-vis spectrophotometry, measure the absorption of light as it passes through a sample of fixed length. The Beer-Lambert Law states that the absorbance of a solution is directly proportional to the concentration of the absorbing species in the solution and the path length. For one photon wavelength, Beer's Law is given by:

$$A = -\log_{10}\left(\frac{I}{I_0}\right) = \epsilon c l \qquad \text{Eq A.3}$$

where $A$ is the absorption, $I_0$ is the intensity of the incident light, $I$ is the transmitted intensity, $\epsilon$ is a constant known as the molar absorptivity or extinction coefficient, $c$ is the molar

concentration of the solution, and *l* is the path length the light travels through. Absorption is a unitless value, so the extinction coefficient has units of $M^{-1}cm^{-1}$. Thus, for a fixed path length (the standard path length is 1 cm), optical absorbance spectroscopy can be used to determine the concentration of the absorber in a solution.

The oxidation states of various actinide solutions were determined using an OceanOptics S2000 fiber optic spectrometer. A diagram of the setup is shown in Figure A 4. Light from a combined tungsten/halogen lamp (LS-1), a versatile white light source optimized for the visible and near-infrared (vis-NIR) energy range, travels through a fiber optic (shown in blue) and passes through a filter (when applicable), the sample, and then to the spectrometer. The filter was used to attenuate some light so that the intensity going through the sample was appropriate to be able to measure absorbance. The diode-array detector of the S2000 records the absorbance on all selected wavelengths within a spectral range of 350-1000 nm simultaneously, but in practice, the region below 450 nm was very noisy and deemed unreliable. To minimize noise, an integration interval of 10 s was employed for each absorbance measurement. Additionally, the lamp was always turned on at least 30 mins before collecting spectra to avoid any artifacts caused by temperature fluctuations. Prior to measuring each actinide solution, reference light and dark spectra were collected. The reference was measured with a cuvette containing only the background electrolyte; the dark was measured by blocking all light. The instrument's software subtracts the reference light spectra from the sample spectra. Solutions were placed in quartz cuvettes with a 1 cm path length, and the sample holder has an opaque black cover to shield the sample from ambient light.

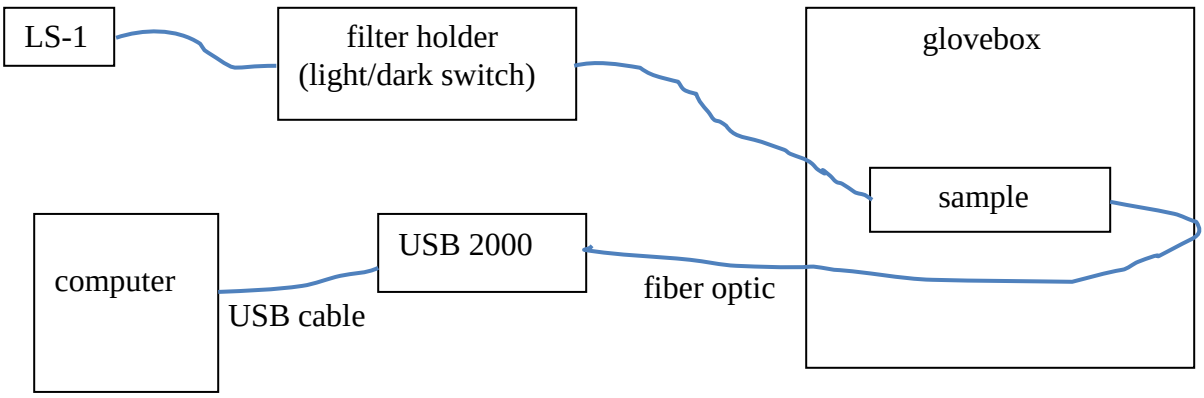


Figure A 4: Schematic diagram of vis-NIR spectrometer setup used for optical absorbance spectroscopy. Adapted from Dr. Paul Ellison.

The sharp peaks and relatively low extinction coefficients of actinide ions result from the dipole forbidden f-f electronic transitions. For all actinide ions, both the highest occupied molecular orbital (HOMO) and the lowest unoccupied molecular orbital (LUMO) are f orbitals, and f-f transitions are forbidden by the azimuthal quantum number ($\Delta l = \pm 1$) and Laporte ($g \rightarrow u$) electric dipole selection rules. However, the extinction coefficients observed for spin-allowed, Laporte forbidden f-f transitions are higher than those typical for similar d-d transitions of transition metal complexes. The selection rules are slightly relaxed due to increased spin-orbit coupling, which is a relativistic effect as the electrons' radial velocity

increases with Z. It is the absorbance in the visible region that gives the distinctive colors of early actinide solution.

It is important to use a background electrolyte that does not complex with the actinide of interest. The perchlorate anion ($ClO_4^-$) is used as a non-complexing background electrolyte for measurements in the vis-NIR energy range described in this work. Perchloric acid has been shown to not form solution complexes with the uranyl cation, $UO_2^{2+}$,[220] so by analogy, suggests complex formation does not occur with the plutonyl cation, $PuO_2^{2+}$.

## A.5 X-ray Absorption Spectroscopy

XAS uses high energy X-rays* to probe the core electronic structure and coordination environment of atomic species. XAS is a powerful technique that provides element-specific information about the local coordination environment of a system, and is particularly useful for studying environmental contaminants at low contaminant concentrations (< 1%).[25,79,80] One of the primary advantages of XAS is the ability to study systems *in situ*, allowing for direct and nondestructive measurements without influencing the system. Below is an introduction to XAS, including a brief discussion of the theory behind XAS and the practical setup to conduct XAS. The seminal text by Teo[221] and textbooks by Stern[180] and Bunker[199] provide detailed discussion of the theory and experimental considerations of XAS and its related components.

XAS refers to the measurement of the X-ray photoabsorption coefficient μ(E), which describes how strongly X-rays are absorbed as a function of incident X-ray energy *E*. An incoming photon of sufficient energy ejects a bound electron from a core-level shell of a target atom, and the ejected electron interacts with electrons of the surrounding atoms. The equation defining the quantitative relationship between the photon, the ionization energy of a bound electron, and the kinetic energy of the ejected electron is given by Einstein in his Nobel Prize winning paper on the photoelectric effect:[222]

$$h\nu = IE + \frac{1}{2} m_e v^2 \qquad \text{Eq A.4}$$

where $h\nu$ is the energy of the incoming photon, *IE* is the specific ionization energy of an electron in a particular orbital, $m_e$ is the rest mass of an electron, and $v$ is the velocity of the photoelectron.

A sample absorbs X-ray by the following equation:

$$I = I_0 e^{-\mu x} \qquad \text{Eq A.5}$$

where $I$ is the intensity of the transmitted photon, $Io$ is the incident photon energy, $\mu$ is the absorption cross-section of the material, and $x$ is the thickness of the material. Figure A 5 shows a plot of the absorption cross-section for plutonium.[223,224] Generally, the absorption decreases smoothly as the energy increase. However, there are sharp discontinuities in the absorption

* X-rays and γ-rays have similar properties, but the distinction between the two come from their origins and energy ranges. γ-rays are emitted from nuclei, decaying from excited states to states of lower energy. X-rays are emitted from the electron shell of atoms, usually electrons passing from states of higher energy to those of lower energy. X-rays are also produced when electrons are slowed down in the field of nuclei, and this phenomenon is known as "bremsstrahlung". Though there is an overlap in the energy range, X-rays range in energy from 100 eV to 150 keV, whereas γ-rays have energies of 10 keV to $10^4$ MeV.

spectrum called absorption edges. These edges coincide with the photoionization of core-level electrons. The corresponding electrons that result in the $L_I$, $L_{II}$, and $L_{III}$-edges of the actinides are the 2s, $2p_{1/2}$, and $2p_{3/2}$ orbital electrons, respectively.

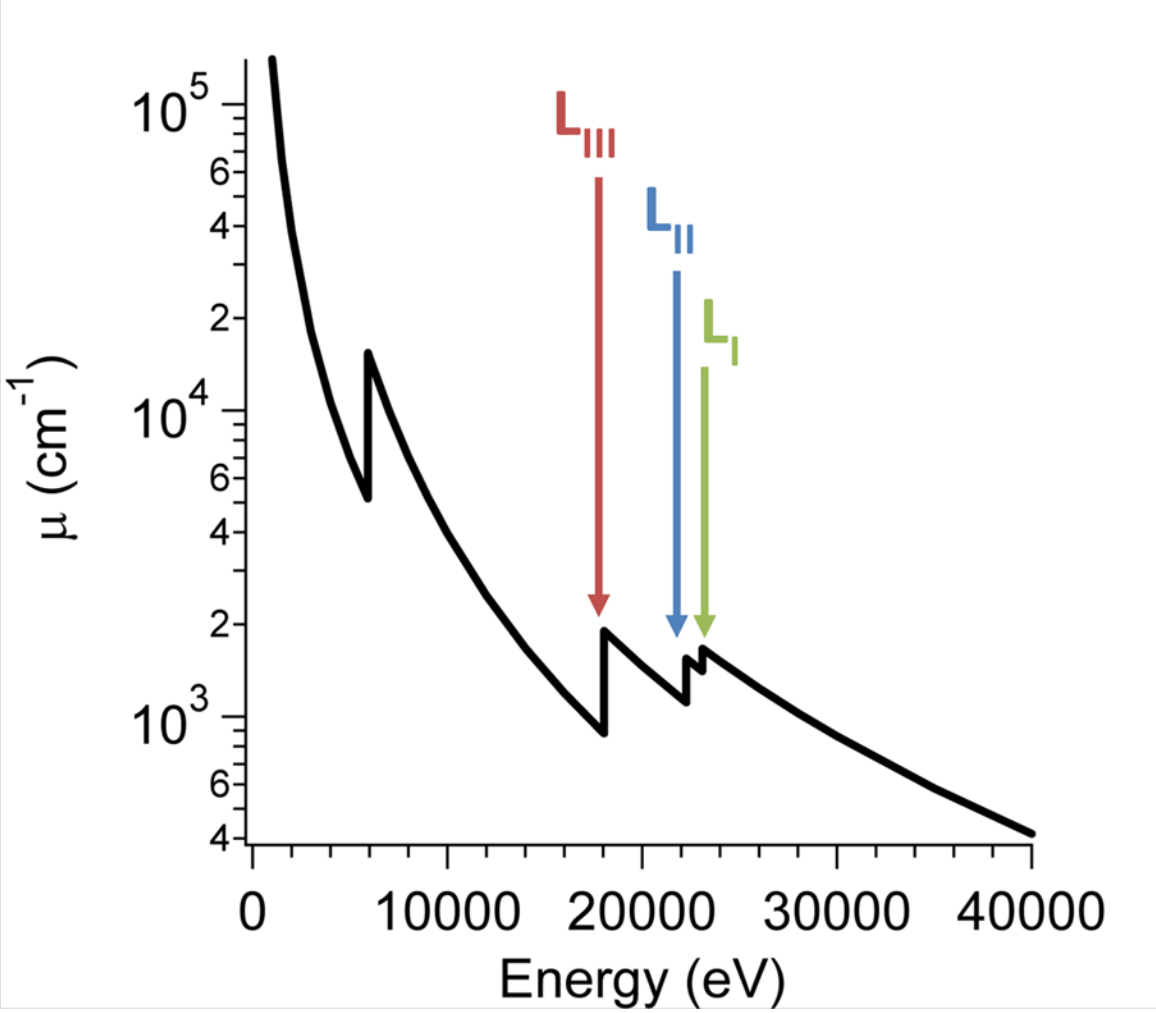


Figure A 5: Log plot of X-ray absorption cross-section as a function of photon energy for plutonium. The $L_I$-edge, $L_{II}$-edge, and $L_{III}$-edge positions arise due to photoelectrons in the 2s and 2p orbitals. Fine structure is not shown. Data from McMaster X-ray cross-section tables.[224]

XAS includes both XANES and EXAFS. When working with lighter elements, XAS is sometimes referred to as near-edge X-ray absorption fine structure (NEXAFS) spectroscopy. However the two spectroscopies (XANES and NEXAFS) are a result of the same physical phenomenon and both terms can be used interchangeably.

XANES

Figure A 6 takes a closer look at the $L_{III}$-edge shown in Figure A 5. The absorbance spectrum shows a sudden increase in absorbance, which corresponds to the binding energy of the electron, followed by energy oscillations at higher energies. The observed fine structure at the

photoabsorption edge was first described by Kossel in 1920.[225,226] It was referred to as the "Kossel structure" but nowadays, the main peak in the absorption spectrum is referred to as the "absorption edge" or colloquially as the "white-line". The XANES region is generally considered between 5 eV below to about 150 keV above the edge. The absorption cross-section, $\mu$, is a function of incident photon energy and can be calculated from first principles using Fermi's so-called Golden Rule:

$$P_{if} = \frac{2\pi}{\hbar}\left| f|V(t)|i \right|^2 \bullet \rho_f(E) \qquad \text{Eq A.6}$$

where $P_{if}$ is the probability per unit time of a transition occurring from the initial state, $|i\rangle$, to the final state, $|f\rangle$, given a perturbation, $V(t)$, and the final state density of states, $\rho_f(E)$. Note that for XANES spectra, $|f\rangle$ describes an unoccupied bound state of the system.

For high Z materials such as the actinides, the very short core-hole lifetime causes spectral broadening, resulting in the loss of sharp structure. This effect is beneficial to actinide chemists who use the position and shape of the $L_{III}$-edge as a measure of the actinide oxidation state, independent of the local molecular structure.[25] This can only be achieved because of the core-hole broadening (in accordance with the uncertainty principle) found in these elements. Because XANES arises from transitions to bound states in the system, XANES measurements are a direct method to determine the electronic structure of the atom and density of states at and around the absorption edge.

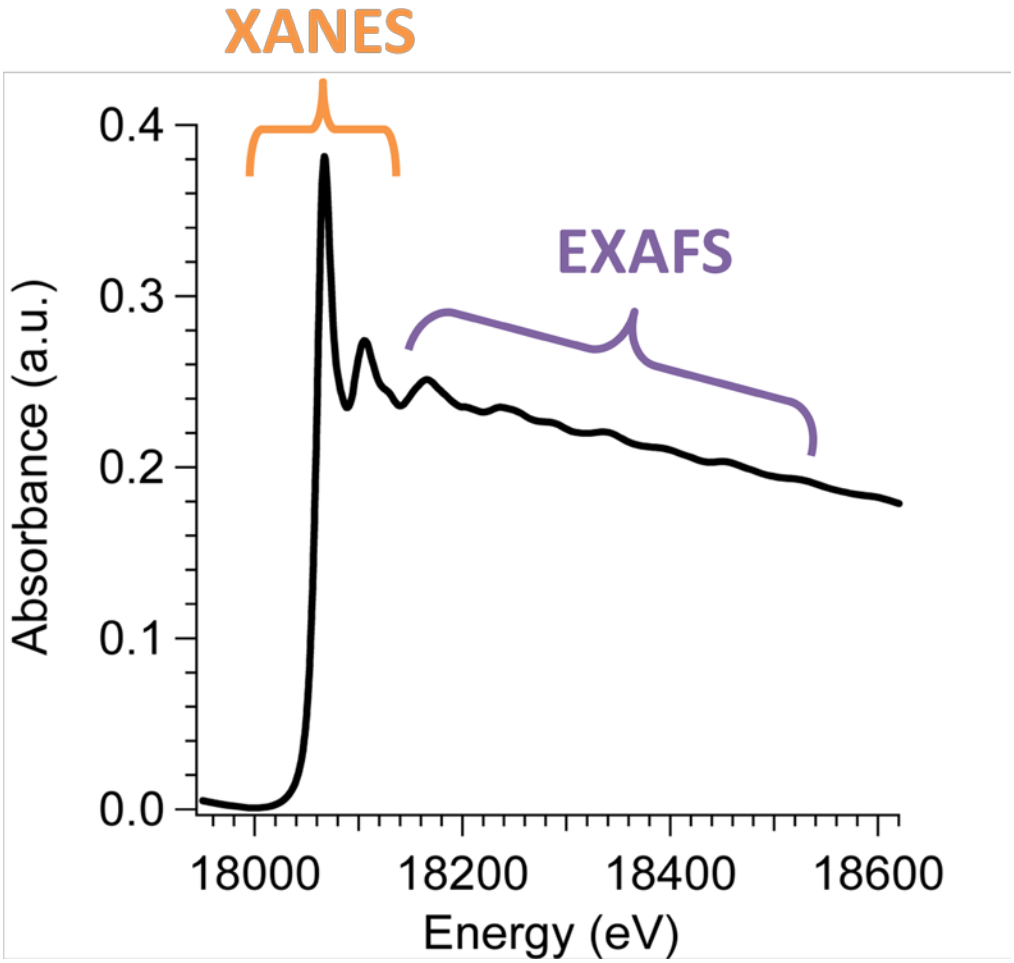


Figure A 6: XAS spectrum of the $L_{III}$-edge of plutonium with the XANES and EXAFS regions labeled.

XANES measurements provide a direct, nondestructive *in-situ* method of measuring a sample's oxidation state.[25,60,149] The $L_{III}$-edge of the actinides corresponds to the $2p_{3/2} \rightarrow 6d$ electronic transition. The exact photon energy required for excitation, however, depends on the electronic structure of the whole system, which takes into account the atom's oxidation state. For an actinide ion, changes in oxidation state correlate with changes in the electron occupancy for the 7s and/or 5f orbitals.[*] The electrons in these valence orbitals have a nonzero probability of being closer to the nucleus than the electron in the $2p_{3/2}$ orbital, and as such, the 7s and/or 5f electrons partially shield the $2p_{3/2}$ electron. Shielding means the $2p_{3/2}$ electron feels a smaller effective nuclear charge which results in a smaller Coulombic attraction between the nucleus and the $2p_{3/2}$ electron. This smaller attractive force results in a lower energy X-ray required to eject the $2p_{3/2}$ electron and the XANES absorption edge is shifted to lower energies. An increase of oxidation state means electrons are removed from the valence orbitals, resulting in lesser ability

[*] The electronic configurations of plutonium and neptunium are $[Rn]7s^25f^6$ and $[Rn]7s^25f^5$, respectively.

to shield the $2p_{3/2}$ electron from the nucleus. With a larger effective nuclear charge, the Coulombic attractive force between the nucleus and the $2p_{3/2}$ electron is greater, meaning a higher energy X-ray is required to eject the $2p_{3/2}$ electron and so the XANES absorption edge is shifted to higher energies. Therefore, as the oxidation state increases, the position of the XANES absorption edge increases to higher energy.

EXAFS

Various fine structures are present in the absorption spectrum at energies about the white line. The oscillations were first described by Kronig in 1931.[227,228] At the time, the feature was referred to as the "Kronig structure". Figure A 6 shows the region in the XAS spectrum commonly referred to as EXAFS, about 100 eV to 2000 eV above the edge. However, there is no specific point that divides the XANES and the EXAFS regions. In fact, the EXAFS region blends into the XANES region all the way up to the absorption edge, and as such, the same structural information is contained in both the XANES from the EXAFS portions of the XAS spectrum.

The oscillations shown in Figure A 6 are a result of changes in the absorption cross-section as a function of energy, caused by scattering from neighboring atoms. Just as with XANES, the fine structure can again be described from first principles using Fermi's Golden Rule (Eq A.6). The difference, however, is that for EXAFS, the final state,$|f\rangle$, describes the continuum state where a photoelectron exists in the field of the probed atom with one positive charge.

EXAFS spectra come from interference of the ejected photoelectron with neighboring atoms, and thus contain information about the molecular coordination environment. Most of the EXAFS oscillations are accounted for by the ejected photoelectrons being backscattered by a single neighboring atom back towards the central atom, referred to a single-scattering path. However, the spectra also contain significant contributions from multiple scattering paths, especially for the actinyl ions.

Much trepidation is taken with EXAFS, as interpreting EXAFS spectra can be complicated, both in processing the data and in determining a hypothetical model to fit the data. The EXAFS oscillations are given by:

$$\chi(E) = \frac{\left(\mu(E) - \mu_0(E)\right)}{\mu_0(E)} \qquad \text{Eq A.7}$$

where $\mu$ is the measured XAS absorption and $\mu_0$ is the absorption coefficient of the atom in its environment within the sample but without scattering from neighboring atoms, which can be considered the background. Background subtraction is performed in the pre-edge and post-edge regions, followed by normalization of the absorption edge to a value of 1. The energy threshold $E_0$ must then be estimated. Often the energy value of the first inflection point on the absorption edge is used, though another approximation to $E_0$ is the energy where the absorption is halfway of the edge. This is simply an initial guess, and further refinement of $E_0$ occurs later in the data analysis process. Finally, a cubic spline is fit above the absorption edge and subtracted out to remove background effects.

Once the EXAFS oscillations are properly isolated, the data is converted from energy-space (units of eV) to *k*-space (units of $Å^{-1}$). This conversion is to consider the

wavevector of the ejected photoelectron instead of the energy of the photoelectron. The wavevector (*k*) of the ejected photoelectron is:

$$k = \sqrt{\frac{2m_e}{\hbar^2}\left(E - E_0\right)} \approx \sqrt{0.2628\left(E - E_0\right)} \qquad \text{Eq A.8}$$

where $E_0$ is the ionization energy of the ejected core-level electron, $E$ is the energy of the emitted photoelectron, and $m_e$ is the rest mass of an electron. The first part of Eq A.8 uses constants given in SI units, whereas the second part converts them to atomic units, which vastly simplifies calculations. The EXAFS spectrum, $\chi(k)$, is conventionally weighted by $k^3$ and then usually Fourier transformed into *r*-space. This yields a plot with the abscissa representative of distance to neighboring atoms and magnitude related to the number of neighboring atoms at that distance. It is important to note that peaks in the *r*-space plot do not correlate exactly with the bond distances of neighboring atom shells, as the Fourier transform of $k^3 \cdot \chi(k)$ is not a radial pair distribution function (rPDF). The Fourier transforms (FTs) represent a pseudo-radial distribution function of the atom's near-neighbor environment, where peaks representing the near neighbors appear at lower R values relative to their true distance from the central atom depending on the phase shift of the backscattering atom.

The Debye-Waller factor, $\sigma^2$, is a measure of the disorder associated with the system. It has two components which account for the effects of thermal and static disorder.[180]

$$\sigma^2 = \sigma_s^2 + \sigma_T^2 \qquad \text{Eq A.9}$$

At low temperatures, the thermal contribution to the Debye-Waller factor should be minimal, so a good approximation of the Debye-Waller factor is then a measure of only the static component at 30 K.

Figure A 7 shows the EXAFS spectra of $PuO_{2(s)}$ in both *k*-space and *r*-space. Representing the data in *k*-space or *r*-space is equally valid because the same information is contained in either plot. However, EXAFS spectra in *r*-space provide a more intuitive representation of the data, where peaks correspond to groups of atoms at different distances. It is visually easier to see that there are 2 shells of atoms around each central plutonium atom in $PuO_{2(s)}$. The first shell at ~1.8 r + Δ (Å) is a shell of oxygen atoms and the second shell at ~3.8 r + Δ (Å) is a shell of plutonium atoms.

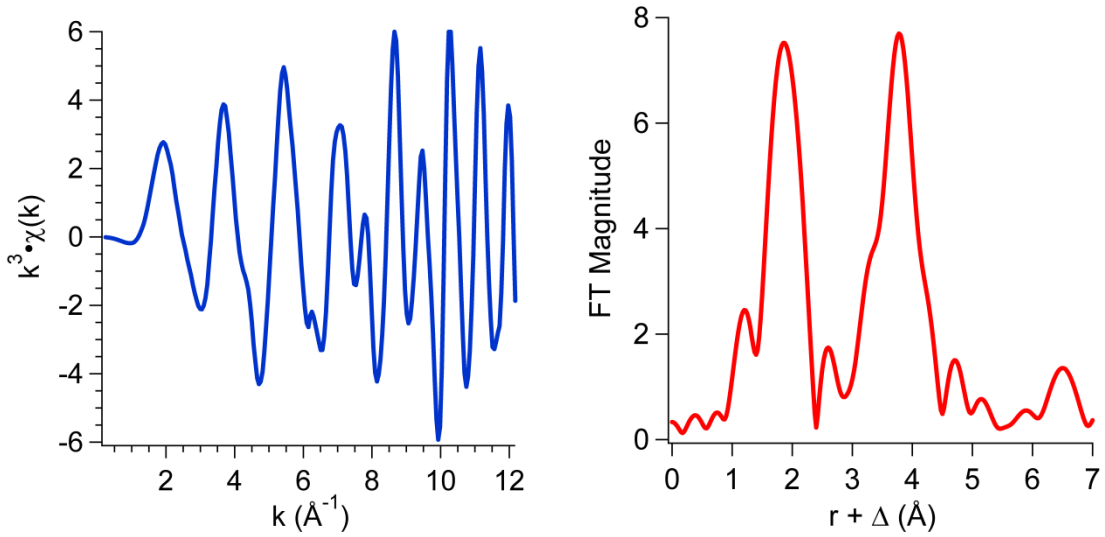


Figure A 7: Plot of the EXAFS oscillations for $PuO_{2(s)}$ in (a) *k*-space and (b) the Fourier transform in *r*-space.

XAS Beamline Setup

XAS can be conducted in regular laboratories using conventional X-ray sources, but more often, experiments are carried out at large synchrotron user facilities. Synchrotrons provide high intensity X-ray beams with narrow energy dispersion, necessary for collecting quality spectra in a timely manner. In this section, the apparatuses and setups to conduct XAS is presented.

Synchrotron radiation is electromagnetic radiation emitted by electrons as they travel at relativistic speeds along a curved path. Electrons travel at relativistic speeds in the storage ring of a synchrotron. As electrons pass through an insertion device (bending magnets, wigglers or undulators), the trajectory of the electron beam oscillates back and forth, causing electrons to accelerate and emit electromagnetic radiation. White light is generated but monochromatic light is ideal for XAS measurements. Much of the white light is filtered away with a silicon double-crystal monochromator, which uses Bragg diffraction to select light of a desired energy. The monochromator crystals are rotated to an appropriate angle to allow photons of only a certain energy through.

XAS is typically measured in several modes: transmission, fluorescence, and electron yield. For the XAS experiments described in this work, transmission mode and fluorescence mode was used. Transmission mode is the most straightforward, where the X-ray flux is measured before and after the beam passes through a sample. Figure A 8 shows a schematic for a typical beamline setup to collect XAS data in transmission mode. The white light from the synchrotron passes through the monochromator, resulting in photons of a certain energy. The X-rays are then redefined by x-y collimating slits and pass through the first ionization chamber, conventionally called $I_0$. The photon flux measured at $I_0$ is considered the initial photon flux before any X-ray absorption with the sample has occurred. The X-rays are then directed to and consequently interact with the sample. Any photons that are not absorbed or scattered then pass

through the second ionization chamber, conventionally called $I_1$. Absorbance is calculated with Beer's Law and the ratio between $I_0$ and $I_1$:

$$\mu x = \ln\left(\frac{I_0}{I_1}\right) \qquad \text{Eq A.10}$$

where $\mu$ is the linear absorption coefficient of the material and $x$ is the thickness of the sample. When collecting data in transmission mode, the sample is usually positioned normal to the X-ray beam. This geometry exposes the maximum amount of sample to the X-ray beam. Notice the similarity between Eq A.10 and Beer's Law for vis-NIR spectroscopy. Often times a reference sample is collected at the same time for energy calibration purposes. In this case, the reference sample is placed between the second and third ionization chambers (conventionally called $I_1$ and $I_2$). The absorption spectrum for the reference is given by:

$$\mu x = \ln\left(\frac{I_1}{I_2}\right) \qquad \text{Eq A.11}$$

Using the setup shown in Figure A 8, it is possible to collect two sample XAS spectra in transmission mode concurrently. This is normally not done, however, because beam attenuation occurs as the X-ray beam traverses the sample in the first position and greatly reduces the photon flux. Furthermore, inhomogeneities or artifacts in the sample in the first position could affect the data collected for the sample in the second position. Concern is not taken if this occurs with a standard placed in the second position because often the standard is simply used for energy calibration, which does not require high quality data.

In fluorescence mode, the incident flux $I_0$ and the fluorescence photons $I_f$ are measured. Fluorescence X-rays are emitted when higher energy electrons decay to fill the core-level holes left by the ejected photoelectrons. Measuring fluorescence is helpful when working with trace elements in the measured sample. Additionally, the signal-to-noise ratio is improved. The XAS beamline setup is almost identical to that of transmission mode with the exception of an added fluorescence detector placed 90° with respect to the X-ray beam, directed at the sample (Figure A 9). When collecting data in fluorescence mode, the sample is usually rotated 45° with respect to the beam, in order that fluorescence photons emitted from the sample are not blocked by the sides of the sample holder.

The fluorescence detector can be an energy insensitive detector, such as a Lytle detector (not discussed) or an energy resolving detector, such as a semiconductor detector. The benefit of energy resolving detectors is the ability to separate fluorescence photons by energy and only count fluorescence photons of certain energy. Energy discrimination also allows for differentiation of fluorescence photons from other elements in the sample and elastic scatter of the incident X-ray beam by the sample. Semiconductor detectors are immensely useful when working with environmental samples. Similar to the detectors used in $\gamma$ spectroscopy, HPGe detectors were used to measure X-ray fluorescence in XAS.

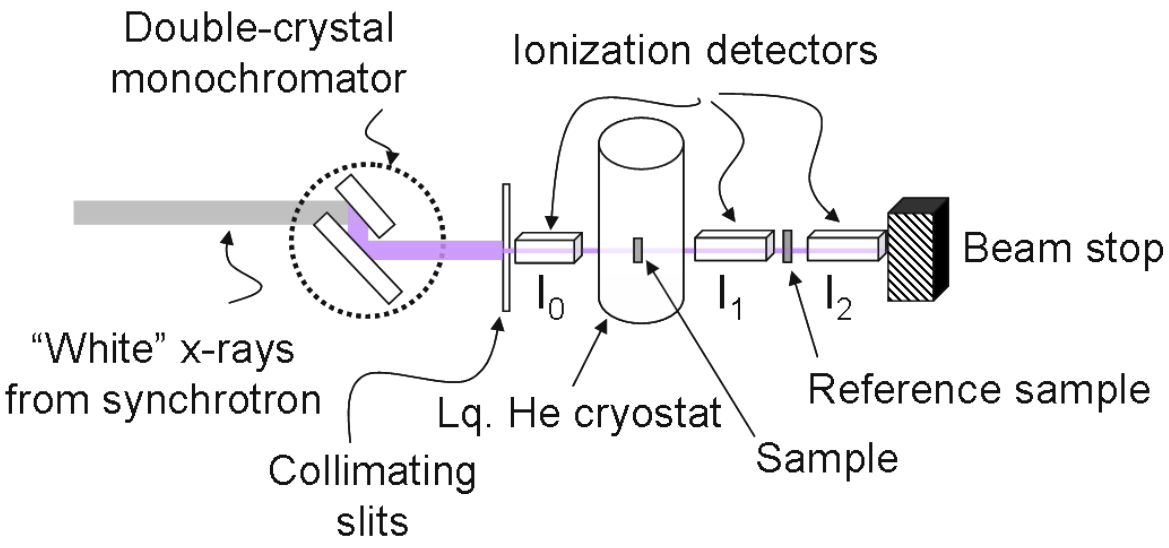


Figure A 8: Schematic of a typical experimental beamline set-up for XAS collection in transmission mode. Provided by Dr. Yung Jin Hu.

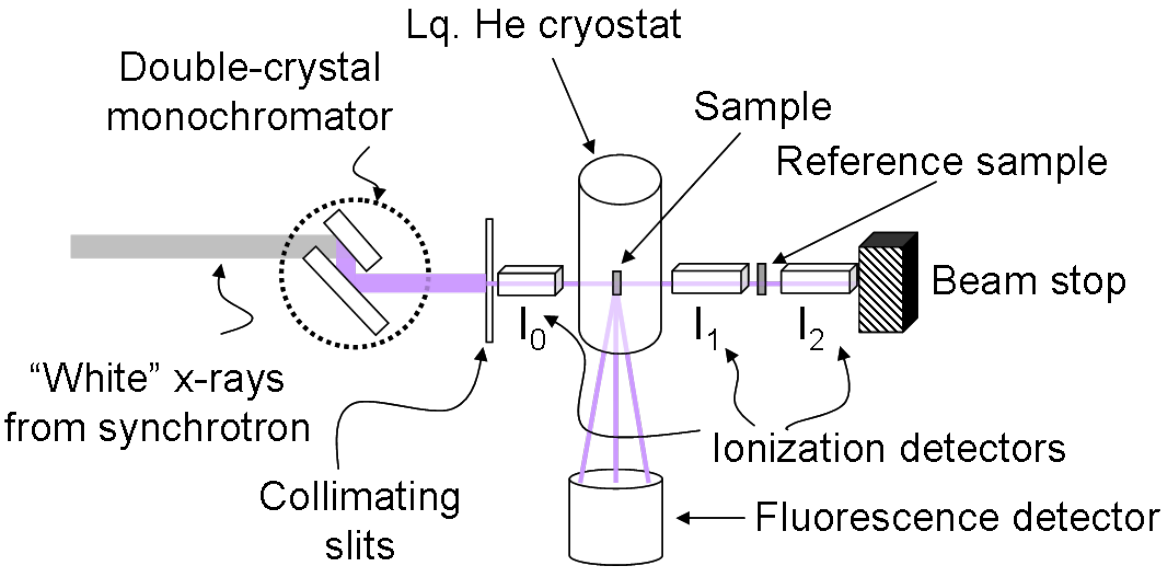


Figure A 9: Schematic of a typical experimental beamline set-up for XAS collection in fluorescence mode. Provided by Dr. Yung Jin Hu.

# B. ANION EXCHANGE

## B.1 Ion Exchange

Ion exchange is one of the most common radiochemical separation techniques due to its high selectivity and the ability to perform separations rapidly[*]. Ion exchange involves a solid material (resin) that can reversibly bind and release ions from a solution with no substantial change in the structure of the resin. Ion exchange resins are typically porous, crosslinked polystyrenes with attached functional groups. Commercially available resins are typically copolymers of styrene and divinylbenzene, which contain either sulfonic acid or quaternary ammonium groups. The divinylbenzene is added to produce crosslinking between the polystyrene chains, giving the polymer a three-dimensional structure that increases its rigidity. Attached to the resin is the active group that binds the exchangeable ions; the ion-active group is immobile and fixed to the polymer. Most cation exchangers (such as Dowex 50) contain free sulfonic acid groups, $SO_3H$, where the cation replaces the hydrogen ion. The polymer beads of anion exchangers (such as Dowex 1) are functionalized with quaternary amine groups, such as $CH_2N(CH_3)_3Cl$ where the anion replaces the chloride ion. The resins are generally manufactured in the form of small spherical beads, with resin particles having diameters of 0.08-0.16 mm and exchange capacities of 3-5 meq per gram of dry resin.

Commercially available resins commonly used in actinide chemistry are the Dowex and BioRad brands. BioRad takes Dowex resin and purifies it, so BioRad resin is cleaner than Dowex resin.

The ion exchange process usually involves a solution that is run through a column packed with resin beads. Ions to be separated are sorbed onto the resin. In a later step, these ions can be removed from the resin by elution with another suitable solution. Complexing agents, which form complexes of varying solubility with the absorbed ions, are used as eluants. Interaction of metal ion with resin not only depends on the ion-exchange equilibrium, but also the metal/ligand equilibrium. Separations are often performed using the fact that different metals form complexes at different strengths. A competition occurs between the complexing agent and the resin for each ion, and each ion will be exchanged between the resin and the complexing agent several times as it moves down the column, akin to a distillation process. The rates at which the different ions move down the column vary, resulting in spatial separation between "bands" of different ions. The ions can then be collected individually in successive eluant fractions.

The effectiveness of a separation between the solution and the ion exchange resin can be calculated using the distribution constant:

$$K_D = \frac{\text{Activity (per g solid)}}{\text{Activity (per mL liquid)}} \qquad \text{Eq B.1}$$

Conveniently, as $K_D$ is a ratio of two values, there is no need to worry about the background or efficiency of a detector, as the terms will cancel out. Working with radioactive material allows the measurement of a particular radionuclide both in solution and attached to the ion-exchange resin, as the activity of the radionuclide is directly proportional to the concentration.

[*] The field of ion exchange chromatography was significantly developed during the Manhattan Project when the need arose for an efficient process to chemically separate similar rare earth elements using ion exchange columns.

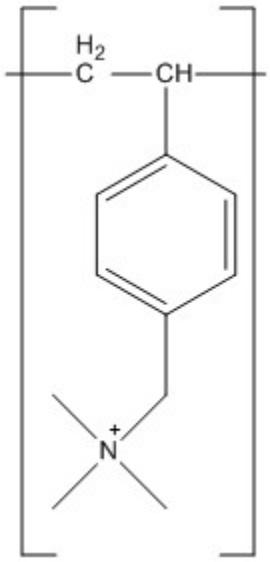


Figure B 1: The molecular structure of the anion exchange resin, BioRad AG 1-X8, which has trimethylbenzylammonium as the ion active group.

$$\left[MCl_x\right]^-_{(aq)} + \left[R\cdots N\left(CH_3\right)_4\right]^+ Cl^-_{(s)} \rightleftharpoons \left[R\cdots N\left(CH_3\right)_4\right]^+ \left[MCl_x\right]^-_{(s)} + Cl^-_{(aq)} \qquad \text{Eq B.2}$$

where $N(CH_3)_4^+$ is the ion active group that is bound to the resin, $[R\ldots N(CH_3)_4]^+$ is the resin, $[MCL_x]^-$ is the metal-chloride anion complex of unknown charge, and $Cl^-$ is the exchangeable ion.

## B.2 Dissolution of $PuO_{2(s)}$

As the $PuO_2$ powder is "weapons grade", it consists of at least 93% Pu-239, but small amounts of other plutonium isotopes are present. The largest chemical impurity to contend with is Am-241, which grows in from the decay of Pu-241 (a β emitter, half-life of 14.3 y). Anion exchange is used to separate and purify Pu-239 from Am-241 and other transuranic impurities.

An aliquot of the highly concentrated dark green Pu(IV) solution was evaporated to dryness over low heat in the custom boiling flask. The perchlorate acid fumes were captured with the bubbler system. The residue was reconstituted in 0.5 mL concentrated $HNO_3$.

## B.3 Experiments with Plutonium

All manipulations of plutonium were performed in a negative pressure glovebox in equilibrium with air. When heating, refluxing, and boiling, plutonium solutions were contained in a custom-made Teflon boiling flask with a long arm that connects to a bubbler system. A gentle, continuous flow of high-purity $Ar_{(g)}$ enters at the neck of the flask and makes its way through the arm, and continues through a series of three bubblers, filled with water, 7 M NaOH, and water, respectively. This was done to prevent the accumulation of hot acid vapors inside the glovebox and to contain perchlorate.

Perchloric acid must be handled with extreme caution. Many perchlorate salts and compounds are sensitive to shock and are explosive when dry at elevated temperatures. Hot perchloric acid is a very strong oxidizer, and any trace organic material in contact with perchloric acid at elevated temperatures can cause explosions. All acids and bases, particularly hydrofluoric acid (HF) are corrosive and should be handled only after proper training.

## B.4 Anion Exchange of Plutonium

Ion exchange is used to separate plutonium from fission products, lanthanides, and other transuranic impurities. Plutonium readily sorbs to cation exchange resins. Retention of plutonium by cation exchange resin decreases with increasing acid concentrations, and because metal speciation does not vary much at low acidities, cation exchange is infrequently used to purify or separate plutonium. Tetravalent plutonium readily forms anionic complexes, but trivalent actinides do not form anionic complexes in high acid conditions (10-12 M HCl or 7-8 M $NO_3$). This difference is advantageous to separate radionuclides, as plutonium can by eluted from an anion exchange column by reduction to Pu(III), removing trivalent actinides while Pu(IV) remains stuck to the column, or controlling the acidity.[*]

The anion exchange resin used in this separation procedure, BioRad AG 1-X8, has trimethylbenzylammonium as the ion-active group (Figure B 1) formed by a copolymerization of styrene and 8% divinylbenzene. Because the resin is $Cl^-$ form, the exchange of anions is between chloride ions from the resin and metal complex anions in solution. That is, the metal-chloride complexes in solution will attach to the $[N(CH_3)_4]^+$ group and $Cl^-$ will be exchanged for the anion complex. Other details about this resin are as follows: 100-200 mesh which indicates a particle size of 106-180 μm and the capacity is 1.2 mmol/mL.

An anion exchange column was packed with Bio-Rad AG 1-X8 resin (reformed in nitrate) and then conditioned with 8 M $HNO_3$. The plutonium solution was carefully loaded onto the column in as small a volume as possible. The Pu(IV) is bound to the resin as a dark green band of $Pu(NO_3)_6$. The vial containing the plutonium solution is rinsed with 8 M $HNO_3$ and the vial washings are added to the column. The column is then washed with 8 M $HNO_3$ to remove Am-241, which is present in solution as the daughter product of Pu-241 After the plutonium solution was loaded on, the column was washed with several free column volumes of 10 M HCl. When the HCl reaches the green band, it turns pink in color, as the Pu(IV) species changes to the plutonium chloride species. The 10 M HCl removes any lanthanides and fission products from the column. Pu(III) was then slowly eluted from the column with a 9:1 mixture of concentrated HCl and freshly distilled HI. Finally, the column is washed with 1 M HCl to remove any remaining tetravalent actinides. The reduction reaction of Pu(IV) to Pu(III) by $I^-$ is shown below, a flow chart of the anion exchange procedure used is shown in Figure B 2, and the fractions collected from the column are described in Figure B 3.

Note: the anion exchange procedure performed in this work rely on the stronger complexation of An(IV) by $NO_3^-$ and $Cl^-$ anions than any other oxidation state and the displacement of nitrate anion by the chloride anion in the Pu(IV) complex. High separation factors are achieved with this anion exchange procedure, but come at the detriment of being a

[*] In practice, elution of plutonium by reduction to Pu(III) works well in all concentrations of HCl, but $HNO_3$ is too oxidizing. Pu(IV) can be eluted in dilute $HNO_3$(<0.5 M) because only neutral complexes form at low nitrate concentrations.

complicated and messy micro-scale procedure, as the resin is destroyed by the HI and cannot be reused.

After anion exchange, the fraction containing $Pu(III)Cl_3$ in the HCl/HI mixture was refluxed with concentrated $HNO_3$. The HI was boiled away, and repeated evaporations of the eluent over low heat in the boiling flask were performed, redissolving each time with concentrated $HNO_3$ to ensure any organic material is digested. The final residue was reconstituted in 500 µL of concentrated $HClO_4$ and boiled a final time to ensure plutonium is completely oxidized to Pu(VI). The perchloric acid fumes were captured with the bubbler system.

$$2Pu^{4+} + 2I^{-} \rightleftharpoons 2Pu^{3+} + I_2 \qquad \text{Eq B.3}$$

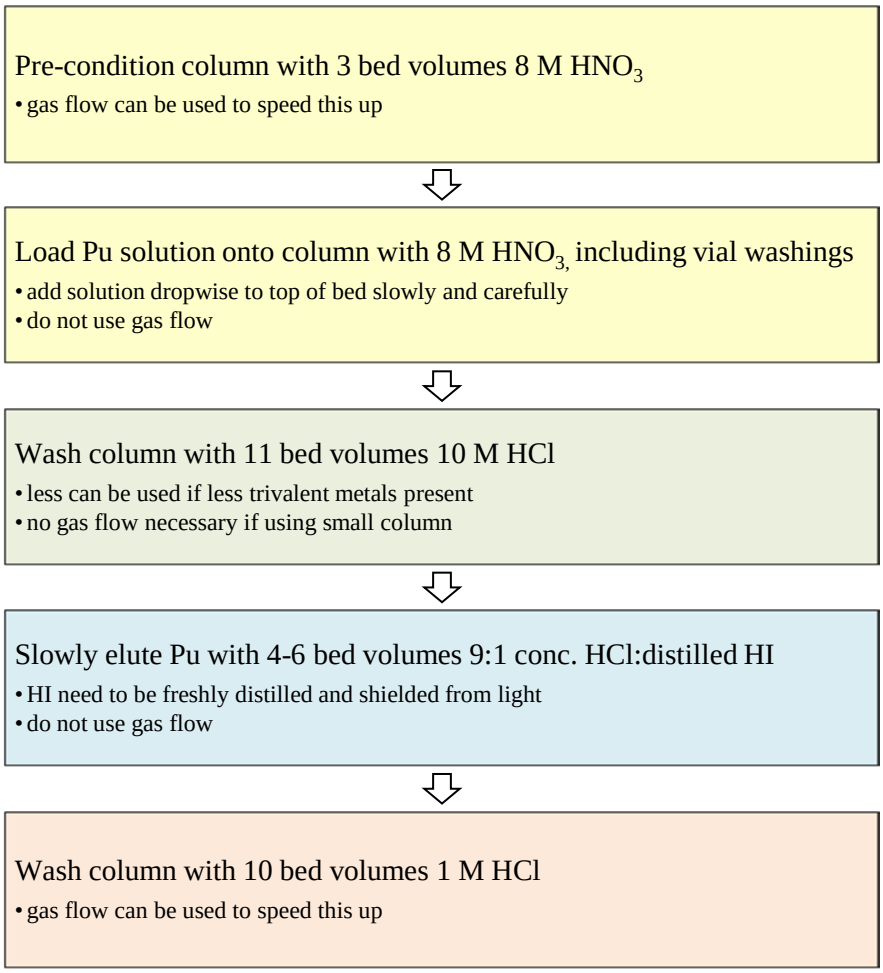


Figure B 2: Flow chart describing the anion exchange procedure used for plutonium purification.

| Fraction | Description |
|---|---|
| Fraction 1 | Contains Am-241 and other metals in oxidation states other than +4 that do not form anionic complexes in 8 M $HNO_3$. Any Pu(III), Pu(V), or Pu(VI) present in the loading solution will also elute here. Fraction 1 is slightly yellow colored. |
| Fraction 2 | Contains all non-tetravalent species that did not elute in Fraction 1 in 10 M HCl. Many bed volumes are used if the amounts of non-plutonium species in the loading solution are unknown or known to be high (ex: a $LaF_3$ co-precipitation was performed). Less bed volumes (3-4) could be used if the loading solution was relatively pure. It is important to completely flush out the $HNO_3$ from the previous steps. Fraction 2 is clear. |
| Fraction 3 | Contains $Pu(III)Cl_3$ in 9:1 conc. HCl:distilled HI mixture. The HI reduces Pu(IV) to Pu(III) and quickly becomes $I_2$ and $HI_3^-$, causing the resin to turn dark reddish-brown. As $Pu(III)Cl_3$ elutes from the column, the drops are blue colored. |
| Fraction 4 | Contains U(IV), Np(IV), and any other tetravalent species that were not reduced by $I^-$ in 1 M HCl. Also contains tailings from the plutonium band. Fraction 4 is yellow-brown colored, due to trace HI on the resin. |

Figure B 3: Description of the four fractions collected from the anion exchange procedure used for plutonium purification.

## B.5 Experiments with Neptunium

Anion exchange of neptunium was performed in a negative pressure glovebox in equilibrium with air. A duplicate setup of the boiling flask and bubler system described for plutonium manipulations was used when heating, refluxing, and boiling neptunium solutions. Batch sorption experiments and preparation of XAS samples were performed on the benchtop under atmospheric conditions.

## B.6 Anion Exchange of Neptunium

Various methods based on ion-exchange chromatography have been used for the separation of neptunium ions.[91] Np(IV) and Np(VI) form anionic chloride or nitrate complexes in aqueous solutions containing high concentration of chloride or nitrate ions ($Np(NO_3)_6^{2-}$ and $NpCl_6^-$). The complexes strongly sorb to anion exchange resins at 7-8 $HNO_3$.

To reduce the amount of daughter product Pa-233 and remove any transuranic impurities, a concentrated neptunium solution was purified using anion exchange. The separation procedure used in this work is based on the procedure by Hursthouse *et al.*[229] Np-237 was received as a mixture of Np(V)/Np(VI) in 1M $HClO_4$. The pentavalent and hexavalent oxidation states were confirmed using vis-NIR spectroscopy. The solution was boiled to dryness and the residue was dissolved in 1 M $HClO_4$. The neptunium hydroxide was precipitated with an excess of 10 M NaOH. The precipitate was then dissolved in 9.3 M $HNO_3$ and an excess of ferrous

sulfamate ($Fe(NH_2SO_3)_2$) was added to the neptunium solution. This reduces Np(VI) to Np(V) while Pa(V) remains in the pentavalent state. The solution was then headed for 30 min at 55 °C. This heat kill step oxidizes excess Fe(II) to Fe(III) and is necessary to minimize excessive gassing in the column.

An anion exchange column was packed with Bio-Rad AG 1-X4 resin (50-100 mesh which indicates a particle size of 106-180 μm, reformed in nitrate) and then conditioned with 8 M $HNO_3$. The neptunium solution was carefully loaded onto the column in as small a volume as possible. The Np(IV)-nitrate complex ($Np(NO_3)_6^{2-}$) can be seen in the green band at the top of the column. The vial containing the neptunium solution is rinsed with 8 M $HNO_3$ and the vial washings are added to the column. The column is then washed with 8 M $HNO_3$ to remove Pa(V), which is present as the daughter product of Np-237. Fe(III) is eluted with 5.5 M $HNO_3$ and finally Np(IV) is eluted from the column using 0.3 M $HNO_3$. A flow chart of the anion exchange procedure used is shown in Figure B 4.

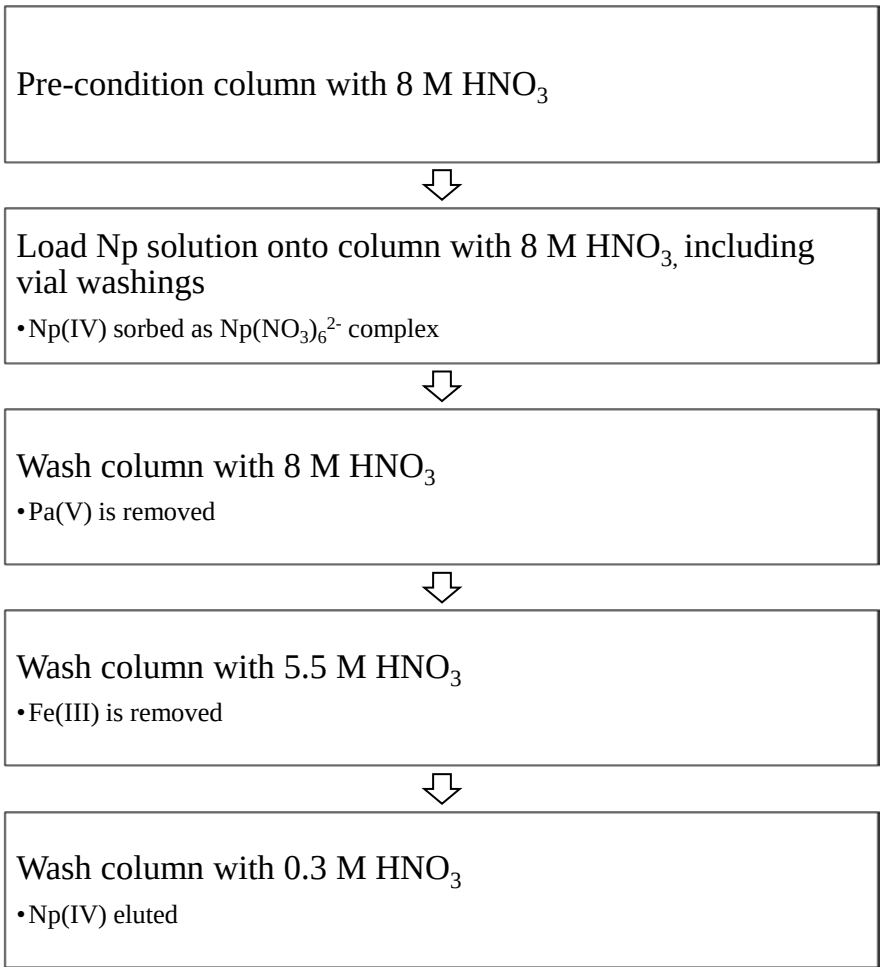


Figure B 4: Flow chart describing the anion exchange procedure used to separate Pa(V) and Fe(III) from neptunium solution.

# C. ELECTROCHEMISTRY

## C.1 Making Ag/AgCl Electrodes

A three-electrode cell consists of a reference electrode, a working electrode, and a counter electrode. The reference electrode is commonly a Ag/AgCl electrode, which has a redox potential of +0.196 V versus the SHE at 25 °C.[230] Ag/AgCl electrodes can be easily constructed with a handful of materials that are commonly available in labs: a Ag/AgCl wire, a glass pipet, a rubber septum, a Vycor frit, and heat shrink tubing.

Making a Ag/AgCl wire simply requires silver wire, NaCl solution, and a battery. The appropriate wires are attached to a galvanostat and immersed in 3 M NaCl. In this three-electrode cell, a Ag/AgCl electrode is the reference electrode, silver wire is the working electrode, and platinum wire is the counter electrode (Figure C 1). To plate AgCl onto the silver wire, the galvanostat should be set to -5 μA and allowed to react for several hours.

To make the electrode body of a Ag/AgCl electrode, a glass pipet is cut length (~5 cm) and the ends are fire polished. It is helpful to flair out the glass at the end of the electrode body, to better attach the glass frit with the heat shrink tubing. A thirsty glass frit (Vycor) is cut (~3-4 mm) and attached to the electrody body with heat shrink tubing. This frit allows for electrical contact between the fill solution inside the reference electrode and the outside solution. The AgCl-coated silver wire is carefully threaded through a rubber septum and placed into the glass electrode body. Figure C 2 shows a schematic for assembling the reference electrode.

Common electrode fill solutions include saturated KCl (~3.5 M) and 3 M NaCl. Because the experiments described in this work often use perchlorate, and the insoluble $KClO_4$ solid could form at the electrode junction and block the glass frit, 3 M NaCl fill solutions were used to avoid precipitation of $KClO_4$.

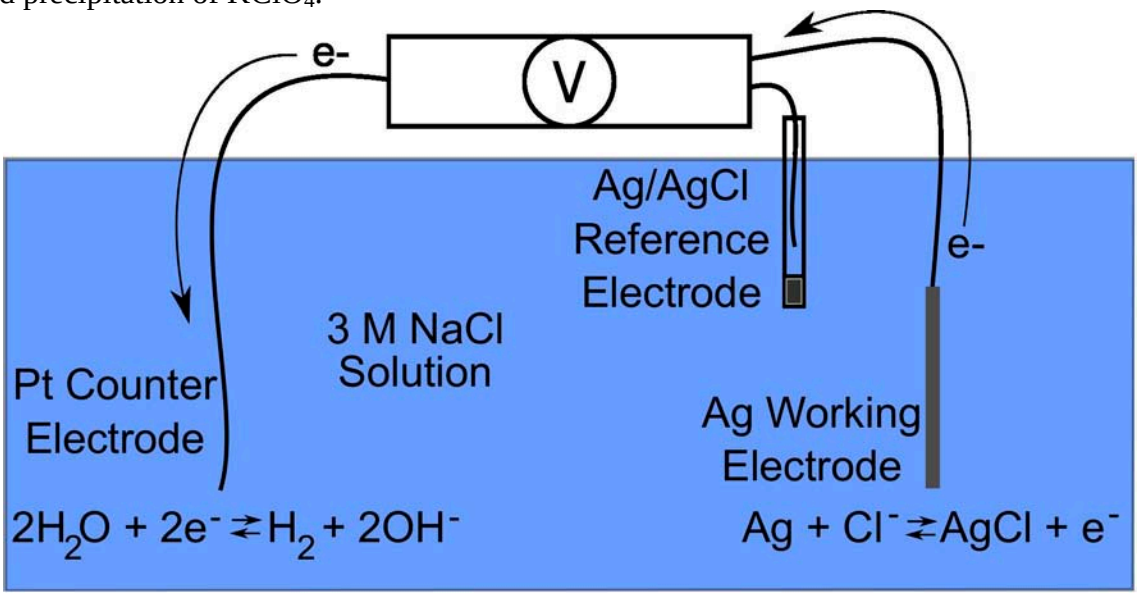


Figure C 1: Schematic of a galvanic Ag/AgCl plating cell. Provided by Dr. Yung Jin Hu.

.

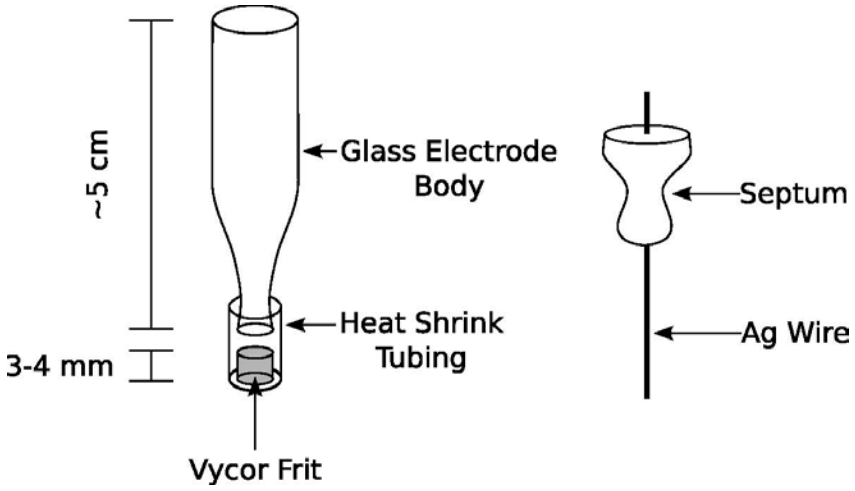


Figure C 2: Schematic of the Ag/AgCl electrode. Provided by Dr. Yung Jin Hu.

## C.2 Electrochemistry Setup

For the electrochemistry conducted in this work, the three-electrode cell consists of a Ag/AgCl reference electrode, platinum mesh as the working electrode, and a platinum wire counter electrode (Figure C 3). The large surface area of the working electrode allows for electrochemical reactions to occur faster, as there is a greater area for the analyte to diffuse towards. Care must be taken that the working electrode and counter electrode do not come into contact with each other; otherwise, the circuit is completed and no electrochemical reaction will occur at either electrode. The platinum wire can be isolated in a glass electrode body (similar to one shown in Figure C 2). However, a large amount of heat is given off when electrochemically adjusting high concentrations of analyte, which can crack the Vycor frit. The electrochemical processes are controlled by an AMEL potentiostat.

Figure C 3: A picture of the electrochemical cell used in this work that shows the Ag/AgCl reference electrode (right side), platinum mesh working electrode, and Pt wire counter electrode (left side).

## C.3 Chemical Adjustment of Oxidation States

In addition to electrolysis, the role of oxidants and reductants is paramount. In particular, nitrite (added in the form of $NaNO_2$) is very useful because it serves to both oxidize tetravalent neptunium to the pentavalent state and at the same time reduce hexavalent neptunium and adjust plutonium to the tetravalent state. Similarly, ferrous sulfamate ($Fe(NH_2SO_3)_2$) plays a dual role. Neptunium is reduced to Np(IV) and all plutonium species are reduced to Pu(III).

## C.4 Electrochemical Preparation of Plutonium

The complicated redox chemistry of plutonium requires solutions of varying oxidation states, which can be prepared electrochemically with use of a potentiostat and three-electrode cell. Figure C 4 shows the current-voltage diagram for plutonium in 1 M $HClO_4$, and Table C 1 summarizes the potentials to apply versus a Ag/AgCl reference electrode to obtain the various plutonium oxidation states.[231] Note the large overpotential required for reduction of Pu(VI) to Pu(III), as the Pu–O bonds of the plutonyl moiety must be broken.

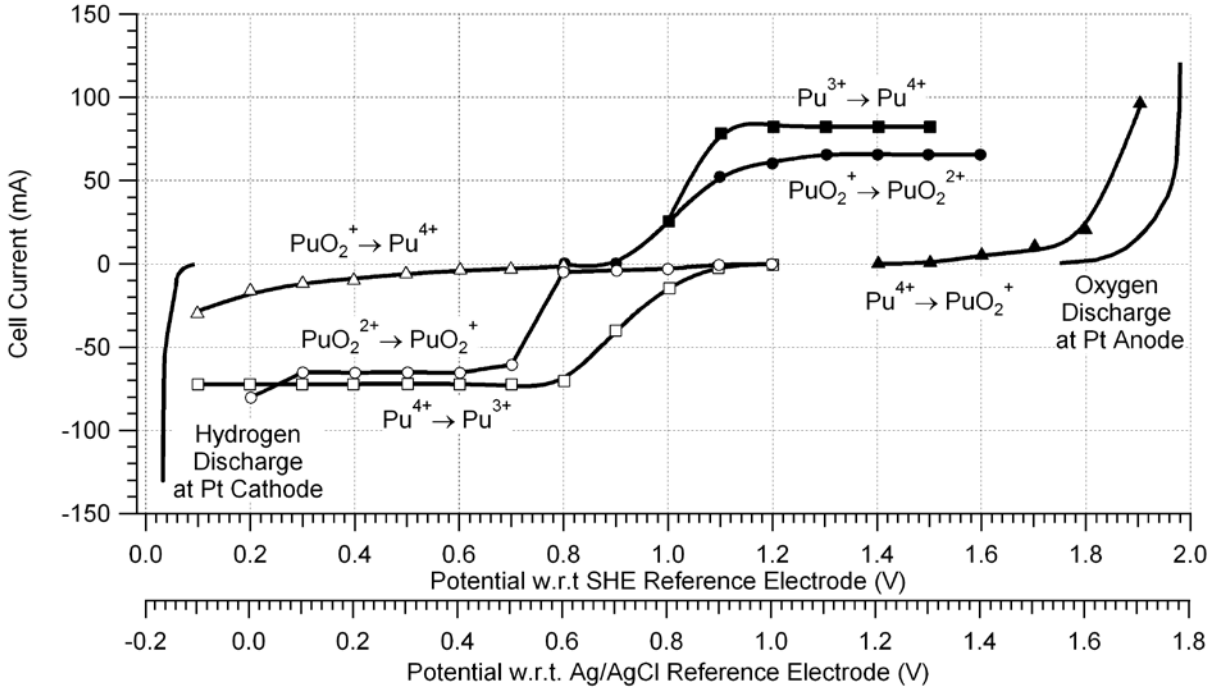


Figure C 4: Current voltage diagram for plutonium in 1 M $HClO_4$ with potentials referenced with respect to the SHE and a Ag/AgCl electrode. Adapted from Cohen.[231]

| Reaction | Potential vs. Ag/AgCl reference electrode |
|---|---|
| $Pu(VI) \rightarrow Pu(V)$ | 0.70 V at pH 3 |
| $Pu(III) \rightarrow Pu(IV)$ | 1.00-1.10 V in 1 M $HClO_4$ |
| $Pu(VI) \rightarrow Pu(III)$ | 0 V in 1 M $HClO_4$ |
| any oxidation state $\rightarrow Pu(IV)$ | boil in $HClO_4$ |

Table C 1: Applied potentials to obtain various plutonium oxidation states with electrochemistry. Values taken from Cohen.[231]

Preparation of Pu(III)

A solution of Pu(III) can be electrochemically prepared by applying a voltage between 0 -0.9 V (relative to the SHE), regardless of plutonium oxidation state. The Pu(VI) to Pu(V) to Pu(IV) to Pu(III) reduction reactions will occur rapidly.

Pu(III) can also be prepared by reduction of Pu(IV) using Zn metal or $I^-$ in a HI/HCl mixture. The latter is the preferred reducing method used in anion exchange (Appendix B).

Preparation of Pu(IV)

A solution of Pu(IV) can be electrochemically prepared from a starting solution of Pu(III) and applying a voltage between 1.0-1.4 V (relative to the SHE). The oxidation of Pu(III) to Pu(IV) occurs rapidly. For this reaction, the high overpotential required to oxidize Pu(IV) to Pu(V) is beneficial.

Pu(IV) is often prepared by the addition of sodium nitrite ($NaNO_2$), regardless of plutonium oxidation state. While the reduction of Pu(V) to Pu(IV) occurs slowly, due to breaking the Pu–O bonds of the plutonyl moiety, the reduction of Pu(VI) to Pu(V) and and oxidation of Pu(III) to Pu(IV) occur rapidly. Add $NaNO_2$ slowly to the plutonium solution, as gas will be evolved.

Preparation of Pu(VI)

A solution of Pu(VI) can be electrochemically prepared by applying a positive voltage to the cell. However, the Pu(IV) to Pu(V) oxidation reaction requires a high overpotential, due to the formation of the Pu–O bonds of the plutonyl moiety.

Pu(VI) is easily prepared by boiling in $HClO_4$, regardless of plutonium oxidation state. Care should be taken to ensure no organics are present, which is often accomplished by boiling the plutonium solution to near-dryness several times with $HNO_3$. The acid digestion should destroy all organics. Concentrated $HClO_4$ is added to the plutonium solution (cooled to room temperature) and boiled for several hours. This method of preparing Pu(VI) is advantageous because the high boiling point of $HClO_4$ (203 °C) means any leftover $HNO_3$ will also be boiled off (120.5 °).

## C.5 Electrochemical Preparation of Neptunium

Solutions of neptunium with varying oxidation states can be prepared electrochemically with use of a potentiostat and three-electrode cell. Figure C 5 shows a current-voltage diagram for neptunium in 1 M $HClO_4$. Note that Cohen originally generated these curves as oxidation potentials, and thus why the sign is switched for reduction potentials. Table C 2 summarizes the potentials to apply versus a Ag/AgCl reference electrode to obtain the various neptunium oxidation states.[102]

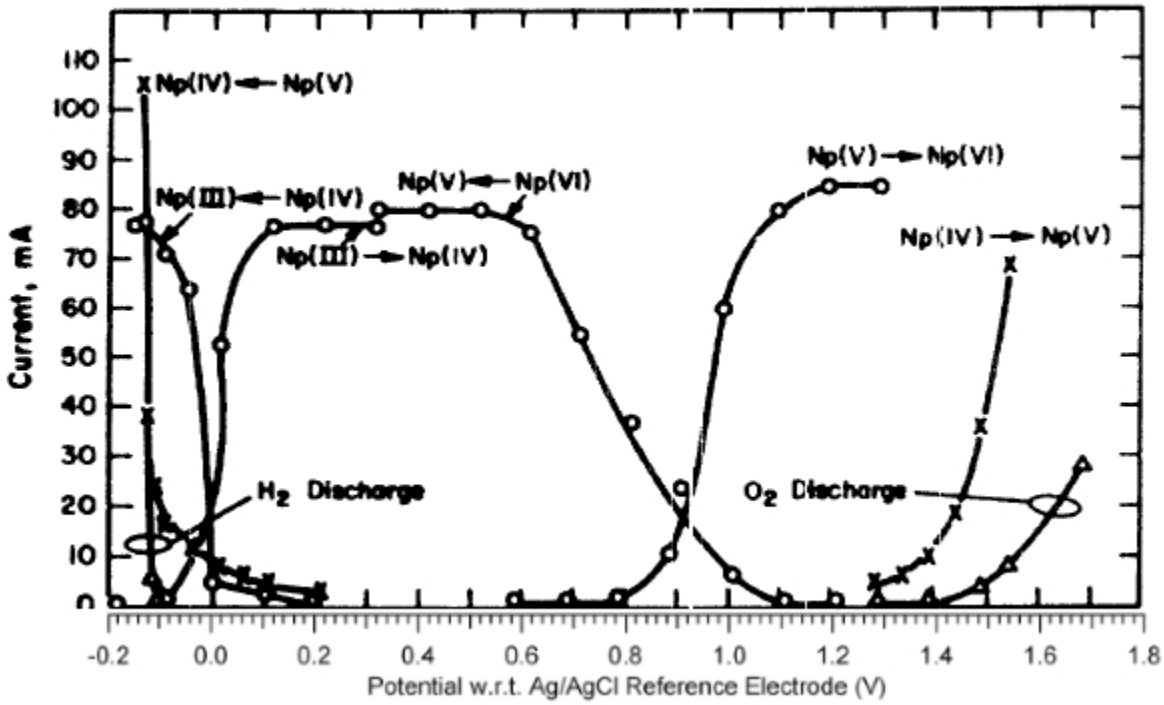


Figure C 5: Current voltage diagram for neptunium in 1 M $HClO_4$ with potentials referenced with respect to the SHE and a Ag/AgCl electrode. Adapted from Burney and Harbour.[91]

| Reaction | Potential to Apply | Ref |
|---|---|---|
| oxidize $Np(III) \rightarrow Np(IV)$ | +0.04 V | 81 |
| oxidize $Np(V) \rightarrow Np(VI)$ | +1.20 V | 81 |
| reduce $Np(V) \rightarrow Np(III)$ | -0.20 V | 81 |
| reduce $Np(VI) \rightarrow Np(V)$ | +0.4 V | 102 |
| *rest potential of Np(V)* | +0.689 V | 102 |

Table C 2: Applied potentials to obtain various neptunium oxidation states with electrochemistry in 1 M $HClO_4$ with Ag/AgCl reference electrode.

# D. PHREEPLOT INPUT FILES FOR SPECIATION DIAGRAMS

## D.1 Speciation Diagram of Pu(VI) in 0.01 M $NaClO_4$

```
SPECIATION
  JobTitle                              "Pu(VI) speciation diagram, 0.01 M
NaClO4"
  calculationType                       species
  calculationMethod                     1
  database                              forPudeletedentriesfromllnl.dat
  # species and their names vary with database
  mainSpecies                           "Pu(6)"
  xtitle                                   pH
  xmin                                  2.04
  xmax                                  11.0
  # pH range (x-axis) from 3 - 10 in 300 steps
  ytitle                                   "% of Pu(VI) species"
  resolution                            300
  # 300 points per curve; should get nice smooth lines
  numericTags                           <pCO2> = "-3.5" \
                                        <pO2> = "-0.677"
  # atmospheric pO2

PLOT
  plotTitle                             "speciation diagram for Pu(VI) <br> in
0.01 M NaClO<sub>4</sub>"
  pxmin                                 2.0
  # sets lower limit on x-axis
  pxmax                                 11.0
  # sets upper limit on x-axis
  pxmajor                               1.0
  # major ticks and numbering
  pxminor                               0.5
  # minor ticks
  pymin                                 0
  # sets lower limit on y-axis
  pymax                                 100
  # sets upper limit on y-axis
  pymajor                               10.0
  # major ticks and numbering
  pyminor                               5
  # minor ticks
  useLineColorDictionary                1
  # uses the colors specified in linecolor.dat
  lines                                 PuO2+2 PuO2OH+ PuO2(OH)2(PuO2)2(OH)2+2
PuO2CO3 PuO2(CO3)2-2 PuO2(CO3)3-4 PuO2Cl+
  # explicit naming of species - order defined in user_punchNp.inc
  customXcolumn                         1
  # use first column as defined by include files (it would be "pH")
  labelSize                             2
  # controls the size of the curve labels inside plot
  minimumYValueForPlotting              0.01
  # omit any curve with max(concn)<0.01%
```

```
  legendTitle                         "Pu(VI) species"
  legendTextSize                      2
  #reduces the size of the legend text
  pdf                                 T
  # makes a pdf file
  png                                 T
   # makes a png file
  jpg                                 T
   # makes a jpg file
  epsi                                T
   # makes an epsi file
  eps                                 T
   # makes an eps file
  out                                 T
   # makes an Excel spreadsheet

CHEMISTRY

include 'speciesvsph.inc'
# PHREEQC code to generate species-conc pairs; this file exports the required
x-axis(pH), y-axis (%) value pairs.  Edit if you're brave enough...

PHASES
Fix_H+
   H+ = H+
   log_k 0.0

SELECTED_OUTPUT
    -high_precision       true
    -reset                false
    # omit all default output

SOLUTION 1
# first simulation - initial solution
   temp      25
   pH        7
   # pH just for initial solution concentration
   units     mol/L
   density   1
   pe            8
   Pu        1e-6
   # total Pu
   Na        0.01
   Cl(7)     0.01 charge

END

USE solution 1
# second simulation - loop on this one
EQUILIBRIUM_PHASES
   CO2(g)    <pCO2> 1.0
   O2(g)     <pO2> 0.1
   Fix_H+  -<x_axis>  NaOH 10
      -force_equality true

END
```

## D.2 Speciation Diagram of Np(V) in 0.01 M $NaClO_4$

```
SPECIATION
  JobTitle                              "Np(V) speciation diagram, 0.01 M
NaClO4"
  calculationType                       species
  calculationMethod                     1
  database                              forNpdeletedentriesfromllnl.dat
  # species and their names vary with database
  mainSpecies                           "Np(5)"
  xtitle                                pH
  xmin                                  2.04
  xmax                                  11.0
  # pH range (x-axis) from 3 - 10 in 300 steps
  ytitle                               "% of Np(V) species"
  resolution                            300
  # 300 points per curve; should get nice smooth lines
  numericTags                           <pCO2> = "-3.5" \
                                        <pO2> = "-0.677"
  # atmospheric pO2

PLOT
  plotTitle                             "speciation diagram for Np(V) <br> in
0.01 M NaClO<sub>4</sub>"
  pxmin                                 2.0
  # sets lower limit on x-axis
  pxmax                                 11.0
  # sets upper limit on x-axis
  pxmajor                               1.0
  # major ticks and numbering
  pxminor                               0.5
  # minor ticks
  pymin                                 0
  # sets lower limit on y-axis
  pymax                                 100
  # sets upper limit on y-axis
  pymajor                               10.0
  # major ticks and numbering
  pyminor                               5
  # minor ticks
  useLineColorDictionary                1
  # uses the colors specified in linecolor.dat
  lines                                 NpO2+ NpO2OH NpO2(OH)2- NpO2CO3-
NpO2(CO3)2-3 NpO2(CO3)3-5 NpO2Cl NpO2Cl2-
  # explicit naming of species - order defined in user_punchNp.inc
  customXcolumn                         1
  # use first column as defined by include files (it would be "pH")
  labelSize                             2
  # controls the size of the curve labels inside plot
  minimumYValueForPlotting              0.01
  # omit any curve with max(concn)<0.01%
  legendTitle                          "Np(V) species"
  legendTextSize                       2
  #reduces the size of the legend text
  pdf                                  T
  # makes a pdf file
```

```
  png                               T
   # makes a png file
  jpg                               T
   # makes a jpg file
  epsi                              T
   # makes an epsi file
  eps                               T
   # makes an eps file
  out                           T
   # makes an Excel spreadsheet

CHEMISTRY

include 'speciesvsph.inc'
# PHREEQC code to generate species-conc pairs; this file exports the required
x-axis(pH), y-axis (%) value pairs.  Edit if you're brave enough...

PHASES
Fix_H+
   H+ = H+
   log_k 0.0

SELECTED_OUTPUT
    -high_precision       true
    -reset                false
    # omit all default output

SOLUTION 1
# first simulation - initial solution
   temp      25
   pH        7
   # pH just for initial solution concentration
   units     mol/L
   density   1
   pe            8
   Np        1e-6
   # total Np
   Na        0.01
   Cl(7)     0.01 charge

END

USE solution 1
# second simulation - loop on this one
EQUILIBRIUM_PHASES
   CO2(g)    <pCO2> 1.0
   O2(g)     <pO2> 0.1
   Fix_H+  -<x_axis>  NaOH 10
      -force_equality true

END
```

## D.3 Speciation Diagram of Carbonate

```
SPECIATION
  JobTitle                              "carbonate speciation diagram, 0.01 M
NaClO4"
  calculationType                       species
  calculationMethod                     1
  database                              forCdeletedentriesfromllnl.dat
  # species and their names vary with database
  mainSpecies                           C
  xtitle                        pH
  xmin                                  2
  xmax                                  12
  # pH range (x-axis) from 3 - 10 in 300 steps
  ytitle                        "% of carbonate species"
  resolution                            300
  # 300 points per curve; should get nice smooth lines
  numericTags                           <pCO2> = "-3.5" \
                                        <pO2> = "-0.677"
  # atmospheric CO2 and O2

PLOT
  plotTitle                             "speciation diagram for carbonate <br>
in 0.01 M NaClO<sub>4</sub>"
  pxmin                                 2.0
  # sets lower limit on x-axis
  pxmax                                 12.0
  # sets upper limit on x-axis
  pxmajor                               1.0
  # major ticks and numbering
  pxminor                               0.5
  # minor ticks
  pymin                                 0
  # sets lower limit on y-axis
  pymax                                 100
  # sets upper limit on y-axis
  pymajor                               10.0
  # major ticks and numbering
  pyminor                               5
  # minor ticks
  useLineColorDictionary                1
  # uses the colors specified in linecolor.dat
  lines                                 CO2 HCO3- CO3-2 NaCO3- NaHCO3
  # explicit naming of species - order defined in user_punchNp.inc
  customXcolumn                         1
  # use first column as defined by include files (it would be "pH")
  labelSize                             2
  # controls the size of the curve labels inside plot
  minimumYValueForPlotting              0.01
  # omit any curve with max(concn)<0.01%
  legendTitle                       "carbonate species"
  legendTextSize              2
  #reduces the size of the legend text
  pdf                         T
  # makes a pdf file
  png                               T
```

```
   # makes a png file
  jpg                              T
   # makes a jpg file
  epsi                             T
   # makes an epsi file
  eps                              T
   # makes an eps file
  out                           T
   # makes an Excel spreadsheet
  ai                               F
   # will NOT make an ai file

CHEMISTRY

include 'speciesvsph.inc'
# PHREEQC code to generate species-conc pairs; this file exports the required
x-axis(pH), y-axis (%) value pairs.  Edit if you're brave enough...

PHASES
Fix_H+
   H+ = H+
   log_k 0.0

SELECTED_OUTPUT
    -high_precision       true
    -reset                false
    # omit all default output

SOLUTION 1
# first simulation - initial solution
   temp      25
   # carbonate speciation at least depends on temperature
   pH        7
   # pH just for initial solution concentration
   units     mol/L
   C(4)      1e-6 as HCO3
   # total C
   Na        0.1
   # background electrolyte
   Cl(7)     0.1 charge

END

USE solution 1
# second simulation - loop on this one
EQUILIBRIUM_PHASES
#   CO2(g)    <pCO2>
#   O2(g)     <pO2>
   Fix_H+  -<x_axis>  NaOH 10
      -force_equality true

END
```

# BIBLIOGRAPHY


(1) Silva, R. J.; Nitsche, H. Environmental Chemistry. In *Advances in Plutonium Chemistry 1967-2000*; Hoffman, D. C., Ed.; American Nuclear Society: La Grange Park, IL, 2002; pp 89–111.

(2) Choppin, G. R. Actinide Speciation in the Environment. *J. Radioanal. Nucl. Chem.* **2007**, *273* (3), 695–703.

(3) Riley, R. G.; Zachara, J. M. *Chemical Contaminants on DOE Lands and Selection of Contaminant Mixtures for Subsurface Science Research, DOE/ER-0547T*; 1992.

(4) Cantrell, K. J. *Transuranic Contamination in Sediment and Groundwater at the U.S. DOE Hanford Site PNNL-18640 2*; 2009.

(5) Felmy, A. R.; Cantrell, K. J.; Conradson, S. D. Plutonium Contamination Issues in Hanford Soils and Sediments: Discharges from the Z-Plant (PFP) Complex. *Phys. Chem. Earth* **2010**, *35* (6–8), 292–297.

(6) Cantrell, K. J.; Felmy, A. R. *Plutonium and Americium Geochemistry at Hanford : A Site-Wide Review PNNL-21651*; 2012.

(7) Smith, D. K.; Finnegan, D. L.; Bowen, S. M. An Inventory of Long-Lived Radionuclides Residual from Underground Nuclear Testing at the Nevada Test Site, 1951-1992. *J. Environ. Radioact.* **2003**, *67* (1), 35–51.

(8) Carlton, W. H.; Evans, A. G.; Geary, L. A.; Murphy, C. E. J.; Pinder, J. E.; Strom, R. N. *Assessment of Plutonium in the Savannah River Site Environment WSRC-92-879*; Aiken, SC, 1992.

(9) Carlton, W. H. *Assessment of Neptunium, Americium, and Curium in the Savannah River Site Environment WSRC-TR-97*; Aiken, SC, 1997.

(10) *Chernobyl: Assessment of Radiological and Health Impacts*; 2002.

(11) Novikov, A. P.; Kalmykov, S. N.; Utsunomiya, S.; Ewing, R. C.; Horreard, F.; Merkulov, A.; Clark, S. B.; Tkachev, V. V; Myasoedov, B. F. Colloid Transport of Plutonium in the Far-Field of the Mayak Production Association, Russia. *Science (80-. ).* **2006**, *314* (5799), 638–641.

(12) Jiménez-Ramos, M. C.; García-Tenorio, R.; Vioque, I.; Manjón, G.; García-León, M. Presence of Plutonium Contamination in Soils from Palomares (Spain). *Environ. Pollut.* **2006**, *142* (3), 487–492.

(13) Lehto, J.; Hou, X. *Chemistry and Analysis of Radionuclides: Laboratory Techniques and Methodology*; Wiley-VCH, 2011.

(14) *The Disposal of Radioactive Waste on Land*; 1957.

(15) Patel, P.; Ewing, R. United States Launches New Direction to Manage. *MRS Bull.* **2013**, *38* (March), 206–207.

(16) Bodansky, D. *Nuclear Energy - Principles, Practices, and Prospects*, 2nd ed.; Springer, 2004.

(17) Wydler, P.; Baetslé, L. H. Closing the Nuclear Fuel Cycle: Issues and Perspectives. In *Actinide and Fission Product Partitioning and Transmutation*; OECD Nuclear Energy Agency, 2000; pp 31–49.

(18) *Yucca Mountain Science and Engineering Report: Technical Information Supporting Site Recommendation Consideration Rev. 1*; North Las Vegas, NV, 2002.

(19) Brown, G. E.; Foster, A. L.; Ostergren, J. D. Mineral Surfaces and Bioavailability of Heavy Metals: A Molecular-Scale Perspective. *Proc. Natl. Acad. Sci.* **1999**, *96* (7), 3388–

3395.
(20) Schwertmann, U.; Cornell, R. M. *The Iron Oxides: Structure, Properties, Reactions, Occurences and Uses*, 2nd ed.; Wiley-VCH: Weinheim, Germany, 2003.
(21) Tochiyama, O.; Endo, S.; Inoue, Y. Sorption of Neptunium(V) on Various Iron Oxides and Hydrous Iron Oxides. *Radiochim. Actaca Acta* **1995**, *68* (2), 105–111.
(22) *Minerals in Soil Environments*, 2nd ed.; Dixon, J. B., Weed, S. B., Eds.; Soil Science Society of America: Madison, WI, 1989.
(23) Lemire, R. J.; Berner, U.; Musikas, C.; Palmer, D. A.; Taylor, P.; Tochiyama, O. *Chemical Thermodynamics of Iron Part 1*; Agency, O. N. E., Ed.; 2013; Vol. 13a.
(24) Combes, J. M.; Chisholmbrause, C. J.; Brown, G. E.; Parks, G. A.; Conradson, S. D.; Eller, P. G.; Triay, I. R.; Hobart, D. E.; Meijer, A.; Chisholm-Brause, C. J.; et al. EXAFS Spectroscopic Study of Neptunium(V) Sorption at the Alpha-FeOOH/Water Interface. *Environ. Sci. Technol.* **1992**, *26* (2), 376–382.
(25) Nitsche, H. Synchrotron X-Ray-Absorption Spectroscopy - a New Tool for Actinide and Lanthanide Speciation in Solids and Solution. *J. Alloys Compd.* **1995**, *223* (2), 274–279.
(26) Cleveland, J. M. *The Chemistry of Plutonium*, 2nd ed.; American Nuclear Society: La Grange Park, IL, 1979.
(27) Meitner, L.; Frisch, O. R. Disintegration of Uranium by Neutrons: A New Type of Nuclear Reaction. *Nature* **1939**, *143*, 239–240.
(28) Seaborg, G. T. The Transuranium Elements. *Science (80-. ).* **1946**, *104* (2704), 379–386.
(29) Clark, D. L. The Chemical Complexities of Plutonium. *Los Alamos Sci.* **2000**, No. 26, 364–381.
(30) Seaborg, G. T.; McMillan, E. M.; Kennedy, J. W.; Wahl, A. C. Radioactive Element 94 from Duterons on Uranium. *Phys. Rev.* **1946**, *69*, 366–367.
(31) Seaborg, G. T.; Wahl, A. C.; Kennedy, J. W. Radioactive Element 94 from Deuterons on Uranium. *Phys. Rev.* **1946**, *69*, 367.
(32) Kennedy, J. W.; Seaborg, G. T.; Segrè, E.; Wahl, A. C. Properties of 94(230). *Phys. Rev.* **1946**, *70*, 555.
(33) Balraj, S.; Tuli, J. K. National Nuclear Data Center. *Nucl. Data Sheets* **2005**.
(34) Rabideau, S. W.; Bradley, M. J.; Cowan, H. D. *Alpha-Particle Oxidation and Reduction in Aqueous Plutonium Solutions LAMS-2236*; 1958.
(35) Kennedy, J. W.; Wahl, A. C. Search for Spontaneous Fission in 94-239. *Phys. Rev.* **1946**, *69*, 367.
(36) EXFOR Database. *Nucl. Data Sheets* **2010**.
(37) *Nuclear and Radiochemistry: Fundamentals and Applications, Volume 1*, Third.; Lieser, K. H., Kratz, J.-V., Eds.; Wiley-VCH, 2013.
(38) Loveland, W. D.; Morrissey, D. J.; Seaborg, G. T. *Modern Nuclear Chemistry*; John Wiley & Sons, 2006.
(39) Seaborg, G. T.; Loveland, W. D. *The Elements Beyond Uranium*; John Wiley & Sons, 1990.
(40) Choppin, G. R. Actinide Speciation in the Environment. *Radiochim. Acta* **2003**, *91* (11), 645–649.
(41) Newton, T. W.; Hobart, D. E.; Palmer, P. D. The Formation of Pu (IV)-Colloid by the Alpha-Reduction of Pu(V) or Pu(VI) in Aqueous Solutions. *Radiochim. Acta* **1986**, *39* (3), 139–147.
(42) Büppelmann, K.; Kim, J. I.; Lierse, C. H. The Redox-Behaviour of Plutonium in Saline

Solutions under Radiolysis Effects. *Radiochim. Acta* **1988**, *44/45*, 65–70.
(43) *The Chemistry of the Actinide Elements*, 2nd ed.; Katz, J. J., Seaborg, G. T., Morss, L. R., Eds.; Springer, 1986.
(44) Shannon, R. D. Revised Effective Ionic Radii and Systematic Studies of Interatomic Distances in Halides and Chalcogenides. *Acta Crystallogr. Sect. A* **1976**, *32* (5), 751–767.
(45) Allen, P. G.; Bucher, J. J.; Shuh, D. K.; Edelstein, N. M.; Reich, T. Investigation of Aquo and Chloro Complexes of UO22+, NpO2+, Np4+, and Pu3+ by X-Ray Absorption Fine Structure Spectroscopy. *Inorg. Chem.* **1997**, *36* (21), 4676–4683.
(46) Allen, P. G.; Veirs, D. K.; Conradson, S. D.; Smith, C. A.; Marsh, S. F. Characterization of Aqueous plutonium(IV) Nitrate Complexes by Extended X-Ray Absorption Fine Structure Spectroscopy. *Inorg. Chem.* **1996**, *35* (Iv), 2841–2845.
(47) Panak, P. J.; Booth, C.; Caulder, D. L.; Bucher, J. J.; Shuh, D. K.; Nitsche, H. X-Ray Absorption Fine Structure Spectroscopy of Plutonium Complexes with Bacillussphaericus. *Radiochim. Acta* **2002**, *90* (6), 315–321.
(48) Choppin, G. R.; Rao, L. F. Complexation of Pentavalent and Hexavalent Actinides by Fluoride. *Radiochim. Acta* **1984**, *37* (3), 143–146.
(49) Choppin, G. R. Solution Chemistry of the Actinides. *Radiochim. Acta* **1983**, *32*, 43–53.
(50) Zavarin, M.; Powell, B. A.; Bourbin, M.; Zhao, P.; Kersting, A. B. Np(V) and Pu(V) Ion Exchange and Surface-Mediated Reduction Mechanisms on Montmorillonite. *Environ. Sci. Technol.* **2012**, *46* (5), 2692–2698.
(51) Clark, D. L.; Hecker, S. S.; Jarvinen, G. D.; Neu, M. P. Plutonium. In *The Chemistry of the Actinide and Transactinide Elements*; Morss, L. R., Edelstein, N. M., Fuger, J., Eds.; Springer, 2010; pp 813–1264.
(52) Connick, E. Mechanism of the Disproportionation of Plutonium(V). *J. Am. Chem. Soc.* **1949**, *71* (5), 1528–1533.
(53) Rabideau, S. W. Equilibria and Reaction Rates in the Disproportionation of Pu(IV). *J. Am. Chem. Soc.* **1953**, *75* (4), 798–801.
(54) Rabideau, S. W. The Kinetics of the Disproportionation of Plutonium(V). *J. Am. Chem. Soc.* **1957**, *79* (24), 6350–6353.
(55) Steele, H.; Taylor, R. J. A Theoretical Study of the Inner-Sphere Disproportionation Reaction Mechanism of the Pentavalent Actinyl Ions. *Inorg. Chem.* **2007**, *46* (16), 6311–6318.
(56) Madic, C.; Begun, G. M.; Hobart, D. E.; Hahn, R. L. Raman Spectroscopy of Neptunyl and Plutonyl Ions in Aqueous Solution: Hydrolysis of Np(V1) and Pu(V1) and Disproportionation of Pu(V). *Inorg. Chem.* **1984**, *23* (13), 1914–1921.
(57) Silver, G. L. Plutonium Hydrolysis and Disproportionation Reactions. *J. Radioanal. Nucl. Chem.* **2011**, *288* (1), 257–260.
(58) Stumm, W.; Morgan, J. J. *Aquatic Chemistry: Chemical Equilibria and Rates in Natural Waters*, Third.; John Wiley & Sons, 1996.
(59) Conradson, S. D.; Abney, K. D.; Begg, B. D.; Brady, E. D.; Clark, D. L.; den Auwer, C.; Ding, M.; Dorhout, P. K.; Espinosa-Faller, F. J.; Gordon, P. L.; et al. Higher Order Speciation Effects on Plutonium L-3 X-Ray Absorption near Edge Spectra. *Inorg. Chem.* **2004**, *43* (1), 116–131.
(60) Conradson, S. D.; Mahamid, A.; Clark, D. L.; Hess, N. J.; Hudson, E. A.; Neu, M. P.; Palmer, P. D.; Runde, W. H.; Tait, C. D. Oxidation State Determination of Plutonium Aquo Ions Using X-Ray Absorption Spectroscopy. *Polyhedron* **1998**, *17* (4), 599–602.

(61) Matonic, J. H.; Scott, B. L.; Neu, M. P. High-Yield Synthesis and Single-Crystal X-Ray Structure of a plutonium(III) Aquo Complex: [Pu(H2O)9][CF3SO3]3. *Inorg. Chem.* **2001**, *40* (12), 2638–2639.
(62) Lemire, R. J.; Fuger, J.; Nitsche, H.; Potter, P.; Rand, M. H.; Rydberg, J.; Spahiu, K.; Sullivan, J. C.; Ullman, W. J.; Vitorge, P.; et al. *Chemical Thermodynamics of Neptunium and Plutonium*; OECD Nuclear Energy Agency, Ed.; 2001; Vol. 4.
(63) Guillaumont, R.; Fanghänel, T.; Fuger, J.; Grenthe, I.; Neck, V.; Palmer, D. A.; Rand, M. H. *Vol. 5 of Chemical Thermodynamics: Update on the Chemical Thermodynamics of Uranium, Neptunium, Plutonium, Americium and Technetium*; OECD Nuclear Energy Agency, Ed.; Elsevier, 2003.
(64) Knopp, R.; Neck, V.; Kim, J. I. Solubility, Hydrolysis and Colloid Formation of plutonium(IV). *Radiochim. Acta* **1999**, *86* (3–4), 101–108.
(65) ESRL. Global Greenhouse Gas Reference Network http://www.esrl.noaa.gov/gmd/ccgg/trends/weekly.html (accessed Jul 20, 2004).
(66) Clark, D. L.; Hobart, D. E.; Neu, M. P. Actinide Carbonate Complexes and Their Importance in Actinide Environmental Chemistry. *Chem. Rev.* **1995**, *95*, 25–48.
(67) Choppin, G. R.; Bond, A. H.; Hromadka, P. M. Redox Speciation of Plutonium. *J. Radioanal. Nucl. Chem.* **1997**, *219* (2), 203–210.
(68) Runde, W. The Chemical Interactions of Actinides in the Environment. *Los Alamos Sci.* **2000**, *103* (26), 392–411.
(69) Choppin, G. R. Actinides in Environment and Waste Disposal Problem. *J. Radioanal. Nucl. Chem.* **1991**, *147* (1), 109–116.
(70) Neck, V.; Altmaier, M.; Fanghänel, T. Solubility of Plutonium Hydroxides/hydrous Oxides under Reducing Conditions and in the Presence of Oxygen. *Comptes Rendus Chim.* **2007**, *10* (10–11), 959–977.
(71) Neck, V.; Kim, J. I. Solubility and Hydrolysis of Tetravalent Actinides. *Radiochim. Acta* **2001**, *89* (1), 1–16.
(72) Powell, B. A.; Dai, Z.; Zavarin, M.; Zhao, P.; Kersting, A. B. Stabilization of Plutonium Nano-Colloids by Epitaxial Distortion on Mineral Surfaces. *Environ. Sci. Technol.* **2011**, *45* (7), 2698–2703.
(73) Soderholm, L.; Almond, P. M.; Skanthakumar, S.; Wilson, R. E.; Burns, P. C. The Structure of the Plutonium Oxide Nanocluster [Pu38O 56Cl54(H2O)8]14-. *Angew. Chemie - Int. Ed.* **2008**, *47* (2), 298–302.
(74) Johnson, J.; Anderson, G.; Parkhurst, D. thermo.com.V8.R6.230 Database.
(75) Charlton, S. R.; Parkhurst, D. L. Modules Based on the Geochemical Model PHREEQC for Use in Scripting and Programming Languages. *Comput. Geosci.* **2011**, *37* (10), 1653–1663.
(76) Nitsche, H.; Lee, S. C.; Gatti, R. C. Determination of Plutonium Oxidation-States at Trace Levels Pertinent to Nuclear Waste-Disposal. *J. Radioanal. Nucl. Chem.* **1988**, *124* (1), 171–185.
(77) Knoll, G. F. *Radiation Detection and Measurement*, 4th ed.; Wiley, 2011.
(78) Cohen, D. The Absorption Spectra of Plutonium Ions in Perchloric Acid Solutions. *J. Inorg. Nucl. Chem.* **1961**, *18*, 211–218.
(79) Hayes, K. F.; Roe, A. L.; Brown, G. E.; Hodgson, K. O.; Leckie, J. O.; Parks, G. A. In Situ X-Ray Absorption Study of Surface Complexes: Selenium Oxyanions on α-FeOOH. *Science (80-. ).* **1987**, *238* (4828), 783–786.

(80) Chisholm-Brause, C. J.; Roe, A. L.; Hayes, K. F.; Brown, G. E.; Parks, G. A.; Leckie, J. O. XANES and EXAFS Study of Aqueous Pb(II) Adsorbed on Oxide Surfaces. *Phys. B Condens. Matter* **1989**, *158* (1–3), 674–675.
(81) Yoshida, Z.; Johnson, S. G.; Kimura, T.; Krsul, J. R. Neptunium. In *The Chemistry of the Actinide and Transactinide Elements*; Morss, L. R., Edelstein, N. M., Fuger, J., Eds.; Springer, 2010; pp 699–812.
(82) Dange, S. P.; Gubbi, G. K.; Ramaswami, A.; Manohar, S. B. Synthesis of Isotopically Pure 236Pu Tracer. *BARC Newsletter*. 2003, pp 1–5.
(83) YAMANA, H.; YAMAMOTO, T.; KOBAYASHI, K.; MITSUGASHIRA, T.; MORIYAMA, H. Production of Pure 236Pu Tracer for the Assessment of Plutonium in the Environment. *J. Nucl. Sci. Technol.* **2001**, *38* (10), 859–865.
(84) McMillan, E. Radioactive Recoils from Uranium Activated by Neutrons. *Phys. Rev.* **1939**, *55* (5), 510.
(85) McMillan, E.; Abelson, P. H. Radioactive Element 93. *Phys. Rev.* **1940**, *57* (12), 1185–1186.
(86) Silva, R. J.; Nitsche, H. Actinide Environmental Chemistry. *Radiochim. Acta* **1995**, *70–71* (Supplement), 377–396.
(87) Clark, D. L.; Conradson, S. D.; Ekberg, S. A.; Hess, N. J.; Neu, M. P.; Palmer, P. D.; Runde, W.; Drew Tait, C. EXAFS Studies of Pentavalent Neptunium Carbonato Complexes. Structural Elucidation of the Principal Constituents of Neptunium in Groundwater Environments. *J. Am. Chem. Soc.* **1996**, *118* (8), 2089–2090.
(88) Antonio, M. R.; Soderholm, L.; Williams, C. W.; Blaudeau, J. P.; Bursten, B. E. Neptunium Redox Speciation. *Radiochim. Acta* **2001**, *89* (1), 17–25.
(89) Skanthakumar, S.; Antonio, M. R.; Soderholm, L. A Comparison of neptunyl(V) and neptunyl(VI) Solution Coordination: The Stability of Cation-Cation Interactions. *Inorg. Chem.* **2008**, *47* (11), 4591–4595.
(90) Ikeda-Ohno, A.; Hennig, C.; Rossberg, A.; Funke, H.; Scheinost, A. C.; Bernhard, G.; Yaita, T. Electrochemical and Complexation Behavior of Neptunium in Aqueous Perchlorate and Nitrate Solutions. *Inorg. Chem.* **2008**, *47* (18), 8294–8305.
(91) Burney, G.; Harbour, R. *Radiochemistry of Neptunium*; National Academies, 1974.
(92) Hindman, J. C.; Sullivan, J. C.; Cohen, D. Kinetics of Reactions between Neptunium Ions. The Neptunium (IV)-Neptunium (VI) Reaction in Perchlorate Solution. *J. Am. Chem. Soc.* **1954**, *4682* (12), 3278–3280.
(93) Meinrath, G. Np(V) Carbonates in Solid State and Aqueous Solution. *J. Radioanal. Nucl. Chem.* **1994**, *186* (3), 257–272.
(94) Maya, L. Hydrolysis and Carbonate Complexation of dioxoneptunium(V) in 1.0 M NaClO4 at 25C. *Inorg. Chem.* **1983**, *22* (14), 2093–2095.
(95) Lierse, C.; Treiber, W.; Kim, J. I. Hydrolysis Reactions of neptunium(V). *Radiochim. Acta* **1985**, *38*, 27–28.
(96) Neck, V.; Kim, J. I.; Kanellakopulos, B. Solubility and Hydrolysis Behaviour of neptunium(V). *Radiochim. Acta* **1992**, *56*, 25–30.
(97) Sjoblom, R.; Hindman, J. C. Spectrophotometry of Neptunium in Perchloric Acid Solutions. *J. Am. Chem. Soc.* **1951**, *73* (15), 1744–1751.
(98) Hagan, P. G.; Cleveland, J. M. The Absorption Spectra of Neptunium Ions in Perchloric Acid Solution. *J. Inorg. Nucl. Chem.* **1966**, *28* (12), 2905–2909.
(99) Friedman, H. A.; Toth, L. M.; Osborne, M. M. The Photochemistry of Neptunium in

Aqueous Perchloric Acid Solutions. *J. Inorg. Nucl. Chem.* **1979**, *41* (9), 1339–1345.
(100) Friedman, H. A.; Toth, L. M. Absorption Spectra of Np (III),(IV),(V) and (VI) in Nitric Acid Solution. *J. Inorg. Nucl. Chem.* **1980**, *42* (November 1979), 1347–1349.
(101) Precek, M.; Paulenova, A. Kinetics of Reduction of Hexavalent Neptunium by Nitrous Acid in Solutions of Nitric Acid. *J. Radioanal. Nucl. Chem.* **2010**, *286* (3), 771–776.
(102) Soderholm, L.; Antonio, M. R.; Williams, C.; Wasserman, S. R. XANES Spectroelectrochemistry: A New Method for Determining Formal Potentials. *Anal. Chem.* **1999**, *71* (20), 4622–4628.
(103) Reich, T.; Baraniak, L.; Bernhard, G.; Funke, H.; Geipel, G.; Hennig, C.; Roßberg, A. *Determination of Radionuclide Speciation in Aqueous Solutions by EXAFS Spectroscopy*; 1999.
(104) Sposito, G. *The Chemistry of Soils*, 1st ed.; Oxford University Press, 1989.
(105) Koretsky, C. The Significance of Surface Complexation Reactions in Hydrologic Systems: A Geochemist's Perspective. *J. Hydrol.* **2000**, *230* (3–4), 127–171.
(106) Duff, M. C.; Hunter, D. B.; Hobbs, D. T.; Jurgensen, A.; Fink, S. D. *Characterization of Plutonium , Neptunium , Strontium on Manganese Solids from Permanganate Reduction WSRC-TR-2002-00366*; Aiken, SC, 2002.
(107) Goldberg, S. Adsorption Models Incorporated into Chemical Equilibrium Models: In Chemical Equilibrium and Reaction Models. In *Chemical Equilibrium and Reaction Models*; Loeppert, R. H., Schwab, A. P., Goldberg, S., Eds.; Soil Science Society of America and American Society of Agronomy: Madison, WI, 1995; Vol. 42, pp 75–95.
(108) Stumm, W.; Huang, C. P.; Jenkins, S. R. Specific Chemical Interaction Affecting the Stability of Dispersed Systems. *Croat. Chem. Acta* **1970**, *42*, 223–245.
(109) Huang, C. P.; Stumm, W. Specific Adsorption of Cations on Hydrous γ-Al2O3. *J. Colloid Interface Sci.* **1973**, *43* (2), 409–420.
(110) Dzombak, D. A.; Morel, F. M. M. *Surface Complexation Modeling: Hydrous Ferric Oxide*; John Wiley & Sons, 1990.
(111) Schindler, P. W.; Gamsjäger, H. Acid - Base Reactions of the TiO2 (Anatase) - Water Interface and the Point of Zero Charge of TiO2 Suspensions. *Kolloid-Zeitschrift Zeitschrift für Polym.* **1972**, *250* (7), 759–763.
(112) Schindler, P. W.; Fürst, B.; Dick, R.; Wolf, P. U. Ligand Properties of Surface Silanol Groups. I. Surface Complex Formation with Fe3+, Cu2+, Cd2+, and Pb2+. *J. Colloid Interface Sci.* **1976**, *55* (2), 469–475.
(113) Davis, J. A.; James, R. O.; Leckie, J. O. Surface Ionization and Complexation at the Oxide/Water Interface: I. Computation of Electrical Double Layer Properties in Simple Electrolytes. *J. Colloid Interface Sci.* **1978**, *63* (3), 480–499.
(114) Davis, J. A.; Leckie, J. O. Surface Ionization and Complexation at the Oxide/Water Interface II. Surface Properties of Amorphous Iron Oxyhydroxide and Adsorption of Metal Ions. *J. Colloid Interface Sci.* **1978**, *67* (1), 90–107.
(115) Davis, J.; James, R.; Leckie, J. Surface Ionization and Complexation at the Oxide/Water Interface 3. Adsorption of Anions. *J. Colloid Interface Sci.* **1980**, *74* (1), 32–43.
(116) Sposito, G. The Operational Definition of the Zero-Point of Charge in Soils. *Soil Sci. Soc. Am. J.* **1981**, *45* (2), 292–297.
(117) Parks, G. A.; de Bruyn, P. L. The Zero Point of Charge of Oxides 1. *J. Phys. Chem.* **1962**, *66* (6), 967–973.
(118) Sposito, G. *The Chemistry of Soils*, 2nd ed.; Oxford University Press: New York, 2008.

(119) Stumm, W. *Chemistry of the Solid-Water Interface: Processes at the Mineral-Water and Particle-Water Interface in Natural Systems*; 1992.
(120) Cristiano, E.; Hu, Y.-J.; Siegfried, M.; Kaplan, D.; Nitsche, H. A Comparison of Point of Zero Charge Measurement Methodology. *Clays Clay Miner.* **2011**, *59* (2), 107–115.
(121) Tourinho, F. A.; Campos, A. F. C.; Aquino, R.; Lara, M. C. F. L.; da Silva, G. J.; Depeyrot, J. Surface Charge Density Determination in Electric Double Layeres Magnetic Fluids. *Brazilian J. Phys.* **2002**, *32* (2B), 501–508.
(122) Noh, J. S.; Schwarz, J. A. Estimation of the Point of Zero Charge of Simple Oxides by Mass Titration. *J. Colloid Interface Sci.* **1989**, *130* (1), 157–164.
(123) Mustafa, S.; Dilara, B.; Nargis, K.; Naeem, A.; Shahida, P. Surface Properties of the Mixed Oxides of Iron and Silica. *Colloids Surfaces a-Physicochemical Eng. Asp.* **2002**, *205* (3), 273–282.
(124) Schulze, D. G. The Influence of Aluminum on Iron Oxides. VIII. Unit-Cell Dimensions of Al-Substituted Goethites and Estimation of Al from Them. *Clays Clay Miner.* **1984**, *32* (1), 36–44.
(125) Schwertmann, U.; Taylor, R. M. Iron Oxides. In *Minerals in Soil Environments*; Dixon, J. B., Weed, S. B., Eds.; Soil Science Society of America, 1989; pp 379–438.
(126) Manceau, A.; Schlegel, M. L.; Musso, M.; Sole, V. A.; Gauthier, C.; Petit, P. E.; Trolard, F. Crystal Chemistry of Trace Elements in Natural and Synthetic Goethite. *Geochim. Cosmochim. Acta* **2000**, *64* (21), 3643–3661.
(127) Goldsztaub, M. S. No Title. *Bull. Soc. Fr. Miner.* **1935**, *58*, 6–67.
(128) Hoppe, V. W. No Title. *Z. Krist.* **1940**, *103*, 73–89.
(129) Szytula, A.; Burewicz, A.; Dimitrijevic, Z.; Krasnicki, S.; Rzany, H.; Todorovic, J.; Wanic, A.; Wolski, W. Neutron Diffraction Studies of Alpha-FeOOH. *Phys. Status Solidi* **1968**, *429* (2), 429–434.
(130) Gualtieri, A. F.; Venturelli, P. In Situ Study of the Goethite-Hematite Phase Transformation by Real Time Synchrotron Powder Diffraction. *Am. Mineral.* **1999**, *84* (5–6), 895–904.
(131) Yang, H. X.; Lu, R.; Downs, R. T.; Costin, G. Goethite, Alpha-FeO(OH), from Single-Crystal Data. *Acta Crystallogr. Sect. E-Structure Reports Online* **2006**, *62*, I250–I252.
(132) Böhm, J. Über Aluminium- Und Eisenhydroxyde. *I. Z. Anorg. Allg. Chem.* **1925**, *149*, 203–216.
(133) Trolard, F.; Bourrie, G.; Jeanroy, E.; Herbillon, A. J.; Martin, H. Trace Metals in Natural Iron Oxides from Laterites: A Study Using Selective Kinetic Extraction. *Geochim. Cosmochim. Acta* **1995**, *59* (7), 1285–1297.
(134) Norrish, K.; Taylor, R. M. The Isomorphous Replacement of Iron by Aluminium in Soil Goethites. *J. Soil Sci.* **1961**, *12* (2), 294–306.
(135) Fey, M. V.; Dixon, J. B. Synthesis and Properties of Poorly Crystalline Hydrated Aluminous Goethites. *Clays Clay Miner.* **1981**, *29* (2), 91–100.
(136) Schwertmann, U. The Influence of Aluminium on Iron Oxides: IX. Dissolution of Al-Goethites in 6 M HCl. *Clay Miner.* **1984**, *19* (1), 9–19.
(137) Schulze, D. G.; Schwertmann, U. The Influence of Aluminium on Iron Oxides: X. Properties of Al-Substituted Goethites. *Clay Miner.* **1984**, *19* (4), 521–539.
(138) Schwertmann, U.; Cambier, P.; Murad, E. Properties of Goethites of Varying Crystallinity. *Clays Clay Miner.* **1985**, *33* (5), 369–378.
(139) Schulze, D. G.; Schwertmann, U. The Influence of Aluminium on Iron Oxides: XIII.

Properties of Goethites Synthesized in 0.3 M KOH at 25 C. *Clay Miner.* **1987**, *22*, 83–92.
(140) Hazemann, J.-L.; Berar, J.-F.; Manceau, A. Rietveld Studies of the Aluminium-Iron Substitution in Synthetic Goethite. *Mater. Sci. Forums* **1991**, *79–82*, 821–826.
(141) Schwertmann, U.; Carlson, L. Aluminum Influence on Iron Oxides: XVII. Unit-Cell Parameters and Aluminum Substitution of Natural Goethites. *Soil Sci. Soc. Am. J.* **1994**, *58* (1), 256–261.
(142) Sudakar, C.; Subbanna, G. N.; Kutty, T. R. N. Effect of Cationic Substituants on Particle Morphology of Goethite and the Magnetic Properties of Maghemite Derived from Substituted Goethite. *J. Mater. Sci.* **2004**, *39* (13), 4271–4286.
(143) Alvarez, M.; Rueda, E. H.; Sileo, E. E. Simultaneous Incorporation of Mn and Al in the Goethite Structure. *Geochim. Cosmochim. Acta* **2007**, *71* (4), 1009–1020.
(144) Schwertmann, U.; Cornell, R. M. *Iron Oxides in the Laboratory: Preparation and Characterization*, 2nd ed.; Wiley-VCH, 2000.
(145) Kosmulski, M. pH Dependent Surface Charging and Points of Zero Charge. III. Update. *J. Colloid Interface Sci.* **2006**, *298* (2), 730–741.
(146) Kosmulski, M. Compilation of PZC and IEP of Sparingly Soluble Metal Oxides and Hydroxides from Literature. *Adv. Colloid Interface Sci.* **2009**, *152* (1–2), 14–25.
(147) Hu, Y.-J.; Kestrel Schwaiger, L.; Booth, C. H.; Kukkadapu, R. K.; Cristiano, E.; Kaplan, D.; Nitsche, H. Molecular Interactions of plutonium(VI) with Synthetic Manganese-Substituted Goethite. *Radiochim. Acta* **2010**, *98* (9–11), 655–663.
(148) Bauer, E. D.; Thompson, J. D.; Sarrao, J. L.; Morales, L. A.; Wastin, F.; Rebizant, J.; Griveau, J. C.; Javorsky, P.; Boulet, P.; Colineau, E.; et al. Structural Tuning of Unconventional Superconductivity in PuMGa5 (M=Co, Rh). *Phys. Rev. Lett.* **2004**, *93* (14), 1–4.
(149) Conradson, S. D. Application of X-Ray Absorption Fine Structure Spectroscopy to Materials and Environmental Science. *Appl. Spectrosc.* **1998**, *52* (7), 252A–279A.
(150) Booth, C. H. Real-Space X-Ray Analysis Package (RSXAP).
(151) Li, G. G.; Bridges, F.; Booth, C. H. X-Ray-Absorption Fine-Structure Standards - a Comparison of Experiment and Theory. *Phys. Rev. B* **1995**, *52* (9), 6332–6348.
(152) Hayes, T. M.; Boyce, J. B. Extended X-Ray Absorption Fine Structure Spectroscopy. In *Solid State Physics, Volume 37*; Ehrenreich, H., Seitz, F., Turnbull, D., Eds.; Academic Press: New York, NY, 1982; pp 178–351.
(153) Keeney-Kennicutt, W. L.; Morse, J. W. The Redox Chemistry of Pu(V)O2+ Interaction with Common Mineral Surfaces in Dilute Solutions and Seawater. *Geochim. Cosmochim. Acta* **1985**, *49* (12), 2577–2588.
(154) Sanchez, A. L.; Murray, J. W.; Sibley, T. H. The Adsorption of Plutonium IV and V on Goethite. *Geochim. Cosmochim. Acta* **1985**, *49* (11), 2297–2307.
(155) Powell, B. A.; Fjeld, R. A.; Kaplan, D. I.; Coates, J. T.; Serkiz, S. M. Pu(V)O2+ Adsorption and Reduction by Synthetic Hematite and Goethite. *Environ. Sci. Technol.* **2005**, *39* (7), 2107–2114.
(156) Sowden, R. G. No Title. *J. Nucl. Mater.* **1963**, *8*, 81.
(157) Romanchuk, A. Y.; Kalmykov, S. N.; Aliev, R. A. Plutonium Sorption onto Hematite Colloids at Femto- and Nanomolar Concentrations. *Radiochim. Acta* **2011**, *99* (3), 137–144.
(158) Hixon, A. E.; Arai, Y.; Powell, B. A. Examination of the Effect of Alpha Radiolysis on plutonium(V) Sorption to Quartz Using Multiple Plutonium Isotopes. *J. Colloid Interface*

*Sci.* **2013**, *403*, 105–112.
(159) Wilk, P. A.; Shaughnessy, D. A.; Wilson, R. E.; Nitsche, H. Interfacial Interactions between Np(V) and Manganese Oxide Minerals Manganite and Hausmannite. *Environ. Sci. Technol.* **2005**, *39* (8), 2608–2615.
(160) Parsons-Moss, T. Interactions of Plutonium and Lanthanides with Ordered Mesoporous Materials, University of California, Berkeley, 2014.
(161) Hu, Y.-J. Reaction of Plutonium(VI) with the Manganese-Substituted Iron Oxide Mineral Goethite, University of Califonia, Berkeley, 2011.
(162) Allen, P. G.; Bucher, J. J.; Clark, D. L.; Edelstein, N. M.; Ekberg, S. A.; Gohdes, J. W.; Hudson, E. A.; Kaltsoyannis, N.; Lukens, W. W.; Neu, M. P.; et al. Multinuclear NMR, Raman, EXAFS, and X-Ray Diffraction Studies of Uranyl Carbonate Complexes in near-Neutral Aqueous Solution. X-Ray Structure of [C(NH2)3]6[(UO2)3(CO3)6].cntdot.6.5H2O. *Inorg. Chem.* **1995**, *34* (19), 4797–4807.
(163) Williams, A. G. B.; Scherer, M. M. Spectroscopic Evidence for Fe(II)-Fe(III) Electron Transfer at the Iron Oxide-Water Interface. *Environ. Sci. Technol.* **2004**, *38* (18), 4782–4790.
(164) Waite, T. D. Photo-Redox Processes at the Mineral-Water Interface. In *Volume 23: Mineral-Water Interface Geochemistry*; Hochella, J. M. F., White, A. F., Eds.; Mineralogical Society of America, 1990; pp 559–903.
(165) Qian, X.; Zhang, X.; Bai, Y.; Li, T.; Tang, X.; Wang, E.; Dong, S. Photoelectrochemical Characteristics of a-Fe2O3 Nanocrystalline Semiconductor Thin Film. *J. Nanoparticle Res.* **2000**, *2* (2), 191–198.
(166) Gratzel, M. *Heterogenous Photochemical Electron Transfer*; CRC Press: Boca Raton, FL, 1988.
(167) Iwamoto, M.; Abe, T.; Tachibana, Y. Control of Bandgap of Iron Oxide through Its Encapsulation into SiO2- Based Mesoporous Materials. *J. Mol. Catal. A Chem.* **2000**, *155* (1–2), 143–153.
(168) Leland, J. K.; Bard, A. J. Photochemistry of Colloidal Semiconducting Iron Oxlde Polymorphs. *J. Phys. Chem.* **1987**, *91* (19), 5076–5083.
(169) Sherman, D. M. Electronic Structures of iron(III) and manganese(IV) (Hydr)oxide Minerals: Thermodynamics of Photochemical Reductive Dissolution in Aquatic Environments. *Geochim. Cosmochim. Acta* **2005**, *69* (13), 3249–3255.
(170) Ewing, R. C. Long-Term Storage of Spent Nuclear Fuel. *Nat. Mater.* **2015**, *14* (3), 252–257.
(171) Zanonato, P.; Di Bernardo, P.; Bismondo, A.; Liu, G.; Chen, X.; Rao, L. Hydrolysis of Uranium(VI) at Variable Temperatures (10-85°C). *J. Am. Chem. Soc.* **2004**, *126* (17), 5515–5522.
(172) Itagaki, H.; Nakayama, S.; Tanaka, S.; Yamawaki, M. Effect of Ionic Strength on the Solubility of Neptunium(V) Hydroxide. *Radiochim. Acta* **1992**, *58/59*, 61–66.
(173) Lemire, B. R. J.; Boyer, G. D.; Campbell, A. B. The Solubilities of Sodium and Potassium Dioxoneptunium(V) Carbonate Hydrates at 30, 50 and 75°C. *Radiochim. Acta* **1993**, *61* (2), 57–63.
(174) Nitsche, H.; Gatti, R. C.; Standifer, E. M. *Measured Solubilities and Speciations of Neptunium, Plutonium, and Americium in a Typical Groundwater (J-13) Porn the Yucca Mountain Region Milestone Report 3010- WBS 1.2.3 .4.1.3.1 LA-12562-MS*; 1993.
(175) Nitsche, H.; Roberts, K.; Becraft, K.; Prussin, T.; Keeney, D.; Carpenter, S.; Hobart, D.

*Solubility and Speciation Results from Over- and Under-Saturation Experiments on Neptunium, Plutonium and Americium in Water from Yucca Mountain Region Well UE-25p#1. Report LA-13017-MS.*; 1995.

(176) Neck, V.; Fanghänel, T.; Rudolph, G.; Kim, J. I. Thermodynamics of Neptunium(Y) in Concentrated Salt Solutions: Chloride Complexation and Ion Interaction (Pitzer) Parameters for the NpO+2 Ion. *Radiochim. Acta* **1995**, *69* (1), 39–48.

(177) Fanghänel, T.; Neck, V.; Kim, J. I. Thermodynamics of Neptunium(V) in Concentrated Salt Solutions: II. Ion Interaction (Pitzer) Parameters for Np(V) Hydrolysis Species and Carbonate Complexes. *Radiochim. Acta* **1995**, *69* (3), 169–176.

(178) Bearden, J. A.; Burr, A. F. Reevaluation of X-Ray Atomic Energy Levels. *Rev. Mod. Phys.* **1967**, *39* (1), 125–142.

(179) Rehr, J. J.; Albers, R. C. Theoretical Approaches to X-Ray Absorption Fine Structure. *Rev. Mod. Phys.* **2000**, *72* (3), 621–654.

(180) *X-Ray Absorption: Principles, Applications, Techniques of EXAFS, SEXAFS and XANES*; Koningsberger, D. C., Prins, R., Eds.; John Wiley and Sons: New York, NY, 1988.

(181) Ravel, B.; Newville, M. ATHENA, ARTEMIS, HEPHAESTUS: Data Analysis for X-Ray Absorption Spectroscopy Using IFEFFIT. *J. Synchrotron Radiat.* **2005**, *12* (4), 537–541.

(182) Webb, S. M. SIXPack a Graphical User Interface for XAS Analysis Using IFEFFIT. *Phys. Scr.* **2005**, *115*, 1011–1014.

(183) de Leon, J.; Rehr, J. J.; Zabinsky, S. I.; Albers, R. C. Ab Initio Curved-Wave X-Ray-Absorption Fine Structure. *Phys. Rev. B* **1991**, *44* (9), 4146–4156.

(184) Rehr, J. J.; Albers, R. C. Scattering-Matrix Formulation of Curved-Wave Multiple-Scattering Theory: Application to X-Ray-Absorption Fine Structure. *Phys. Rev. B* **1990**, *41* (12), 8139–8149.

(185) Rehr, J. J.; de Leon, J.; Zabinsky, S. I.; Albers, R. C. Theoretical X-Ray Absorption Fine Structure Standards. *J. Am. Chem. Soc.* **1991**, *113* (14), 5135–5140.

(186) Rehr, J. J.; Albers, R. C.; Zabinsky, S. I. High-Order Multiple-Scattering Calculations of X-Ray-Absorption Fine Structure. *Phys. Rev. Lett.* **1992**, *69* (23), 3397–3400.

(187) Newville, M. EXAFS Analysis Using FEFF and FEFFIT. *J. Synchrotron Radiat.* **2001**, *8* (2), 96–100.

(188) Pabalan, R. T.; Turner, D. R.; Bertetti, F. P.; Prikryl, J. D. UraniumVI Sorption onto Selected Mineral Surfaces: Key Geochemical Parameters. In *Adsorption of Metals by Geomedia: Variables, Mechanisms, and Model Applications*; Jenne, E. A., Ed.; Elsevier, 1998; pp 99–130.

(189) Wang, P. M.; Anderko, A.; Turner, D. R. Thermodynamic Modeling of the Adsorption of Radionuclides on Selected Minerals. I: Cations. *Ind. Eng. Chem. Res.* **2001**, *40* (20), 4428–4443.

(190) Girvin, D. C.; Ames, L. L.; Schwab, A. P.; McGarrah, J. E. Neptunium Adsorption on Synthetic Amorphous Iron Oxyhydroxide. *J. Colloid Interface Sci.* **1991**, *141* (1), 67–78.

(191) Kohler, M.; Honeyman, B. D.; Leckie, J. O. Neptunium(V) Sorption on Hematite (Alpha-Fe2O3) in Aqueous Suspension : The Effect of CO2. *Radiochim. Acta* **1999**, *85*, 33–48.

(192) Nakata, K.; Nagasaki, S.; Tanaka, S.; Sakamoto, Y.; Tanaka, T.; Ogawa, H. Sorption and Reduction of neptumium(V) on the Surface of Iron Oxides. *Radiochim. Acta* **2002**, *90* (9–11), 665–669.

(193) Khasanova, A. B.; Kalmykov, S. N.; Perminova, I. V.; Clark, S. B. Neptunium Redox Behavior and Sorption onto Goethite and Hematite in the Presence of Humic Acids with

Different Hydroquinone Content. *J. Alloys Compd.* **2007**, *444–445* (SPEC. ISS.), 491–494.
(194) Kalmykov, S. N.; Romanchuk, A. Y. Actinides Sorption onto Hematite: Experimental Data, Surface Complexation Modeling and Linear Free Energy Relationship. *Radiochim. Acta* **2014**, *102* (4), 303–310.
(195) Turner, D. R. Neptunium(V) Sorption on Montmorillonite: An Experimental and Surface Complexation Modeling Study. *Clays Clay Miner.* **1998**, *46* (3), 256–269.
(196) Bandura, A. V.; Lvov, S. N. The Ionization Constant of Water over Wide Ranges of Temperature and Density. *J. Phys. Chem. Ref. Data* **2006**, *35* (1), 15–30.
(197) Hsi, C. D.; Langmuir, D. Adsorption of Uranyl onto Ferric Oxyhydroxides: Application of the Surface Complexation Site-Binding Model. *Geochim. Cosmochim. Acta* **1985**, *49* (9), 1931–1941.
(198) Amayri, S.; Breckheimer, M.; Drebert, J.; Reich, T. EXAFS Study of Neptunium(V) Sorption onto Hematite. In *Speciation Techniques and Facilities for Radioactive materials at Synchrotron Light Sources*; OECD Nuclear Energy Agency, 2007; pp 163–173.
(199) Bunker, G. *Introduction to XAFS: A Practical Guide to X-Ray Absorption Fine Structure Spectroscopy*; Cambridge University Press Cambridge: UK, 2010.
(200) Forbes, T. Z.; Burns, P. C.; Skanthakumar, S.; Soderholm, L. Synthesis , Structure , and Magnetism of Np2O5. *J. Am. Chem. Soc.* **2007**, *129* (10), 2760–2761.
(201) Lu, N.; Reimus, P. W.; Parker, G. R.; Conca, J. L.; Triay, I. R. Sorption Kinetics and Impact of Temperature, Ionic Strength and Colloid Concentration on the Adsorption of Plutonium-239 by Inorganic Colloids. *Radiochim. Acta* **2003**, *91* (12), 713–720.
(202) Estes, S. L.; Arai, Y.; Becker, U.; Fernando, S.; Yuan, K.; Ewing, R. C.; Zhang, J.; Shibata, T.; Powell, B. A. A Self-Consistent Model Describing the Thermodynamics of Eu(III) Adsorption onto Hematite. *Geochim. Cosmochim. Acta* **2013**, *122*, 430–447.
(203) Rao, L. Thermodynamics of Actinide Complexation in Solution at Elevated Temperatures: Application of Variable-Temperature Titration Calorimetry. *Chem. Soc. Rev.* **2007**, *36* (6), 881–892.
(204) Hayes, K. F.; Papelis, C.; Leckie, J. O. Modeling Ionic Strength Effects on Anion Adsorption at Hydrous Oxide/solution Interfaces. *J. Colloid Interface Sci.* **1988**, *125* (2), 717–726.
(205) Chassé, A. W.; Ohno, T.; Higgins, S. R.; Amirbahman, A.; Yildirim, N.; Parr, T. B. Chemical Force Spectroscopy Evidence Supporting the Layer-by-Layer Model of Organic Matter Binding to Iron (Oxy)hydroxide Mineral Surfaces. *Environ. Sci. Technol.* **2015**, *49*, 9733–9741.
(206) Hayes, K. F.; Leckie, J. O. Modeling Ionic-Strength Effects on Cation Adsorption At Hydrous Oxide-Solution Interfaces. *J. Colloid Interface Sci.* **1987**, *115* (2), 564–572.
(207) Lützenkirchen, J. Ionic Strength Effects on Cation Sorption to Oxides: Macroscopic Observations and Their Significance in Microscopic Interpretation. *J. Chromatogr. A* **1997**, *195* (1), 149–155.
(208) Brown, G. E.; Henrich, V. E.; Casey, W. H.; Clark, D. L.; Eggleston, C.; Felmy, A.; Goodman, D. W.; Grtzel, M.; Maciel, G.; Mccarthy, M. I.; et al. Metal Oxide Surfaces and Their Interactions with Aqueous Solutions and Microbial Organisms Microbial Organisms. *Chem. Rev.* **1999**, *99*, 77–174.
(209) Nakayama, S.; Sakamoto, Y. Sorption of Neptunium on Naturally-Occurring Iron-Containing Minerals. *Radiochim. Acta* **1991**, *52/53*, 153–157.

(210) Arai, Y.; Moran, P. B.; Honeyman, B. D.; Davis, J. A. In Situ Spectroscopic Evidence for neptunium(V)-Carbonate Inner-Sphere and Outer-Sphere Ternary Surface Complexes on Hematite Surfaces. *Environ. Sci. Technol.* **2007**, *41* (11), 3940–3944.
(211) Müller, K.; Gröschel, A.; Rossberg, A.; Bok, F.; Franzen, C.; Brendler, V.; Foerstendorf, H. In Situ Spectroscopic Identification of neptunium(V) Inner-Sphere Complexes on the Hematite-Water Interface. *Environ. Sci. Technol.* **2015**, *49* (4), 2560–2567.
(212) Lu, N.; Cotter, C. R.; Kitten, H. D.; Bentley, J.; Triay, I. R.; Lu, B. N.; Cotter, C. R.; Kitten, H. D.; Bentley, J.; Triay, I. R. Reversibility of Sorption of Plutonium-239 onto Hematite and Goethite Colloids. *Radiochim. Acta* **1998**, *83* (4), 167–173.
(213) Lu, N.; Triay, I. R.; Cotter, C. R.; Kitten, H. D.; Bentley, J. *Reversibility of Sorption of Plutonium-239 onto Colloids of Hematite, Goethite, Smectite, and Silica : A Milestone Final Report of YMP, July 10, 1998*; 1998.
(214) Powell, B. A.; Fjeld, R. A.; Kaplan, D. I.; Coates, J. T.; Serkiz, S. M. Pu(V)O2+ Adsorption and Reduction by Synthetic Magnetite (Fe3O4). *Environ. Sci. Technol.* **2004**, *38* (22), 6016–6024.
(215) Tsoulfanidis, N.; Landsberger, S. *Measurement and Detection of Radiation*, 4th ed.; CRC Press: Boca Raton, FL, 2015.
(216) Leo, W. R. *Techniques for Nuclear and Particle Physics Experiments: A How-to Approach*, 2nd ed.; Springer, 1994.
(217) McDowell, W. J.; McDowell, B. L. *Liquid Scintillation Alpha Spectrometry*; CRC Press: Boca Raton, FL, 1994.
(218) Salonen, L. Liquid Scintillation Spectrometry 1992. In *Radiocarbon 1993*; Noakes, J. E., Schönhofer, F., Polach, H. A., Eds.; Michigan, 1993; pp 361–372.
(219) Roessler, N.; Valenta, R. J.; Cauter, S. van. Time-Resolved Liquid Scintillation Counting. In *Liquid Scintillation Counting and Organic Scintillators*; Ross, H., Noakes, J. E., Spaulding, J. D., Eds.; Lewis Publishers, Inc.: Michigan, 1991; pp 501–511.
(220) Sémon, L.; Boehme, C.; Billard, I.; Hennig, C.; Lützenkirchen, K.; Reich, T.; Roßberg, A.; Rossini, I.; Wipff, G. Do Perchlorate and Triflate Anions Bind to the Uranyl Cation in an Acidic Aqueous Medium? A Combined EXAFS and Quantum Mechanical Investigation. *Chemphyschem* **2001**, *2* (10), 591–598.
(221) Teo, B. K. *EXAFS: Basic Principles and Data Analysis*; Springer: New York, 1986; Vol. 9.
(222) Einstein, A. On a Heuristic Viewpoint Concerning the Production and Transformation of Light. *Ann. Phys.* **1905**, *17* (6), 132–148.
(223) Victoreen, J. A. The Absorption of Incident Quanta by Atoms as Defined by the Mass Photoelectric Absorption Coefficient and the Mass Scattering Coefficient. *J. Appl. Phys.* **1948**, *19* (9), 855–860.
(224) McMaster, W. H.; Del Grande, N. K.; Mallett, J. H.; Hubbell, J. H. *Compilation of X-Ray Cross Sections UCRL--50174(Sec.2)(Rev.1)*; 1969.
(225) Kossel, W. Zum Bau Der Rontgenspektren. *Zeitschrift für Phys.* **1920**, *1* (1), 119–134.
(226) Kossel, W. ??ber Die Ausbildung Der R??ntgenserien Mit Wachsender Ordnungszahl. *Zeitschrift für Phys.* **1920**, *2* (5), 470–478.
(227) Kronig, R. de L. Zur Theorie Der Feinstruktur in Den Röntgenabsorptionsspektren. *Zeitschrift für Phys.* **1931**, *70* (5), 317–323.
(228) Kronig, R. D. L. Zur Theorie Der Feinstruktur in Den Röntgenabsorptionsspektren.III. *Zeitschrift für Phys.* **1932**, *75* (7), 468–475.

(229) Hursthouse, A. S.; Baxter, M. S.; McKay, K.; Livens, F. R. Evaluation of Methods for the Assy of Neptunium and Other Long-Lived Actinides in Environmental Matrices. *J. Radioanal. Nucl. Chem. Artic.* **1992**, *157* (2), 281–294.
(230) Bott, A. W. Voltammetric Determination of Trace Concentrations of Metals in the Environment. *Curr. Sep.* **1995**, *14* (1), 24–30.
(231) Cohen, D. Electrochemical Studies of Plutonium Ions in Perchloric Acid Solution. *J. Inorg. Nucl. Chem.* **1961**, *18* (1949), 207–210.
(232) Begg, J. D.; Zavarin, M.; Tumey, S. J.; Kersting, A. B. Plutonium Sorption and Desorption Behavior on Bentonite. *J. Environ. Radioact.* **2015**, *141*, 106–114.